# DESIGN AND SYNTHESIS OF THIAZOLE-BASED SMALL MOLECULES TO INHIBIT THE INFLAMMATORY CYTOKINE ONCOSTATIN M

by

Samuel Randall

A thesis

submitted in partial fulfillment

of the requirements for the degree of

Master of Science in Chemistry

Boise State University

May 2022

BOISE STATE UNIVERSITY GRADUATE COLLEGE

# DEFENSE COMMITTEE AND FINAL READING APPROVALS

of the thesis submitted by

Samuel Randall

Thesis Title: Design and Synthesis of Thiazole-Based Small Molecules to Inhibit the Inflammatory Cytokine Oncostatin M

Date of Final Oral Examination: 30 November 2021

The following individuals read and discussed the thesis submitted by student Samuel Randall, and they evaluated their presentation and response to questions during the final oral examination. They found that the student passed the final oral examination.

| | |
|---|---|
| Don Warner, Ph.D. | Chair, Supervisory Committee |
| Lisa Warner, Ph.D. | Member, Supervisory Committee |
| Henry Charlier, Ph.D. | Member, Supervisory Committee |

The final reading approval of the thesis was granted by Don Warner, Ph.D., Chair of the Supervisory Committee. The thesis was approved by the Graduate College.

## DEDICATION

I would like to dedicate this thesis to the mother, Dena Gambrel. She has worked incredibly hard for her three sons to have the best life she could give them. She has always been there through the most challenging times in our life, and I am so grateful for the unconditional love she has expressed throughout my childhood and adulthood years.

ACKNOWLEDGMENTS

First and foremost, I would like to thank Dr. Don Warner for his time to be a first-class mentor and teacher. I feel like I have grown tremendously as a chemist and even more as a person while working in Dr. Warner's lab. The time he dedicates towards the growth and development of his students speaks volumes about his character. It was not uncommon that he would work beyond regular hours to answer any questions regarding my research or questions in general. I am also very appreciative of the honest, critical feedback I have received from him throughout my study. He is truly one of the highlights of the Boise State University chemistry department, and I would not be in the position I am today if I was not a member of his research group

I would also like to thank the entirety of the Dr. Don Warner lab and others from the Department of Chemistry and Biochemistry. From pulling capillary tubes and cutting TLC plates to reviewing critical data and documents, my lab-mates were always there for me. I would like to thank Joseph Tuccinardi and Riley Olsen for training me during my first weeks when I was learning the basics of organic synthesis. Also, I would like to thank Grace Coughlin and Ashley Tran for their work in preparing and subjecting oncostatin M to fluorescence quenching assays with my small molecules. Also, I would like to thank both Jeremy Daniels and Tyson Hardy from the stockroom. In addition, I am appreciative of Dr. Joseph Dumais for keeping the NMR instrumentation up and running.

Collaborative efforts among the Don Warner lab, the Jorcyk lab, the Lisa Warner lab, and the Boise State University Biomolecular Research Center (BRC) have been

critical to the success of my work at BSU. The Jorcyk lab has played a considerable role in my research, as they have performed ELISA and Western blot experiments. More specifically, I would like to acknowledge Cody Wolfe and Cooper McGrath for their work in subjecting my small molecules to ELISA experiments. The Lisa Warner lab has also been instrumental to the success of my work. Dr. Lisa Warner has always made herself available to help answer my questions concerning assays and techniques used for the drug discovery process. I would also like to thank Aaron Ajeti for his work in the chemical shift perturbation experiments. Also, I would like to acknowledge Xinzhu Pu and Luke Woodbury for their work in characterizing my small molecules by high-resolution mass spectrometry.

I want to thank my committee members, Dr. Don Warner, Dr. Lisa Warner, and Dr. Henry Charlier. You have all had a smiling reception to any of my questions concerning my research. I would like to express my gratitude towards the Boise State Department of Chemistry and Biochemistry for granting me a teaching assistantship, which allowed me to develop my skills as a competent teacher and researcher. In addition, I am very appreciative of the late Dr. Bob Hibbs, as I was awarded the Bob Hibbs research assistantship in the Fall of 2020.

The work in this thesis was supported by the METAvivor Quinn Davis Northwest Arkansas METSqueradeFund, an Institutional Development Awards (IDeA) from the National Institute of General Medical Sciences of the National Institutes of Health under Grant #P20GM103408. Support was also received from the Biomolecular Research Center at Boise State University with funding from the Institutional Development Awards (IDeA) from the National Institute of General Medical Sciences of

the National Institutes of Health under Grants #P20GM103408, P20GM109095, and 1C06RR020533. Additional support for the Biomolecular Research Center was received from the National Science Foundation, Grants #0619793 and #0923535; the MJ Murdock Charitable Trust; Lori and Duane Stueckle, and the Idaho State Board of Education. The images contained in this document were created with Biorender.com and Inkscape.com.

ABSTRACT

The body's innate ability to produce an inflammatory response due to tissue irritation or damage is essential for growth and survival. The inflammatory response can be triggered by numerous stimuli, including physical trauma, inhalation of dangerous debris (such as silica and asbestos), tobacco/alcohol consumption, microbiota, diet, and other lifestyle stressors. In a well-orchestrated inflammatory response, the circulatory system increases blood flow and capillary permeability in the inflamed area to deliver nutrients, white blood cells, and inflammatory mediating molecules. However, a dysregulated inflammatory response can lead to chronic inflammation. Emerging evidence continues to frame oncostatin M (OSM) as a pro-inflammatory cytokine that drives chronic inflammation. The overexpression of OSM has been implicated in the maintenance of several chronic inflammatory diseases, such as rheumatoid arthritis, inflammatory bowel disease, metabolic syndrome, systemic sclerosis, lupus, and many different forms of cancer. Therefore, OSM presents itself as a potential therapeutic target.

To the best of our research group's knowledge, no clinically approved drugs inhibit OSM signaling. Therefore, 26 lead small molecule inhibitors (SMIs) were generated by high-throughput virtual screening of ~1.65 million compounds targeting the putative receptor binding site of OSM. Out of the 26 compounds subjected to an enzyme-linked immunosorbent assay, SMI-8 was identified as one of the most potent inhibitors of OSM signaling. However, the predicted toxicity and stereoselective synthesis of SMI-8 makes the compound a poor drug candidate. So, mono- and bisthiazole-based analogs of

SMI-8 were designed and synthesized using five distinct synthetic pathways to produce a total of 35 compounds. Enzyme-linked immunosorbent assay (ELISA) experiments and Western blot assays were performed to determine the inhibitory activity of several of the analogs. In addition, fluorescence quenching assays, differential scanning fluorimetry experiments, and chemical shift perturbation experiments identified direct binding properties of the SMIs.

ELISA experiments revealed that almost all the SMI-8 analogs tested effectively decreased the amount of pSTAT3 expressed in T47D human breast cancer cells. Tryptophan fluorescence quenching assays determined the dissociation constant ($K_D$) values of SMI-8 and a structurally similar analog, SMI-8S, which were $6 \pm 1$ μM, and $14 \pm 3$ μM, respectively. Unfortunately, the fluorescence quenching assay could not be used to study the binding affinity of other analogs, as they were found to fluoresce at the same wavelength as the tryptophan residue of the OSM protein.

In an attempt to solve this problem, differential scanning fluorimetry (DSF) experiments were used to determine the relative binding characteristics of the compounds. The data obtained from the DSF experiments suggest that most of the analogs tested bind to the unfolded state of OSM, as the ligands decrease the melting temperature of the protein. In addition, a chemical shift perturbation (CSP) experiment suggests that SMI-8S interacts with the amino acids Gln90, Arg91, and Leu 92 at the putative receptor binding site of OSM. The data, findings, and research within this thesis provide enough evidence to support the idea that SMIs can target OSM as a practical approach to treating various chronic inflammatory diseases.

TABLE OF CONTENTS

LIST OF TABLES

LIST OF FIGURES

LIST OF ABBREVIATIONS

| | |
|---|---|
| ADMET | Absorption, distribution, metabolism, excretion, and toxicity |
| AML | Acute myeloid leukemia |
| BAX | B cell lymphoma-2 associated X-protein |
| BCL-2 | B cell lymphoma-2 |
| BMe | beta-mercaptoethanol |
| BOILED | Brain or intestinal estimated permeation method |
| BSU | Boise State University |
| CD | Crohn's disease |
| COPD | Chronic obstructive pulmonary disease |
| CSP | Chemical shift perturbation |
| DME | Dimethoxyethane |
| DMF | Dimethylformamide |
| DMSO | Dimethyl sulfoxide |
| DNA | Deoxyribonucleic acid |
| DSF | Differential scanning fluorimetry |
| dsSSc | Diffuse systemic sclerosis |
| ELISA | Enzyme-linked immunosorbent assay |
| FLS | Fibroblast-like synoviocytes |
| FEB | Free energy of binding |
| FQ | Fluorescence quenching |

| | |
|---|---|
| HDMECs | Human dermal microvascular endothelial cells |
| HER2 | Human epidermal growth factor receptor 2 |
| hGH | Human growth hormone |
| HMPA | Hexamethylphosphoramide |
| HPLC | High-performance liquid chromatography |
| HRMS | High-resolution mass spectrometry |
| HSQC | Heteronuclear Single Quantum Coherence |
| IBD | Irritable bowel disease |
| $IC_{50}$ | Half-maximal inhibitory concentration |
| ICAM1 | Intercellular adhesion molecule 1 |
| JAK | Janus kinase |
| $K_D$ | Dissociation constant |
| lcSSC | Limited systemic sclerosis |
| LIF | Leukemia inhibitory factor |
| LIFR | Leukemia inhibitory factor receptor |
| mAb | Monoclonal antibody |
| MAPK | Mitogen-activated protein kinase |
| MMP-1 | Matrix metalloproteinase-1 |
| MP | Melting point |
| NMR | Nuclear magnetic resonance |
| OSM | Oncostatin M |
| OSMRβ | Oncostatin M receptor beta |
| qPCR | Quantitative polymerase chain reaction |

| | |
|---|---|
| PDB | Protein data bank |
| PPI | Protein-protein interaction |
| QSAR | Quantitative structure-activity relationship |
| RA | Rheumatoid arthritis |
| RANK | Receptor activator of nuclear factor kappa beta |
| SMI | Small molecule inhibitor |
| SPR | Surface plasmon resonance |
| SSc | Systemic sclerosis |
| STAT | Signal transducer and activator of transcription |
| STD-NMR | Saturation transfer difference-nuclear magnetic resonance |
| TBAI | Tetra-n-butylammonium iodide |
| TCEP | Tris(2-carboxyethyl)phosphine |
| TNBC | Triple negative breast cancer |
| TNF-α | Tumor necrosis factor-alpha |
| TSA | Thermal shift assay |
| UC | Ulcerative colitis |
| WT | Wild type |

# CHAPTER ONE: INTRODUCTION

## 1.1 Overview of Chapter One

Acute inflammation is the body's normal, healthy response to physical trauma and foreign invaders. In contrast, chronic inflammation is characterized by slow, long-term inflammation that can last months to years without resolve. Due to the societal and economic burden, chronic inflammatory diseases pose a serious threat to humankind, and therefore, it is necessary to understand what causes them. Evidence suggests that oncostatin M has a role in upregulating inflammatory pathways that drive chronic inflammatory diseases such as irritable bowel disease (IBD), rheumatoid arthritis (RA), metastasis of breast cancer, and systemic sclerosis (SSc). Currently, no small molecule inhibitors that target oncostatin M have been published. We hypothesize that a small molecule inhibitor can be synthesized that selectively binds to the active site of oncostatin M, thereby rendering it unable to signal.

## 1.2 A Brief Overview of Inflammation

### 1.2.1 Acute Inflammation

Inflammation is the natural, biological response to numerous damaging incidents: physical trauma, foreign invaders/pathogens, toxic compounds, or autoimmune responses. The acute inflammatory process consists of separate, antagonistic processes in the body. The first step pertains to the initial inflammatory response to the stimuli where cells are recruited to the area of damage; the latter step is the removal of damaged cells, tissue, and perhaps foreign invaders.[1] The first part is typically referred to as the initial

response, and the latter part is commonly referred to as the resolution stage. A typical acute inflammatory response lasts only a few days.[2] Overall, the main objective of the body during an immune response is to increase blood flow to the injured area in order to deliver nutrients, as well as remove any injured or compromised tissue. The rest of this section will discuss the basic mechanisms observed during an acute inflammatory response.

Figure 1.1 outlines the acute inflammatory response in 3 basic steps. In panel 1, histamine is released mainly by mast cells in response to a traumatic event.[2] Once released, histamine acts upon the H1-receptors of the vascular endothelial cells to cause vasodilation, which widens the blood vessels to increase blood flow to tissues. In addition, proteins known as cytokines are released by macrophages and other leukocytes. Cytokines are low molecular weight proteins that are involved in mediating cell signaling and inflammatory responses. As seen in panel 2, some cytokines can also act as chemotactic factors, which means they can recruit leukocytes such as neutrophils and monocytes to the specific site of damage through a process called chemotaxis.[3] Panel 3 depicts the resolution stage, where tissue healing occurs and tissue homeostasis is achieved.

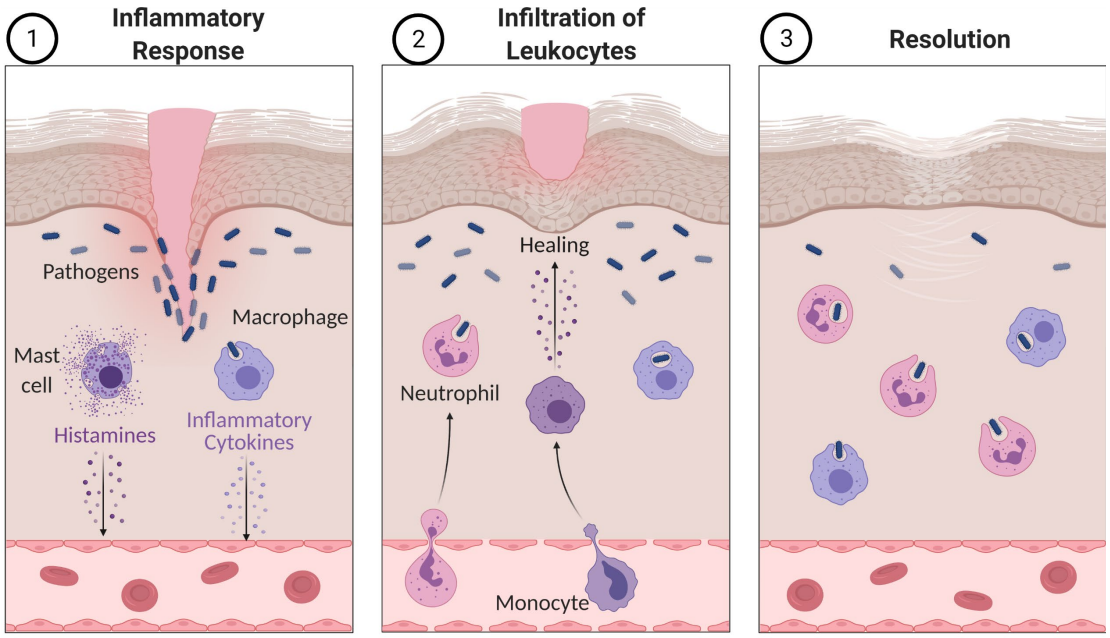


**Figure 1.1 The acute inflammatory response**

(**1**) Physical trauma, or foreign invaders signal the mast cells to release histamine, as well as signal for the release of cytokines from macrophages. (**2**) White blood cells such as neutrophils, monocytes, and macrophages invade the damaged tissue. (**3**) Once the tissue is healed, or the foreign invader is neutralized, cellular debris is transported away from the injury site, and normal tissue function can resume.

In addition to releasing histamine, leukocytes also have a specific role in identifying proteins and carbohydrates that are foreign to the body and releasing inflammatory mediators such as cytokines. Leukocytes residing in the tissue and circulating leukocytes can recognize damaged cells or foreign invaders using pattern recognition receptors (PRRs). These PRRs directly or indirectly detect pathogen-associated molecular patterns (PAMPs). PAMPs include foreign structures, such as proteins and nucleic acids, that belong to invading organisms.[3] PRRs are typically found in the cytosol or on the cell surface itself. In response to PAMPs, PRRs can trigger activating transcription factors such as nuclear factor-kappa beta, activator protein-1, cAMP element-response binding protein, CCAAT-enhancer-binding proteins, and interferon regulatory factors. Once transcribed in the body, these factors can upregulate

the production of cytokines.[4] These small signaling proteins can then further drive the inflammatory response by recruiting more leukocytes to the area of inflammation.

### 1.2.2 Chronic Inflammation

In contrast to acute inflammation, chronic inflammation is characterized by a long-term inflammatory response that can last months to years.[5] Figure 1.2 illustrates a simplified example of chronic inflammation occurring in nerve tissue driven in part by cytokines. In panel 1, resident macrophages can be seen secreting cytokines into the tissue due to trauma. Afterward, panel 2 depicts other macrophages migrating into the tissue space as a result of cytokine signaling. In contrast to acute inflammation, the healing process is stalled at this point, and tissue remodeling fails to occur. Next, panel 3 shows that the newly recruited macrophages are releasing cytokines as well as growth factors.[6] Finally, panel 4 shows a hypothetical height of disease severity where long-term resident macrophages are expressing a pro-inflammatory phenotype and resolution of the wound has not occurred. The accumulation of macrophages at damaged tissue(s) is a strong indicator of chronic inflammation due to their release of cytokines, chemokines, and growth factors.[6-9]

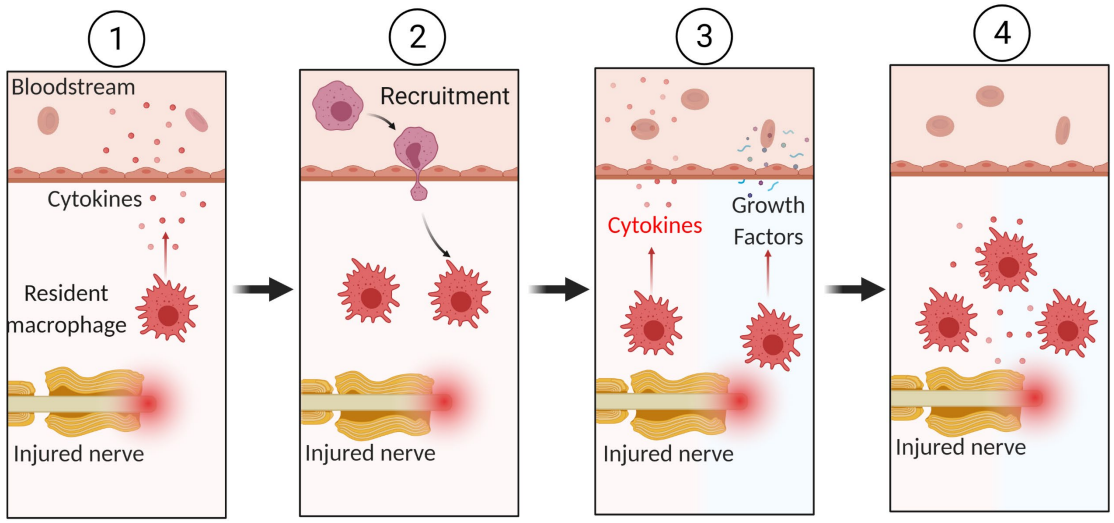


**Figure 1.2 Cytokines maintain chronic inflammation**

(**1**) Upon initial injury, resident macrophages and other leukocytes release pro-inflammatory cytokines and chemokines to attract more leukocytes to the area of inflammation. (**2**) The recruitment of macrophages continues without healing occurring at the site of injury. (**3**) As more macrophages are recruited to the area of inflammation, cytokines and growth factors continue to accumulate in the tissue. (**4**) Over time, long term resident macrophages accumulate in the tissue.

Unlike acute inflammation, chronic inflammatory conditions can result in considerable economic and societal burdens, severely reduced quality of life, and death. These economic burdens include added overall expenditures in one's yearly budget and loss of wages due to complicating factors. The financial burden that is experienced by patients dealing with chronic inflammatory diseases is considerable for the average American. Patients that suffer from inflammatory conditions in the United States spend approximately $38,000 more a year on additional expenditures than healthy individuals.[10] This translates to a loss of half of the income in a typical American household, considering that the median household income from 2015-2019 was $62,843.[11] To make matters worse, those who suffer from chronic inflammatory diseases have a higher chance of missing work, resulting in lost wages. For example, 24% of the individuals who suffer from chronic obstructive pulmonary disease (COPD) report being unable to work, while 5% of patients without COPD report being unable to work.[12] Also, rheumatic

conditions are the leading cause of work disability among adults in the United States.[13] Finally, evidence shows that such diseases impact the quality of life; a study examined the self-reported quality of life of patients with rheumatoid arthritis (RA) and found that the patients were 30% more likely to need assistance with personal care than people who did not have RA.[14]

Although the development of chronic inflammatory diseases involves many risk factors, evidence suggests cytokine-mediated signaling plays a significant role in maintaining chronic inflammation. For example, the inhibition of the cytokine tumor necrosis factor-alpha (TNF-α) has been beneficial for RA patients. A meta-analysis of data retrieved from PubMed and ISI Web of Knowledge databases revealed eight randomized control trials (260 participants total) in which anti-TNF-α therapy significantly reduced insulin resistance in patients with rheumatoid arthritis and improved their insulin sensitivity.[15] This is an important finding, as insulin resistance is associated with RA.[16] Similar effects have been observed with the inhibition of the cytokine interleukin-1 beta. A double-blind, randomized control trial administering anti-IL-1β monoclonal antibodies (mAbs) assessed more than 10,000 adults with a previous history of myocardial infarction events and elevated circulating C-reactive protein levels, which is a standard biomarker for general inflammation.[17] It was found that the administration of an anti-IL-1β mAb significantly reduced the rates of nonfatal myocardial infarction and levels of C-reactive protein. Clinical trials such as these suggest that pro-inflammatory cytokines should be further investigated as biomarkers and therapeutic targets for chronic inflammatory diseases.

## 1.3 Oncostatin M

### 1.3.1 Interleukin-6 Family of Cytokines

Cytokines are cell-secreted small molecular weight proteins (15-20 kDa) that work to orchestrate the body's natural immune response during periods of acute and chronic inflammation.[18] It was not until the 1970s that the Kishimoto group identified the prototypical glycoprotein 130 (gp130) family cytokine interleukin-6 (IL-6), which is released by T cells for the purpose of maturation and development of B cells into antibody-producing plasma cells.[19] Therefore, IL-6 was first named B cell stimulatory factor 2. The biological relevance of IL-6 continued to increase as other factors such as hepatocyte-stimulating factor and plasmacytoma growth factor were also identified as IL-6.[20, 21] As time passed, other distinct cytokines were observed to elicit cellular responses by binding to the gp130 receptor as well. These cytokines were identified throughout the 80's, 90's, and 2000's, and are collectively called the IL-6 family of cytokines.

The IL-6 family of cytokines is comprised of 8 distinct proteins, which include IL-6, IL-11, IL-27, ciliary neurotrophic factor, leukemia inhibitory factor (LIF), oncostatin M (OSM), cardiotrophin 1, and cardiotrophin-like cytokine. It should be made clear that the IL-6 family of cytokines is also referred to as the gp130 family of cytokines. As they all signal through similar receptor complexes, they share close structural and behavioral characteristics. This structural similarity is not evident in the secondary structure of the protein. Still, it is clearly observed in the tertiary structure, where they all exhibit a four alpha-helical bundle with an up-up-down-down topology.[22] Several distinct yet closely related cell signaling pathways can be triggered by the IL-6 family of cytokines, including the Janus kinase-signal transducer and activator of

transcription (JAK/STAT), the mitogen-activated protein kinase (MAPK), and the phosphoinositide 3-kinase (PI3K) pathways.[23, 24] Therefore, redundancy in signaling pathways allows some IL-6 family cytokines to elicit similar cell responses.

The human body relies critically on the collection of IL-6 type cytokines to orchestrate the innate and adaptive immune system necessary for development.[25] In addition to activating B cells into antibody-producing plasma cells, IL-6 also modulates helper T cell function and survival.[26] Helper T cells are known to be "naïve" as soon as they exit the thymus, and it is not until they encounter antigens presented to them by B cells that they are activated.[27] Interestingly, resting naïve helper T cells undergo apoptosis soon after isolation. Yet, they have an increased lifetime when stimulated with IL-6.[26] In conclusion, the IL-6 family of cytokines is an important collection of proteins that regulate several necessary functions within the human body.

1.3.2 Form and Function of OSM and LIF

Both the structure and function of the OSM and LIF cytokines are strikingly similar, and there is evidence that suggests OSM and LIF share a common evolutionary origin. Due to the physical closeness of the genes on chromosome 22, it is believed that a duplication of a common ancestral gene gave rise to the regions on chromosome 22 that code for OSM and LIF.[28] Both OSM and LIF display similarly placed receptor binding sites, which are illustrated in Figure 1.3. These are commonly referred to as sites II and III and have been identified by alanine mutagenesis studies to play a significant role in forming protein-protein interactions (PPIs) between the cytokines and their appropriate receptors.[29-31]

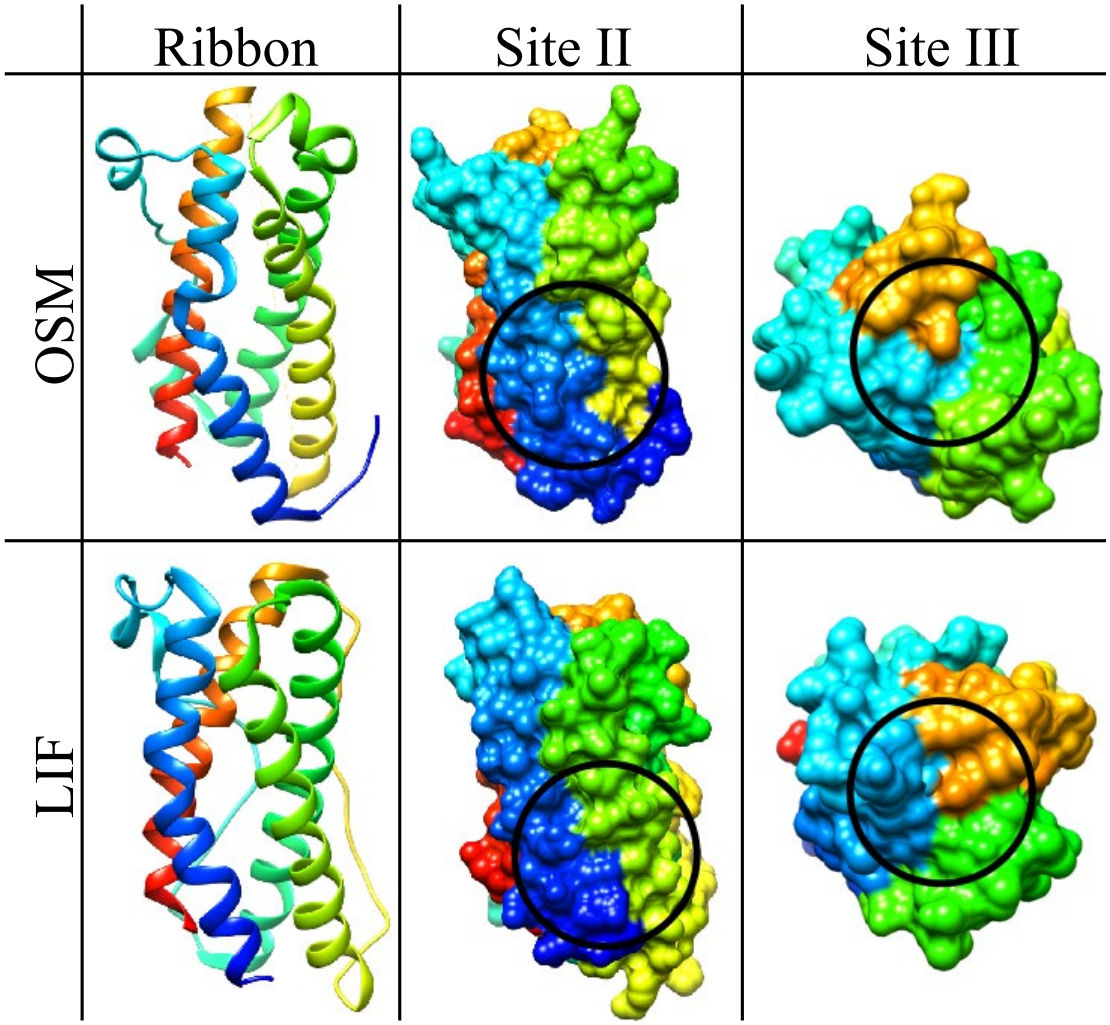


**Figure 1.3 Binding sites of OSM and LIF**

The black circles outline the approximate topography that contains site II and site III for both OSM (PDB: 1EVS) and LIF (PDB: 1EMR). Site III is observed from a top-down view, while site II is observed from a side-view.

In both proteins, site II is dedicated to binding the common gp130 receptor.[31] However, LIF and OSM diverge structurally in respect to site III, which dictates their receptor binding preferences. OSM preferentially forms a signaling complex with gp130 and oncostatin M receptor beta (OSMRβ) to create what is known as the OSMR type II complex. In addition, OSM can also form a lower affinity signaling complex with gp130 and leukemia inhibitory factor receptor (LIFR) to create what is known as the OSMR type I complex.[31] LIF has only been identified to bind to a signaling complex comprised of gp130 and LIFR.[32] A set of experiments performed by Chollangi and coworkers

revealed that a helical loop containing 12 amino acids between the B and C helices at site III of OSM dictates whether OSM preferentially signals through the type I or type II OSMR complex. The authors used surface plasmon resonance (SPR) binding experiments to show that when OSM proteins have this helical loop shortened to 7 or 4 amino acids, it dramatically increases their affinity for the type I complex, but not the type II complex.[31] So, this was identified to be an essential structure that is unique to OSM's signaling.

Both OSM and LIF are cytokines that exhibit pleiotropic function. In the classic sense, pleiotropy refers to the effect a single gene, or protein, has on two seemingly unrelated phenotypic traits. In this context, OSM and LIF are pleiotropic as they mediate the activity, growth, and differentiation of many different cell types. These effects range from the bone remodeling process to hematopoiesis and liver development.[33] In comparison, LIF has been identified as the most pleiotropic cytokine in the IL-6 family and observed to be secreted by a wide variety of cells.[32] OSM is primarily secreted by activated T cells, monocytes, macrophages, polymorphonuclear neutrophils, and dendritic cells.[34]

As seen in panel A of Figure 1.4, OSM (yellow) binds to the transmembrane protein gp130 with relatively low affinity. This binding event alone shows little to no biological response from the cell.[35] It is not until either the transmembrane protein LIFR or the transmembrane protein OSMRβ is recruited that the JAK/STAT, MAPK/ERK, and PI3K/AKT pathways are activated by either receptor complex.[36] As seen in panel B, LIF (purple) most likely binds to LIFR first, then to gp130 second to activate the JAK/STAT, MAPK/ERK, and PI3K/AKT pathways.[32, 37]

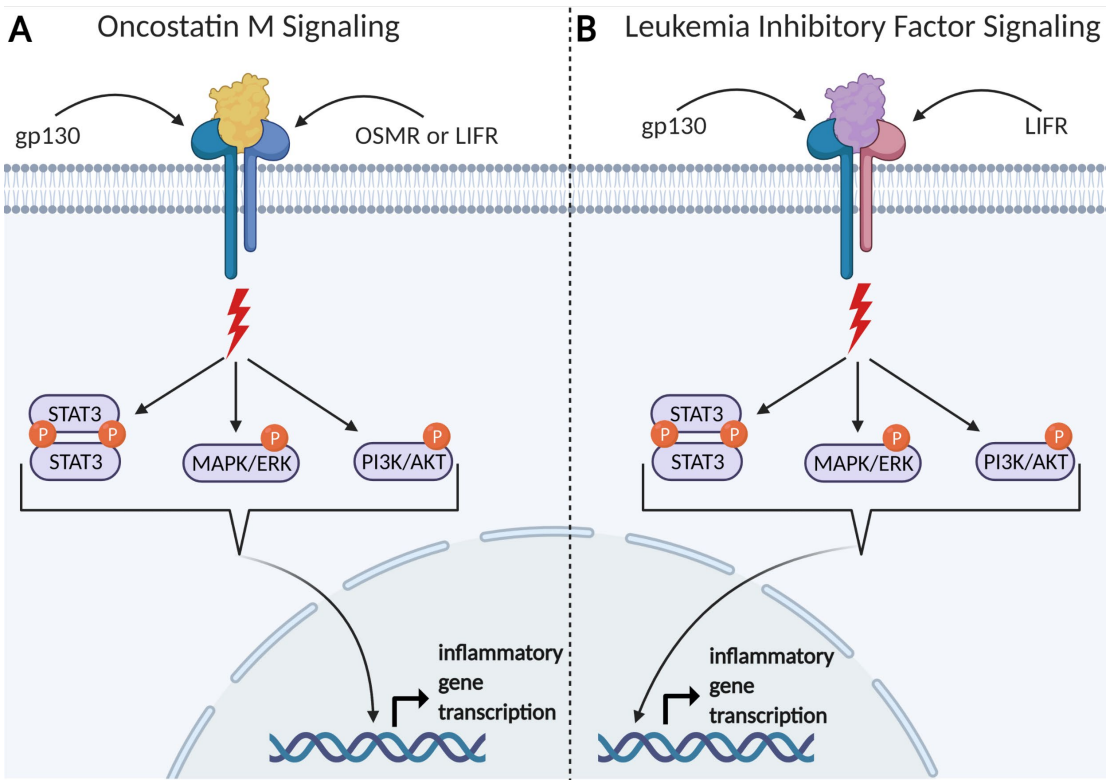


**Figure 1.4 Signaling pathways of LIF and OSM**

(**A**) OSM (yellow) can form a signaling complex with either gp130 and OSMRβ or gp130 and LIFR to upregulate the JAK/STAT, MAPK/ERK, and PI3/AKT pathways. (**B**) LIF (purple) forms a signaling complex with gp130 and LIFR to upregulate the JAK/STAT, MAPK/ERK, and PI3/AKT pathways.

Out of the three pathways, the JAK/STAT signaling cascade is the most mechanistically straightforward and relevant to this document. Upon cytokine binding to the receptor subunits, receptor-associated JAK proteins come in close enough proximity to each other to undergo trans-phosphorylation.[38] The phosphorylated JAK proteins then phosphorylate tyrosine residues on the cytoplasmic tails of transmembrane receptors. These phosphorylated tyrosine residues act as docking sites for the STAT family of proteins, whereupon docking they become phosphorylated. Phosphorylated STAT then dissociates and forms a homodimer or heterodimer STAT complex, which is translocated into the nucleus to upregulate specific transcripts. The JAK/STAT pathway activated by

OSM and LIF controls several biological functions, such as the proper regulation of cell cycle progression and immune system functioning.[39-41]

1.3.3 Chronic Inflammatory Diseases Maintained by OSM

More evidence is emerging that the overexpression of OSM is implicated in numerous chronic inflammatory diseases.[42-48] As a cytokine that regulates pathways in multiple tissues, it is inherently challenging to assign all known functions of OSM when exploring its role in acute and chronic inflammation. Yet, numerous histological investigations and clinical experiments suggest that OSM plays a pivotal role in chronic inflammatory diseases such as rheumatoid arthritis, inflammatory bowel disease, metabolic syndrome, systemic sclerosis, lupus, and many different forms of cancer. This section will serve as a collection of experimental evidence that frames OSM as culpable in contributing to such illnesses.

## 1.4 OSM and Breast Cancer

Evidence suggests that overexpression of OSM and OSMRβ can promote the progression of certain cancers via tumor growth, invasion, and survival.[48] Specifically, OSM has been identified to promote the spread of breast cancer. Breast cancer alone has accounted for 30% of all cancers in women in the year 2021.[49] As such, it is the most commonly diagnosed type of cancer in women, except for skin cancers. The 5-year survival rate for women with localized breast cancer is 99%.[50] However, the high mortality rate that is so commonly associated with breast cancer results from the spreading of cancerous cells to distant sites in the body (metastasis). Once cancer metastasizes to other vital organs, the five-year survival rate for women drops to a bleak

28%. The most common tissues for metastasis to occur in the bones, liver, brain, and lungs.[51]

In order to discuss the role of OSM in breast cancer metastasis, it is necessary to identify the tissues in which breast cancer originates. Breast carcinomas are generally classified as lobular or ductal. Of all newly diagnosed breast cancers, 15-30% are identified as being *in situ* carcinomas; 80% of these carcinomas are identified as ductal carcinoma *in situ*, in which the carcinoma originates inside the milk ducts of the breast.[52, 53] Breast cancer types can be further categorized into four major subtypes, which include luminal A, luminal B, human epidermal growth factor receptor 2 (HER2)-enriched, and triple negative breast cancer (TNBC).[54] All four of these sub-types of breast cancer depend on the expression of estrogen receptor (ER), progesterone receptor (PR), and HER2. Table 1.1 summarizes which types of breast cancers express certain receptors.[55]

**Table 1.1 Receptors present in breast cancer subtypes**
Luminal A and luminal B cells both express PR and ER, but luminal A cells do not express HER2. HER2-enriched cells express HER2 but do not express PR or ER. TNBC does not express any of the receptors discussed.

| | Luminal A | Luminal B | HER2-enriched | TNBC |
|---|---|---|---|---|
| **PR/ER** | + | + | - | - |
| **HER2** | - | + | + | - |

Breast cancer cells have the potential to become metastatic. Metastasis occurs when a cancer cell breaks away from the primary tumor site, enters the bloodstream or lymphatic system, and continues to grow and divide in distant tissue(s).[56] The metastatic cascade is initiated when the tumor cells experience a phenotypic change, called an epithelial to mesenchymal transition. This specific change causes the epithelial cell to be able to detach from the basement membrane and assume a mesenchymal cell phenotype, which includes enhanced migratory capacity and invasiveness. Afterward, the cancer cell

enters the circulatory or lymphatic system through a process called intravasation, where the cancer cell then becomes a circulating tumor cell. Finally, extravasation occurs when the circulating tumor cell travels to a distant tissue site, whereupon it exits the circulatory or lymphatic system into adjacent tissue and creates a new tumor.[57]

OSM has been implicated in upregulating several mechanisms that support cancer growth, metastasis, and survival.[48] Jorcyk and coworkers have shown that OSM increases the metastatic capacity of T-47D breast cancer cells.[42] To determine how OSM affects the detachments of cells, the researchers incubated cancer cells with $^{3}$H-thymidine to radiolabel the DNA to quantify the degree of cellular detachment. Next, the cells were incubated with three different cytokines: OSM, IL-6, and LIF. The percentages of detached cells were quantified as loose cells in the culture media divided by the total number of cells. It was found that OSM induced a detachment of 17%, while untreated cells induced a detachment of 6%. In addition, the introduction of IL-6 induced an 8% detachment, while LIF was observed to have no effect.

In addition, Jorcyk and coworkers showed that OSM significantly increased the invasive capacity of T-47D cells.[42] T-47D cells were treated with OSM and plated in Matrigel-coated invasion chambers for 3 or 5 days. After the allotted time, the invasive cells were stained and counted. It was found that OSM-treated cells showed a 250% increase in invasive capacity compared to untreated cells. Overall, the data suggest that OSM induces an epithelial to mesenchymal transition by the cell detachment assay and significantly increases cancer cell invasiveness.

### 1.5 OSM and Rheumatoid Arthritis

In addition to increasing metastasis in breast cancers, OSM has also been implicated in the pathogenesis of inflammatory joint diseases, such as rheumatoid arthritis (RA). RA is an autoimmune disease typically associated with autoantibodies, matrix metalloproteinases (MMPs), overactivation of osteoclasts, and joint swelling.[58] Not only is the QOL of an RA patient diminished, but the life expectancy is slightly shorter due to accelerated arteriosclerosis.[59] RA is not strictly attributable to genetic factors as environmental factors play a role as well. Such factors include inhalation of dangerous debris particles (such as silica and asbestos), tobacco/alcohol consumption, microbiota, diet, and other lifestyle stressors.[60] Like other chronic inflammatory diseases, RA can either be diagnosed as early-stage or late-stage. However, it is common for RA to be undiagnosed until the later stages, after which medical intervention would most effectively benefit patient prognosis.[61]

Even though RA is considered a systemic disease, the chronic inflammation of RA takes place in the synovial tissue of the joint (synovium). The two sections that constitute the synovium are the intimal and the subintimal layers.[62] The intimal layer is the innermost layer in the joint capsule and serves two purposes. The first purpose is to secrete synovial fluid into the joint space, thereby lubricating and decreasing the friction between the cartilaginous structures. The second purpose is to supply nutrients to the cartilage contained within the joint capsule.[63] Although both discrete layers of the synovium experience physiological changes in response to RA, the intimal layer experiences the most pronounced changes.

A normal, healthy, intimal lining of the synovium is 1-2 cells in depth. However, the influx of both macrophage-like synovial cells and fibroblast-like synoviocytes (FLS) causes the intimal lining to expand to 10-20 cells in depth.[58] As seen in step 1 of Figure 1.5, the macrophage-like synovial cells migrate into the synovial tissue. In step 2, the macrophages become activated by infiltrating T cells, whereupon they secrete cytokines.[58, 64] In step 3, FLS are then activated by the secreted cytokines to produce the devastating matrix-metalloproteases (MMPs) and receptor activator of nuclear factor kappa beta (RANK) ligand. MMPs facilitate cartilage destruction, while RANK ligand upregulates the proliferation and activity of osteoclasts.[65, 66] Finally, step 4 shows an increased number of osteoclasts in the joint, as well as degradation of cartilaginous structures in the joint by MMPs.[67]

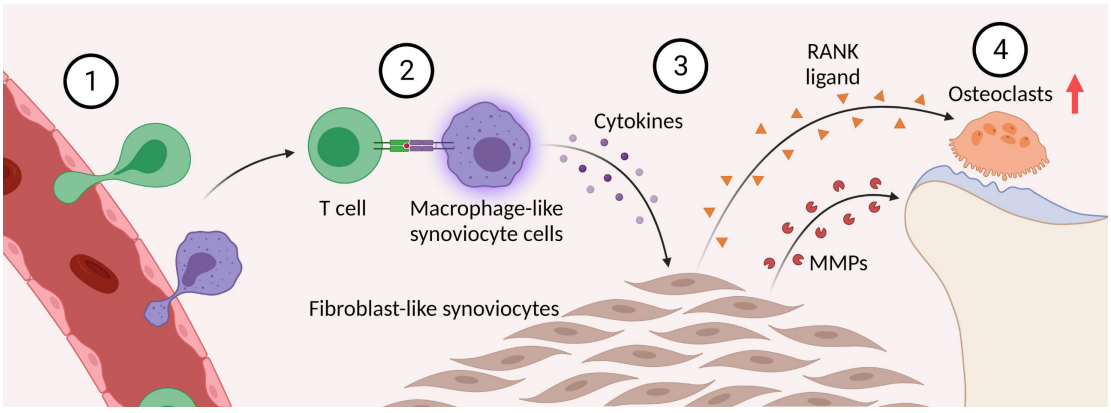


**Figure 1.5 Cytokines work to maintain joint destruction in RA**

(**1**) Leukocytes are attracted to the area in response to the autoimmune reaction in RA,. (**2**) T cells activate macrophages, which results in the secretion of pro-inflammatory cytokines, such as IL-1, IL-6, TNF-alpha, and OSM. (**3**) The cytokines activate fibroblast like synoviocytes to release RANK ligand and MMPs. (**4**) MMPs destroy cartilage and osteoclasts are activated by RANK ligand, resulting in articular cartilage and bone loss.

Research executed by Fearon and coworkers reveals how OSM causes a pro-inflammatory phenotype in FLS, which are identified in the paper as rheumatoid arthritis fibroblasts.[44] In one of the experiments, the authors sought to discover what effect OSM had on the proliferation of the FLS. The FLS were stimulated with OSM for 96 hours, at

which time the cells were lysed and levels of bromodeoxyuridine were quantified via an enzyme-linked immunosorbent assay (ELISA). The cells that were stimulated with OSM resulted in cell proliferation that was approximately twice that of the control group. This supports the position that OSM is involved in the pannus structure's growth- a prominent pathological feature observed in progressed RA. The pannus grows and spreads in a locally invasive tumor-like fashion and is comprised of osteoclasts, macrophages, and invasive fibroblast-like synoviocytes.[58] Once the pannus envelops cartilage and underlying bone it will start to degrade them.

Another key finding in the set of experiments performed by Fearon and coworkers suggests that OSM induces the expression of matrix metalloproteinase-1 (MMP-1), which catabolizes cartilaginous tissue. The authors harvested tissue explants from RA patients to maintain the synovial tissue architecture during the experiment. The explants were stimulated by OSM for 24 hours, lysed, and subjected to promatrix metalloproteinase-1 (proMMP-1) detection by ELISA. ProMMP-1 is simply a proenzyme that upon activation becomes MMP-1.[68] The researchers found that proMMP-1 production in the OSM stimulated explant increased by 154% when compared to the control explant. These data support the idea that OSM can maintain joint destruction by stimulating the production of MMP-1.

Hui and coworkers revealed that OSM is found in elevated amounts in the synovial fluid of patients with RA.[69] In the experiment, cells from synovial fluids were collected from patients with RA or patients with osteoarthritis and subjected to an OSM ELISA. The authors discovered that 90% of the patients with RA had synovial fluid OSM concentrations of 2.36 to 901.75 pg/mL, while there was no detectable OSM in the

synovial fluid of patients with osteoarthritis. It is worth noting that the limit of detection for the ELISA experiments was 2.0 pg/mL for RA synovial fluid and 4.0 pg/mL for osteoarthritis synovial fluid. In combination with the experiments performed by Fearon and coworkers, these findings suggest that OSM promotes tissue inflammation in RA patients and upregulates pathways that destroy cartilaginous and bony structures.

### 1.6 OSM and Irritable Bowel Disease

Irritable bowel disease (IBD) is another condition in which overexpression of OSM is thought to contribute to disease severity. IBD poses an important significance in Western world health, as gastrointestinal disorders are among the most frequent causes for medical health consultations.[70] In fact, IBD has become a major focus worldwide as the incidence and prevalence have been increasing in developed countries around the globe.[71] IBD is clinically identified as one of two sub-types: Ulcerative Colitis (UC) or Crohn's Disease (CD).[72] Currently, there are no non-invasive cures for CD and UC, resulting in individuals who have a considerable likelihood of needing surgery. For individuals with CD, the likelihood of requiring surgery in one's lifetime is 70-80%, while the likelihood of requiring surgery for UC is 20-30%.[73]

Unfortunately, no single symptom or reference allows a clinician to positively diagnose a patient with CD or UC. Instead, a combination of clinical and histological evidence needs to be gathered according to the European Crohn's and Colitis Organization Guideline for Diagnostic Assessment in Inflammatory Bowel Disease. The diagnosis of both UC and CD is "…based on a combination of clinical, biochemical, stool, endoscopic, cross-sectional imaging, and histological investigations."[74] Despite the uncertainty of disease etiology, recent evidence identifies cytokines as key players in

driving intestinal inflammation. According to Sanchez-Muñoz and coworkers, IBD pathogenesis is influenced by cytokine-induced dysregulation of T cells and excessive production of effector T-cells.[75]

Currently, Food and Drug Administration-approved TNF-α monoclonal antibodies (infliximab) are used to treat moderate to severe UC and CD with marked success. Still, an astounding 40% of the patients experience non-responsiveness to the treatment. To make matters worse, patients can become unresponsive to anti-TNF-α mAb therapy over time.[76, 77] These conditions are commonly referred to as a lack of primary response and a loss of response, respectively. The lack of patient response to anti-TNF-α therapies may be due to other cytokines causing inflammation.

More evidence is emerging in the primary literature revealing OSM's role in the pathogenesis of IBD. West and coworkers identified OSM as the most transcriptionally upregulated cytokine in inflamed intestinal mucosa in patients with CD and UC.[43] Additionally, OSMRβ was observed to be upregulated in both CD and UC patients, which suggests a specific role for OSM and OSMRβ in the pathogenesis of IBD. Interestingly, the authors also found that OSM and OSMRβ expression is positively correlated with the severity of intestinal inflammation. Although the authors do not suggest a discrete pathway in which OSM acts to drive IBD, they did show that OSM promotes inflammatory activity in the intestinal stroma.

West and coworkers treated CCD-18Co (human colon) cells with recombinant OSM and used reverse transcription-quantitative polymerase chain reaction to quantify the expression of OSM-associated inflammatory module genes.[43] This was done to observe OSM’s potential role in inducing a pro-inflammatory phenotype among the colon

cells. The authors found that half of the module members were induced by OSM stimulation. Also, the addition of OSM induced the expression of both intercellular adhesion molecule 1 (ICAM1) and podoplanin. This is important, as ICAM1 plays a role in facilitating leukocyte endothelial transmigration.[78] This translates into more leukocytes infiltrating the affected area, which further increases inflammation. In addition, ICAM1 is believed to contribute to further gut permeability by disruption of the endothelial cell junction.[79] The upregulation of podoplanin should be noted as well, as it has been identified to play a role in other chronic inflammatory diseases such as psoriasis, multiple sclerosis, and cancer-associated thrombosis.[80] These data suggest that OSM upregulates migration and invasion-leading of leukocytes, as well as increases gut permeability.

West and coworkers also used an IBD model driven by *Helicobacter hepaticus* to infect wild type (WT) C57BL/6 mice to mimic human IBD conditions.[43] For context, *Helicobacter hepaticus* is a type of bacteria that has been used to induce colitis in mice.[81] Three separate experiments were performed using this model to observe what role OSM has in contributing to IBD pathogenesis. In the first experiment, mice were infected with *Helicobacter hepaticus* to validate the model. The mice were sacrificed after 14 or 21 days, corresponding to peak disease severity. The mice were observed to have a 10-fold increase in leukocytes of the colon lamina propria, along with elevated levels of OSM in colon explant supernatants and stool samples. High levels of expression of both OSM and OSMRβ were detected in the lamina propria as well. In addition, the lamina propria was highly enriched in PDPN cells. This evidence suggests that both OSM and OSMRβ are associated with colitis in this specific model.

In the second experiment, West and coworkers used OSM deficient mice along with co-housed WT mice to observe how the lack of expression of OSM influenced disease progression. At a steady-state of IBD severity, the OSM deficient mice exhibited a normal collection of leukocytes in the lymphoid and intestinal tissue. Also, the OSM deficient mice exhibited normal organ histology. During peak IBD severity, the OSM deficient mice showed less severe symptoms in comparison to their WT littermates. Genomic DNA of *Helicobacter hepaticus* was quantified using quantitative polymerase chain reaction (qPCR) to reveal that bacterial colonization of both mouse groups was the same. This confirms that any changes observed in the experimental groups were not attributable to any possible differences in *Helicobacter hepaticus* colonization. The results from this experiment suggest that OSM dramatically contributes to the severity of IBS.

In the third experiment, West and coworkers treated the infected mice with an OSMRβ-gp130 fusion protein to neutralize OSM. Fusion proteins are two or more domains that have been joined together to transcribe a single polypeptide. This results in two separate proteins linked together that normally would not be. Therefore, the OSMRβ-gp130 fusion protein mimics the OMSR type II receptor complex.[82] The mice treated with the higher affinity OSMRβ-gp130 fusion protein exhibited similar levels of disease severity as that of OSM deficient mice. These experiments collectively suggest that not only does OSM likely play a role in IBD pathology, but it also identifies OSM as a therapeutic target for patients who do not respond to anti-TNF-α therapy.

## 1.7 OSM and Systemic Sclerosis

Finally, OSM has been shown to play a role in the chronic autoimmune disease systemic sclerosis (SSc). Clinical features of the disease include fibrosis, vascular damage, and disruption of innate and adaptive immunity. The most prominent feature of the disease is the progressive fibrosis that occurs in different organs due to excessive deposition of extracellular matrix components.[83] SSc is typically classified into two subsets based on the regions of affected skin. These two subsets include limited systemic sclerosis (lcSSc) and diffuse systemic sclerosis (dsSSc). LcSSc is defined as sclerosis that affects the face and limbs, whereas dsSSc is defined as sclerosis that affects the axial parts of the body, such as the trunk and proximal portions of the limbs.[84, 85] Once diagnosed, the ten-year survival rate for lcSSc patients is 90%, while the ten-year survival rate for dsSSc is 65-82%. Unfortunately, the pathogenesis of both types of sclerosis is still under heavy scrutiny.

However, a set of studies executed by Marden and coworkers examined the possible contribution of the OSM/OSMRβ signaling axis to the development and maintenance of SSc.[46] The authors obtained skin biopsies from human subjects that were healthy or affected with either lcSSc or dsSSc. From the biopsies, human dermal microvascular endothelial cells (HDMECs) were isolated and cultured. Both cells and biopsy tissues were subjected to experiments that quantified the expression of OSM and OSMRβ, mRNA levels of pro-inflammatory genes, and specific cells implicated in the pathogenesis of SSc.

Immunohistochemical staining experiments on the tissue biopsies revealed that both lcSSC and dsSSc tissues had elevated levels of OSMRβ. Surprisingly, the

expression of OSM in both SSc biopsies was comparable to that of the healthy control group. The results from the staining experiment alone reveal that OSM is not expressed in higher amounts than that of healthy patients; however, they do show that OSMRβ is expressed in higher amounts in patients that have either form of SSc. This is important as OSMRβ has been identified as a biomarker for the progression of skin disease in dsSSc patients.[86]

In addition, the authors used real-time PCR to quantify mRNA levels of specific interleukins, chemokines, and cell permeability and adhesion molecules in HDMECs treated with OSM for three and twenty-four-hour time periods. A rapid increase in IL-6 mRNA was observed in the cells treated with OSM during the three-hour mark and remained elevated at the twenty-four-hour mark. Interestingly mRNA levels of OSM were the same as the control group. The only other IL-6 family cytokine that was monitored to increase was IL-33 along with its receptor IL-1R1. The mRNA levels of the chemokines CCL7, CXCL12, and CXCL2 were also observed to be significantly higher than that of the control group at the three-hour and twenty-four-hour time periods. The mRNA levels of ICAM-1 were also found to be upregulated as well. These data suggest that OSM upregulates mRNA levels of other inflammatory cytokines, chemokines, and adhesion molecules, therefore driving inflammation.

Finally, Marden and coworkers explored how OSM possibly mediates collagen deposition in healthy human explant tissues, as collagen deposition correlates with disease activity in SSC.[46, 87] This was accomplished by placing the dermal biopsy tissues on nitrocellulose membranes, treating them with OSM for fourteen days, and staining them on paraffin sections. The OSM-treated explants experienced increased collagen

deposition and an increased number of platelet-derived growth factor receptor beta cells, expressed in the dermal tissue of patients with early SSC.[88] These data show that OSM can increase the common mechanisms in SSc associated with disease severity, such as the deposition of collagen and the expression of pro-inflammatory platelet-derived growth factor receptor beta cells.

Collectively, the data obtained by Marden and coworkers show that OSM upregulates several mechanisms involved in the pathogenesis of SSc. This is supported by the increased expression of OSMRβ in OSM-treated tissue explants. Furthermore, mRNA levels of IL-33, several chemokines, and ICAM-1 were observed to be transcriptionally upregulated in HDMECs treated with OSM. Lastly, the treatment of healthy patient dermal explants showed OSM increases collagen deposition. These sets of experiments highlight OSM as a potential therapeutic target in treating both dsSSc and lcSSc.

## 1.8 Disruption of Protein-Protein Interactions

### 1.8.1 Introduction to Protein-Protein Interactions

The Human Interactome Project is a growing collection of protein-protein interactions (PPIs). Analogous to the Human Genome Project that had its inception in 1990, the Human Interactome Project works to understand and map out the expansive collection of PPIs in the context of human biological systems. Specific requirements need to be met for an interaction to be qualified as a PPI. An association between two proteins is only considered to be a canonical PPI if it meets the following two requirements: Firstly, the interaction between the two proteins has to result in a specific event, and secondly, the interaction must activate a non-generic function.[89] This distinction is

necessary, as the mere "touching" of proteins (such as those experienced in the production, folding, and transport of proteins) are not deemed as PPIs.

1.8.2 Recent Challenges and Successes in Targeting PPIs

It has become more evident that the etiologies of certain diseases arise from dysregulated mechanisms controlled by PPIs. According to Heifetz and coworkers, "There are more than 645,000 reported disease-relevant PPIs in the human interactome…"[90] Modulation of such interactions could prove to be highly promising therapeutic approaches. This sub-chapter will discuss the inherent challenges associated with inhibiting PPIs, and the recent successes researchers and clinicians have had.

Despite modern success in small molecule protein-protein interaction inhibitors and their practical applications, inherent challenges make designing potent, selective, and safe compounds difficult. The limitations arise from the shallow binding "pockets" and the relatively flat, featureless surface areas of proteins. In addition, the sheer difference in the size of the protein-protein interface versus the small molecule-protein interface also makes the inhibition challenging. As the Human Interactome Project contains entities of various sizes and structures, the interfacial buried surface area of the PPI can vary widely. In other words, buried surface area at the protein-protein interface has been measured to span the range of $< 1000$ Å$^2$ to $> 2500$ Å$^2$.[91] In comparison, typical small molecule-protein interfaces constitute a total buried surface area of ~200-1000 Å$^2$.[92] Also, the rational design of lead molecules is daunting as well; there are very few naturally occurring small molecules that mimic the complementary binding partner of the target.

One advancement that has progressed drug discovery is alanine scanning, which identifies important amino acids in binding epitopes on proteins. Essentially, alanine

scanning works by replacing individual amino acids at the putative binding epitope of the protein with a single alanine residue. Alanine is chosen because of its non-bulky, chemically inert character. Afterward, the biological activity of the mutant protein is measured. Cunningham and Wells were the first to use alanine scanning experiments to find "hot spots" to map human growth hormone-receptor interactions.[93] Hot spots are small regions of amino acids in which most of the energy of binding is concentrated. Having no real practical starting point, the authors systematically replaced 7 to 30 residue segments with sequences derived from non-binding hGH (human growth hormone) homologs. As a result, the $NH_2$-terminal portion of helix 1, the COOH-terminal portion of helix 4, and a loop structure that resides between residues 54 and 74 were discovered to be potentially critical in hGH receptor binding. The authors then performed another round of alanine scanning experiments to identify which specific side chains in hGH were most important in receptor binding. A total of 62 single alanine mutant proteins were designed and secreted from *Escherichia coli*, and binding constants were measured and recorded for each mutant.

From the mutagenesis experiments, Cunningham and Wells identified certain regions of amino acids that, when mutated, caused a significant decrease in the binding ability of the proteins.[93] These amino acid residues are confined to three and one-half turns of helix 4. The authors also showed that only a small percentage of the buried side chains in the protein account for a drastic contribution to the binding energy of the entire hGH protein to its receptor. To be more specific, only 8 of the 31 side-chains buried at the PPI accounted for approximately 85% of the binding energy.[94] This finding is significant in the context of inhibiting PPIs with small molecules, as it suggests that small

groups of amino acids can be targeted with a small molecule or biologic that does not necessarily have to mimic the surface area of the complementary receptor protein. Further discussion in this section will cover examples of various protein-protein inhibitors such as monoclonal antibodies and peptide-mimetic small molecule inhibitors.

Monoclonal antibodies (mAbs) deserve due attention as they account for almost a fifth of the Food and Drug Administration's new drug approvals each year.[95] Monoclonal antibodies are immunoglobulins designed to target a single specific antigen. The process of manufacturing mAbs is initiated by injecting mice, rats, or hamsters intraperitoneally with the target antigen. This stimulates the B cells in the spleen to produce antibodies specific to the target antigen injected. Next, the B cells in the spleen of the rodent are harvested and fused with myeloma cells to create the hybridoma cells, which then can divide to produce more antibodies. Once the hybridoma cells have produced enough mAbs, the mAbs are filtered out and purified for further use.[96] Such applications include diagnostic testing in consumer items such as at-home pregnancy tests or clinical applications, such as treating cancer in human patients.[97, 98] In addition, mAbs have also been used to target PPIs.

One such example of a mAb designed to disrupt a PPI is Daclizumab®, used for treating relapsing forms of multiple sclerosis. Daclizumab is a humanized monoclonal antibody developed by Biogen and AbbVie that blocks CD25, the α-subunit of the Interleukin-2 receptor of effector T-cells.[99] It is currently believed that Daclizumab binds reversibly to the subunit receptor CD25, which decreases the consumption of IL-2 by the high-affinity receptor. As a result, the intermediate affinity IL-2 receptor is preferentially activated and induces an IL-2 driven expansion of $CD56^{bright}$ natural killer cells. The

increase in $CD56^{bright}$ natural killer cells has a significant role in the effectiveness of the mAbs, as the natural killer cells are believed to be cytotoxic to auto-antigen activated T cells.[100-102] Since auto-antigen T cells target the host's body in multiple sclerosis, reducing these cells helps alleviate the adverse effects of the disease.[103]

Another method of inhibiting PPIs includes the use of peptide-based protein mimetics. This type of approach has the advantage of mimicking structures and motifs present in the binding partner(s) of the protein. However, the drugs' poor solubility and metabolic instability have been a serious limitation to their uses in clinical applications.[104] Despite these issues, there have been several unique attempts to circumvent them. Such approaches include using macrocycles, constructing shorter peptides, introducing non-natural amino acids and conformationally restricted cyclized peptides.[104] More recently, mimetic applications of protein-protein inhibitors have shown great promise and have considerable room for growth and improvement. A few of these successful protein mimetic small molecule inhibitors (SMIs), along with their design rationale, will be discussed.

Venetoclax was designed to treat acute myeloid leukemia (AML). AML is characterized by the rapid generation of myeloid progenitor cells and abnormal differentiation of the myeloid cells.[105] In healthy subjects, these myeloid progenitor cells differentiate into red blood cells, platelets, and different types of leukocytes.[106] In patients suffering from AML, these myeloid cells differentiate into malignant blood cells, resulting in a loss of function for proper hematopoiesis (production of blood cells). The mainstay treatment for AML includes one, two, or all three of the following approaches: chemotherapy, stem cell transplant, and small molecule therapy.[107] The small molecule

therapies used to help treat AML are designed to reinstate normal apoptosis within the myeloid cells that are rapidly proliferating, thereby treating a component of the disease. The BCL-2 family of proteins regulates both pro-apoptosis and anti-apoptosis mechanisms.[108] Venetoclax was designed to bind to BCL-2 and inhibit the interaction between the two proteins B cell lymphoma-2 (BCL-2) and BCL-2 associated X-protein (BAX), which play a role in regulating apoptosis. Unbound BAX acts as a pro-apoptotic protein but is inhibited when bound to the protein BCL-2. Therefore, Venetoclax binding to BCL-2 results in more unbound BAX that is available to initiate apoptosis in myeloid progenitor cells.

Panel A of Figure 1.6 shows Venetoclax bound to the hydrophobic groove on BCL-2 (PDB ID: 6O0K), which consists of binding sites 1 and 2, as identified by Oltersdorf and coworkers.[109] To design a rational drug, researchers at Abbott pharmaceuticals targeted the hydrophobic groove of the BCL-2 protein by a method known as "SAR by NMR," which is accomplished by obtaining HSQC spectra of $^{15}$N-labeled protein in the absence and presence of possible binding fragments.[110] Specifically, the Abbott researchers screened the fragments contained in the H3 portion of the BAX protein, which has been identified as the portion of the alpha-helix that binds to BCL-2. The fragments that were identified to bind with the greatest affinity were joined together to produce early versions of Venetoclax. Eventually, the final structure of Navitoclax ($K_i$ < 1 nM) was synthesized, as seen in panel B of Figure 1.6.

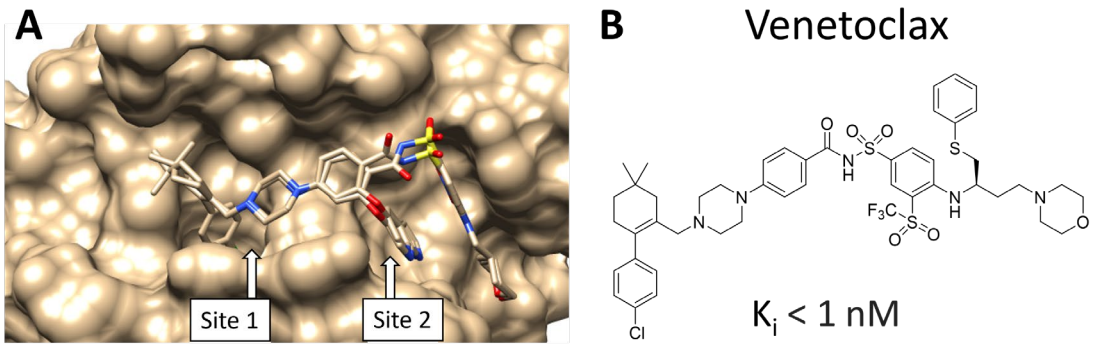


**Figure 1.6 Venetoclax targets site 1 and site 2 of BCL-2**

(**A**) Two similar binding poses of Venetoclax to the BCL-2 protein are shown. The crystal structure of Venetoclax bound and BCL-2 reveals that the compound binds to site 1 and site 2 of the BCL-protein. (**B**) Venetoclax mimics the structure of the BAX protein binding epitope and has a $K_i$ < 1nM.

Lee and Coworkers have also developed a protein mimetic as a potential therapeutic for Alzheimer's disease.[111] These α-helix mimetics were designed to disrupt the p53-MDMX interaction stabilized by three residues (Phe19, Trp23, and Leu26) of p53 and by the hydrophobic pocket of MDMX. As seen in panel A of Figure 1.7, short helical peptides seem to play an essential role as a recognition motif, where side chains exist at the positions: *i*, *i*+3 or *i*+4, and *i*+7. Therefore, the researchers designed a pyrrolopyrimidine-based scaffold with variable R groups that mimicked the spacing seen in the short helical peptide configuration (panel B). The authors then created a 900-member library of compounds that were substituted at the $R_1$, $R_2$, and $R_3$ positions. In order to study the compounds' abilities to disrupt the p53-MDMX interface, the molecules were tested to see how efficiently they could displace a Rhodamine-labeled 15-mer p53 peptide from the MDMX protein using a fluorescence polarization assay. This assay revealed that two analogs, 3a and 3b, had $K_i$ values of 0.62 ± 0.12 μM and 0.45 ± 0.18 μM, respectively.

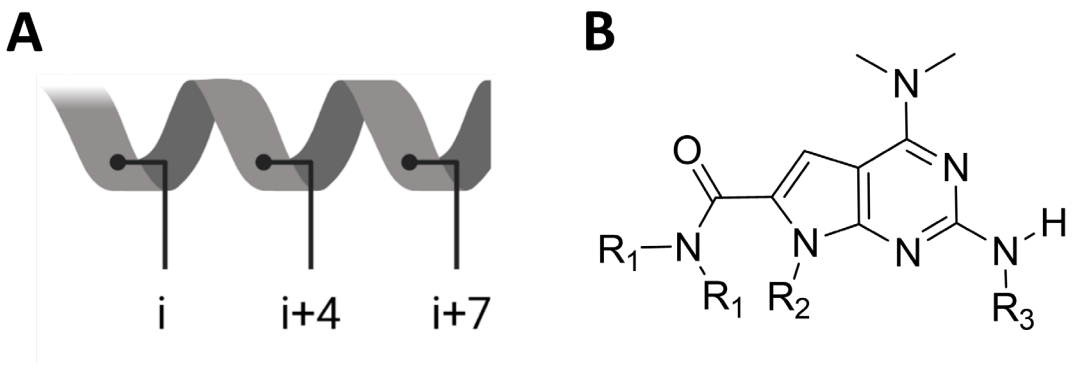


**Figure 1.7 Small molecule α-helix mimetic**

(**A**) Side chains at *i*, *i+3* or *i+4*, and *i+7* positions of the helix play an important role in disrupting PPIs. (**B**) The pyrrolopyrimidine-based scaffold mimics the placement of R groups at the *i*, *i+3* or *i+4*, and *i+7* position.

Ran and coworkers designed and screened peptide-based inhibitors of heat shock factor 1 (HSF1).[112] HSF1 is studied as a biomarker and promising therapeutic target as it is implicated in the migration, invasion, and proliferation of cancer.[113] HSF1 is a transcription factor that regulates the expression of chaperones and other factors involved in cell survival during periods of stress. Crystal structures suggest that the HSF1 oligomers are held together by buried contact surfaces, making the monomers challenging targets. However, the authors used what is referred to as the leucine zipper 4 and oligomerization domain motifs as templates to design peptide mimetics.

To design inhibitors for HSF1, the authors identified which regions of the oligomerization domain and leucine zipper 4 portions contributed to stabilizing the binding event. Next, they designed and synthesized peptides that mimicked discrete stretches of the peptide sequence of both regions. The peptide mimetics of the oligomerization region were found to be poor inhibitors, while the peptide mimetics of the leucine zipper 4 region were found to display moderate affinity to the target via a plate fluorescence assay ($EC_{50}$ ~ 13 μM). The findings support the notion that even deeply buried binding regions of proteins can be targeted.

One of the earliest clinically approved examples of an SMI is Tirofiban (Aggrastat®). First approved for patient use in 1998, the drug was designed to keep platelets in the bloodstream from coagulating, which leads to lower chances of blood clots and heart attacks.[114] To decrease aggregation of platelets, Tirofiban inhibits the PPI between fibrinogen and the platelet integrin receptor glycoprotein llb/lllα. The drug itself is a mimetic of the Arg-Gly-Asp peptide epitope of fibrinogen. In order to produce the first generation of the drug, the authors performed a directed search of the Merck Sample Collection, which allowed them to generate a specific structure using defined distances and atom requirements. The first compound synthesized was named "Lead Compound 1," as seen in panel A of Figure 1.8.

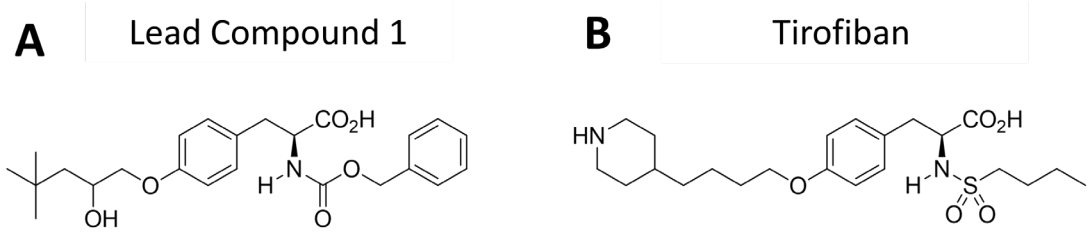


**Figure 1.8 Structure of Lead Compound 1 and Tirofiban**

(**A**) Lead Compound 1 was designed using the Merck Sample Collection. (**B**) Optimization at both termini of the original lead compound 1 lead to the final construction of Tirofiban, a Food and Drug Administration approved SMPPII.

Lead Compound 1 was subjected to a platelet aggregation assay that monitored the change in light transmittance upon the aggregation. The $IC_{50}$ was defined as the concentration necessary to inhibit the change in light transmittance by 50%.[115] This assay revealed that Lead Compound 1 exhibited an $IC_{50}$ of 27 μM, which served as a good starting point. However, further structural changes needed to be made to increase the affinity of the SMI to the substrate. It was discovered that a 4-(4-piperidinyl)butyl linkage at the N terminus of the structure allowed for the deletion of a chiral carbon seen in Lead Compound 1. It was also found that the replacement of the benzyl carbamate group at the

C-terminus with the (S)-butylsulfonylamino group led to increased potency, as well as more favorable physiochemical properties. Interestingly, the dramatic increase in potency with the introduction (S)-butylsulfonylamino was not planned and seemed to be a serendipitous discovery. Together, these changes afforded the final compound Tirofiban, which has an $IC_{50}$ of 9 nM (panel B).[115]

1.8.3 OSM as a Therapeutic Target

Considering OSM has been shown to play a critical role in the maintenance of several chronic inflammatory diseases, it is an obvious therapeutic target. Clinical trials using an anti-OSM monoclonal antibody suggest that OSM can be targeted safely, with minimal side effects.[116, 117] The monoclonal antibody GSK2330811, developed to treat fibrotic and inflammatory diseases, is thought to act by binding to OSM, which prevents ligating the gp130 receptor.[116] GSK2330811 was the first mAb to show target engagement in skin and blood in human patients. In addition, it became the successor mAb to GSK315234, which was discontinued due to a lack of binding affinity towards OSM. In this trial, thirty test subjects were randomized to receive the anti-OSM mAb, and ten received a placebo. Overall, none of the patients experienced any adverse side effects that led to withdrawal from the trial. However, there was an observed dose-dependent reduction in hematocrit, hemoglobin, and platelet count. Therefore, it is conceivable that OSM can be safely targeted with no to minimal side effects.

Previously discussed in the work of West and coworkers, fusion proteins have also been used to inhibit OSM signaling in a murine model of IBD.[43] The authors compared the inhibitory potency of the fusion protein to commercially available anti-OSM polyclonal antibodies, and they found that their most potent fusion protein was 50-

100x more potent than the commercially available polyclonal antibodies. However, fusion proteins that target OSM have not been used in any clinical trials yet.

1.8.4 Targeting the OSM/OSMRβ receptor complex with SMIs

To the best of the knowledge of the Warner research group, there are no small molecules that have been published that directly bind to the active site of OSM, thereby inhibiting the JACK/STAT signaling cascade activated by OSM. A substantial amount of work has been accomplished to identify the hot spot on OSM responsible for forming the type II signaling complex.[29, 30, 118] As seen in Figure 1.9, OSM works to upregulate inflammatory gene transcription by a series of phosphorylation steps involving the JAK and STAT3 proteins. However, an SMI that binds to site III with significant affinity can render OSM unable to upregulate inflammatory gene transcription. Therefore, the key signaling pathway that is culpable of maintaining multiple chronic inflammatory diseases is downregulated.

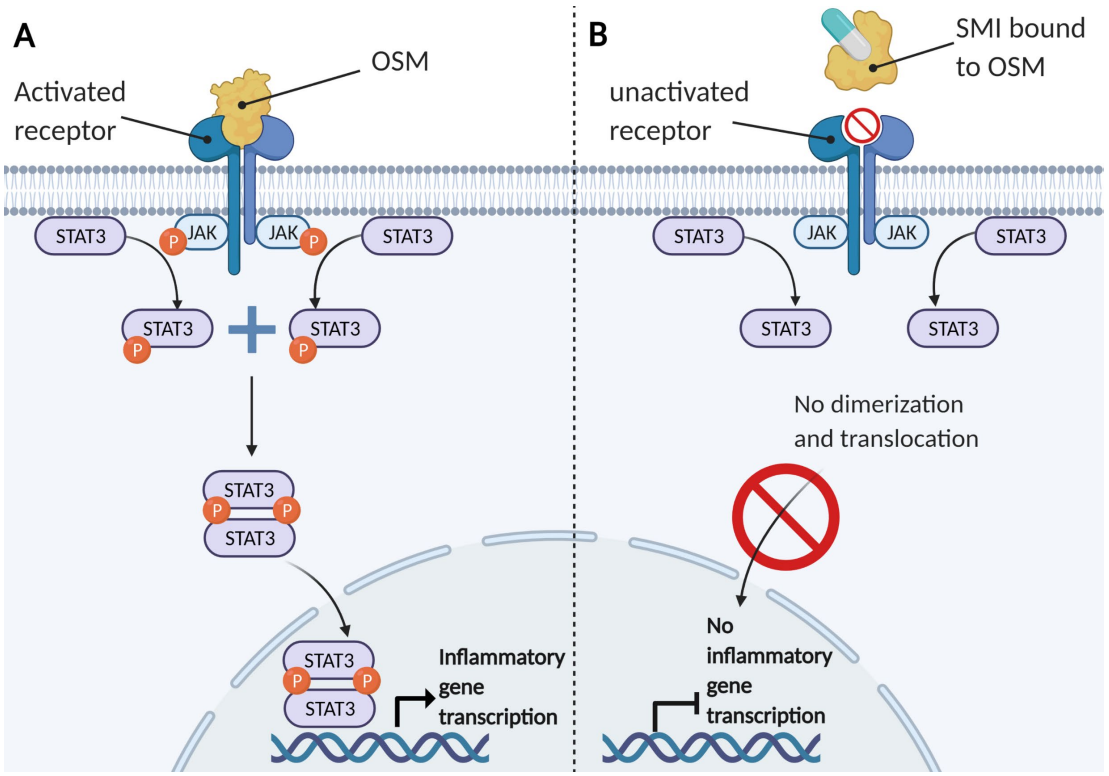


**Figure 1.9 Inhibition of OSM signaling using an SMI**

(**A**) Upon binding with the transmembrane receptors gp130 and OSMR, the OSM protein induces a phosphorylation cascade which results in the dimerization of STAT3 proteins. The STAT3 dimers then get translocated into the nucleus of the cell, where it upregulates inflammatory gene transcription. (**B**) OSM is inhibited by an SMI bound to site III of the protein. As a result, the STAT3 proteins will not dimerize and enter the nucleus. Therefore, no inflammatory gene transcription will be upregulated.

Despite the recent success that monoclonal antibodies have achieved in treating cancers and chronic inflammatory diseases, clinical applications have significant drawbacks. The major challenge that accompanies mAbs therapy is the cost to the patient. The average price of a mAb was $96,731/year (through the years 1997-2016), while the annual cost of small molecules was $730/year in 2013.[119, 120] Oral SMIs are favorable due to their shorter half-life in the body compared to mAbs, which have half-lives between 11-30 days.[121] The long clearance time and half-life of mAbs pose a serious issue if there is a case in which the patient has a severe reaction to the drug or biologic. In contrast, small molecule drugs typically have half-lives on the scale from hours to days.[122-124] Finally,

the size of mAbs limits their ability to penetrate the CNS. This can be an issue if the therapeutic targets have infiltrated CNS tissues.[125]

## 1.9 Summary of Chapter One

This chapter contained a brief discussion of chronic inflammation and how it burdens societies and economies worldwide. In addition, specific pro-inflammatory roles of OSM were identified in breast cancer, rheumatoid arthritis, irritable bowel disease, and systemic sclerosis. Several works were discussed in which small molecule inhibitors were rationally designed to treat different types of cancers, heart attacks, and strokes. Finally, OSM was discussed as a realistic therapeutic target; mAbs have shown that targeting OSM itself does not result in any serious health concerns. The next chapter will discuss how specific OSM amino acids were identified as critical in OSMR type II complex binding. The synthesis and the design of the small molecules targeting OSM will be presented as well.

## 1.10 Chapter One References


1. Hannoodee, S.; Nasuruddin, D. N., Acute inflammatory response. *StatPearls [Internet]* **2020**.
2. Benly, P., Role of histamine in acute inflammation. *Journal of Pharmaceutical Sciences and Research* **2015,** *7* (6), 373.
3. Newton, K.; Dixit, V. M., Signaling in innate immunity and inflammation. *Cold Spring Harb Perspect Biol* **2012,** *4* (3).
4. Pahwa, R.; Goyal, A.; Bansal, P.; Jialal, I., Chronic inflammation. *StatPearls [Internet]* **2018**.
5. Subramanian, S.; Chait, A., The effect of dietary cholesterol on macrophage accumulation in adipose tissue: implications for systemic inflammation and atherosclerosis. *Curr Opin Lipidol* **2009,** *20* (1), 39-44.
6. Krzyszczyk, P.; Schloss, R.; Palmer, A.; Berthiaume, F., The Role of Macrophages in Acute and Chronic Wound Healing and Interventions to Promote Pro-wound Healing Phenotypes. *Front Physiol* **2018,** *9*, 419.
7. Milenkovic, V. M.; Stanton, E. H.; Nothdurfter, C.; Rupprecht, R.; Wetzel, C. H., The Role of Chemokines in the Pathophysiology of Major Depressive Disorder. *Int J Mol Sci* **2019,** *20* (9).
8. Cutolo, M.; Soldano, S.; Smith, V., Pathophysiology of systemic sclerosis: current understanding and new insights. *Expert Rev Clin Immunol* **2019,** *15* (7), 753-764.
9. Yousuf, A.; Ibrahim, W.; Greening, N. J.; Brightling, C. E., T2 Biologics for Chronic Obstructive Pulmonary Disease. *J Allergy Clin Immunol Pract* **2019,** *7* (5), 1405-1416.
10. McCain, J., The Disease Burden of the Most Common Autoimmune Diseases. *Manag Care* **2016,** *25* (7), 28-32.
11. Census Bureau Releases New American Community Survey 5-year Estimates. https://www.census.gov/newsroom/press-releases/2020/acs-5-year.html (accessed November 01).
12. Guarascio, A. J.; Ray, S. M.; Finch, C. K.; Self, T. H., The clinical and economic burden of chronic obstructive pulmonary disease in the USA. *Clinicoecon Outcomes Res* **2013,** *5*, 235-45.
13. Theis, K. A.; Roblin, D. W.; Helmick, C. G.; Luo, R., Prevalence and causes of work disability among working-age US adults, 2011–2013, NHIS. *Disability and health journal* **2018,** *11* (1), 108-115.
14. Arthritis Related Disabilities and Limitations. https://www.cdc.gov/arthritis/data_statistics/Disabilities-Limitations.htm (accessed August 10).
15. Burska, A. N.; Sakthiswary, R.; Sattar, N., Effects of Tumour Necrosis Factor Antagonists on Insulin Sensitivity/Resistance in Rheumatoid Arthritis: A Systematic Review and Meta-Analysis. *PLoS One* **2015,** *10* (6), e0128889.
16. Giles, J. T.; Danielides, S.; Szklo, M.; Post, W. S.; Blumenthal, R. S.; Petri, M.; Schreiner, P. J.; Budoff, M.; Detrano, R.; Bathon, J. M., Insulin resistance in rheumatoid arthritis: disease-related indicators and associations with the presence and progression of subclinical atherosclerosis. *Arthritis Rheumatol* **2015,** *67* (3), 626-636.

17. Ridker, P. M.; Everett, B. M.; Thuren, T.; MacFadyen, J. G.; Chang, W. H.; Ballantyne, C.; Fonseca, F.; Nicolau, J.; Koenig, W.; Anker, S. D., Antiinflammatory therapy with canakinumab for atherosclerotic disease. *New England Journal of Medicine* **2017,** *377* (12), 1119-1131.
18. Zhang, J.-M.; An, J., Cytokines, inflammation, and pain. *Int Anesthesiol Clin* **2007,** *45* (2), 27-37.
19. Kishimoto, T.; Ishizaka, K., Regulation of Antibody Response in Vitro: X. Biphasic Effect of Cyclic AMP on the Secondary anti-Hapten Antibody Response to anti-Immunoglobulin and Enhancing Soluble Factor. *The Journal of Immunology* **1976,** *116* (2), 534-541.
20. Hirano, T.; Yasukawa, K.; Harada, H.; Taga, T.; Watanabe, Y.; Matsuda, T.; Kashiwamura, S.-i.; Nakajima, K.; Koyama, K.; Iwamatsu, A., Complementary DNA for a novel human interleukin (BSF-2) that induces B lymphocytes to produce immunoglobulin. *Nature* **1986,** *324* (6092), 73-76.
21. Gauldie, J.; Richards, C.; Harnish, D.; Lansdorp, P.; Baumann, H., Interferon beta 2/B-cell stimulatory factor type 2 shares identity with monocyte-derived hepatocyte-stimulating factor and regulates the major acute phase protein response in liver cells. *Proceedings of the National Academy of Sciences* **1987,** *84* (20), 7251-7255.
22. Rose-John, S., Interleukin-6 Family Cytokines. *Cold Spring Harb Perspect Biol* **2018,** *10* (2).
23. Heinrich, P. C.; Behrmann, I.; Müller-Newen, G.; Schaper, F.; Graeve, L., Interleukin-6-type cytokine signalling through the gp130/Jak/STAT pathway. *Biochem J* **1998,** *334 ( Pt 2)* (Pt 2), 297-314.
24. Morris, V. A.; Punjabi, A. S.; Lagunoff, M., Activation of Akt through gp130 receptor signaling is required for Kaposi's sarcoma-associated herpesvirus-induced lymphatic reprogramming of endothelial cells. *J Virol* **2008,** *82* (17), 8771-9.
25. Jones, S. A.; Jenkins, B. J., Recent insights into targeting the IL-6 cytokine family in inflammatory diseases and cancer. *Nat Rev Immunol* **2018,** *18* (12), 773-789.
26. Dienz, O.; Rincon, M., The effects of IL-6 on CD4 T cell responses. *Clin Immunol* **2009,** *130* (1), 27-33.
27. van den Broek, T.; Borghans, J. A. M.; van Wijk, F., The full spectrum of human naive T cells. *Nature Reviews Immunology* **2018,** *18* (6), 363-373.
28. Rose, T. M.; Lagrou, M. J.; Fransson, I.; Werelius, B.; Delattre, O.; Thomas, G.; de Jong, P. J.; Todaro, G. J.; Dumanski, J. P., The genes for oncostatin M (OSM) and leukemia inhibitory factor (LIF) are tightly linked on human chromosome 22. *Genomics* **1993,** *17* (1), 136-40.
29. Adrian-Segarra, J. M.; Schindler, N.; Gajawada, P.; Lörchner, H.; Braun, T.; Pöling, J., The AB loop and D-helix in binding site III of human Oncostatin M (OSM) are required for OSM receptor activation. *Journal of Biological Chemistry* **2018,** *293* (18), 7017-7029.
30. Deller, M. C.; Hudson, K. R.; Ikemizu, S.; Bravo, J.; Jones, E. Y.; Heath, J. K., Crystal structure and functional dissection of the cytostatic cytokine oncostatin M. *Structure* **2000,** *8* (8), 863-874.
31. Chollangi, S.; Mather, T.; Rodgers, K. K.; Ash, J. D., A unique loop structure in oncostatin M determines binding affinity toward oncostatin M receptor and leukemia inhibitory factor receptor. *J Biol Chem* **2012,** *287* (39), 32848-59.

32. Nicola, N. A.; Babon, J. J., Leukemia inhibitory factor (LIF). *Cytokine & Growth Factor Reviews* **2015,** *26* (5), 533-544.
33. Richards, C. D., The enigmatic cytokine oncostatin m and roles in disease. *International Scholarly Research Notices* **2013,** *2013*.
34. Suda, T.; Chida, K.; Todate, A.; Ide, K.; Asada, K.; Nakamura, Y.; Suzuki, K.; Kuwata, H.; Nakamura, H., Oncostatin M production by human dendritic cells in response to bacterial products. *Cytokine* **2002,** *17* (6), 335-40.
35. Mosley, B.; De Imus, C.; Friend, D.; Boiani, N.; Thoma, B.; Park, L. S.; Cosman, D., Dual oncostatin M (OSM) receptors. Cloning and characterization of an alternative signaling subunit conferring OSM-specific receptor activation. *J Biol Chem* **1996,** *271* (51), 32635-43.
36. Dey, G.; Radhakrishnan, A.; Syed, N.; Thomas, J. K.; Nadig, A.; Srikumar, K.; Mathur, P. P.; Pandey, A.; Lin, S.-K.; Raju, R.; Prasad, T. S. K., Signaling network of Oncostatin M pathway. *J Cell Commun Signal* **2013,** *7* (2), 103-108.
37. Boulanger, M. J.; Bankovich, A. J.; Kortemme, T.; Baker, D.; Garcia, K. C., Convergent mechanisms for recognition of divergent cytokines by the shared signaling receptor gp130. *Molecular cell* **2003,** *12* (3), 577-589.
38. Kiu, H.; Nicholson, S. E., Biology and significance of the JAK/STAT signalling pathways. *Growth Factors* **2012,** *30* (2), 88-106.
39. Steelman, L. S.; Pohnert, S. C.; Shelton, J. G.; Franklin, R. A.; Bertrand, F. E.; McCubrey, J. A., JAK/STAT, Raf/MEK/ERK, PI3K/Akt and BCR-ABL in cell cycle progression and leukemogenesis. *Leukemia* **2004,** *18* (2), 189-218.
40. Villarino, A. V.; Kanno, Y.; O'Shea, J. J., Mechanisms and consequences of Jak–STAT signaling in the immune system. *Nature Immunology* **2017,** *18* (4), 374-384.
41. Soares-Silva, M.; Diniz, F. F.; Gomes, G. N.; Bahia, D., The Mitogen-Activated Protein Kinase (MAPK) Pathway: Role in Immune Evasion by Trypanosomatids. *Front Microbiol* **2016,** *7*, 183-183.
42. Jorcyk, C. L.; Holzer, R. G.; Ryan, R. E., Oncostatin M induces cell detachment and enhances the metastatic capacity of T-47D human breast carcinoma cells. *Cytokine* **2006,** *33* (6), 323-36.
43. West, N. R.; Hegazy, A. N.; Owens, B. M.; Bullers, S. J.; Linggi, B.; Buonocore, S.; Coccia, M.; Görtz, D.; This, S.; Stockenhuber, K., Oncostatin M drives intestinal inflammation and predicts response to tumor necrosis factor–neutralizing therapy in patients with inflammatory bowel disease. *Nature medicine* **2017,** *23* (5), 579-589.
44. Fearon, U.; Mullan, R.; Markham, T.; Connolly, M.; Sullivan, S.; Poole, A. R.; FitzGerald, O.; Bresnihan, B.; Veale, D. J., Oncostatin M induces angiogenesis and cartilage degradation in rheumatoid arthritis synovial tissue and human cartilage cocultures. *Arthritis & Rheumatism: Official Journal of the American College of Rheumatology* **2006,** *54* (10), 3152-3162.
45. Komori, T.; Morikawa, Y., Oncostatin M in the development of metabolic syndrome and its potential as a novel therapeutic target. *Anatomical Science International* **2018,** *93* (2), 169-176.
46. Marden, G.; Wan, Q.; Wilks, J.; Nevin, K.; Feeney, M.; Wisniacki, N.; Trojanowski, M.; Bujor, A.; Stawski, L.; Trojanowska, M., The role of the oncostatin

M/OSM receptor β axis in activating dermal microvascular endothelial cells in systemic sclerosis. *Arthritis research & therapy* **2020,** *22* (1), 179-179.
47. Robak, E.; Sysa-Jedrzejowska, A.; Stepień, H.; Robak, T., Circulating interleukin-6 type cytokines in patients with systemic lupus erythematosus. *Eur Cytokine Netw* **1997,** *8* (3), 281-6.
48. Masjedi, A.; Hajizadeh, F.; Beigi Dargani, F.; Beyzai, B.; Aksoun, M.; Hojjat-Farsangi, M.; Zekiy, A.; Jadidi-Niaragh, F., Oncostatin M: A mysterious cytokine in cancers. *Int Immunopharmacol* **2021,** *90*, 107158.
49. Society, A. C., Cancer Statistics, 2021. *A Cancer Journal For Clinicians* **2021,** *71* (1), 7-33.
50. ACS Survival Rates for Breast Cancer. https://www.cancer.org/cancer/breast-cancer/understanding-a-breast-cancer-diagnosis/breast-cancer-survival-rates.html (accessed August 11).
51. Patanaphan, V.; Salazar, O. M.; Risco, R., Breast cancer: metastatic patterns and their prognosis. *South Med J* **1988,** *81* (9), 1109-12.
52. Siziopikou, K. P., Ductal carcinoma in situ of the breast: current concepts and future directions. *Archives of pathology & laboratory medicine* **2013,** *137* (4), 462-466.
53. Malhotra, G. K.; Zhao, X.; Band, H.; Band, V., Histological, molecular and functional subtypes of breast cancers. *Cancer Biol Ther* **2010,** *10* (10), 955-60.
54. Yersal, O.; Barutca, S., Biological subtypes of breast cancer: Prognostic and therapeutic implications. *World J Clin Oncol* **2014,** *5* (3), 412-424.
55. Anderson, K. N.; Schwab, R. B.; Martinez, M. E., Reproductive risk factors and breast cancer subtypes: a review of the literature. *Breast Cancer Res Treat* **2014,** *144* (1), 1-10.
56. Kalluri, R.; Weinberg, R. A., The basics of epithelial-mesenchymal transition. *J Clin Invest* **2009,** *119* (6), 1420-1428.
57. Gunasinghe, N. P.; Wells, A.; Thompson, E. W.; Hugo, H. J., Mesenchymal-epithelial transition (MET) as a mechanism for metastatic colonisation in breast cancer. *Cancer Metastasis Rev* **2012,** *31* (3-4), 469-78.
58. Bartok, B.; Firestein, G. S., Fibroblast-like synoviocytes: key effector cells in rheumatoid arthritis. *Immunol Rev* **2010,** *233* (1), 233-55.
59. Gabriel, S. E.; Michaud, K., Epidemiological studies in incidence, prevalence, mortality, and comorbidity of the rheumatic diseases. *Arthritis research & therapy* **2009,** *11* (3), 1-16.
60. Smolen, J. S.; Aletaha, D.; Barton, A.; Burmester, G. R.; Emery, P.; Firestein, G. S.; Kavanaugh, A.; McInnes, I. B.; Solomon, D. H.; Strand, V.; Yamamoto, K., Rheumatoid arthritis. *Nature Reviews Disease Primers* **2018,** *4* (1), 18001.
61. Raciborski, F.; Kłak, A.; Kwiatkowska, B.; Batko, B.; Sochocka-Bykowska, M.; Zoń-Giebel, A.; Gola, Z.; Guzera, Z.; Maślińska, M.; working, t., Diagnostic delays in rheumatic diseases with associated arthritis. *Reumatologia* **2017,** *55* (4), 169-176.
62. Smith, M. D., The normal synovium. *Open Rheumatol J* **2011,** *5*, 100-6.
63. Berumen-Nafarrate, E.; Leal-Berumen, I.; Luevano, E.; Solis, F. J.; Muñoz-Esteves, E., Synovial tissue and synovial fluid. *J Knee Surg* **2002,** *15* (1), 46-8.

64. Yap, H.-Y.; Tee, S. Z.-Y.; Wong, M. M.-T.; Chow, S.-K.; Peh, S.-C.; Teow, S.-Y., Pathogenic Role of Immune Cells in Rheumatoid Arthritis: Implications in Clinical Treatment and Biomarker Development. *Cells* **2018,** *7* (10), 161.
65. Bell, N. H., RANK ligand and the regulation of skeletal remodeling. *J Clin Invest* **2003,** *111* (8), 1120-2.
66. Araki, Y.; Mimura, T., Matrix Metalloproteinase Gene Activation Resulting from Disordred Epigenetic Mechanisms in Rheumatoid Arthritis. *International journal of molecular sciences* **2017,** *18* (5), 905.
67. Firestein, G. S.; Budd, R. C.; Gabriel, S. E.; McInnes, I. B.; O'Dell, J. R., *Kelley's Textbook of Rheumatology E-Book*. Elsevier Health Sciences: 2012.
68. Jozic, D.; Bourenkov, G.; Lim, N. H.; Visse, R.; Nagase, H.; Bode, W.; Maskos, K., X-ray structure of human proMMP-1: new insights into procollagenase activation and collagen binding. *J Biol Chem* **2005,** *280* (10), 9578-85.
69. Hui, W.; Bell, M.; Carroll, G., Detection of oncostatin M in synovial fluid from patients with rheumatoid arthritis. *Ann Rheum Dis* **1997,** *56* (3), 184-187.
70. Spiller, R.; Aziz, Q.; Creed, F.; Emmanuel, A.; Houghton, L.; Hungin, P.; Jones, R.; Kumar, D.; Rubin, G.; Trudgill, N.; Whorwell, P., Guidelines on the irritable bowel syndrome: mechanisms and practical management. *Gut* **2007,** *56* (12), 1770-98.
71. Molodecky, N. A.; Soon, I. S.; Rabi, D. M.; Ghali, W. A.; Ferris, M.; Chernoff, G.; Benchimol, E. I.; Panaccione, R.; Ghosh, S.; Barkema, H. W.; Kaplan, G. G., Increasing incidence and prevalence of the inflammatory bowel diseases with time, based on systematic review. *Gastroenterology* **2012,** *142* (1), 46-54.e42; quiz e30.
72. Cleynen, I.; Boucher, G.; Jostins, L.; Schumm, L. P.; Zeissig, S.; Ahmad, T.; Andersen, V.; Andrews, J. M.; Annese, V.; Brand, S., Inherited determinants of Crohn's disease and ulcerative colitis phenotypes: a genetic association study. *The Lancet* **2016,** *387* (10014), 156-167.
73. Mowat, C.; Cole, A.; Windsor, A.; Ahmad, T.; Arnott, I.; Driscoll, R.; Mitton, S.; Orchard, T.; Rutter, M.; Younge, L.; Lees, C.; Ho, G. T.; Satsangi, J.; Bloom, S., Guidelines for the management of inflammatory bowel disease in adults. *Gut* **2011,** *60* (5), 571-607.
74. Maaser, C.; Sturm, A.; Vavricka, S. R.; Kucharzik, T.; Fiorino, G.; Annese, V.; Calabrese, E.; Baumgart, D. C.; Bettenworth, D.; Borralho Nunes, P., ECCO-ESGAR Guideline for Diagnostic Assessment in IBD Part 1: Initial diagnosis, monitoring of known IBD, detection of complications. *Journal of Crohn's and Colitis* **2019,** *13* (2), 144-164K.
75. Sanchez-Munoz, F.; Dominguez-Lopez, A.; Yamamoto-Furusho, J. K., Role of cytokines in inflammatory bowel disease. *World J Gastroenterol* **2008,** *14* (27), 4280-8.
76. Ben-Horin, S.; Chowers, Y., Tailoring anti-TNF therapy in IBD: drug levels and disease activity. *Nat Rev Gastroenterol Hepatol* **2014,** *11* (4), 243-55.
77. Guerra, I.; Bermejo, F., Management of inflammatory bowel disease in poor responders to infliximab. *Clin Exp Gastroenterol* **2014,** *7*, 359-67.
78. Rahman, A.; Fazal, F., Hug tightly and say goodbye: role of endothelial ICAM-1 in leukocyte transmigration. *Antioxid Redox Signal* **2009,** *11* (4), 823-39.
79. Dragoni, S.; Hudson, N.; Kenny, B. A.; Burgoyne, T.; McKenzie, J. A.; Gill, Y.; Blaber, R.; Futter, C. E.; Adamson, P.; Greenwood, J.; Turowski, P., Endothelial

MAPKs Direct ICAM-1 Signaling to Divergent Inflammatory Functions. *J Immunol* **2017,** *198* (10), 4074-4085.
80. Quintanilla, M.; Montero-Montero, L.; Renart, J.; Martín-Villar, E., Podoplanin in Inflammation and Cancer. *Int J Mol Sci* **2019,** *20* (3).
81. Fox, J. G.; Ge, Z.; Whary, M. T.; Erdman, S. E.; Horwitz, B. H., Helicobacter hepaticus infection in mice: models for understanding lower bowel inflammation and cancer. *Mucosal Immunol* **2011,** *4* (1), 22-30.
82. Chen, X.; Zaro, J. L.; Shen, W.-C., Fusion protein linkers: property, design and functionality. *Adv Drug Deliv Rev* **2013,** *65* (10), 1357-1369.
83. Sobolewski, P.; Maślińska, M.; Wieczorek, M.; Łagun, Z.; Malewska, A.; Roszkiewicz, M.; Nitskovich, R.; Szymańska, E.; Walecka, I., Systemic sclerosis - multidisciplinary disease: clinical features and treatment. *Reumatologia* **2019,** *57* (4), 221-233.
84. Kowal-Bielecka, O., Bielecki M. Twardzina układowa. *Wielka Interna. Reumatologia [Polish]. Puszczewicz M (ed.). Medical Tribune, Warsaw* **2010**, 127-41.
85. Barsotti, S.; Bellando Randone, S.; Guiducci, S.; Della Rossa, A., Systemic sclerosis: a critical digest of the recent literature. *Clin Exp Rheumatol* **2014,** *32* (6 Suppl 86), S194-205.
86. Stifano, G.; Sornasse, T.; Rice, L. M.; Na, L.; Chen-Harris, H.; Khanna, D.; Jahreis, A.; Zhang, Y.; Siegel, J.; Lafyatis, R., Skin gene expression is prognostic for the trajectory of skin disease in patients with diffuse cutaneous systemic sclerosis. *Arthritis & rheumatology* **2018,** *70* (6), 912-919.
87. Martin, P.; Teodoro, W. R.; Velosa, A. P.; de Morais, J.; Carrasco, S.; Christmann, R. B.; Goldenstein-Schainberg, C.; Parra, E. R.; Katayama, M. L.; Sotto, M. N.; Capelozzi, V. L.; Yoshinari, N. H., Abnormal collagen V deposition in dermis correlates with skin thickening and disease activity in systemic sclerosis. *Autoimmun Rev* **2012,** *11* (11), 827-35.
88. Rajkumar, V. S.; Sundberg, C.; Abraham, D. J.; Rubin, K.; Black, C. M., Activation of microvascular pericytes in autoimmune Raynaud's phenomenon and systemic sclerosis. *Arthritis Rheum* **1999,** *42* (5), 930-41.
89. De Las Rivas, J.; Fontanillo, C., Protein-protein interactions essentials: key concepts to building and analyzing interactome networks. *PLoS Comput Biol* **2010,** *6* (6), e1000807.
90. Heifetz, A.; Sladek, V.; Townsend-Nicholson, A.; Fedorov, D. G., Characterizing Protein-Protein Interactions with the Fragment Molecular Orbital Method. *Methods Mol Biol* **2020,** *2114*, 187-205.
91. Chen, J.; Sawyer, N.; Regan, L., Protein-protein interactions: general trends in the relationship between binding affinity and interfacial buried surface area. *Protein Sci* **2013,** *22* (4), 510-5.
92. Smith, R. D.; Hu, L.; Falkner, J. A.; Benson, M. L.; Nerothin, J. P.; Carlson, H. A., Exploring protein-ligand recognition with Binding MOAD. *J Mol Graph Model* **2006,** *24* (6), 414-25.
93. Cunningham, B. C.; Wells, J. A., Comparison of a structural and a functional epitope. *J Mol Biol* **1993,** *234* (3), 554-63.
94. Cunningham, B. C.; Wells, J. A., High-resolution epitope mapping of hGH-receptor interactions by alanine-scanning mutagenesis. *Science* **1989,** *244* (4908), 1081-5.

95. Mullard, A., FDA approves 100th monoclonal antibody product. *Nature* **2021,** *20* (7).
96. Yokoyama, W. M.; Christensen, M.; Santos, G. D.; Miller, D.; Ho, J.; Wu, T.; Dziegelewski, M.; Neethling, F. A., Production of monoclonal antibodies. *Current protocols in immunology* **2013,** *102* (1), 2.5. 1-2.5. 29.
97. Zahavi, D.; Weiner, L., Monoclonal Antibodies in Cancer Therapy. *Antibodies (Basel)* **2020,** *9* (3).
98. Bluestein, D., Monoclonal antibody pregnancy tests. *Am Fam Physician* **1988,** *38* (1), 197-204.
99. Cohan, S. L.; Lucassen, E. B.; Romba, M. C.; Linch, S. N., Daclizumab: Mechanisms of Action, Therapeutic Efficacy, Adverse Events and Its Uncovering the Potential Role of Innate Immune System Recruitment as a Treatment Strategy for Relapsing Multiple Sclerosis. *Biomedicines* **2019,** *7* (1).
100. Martin, J. F.; Perry, J. S.; Jakhete, N. R.; Wang, X.; Bielekova, B., An IL-2 paradox: blocking CD25 on T cells induces IL-2-driven activation of CD56(bright) NK cells. *J Immunol* **2010,** *185* (2), 1311-20.
101. Bielekova, B.; Catalfamo, M.; Reichert-Scrivner, S.; Packer, A.; Cerna, M.; Waldmann, T. A.; McFarland, H.; Henkart, P. A.; Martin, R., Regulatory CD56(bright) natural killer cells mediate immunomodulatory effects of IL-2Ralpha-targeted therapy (daclizumab) in multiple sclerosis. *Proc Natl Acad Sci U S A* **2006,** *103* (15), 5941-6.
102. Xu, W.; Fazekas, G.; Hara, H.; Tabira, T., Mechanism of natural killer (NK) cell regulatory role in experimental autoimmune encephalomyelitis. *J Neuroimmunol* **2005,** *163* (1-2), 24-30.
103. Matsiota-Bernard, P.; Roullet, E.; Ragimbeau, J.; Avrameas, S., T cell activation by autoantigens in multiple sclerosis. *Autoimmunity* **1993,** *16* (4), 237-43.
104. Ran, X.; Gestwicki, J. E., Inhibitors of protein-protein interactions (PPIs): an analysis of scaffold choices and buried surface area. *Curr Opin Chem Biol* **2018,** *44*, 75-86.
105. Khwaja, A.; Bjorkholm, M.; Gale, R. E.; Levine, R. L.; Jordan, C. T.; Ehninger, G.; Bloomfield, C. D.; Estey, E.; Burnett, A.; Cornelissen, J. J.; Scheinberg, D. A.; Bouscary, D.; Linch, D. C., Acute myeloid leukaemia. *Nature Reviews Disease Primers* **2016,** *2* (1), 16010.
106. Jewett, A.; Tseng, H.-C., 35 - Immunotherapy. In *Pharmacology and Therapeutics for Dentistry (Seventh Edition)*, Dowd, F. J.; Johnson, B. S.; Mariotti, A. J., Eds. Mosby: 2017; pp 504-529.
107. Treating Acute Myeloid Leukemia (AML). https://www.cancer.org/cancer/acute-myeloid-leukemia/treating.html (accessed September 30).
108. Lu, H.; Zhou, Q.; He, J.; Jiang, Z.; Peng, C.; Tong, R.; Shi, J., Recent advances in the development of protein–protein interactions modulators: mechanisms and clinical trials. *Signal Transduction and Targeted Therapy* **2020,** *5* (1), 213.
109. Oltersdorf, T.; Elmore, S. W.; Shoemaker, A. R.; Armstrong, R. C.; Augeri, D. J.; Belli, B. A.; Bruncko, M.; Deckwerth, T. L.; Dinges, J.; Hajduk, P. J., An inhibitor of Bcl-2 family proteins induces regression of solid tumours. *Nature* **2005,** *435* (7042), 677-681.
110. Shuker, S. B.; Hajduk, P. J.; Meadows, R. P.; Fesik, S. W., Discovering high-affinity ligands for proteins: SAR by NMR. *Science* **1996,** *274* (5292), 1531-1534.

111. Lee, J. H.; Zhang, Q.; Jo, S.; Chai, S. C.; Oh, M.; Im, W.; Lu, H.; Lim, H.-S., Novel pyrrolopyrimidine-based α-helix mimetics: cell-permeable inhibitors of protein−protein interactions. *Journal of the American Chemical Society* **2011,** *133* (4), 676-679.
112. Ran, X.; Burchfiel, E. T.; Dong, B.; Rettko, N. J.; Dunyak, B. M.; Shao, H.; Thiele, D. J.; Gestwicki, J. E., Rational design and screening of peptide-based inhibitors of heat shock factor 1 (HSF1). *Bioorg Med Chem* **2018,** *26* (19), 5299-5306.
113. Carpenter, R. L.; Gökmen-Polar, Y., HSF1 as a Cancer Biomarker and Therapeutic Target. *Curr Cancer Drug Targets* **2019,** *19* (7), 515-524.
114. Cook, J. J.; Bednar, B.; Lynch Jr, J. J.; Gould, R. J.; Egbertson, M. S.; Halczenko, W.; Duggan, M. E.; Hartman, G. D.; Lo, M. W.; Murphy, G. M., Tirofiban (Aggrastat®). *Cardiovascular Drug Reviews* **1999,** *17* (3), 199-224.
115. Egbertson, M. S.; Chang, C. T.; Duggan, M. E.; Gould, R. J.; Halczenko, W.; Hartman, G. D.; Laswell, W. L.; Lynch, J. J., Jr.; Lynch, R. J.; Manno, P. D.; et al., Non-peptide fibrinogen receptor antagonists. 2. Optimization of a tyrosine template as a mimic for Arg-Gly-Asp. *J Med Chem* **1994,** *37* (16), 2537-51.
116. Reid, J.; Zamuner, S.; Edwards, K.; Rumley, S.-A.; Nevin, K.; Feeney, M.; Zecchin, C.; Fernando, D.; Wisniacki, N., In vivo affinity and target engagement in skin and blood in a first-time-in-human study of an anti-oncostatin M monoclonal antibody. *Br J Clin Pharmacol* **2018,** *84* (10), 2280-2291.
117. Choy, E. H.; Bendit, M.; McAleer, D.; Liu, F.; Feeney, M.; Brett, S.; Zamuner, S.; Campanile, A.; Toso, J., Safety, tolerability, pharmacokinetics and pharmacodynamics of an anti- oncostatin M monoclonal antibody in rheumatoid arthritis: results from phase II randomized, placebo-controlled trials. *Arthritis Research & Therapy* **2013,** *15* (5), R132.
118. Du, Q.; Qian, Y.; Xue, W., Molecular Simulation of Oncostatin M and Receptor (OSM–OSMR) Interaction as a Potential Therapeutic Target for Inflammatory Bowel Disease. *Frontiers in Molecular Biosciences* **2020,** *7* (29).
119. Emerton, D. A., Profitability in the biosimilars market: can you translate scientific excellence into a healthy commercial return. *BioProcess Int* **2013,** *11* (6 suppl), 6-14.
120. Hernandez, I.; Bott, S. W.; Patel, A. S.; Wolf, C. G.; Hospodar, A. R.; Sampathkumar, S.; Shrank, W. H., Pricing of monoclonal antibody therapies: higher if used for cancer. *Am J Manag Care* **2018,** *24* (2), 109-112.
121. Ovacik, M.; Lin, K., Tutorial on Monoclonal Antibody Pharmacokinetics and Its Considerations in Early Development. *Clin Transl Sci* **2018,** *11* (6), 540-552.
122. Ait-Daoud, N.; Hamby, A. S.; Sharma, S.; Blevins, D., A Review of Alprazolam Use, Misuse, and Withdrawal. *J Addict Med* **2018,** *12* (1), 4-10.
123. Markowitz, J. S.; Patrick, K. S., The Clinical Pharmacokinetics of Amphetamines Utilized in the Treatment of Attention-Deficit/Hyperactivity Disorder. *J Child Adolesc Psychopharmacol* **2017,** *27* (8), 678-689.
124. Rossi, A.; Barraco, A.; Donda, P., Fluoxetine: a review on evidence based medicine. *Ann Gen Hosp Psychiatry* **2004,** *3* (1), 2.
125. Aqel, S. I.; Kraus, E. E.; Jena, N.; Kumari, V.; Granitto, M. C.; Mao, L.; Farinas, M. F.; Zhao, E. Y.; Perottino, G.; Pei, W.; Lovett-Racke, A. E.; Racke, M. K.; Fuchs, J. R.; Li, C.; Yang, Y., Novel small molecule IL-6 inhibitor suppresses autoreactive Th17 development and promotes T(reg) development. *Clin Exp Immunol* **2019,** *196* (2), 215-225.

# CHAPTER TWO: DESIGN AND SYNTHESIS OF SMALL MOLECULES

## 2.1 Overview of Chapter Two

As described in chapter 1, there is a considerable amount of evidence that frames OSM as a potential therapeutic target for the treatment of several chronic inflammatory diseases. This highlights a need for affordable small molecule drugs that target OSM and inhibit its pro-inflammatory signaling pathway. The first logical step in designing a small molecule inhibitor for any protein is to understand the landscape of the protein and identify the amino acids that are important for receptor activation. Once a druggable site on the protein is successfully identified, a small molecule inhibitor can be designed. Seminal work for the OSM-SMI project has already been accomplished by a multidisciplinary, collaborative research group consisting of Dr. Don Warner, Dr. Cheryl Jorcyk, Dr. Lisa Warner, Dr. Matt King, and Dr. Danny Xu (Idaho State University). Potential binding sites of OSM were independently identified and were consistent with the three binding sites reported in the literature. These include sites I, II, III. Using a high-throughput virtual screening targeting site III of OSM, 26 structures were identified as potential lead compounds. The most promising lead compounds were identified to be SMI-8, SMI-10, and SMI-26. The design and synthesis of SMI-8 analogs are described herein.

## 2.2 Elucidation of OSM Binding Sites

### 2.2.1 Surface Analysis of OSM Identifies Favorable Binding Sites

Potential ligand binding sites on OSM were predicted by collaborator and computational chemist Dr. Danny Xu using the AutoLigand program.[1] The program was used to scan the surface of the human OSM crystal structure (PDB ID: 1EVS) for potential ligand-binding sites. As seen in panel A of Figure 2.1, three potential sites were identified with favorable energy/volume ratios. As seen in panel B, site III was determined to contain the highest energy of binding while having the smallest volume in the binding pocket (E/V = -2.45). Therefore, site III was identified to be the preferred region of OSM to target with an SMI. It should be noted that the binding sites predicted by Dr. Danny Xu agree with literature that identifies sites I, II, and III as receptor-binding sites.[2-4]

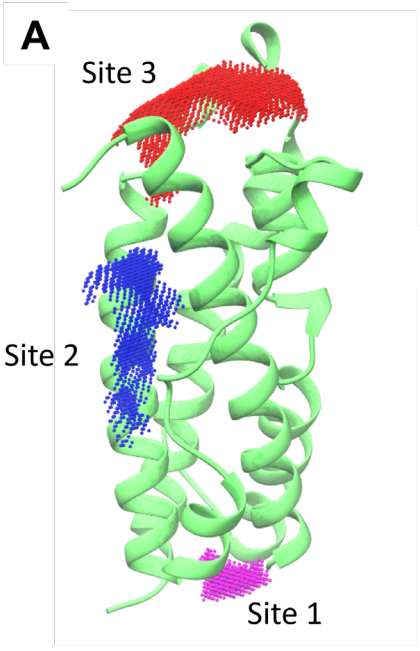


**B**

| | Volume | E/V |
|---|---|---|
| **Site 1** | 77.9 | -2.41 |
| **Site 2** | 162.5 | -2.41 |
| **Site3** | 315.6 | -2.45 |

**Figure 2.1 Predicted binding sites of OSM**
(**A**) Computational modeling of OSM revealed three potential ligand binding sites. (**B**) Site III was calculated to have the highest energy to volume ratio (-2.45 E/V). The data were obtained by Dr. Danny Xu. Image courtesy of Dr. King.

### 2.2.2 *In Vitro* Alanine Scanning Experiments of OSM

Deller and coworkers obtained the first crystal structure of OSM and performed the first set of alanine scanning experiments of the protein in 2000.[3] The crystal structure was obtained first, which allowed the authors to identify amino acid stretches likely to participate in OSMRβ binding. After being identified, these specific stretches were subjected to alanine scanning experiments. These experiments are very important as they provide crucial data regarding the interactions between OSM and OSMRβ, for which a crystal structure has not been obtained. First, Deller and coworkers identified amino acid residues at site II of OSM responsible for OSM-gp130 binding. It was found that the following four amino acid residues were responsible: Gln16, Gln20, Gly120, and Asn124. While the Gln16Ala mutant seemed to have affected OSM binding the least, the mutation of the other three amino acids caused the mutants to experience a significant loss in binding ability. Next, the authors explored how specific mutations of amino acids in site III of OSM altered its ability to bind to OSMRβ. It was found that both Phe160 and Lys163 were critical for stabilizing the OSM-OSMRβ binding event.

Both site II and site III mutants were subjected to a competitive binding assay that assessed their ability to displace biotin-labeled OSM. Site II mutants were used to displace biotinylated OSM from an immobilized gp130 receptor, while site III mutants were used to displace biotinylated OSM from a gp130/LIFR fusion protein receptor. In this experiment, the authors introduced increasing concentrations of OSM alanine mutants to the biotinylated WT OSM bound to an immobilized gp130 receptor. Then, the optical density was measured at 490 to observe the amount of biotinylated WT OSM bound to the gp130 receptor. If the biotin-labeled WT OSM is displaced from the

receptor complex, then the optical density measurements taken at 490 nm should decrease in accordance with the population of displaced WT OSM.

The authors reported "activity values" for the competitive binding assays as $IC_{50}$ quotients, where the $IC_{50}$ of the mutant was divided by the $IC_{50}$ of the biotinylated WT OSM ($IC_{50}$ mutant/$IC_{50}$ WT OSM). To clarify, $IC_{50}$ refers to the concentration of mutant or WT protein required to elicit a 50% inhibition of binding of WT biotinylated OSM. The Gln20Ala, Gly120Ala, and Asn124 (site II) mutants were observed to have activity values of 90, > 100, and > 100, respectively. This translates to a 90-fold increase in the $IC_{50}$ for the Gln20Ala mutant and a greater than 100 fold increase in the $IC_{50}$ values for the Gly120Ala and Asn124Ala mutants. The Phe160Ala and Lys163Ala (site III) mutants were both observed to have activity values > 100. This translates to a greater than 10,000-fold increase in $IC_{50}$ values for both mutants.

Second, site II and site III mutants were subjected to a cell-survivability assay that measured their ability to induce cellular proliferation in Ba/F3 cells. Site II mutants were used to stimulate Ba/F3 cells transfected with human gp130/LIFR, and site III mutants were used to stimulate Ba/F3 cells transfected with human gp130/OSMRβ. This experiment works on the premise that for the Ba/F3 cells to survive and multiply, the gp130/OSMRβ or gp130/LIFR complex must be stimulated by OSM.[5] In this experiment, the authors introduced increasing concentrations of mutants to the Ba/F3 cells to observe a change in optical density measured at 570 nm. If the measured optical density does not increase, then receptor stimulation by OSM is not occurring.

The authors reported "activity values" for the Ba/F3 cell-survival assays as $EC_{50}$ quotients, where the $EC_{50}$ of the mutant is divided by the $EC_{50}$ of WT OSM ($EC_{50}$

mutant/$EC_{50}$). $EC_{50}$ refers to the concentration of mutant required to elicit a response equal to 50% of the maximal response of WT OSM. Gln20Ala, Gly120Ala, and Asn124Ala (site II) mutants were observed to have activity values of 30, > 10,000, and > 10,000 respectively. This translates to a 30-fold increase in $EC_{50}$ for the Gln20 mutant and a greater than 10,000-fold increase in $EC_{50}$ values for both Gly120Ala and Asn124 mutants. The Phe160Ala and Lys163Ala (site III) mutants were both observed to have activity values > 10,000. This translates to a greater than 10,000-fold increase in $EC_{50}$ values for both mutants.

Collectively, the assays suggest that Asn124, Gly120, and Gln20 are a core set of solvent-exposed amino acids necessary for OSM-gp130 binding. When either of these amino acids was mutated, a large decrease in affinity and Ba/F3 cell survivability was observed. In addition, Phe160 and Lys163 were found to be absolutely necessary for OSM's ability to bind to OSMRβ and LIFR, as mutation of these amino acids resulted in the inability to displace WT OSM from a gp130/LIFR fusion protein and completely shut down OSM signaling in Ba/F3 cells.

In 2018, Adrian-Segarra and coworkers revealed a structural motif at site III of OSM that was necessary for stabilizing the binding interaction between OSM and OSMRβ. This was termed the FXXK motif.[2] Similar to the work accomplished by Deller and coworkers in 2000, the study's main objective was to replace specific residues with alanine and evaluate the function of the OSM mutants. Site-directed mutagenesis of OSM was performed by full-plasmid amplification, and *E. coli* was used to express the mutants. The mutants were then purified and used to stimulate A375 melanoma cells to measure OSMRβ activity or human choriocarcinoma cells to measure LIFR activity.

Afterward, the amount of phosphorylated STAT3 (pSTAT3) was quantified by band visualization of horse radish peroxidase-conjugated secondary antibodies. The amount of pSTAT in the cell lysates was used as a metric to identify the degree of OSM signaling.

In addition to the crucial Phe160 and Lys163 residues previously identified by Deller and coworkers, mutation of the amino acids Tyr34, Gln38, Leu40, Lue45, and Cys49 were found to reduce pSTAT3 expression in A375 cells greatly. Interestingly, the Leu40 and Cys49 mutants also caused a reduction of pSTAT3 expression in human choriocarcinoma cells, which means that these amino acids are necessary to activate both type I and type II OSMR complexes. These data suggest that the residues identified in this experiment should be considered as targets in site III of OSM. Figure 2.2 summarizes the key amino acids that were identified in the alanine scanning experiments performed by Adrian-Segarra and coworkers, and Deller and coworkers.

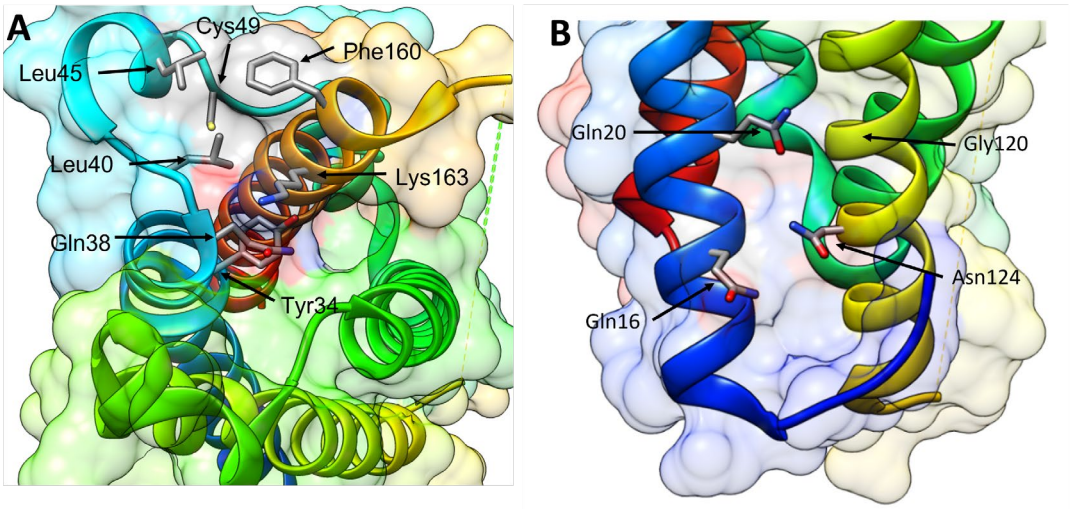


**Figure 2.2 Alanine scanning experiments identify key amino acids**

(A) A top view of OSM overlooking site III depicts the amino acids that were identified to participate in OSM-OSMRβ binding. While Phe160 and Lys163 were identified by Deller and coworkers, Tyr34, Gln38, Leu40, Lue45, Cys49, Phe160, Lys163 were identified by Adrian-Segarra and coworkers. (B) A side view of site II on OSM shows Asn124, Gly120, Gln20, and Gln16, which have been identified by Adrian-Segarra and coworkers as core set of residues necessary for gp130 binding.

In addition, Pro153 and Gly39 mutants were also observed to shut down OSM signaling in A375 cells completely, but their ability to stimulate human choriocarcinoma cells remained unaltered. It is important to note that the point mutations of these residues most likely caused a change in characteristic structural rigidity necessary for OSM to bind to OSMRβ preferentially over LIFR. For example, Gly39 and Pro153 are commonly found in turn and loop structures of proteins.[6] The mutagenesis of these most likely caused a conformational change in OSM, rendering it unable to bind to OSMRβ yet still able to bind to LIFR. In conclusion, the data generated by Adrian-Segarra and coworkers agree with previous findings by Deller and coworkers.

2.2.3 Computational Alanine Scanning Experiments of OSM

Molecular simulation experiments performed by Du and coworkers have given insight as to what residues greatly contribute to the binding interaction at the OSM/OSMRβ interface.[4] As the structure of OSMRβ is unknown, the authors constructed a protein-protein binding region of OSMR that mimics the structure of LIFR. After the OSMRβ construct was virtually generated, a per-residue energy decomposition analysis was performed for the OSM/OSMRβ complex to reveal the energy contribution of single amino acid residues. The amino acids that were predicted to have an energy contribution more negative than -1.0 kcal/mol were classified as important. The per-residue binding energy decomposition predicted four residues in OSM that have already been identified in the literature to be critical to OSM-OSMRβ binding.[2] In agreement with Adrian-Segarra and coworkers, Gly39, Leu40, and Leu45 in the AB loop, and Phe160 in the D helix were identified as significant contributors. Furthermore, six

additional amino acid residues were identified as playing an important role in OSM-OSMRβ binding: Arg36, Asp41, Val42, Arg100, Leu103, and Gln161.

Next, Du and coworkers conducted computational alanine scanning experiments on the residues that were significant contributors to the OSM-OSMRβ binding interaction to discover hot spots between the proteins. The computational experiments revealed that Arg100, Phe160, Leu103, and Gln161 contributed free energies of binding more than 2 Kcal/mol. As such, these amino acids were deemed particularly important for stabilizing the OSM/OSMRβ complex. One of the hot spots was identified as a hydrogen-bond between Arg100 of OSM and Asp262 of OSMRβ. In addition, the authors identified another hydrogen-bond hot spot between Gln161 and Ser223. Lastly, a π-π interaction between Phe160 of OSM and Tyr214 of OSMRβ was identified as a hot spot as well. Table 2.1 summarizes which amino acid residues have been identified in the primary literature to contribute to site II or site III binding of OSM. Notably, the amino acids listed in the site III column present themselves as potential targets as these are shown to stabilize the binding interaction between OSM and OSMRβ.

**Table 2.1 Summary of key amino acids at sites II and III of OSM**
*In vitro* and *in silico* alanine scanning experiments identify amino acids that participate in OSM-gp130 or OSM-OSMRβ binding.

| | **Site II amino Acids** | **Site III amino Acids** |
|---|---|---|
| ***In vitro* alanine scanning experiments** | Gln16, Gln20, Gly120, Asn124 | Tyr34, Gln38, Leu40, Lue45, Cys49, Phe160, Lys163 |
| ***In silico* alanine scanning experiments** | N/A | Arg36, Leu40, Asp41, Val42, Leu45, Arg100, Leu103, Phe160, Gln161 |

## 2.3 Identification of lead SMIs Targeting OSM

### 2.3.1 Identification of OSM-SMIs

Considering the supporting evidence from the alanine scanning experiments and previous work accomplished by Dr. Danny Xu identifying druggable sites on OSM, site III of OSM was the most favorable binding site to target for inhibition by SMIs. So, Dr. Matt King (Boise State University) and Dr. Danny Xu conducted a high-throughput virtual screening of approximately 1.65 million compounds from the National Cancer Institute open database and ZINC databases using AutoDock 4.2 to identify 26 prospective SMIs. The compounds were predicted to have $K_D$ values less than 10 μM and free energies of binding less than -5.0 kcal/mol.

As seen in Figure 2.3, the twenty-six potential lead compounds were purchased and subjected to an ELISA by researchers in the Jorcyk lab at Boise State University. As previously discussed in section 1.3, OSM binding initiates a phosphorylation cascade wherein STAT3 proteins become phosphorylated by JAK proteins. The ELISA experiments measure relative pSTAT3 expression in cell lysates using antibodies that specifically target pSTAT3. So, pSTAT3 can serve as a metric for OSM-induced signaling. To conduct the assay, recombinant human OSM was incubated for 1 hour with or without SMI and was used to stimulate T47D human breast cancer cells. The no treatment cell group (NT, white) received no OSM, resulting in a group that serves as a baseline value for pSTAT3 expression. The OSM cell group (OSM, black) received OSM, which serves as a maximum amount of pSTAT3 expression. The experimental groups (gray) represent cells treated with OSM incubated with the according SMI. The closer the experimental value of pSTAT3 expression levels is to that of the no treatment

group, the better the lead compound. Three of the compounds from the assay were chosen to be optimized: SMI-8, SMI-10, and SMI-26. Even though SMI-23, SMI-24, and SMI-25 were identified as lead compounds by their ability to inhibit OSM signaling, they were not chosen to be further optimized.

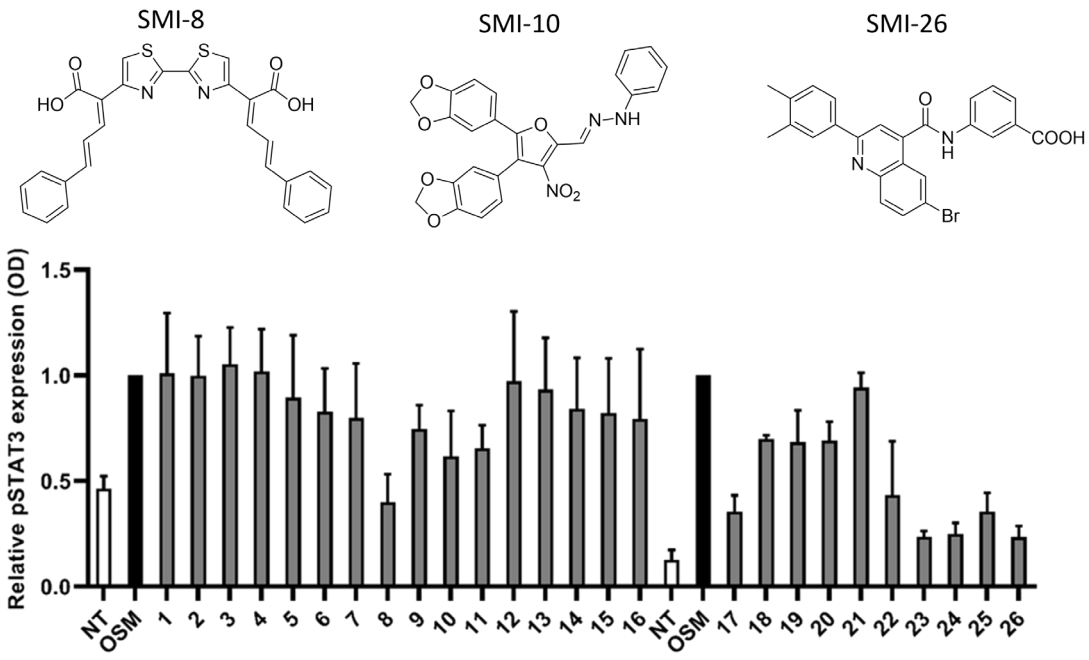


**Figure 2.3 ELISA results of the 26 lead compounds**

A sandwich ELISA using T47D breast cancer cells was conducted in order to determine the inhibitory effects of the computationally predicted SMIs. Recombinant OSM was treated with SMIs (grey) for 1 hour and then used to stimulate T47D cells for 30 minutes. Phosphorylated STAT3 protein (pSTAT3) levels were quantified in the resulting cell lysates. No treatment (white) refers to background levels of pSTAT3 in untreated cells. OSM treatment (black) refers to the maximum pSTAT3 expression in cells. (n = 3, mean ± SD by one-way ANOVA).

Based upon the pSTAT3 ELISA results, SMI-8 quickly emerged as an ideal lead candidate. Unfortunately, there were several concerns with the possible toxicity of SMI-8 as it possesses problematic functional groups. The dienes are predicted to be reactive as the conjugated system allows the molecule to be a Michael acceptor. This is not desirable, as this could result in toxic side effects. In addition, the synthesis is not stereoselective as the dienes isomerize upon synthesis, rendering it impossible to determine which isomers are generated. Therefore, the goal of this research was to design

and make compounds that were like SMI-8 while deleting or changing any functional groups that were predicted to be toxic.

### 2.4 Synthesis and Computational Modeling Results of SMI-8 and Analogs

2.4.1 Synthesis and Computational Modeling of SMI-8

The synthesis of SMI-8 is depicted in Figure 2.4. First, acid-catalyzed bromination at the 4-position of the ethyl-acetoacetate starting material afforded the unstable intermediate ethyl 4-bromoacetoacetate. The bromoalkane was then reacted with dithiooxamide to perform a 5-exo-trig cyclization that resulted in the bisthiazole intermediate. Simultaneous saponification of the esters produced a dicarboxylate, which was then acidified to afford the dicarboxylic acid. Finally, a Perkin reaction using trans-cinnamaldehyde afforded SMI-8.

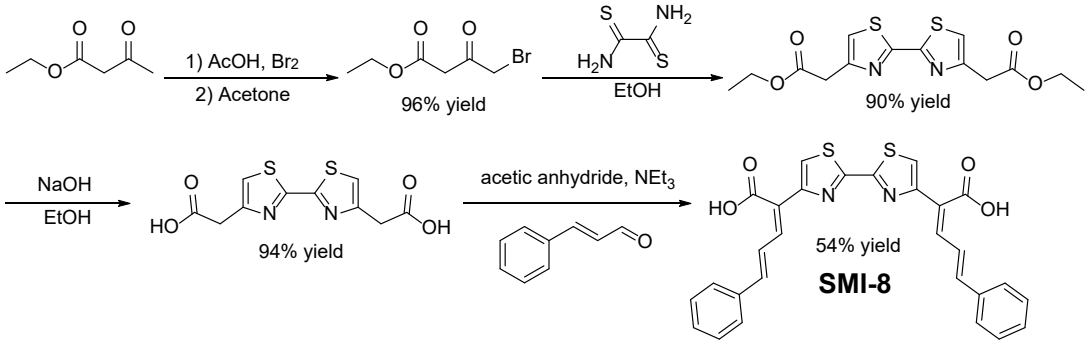


**Figure 2.4 Synthesis of SMI-8**

Virtual ligand docking experiments were conducted to identify key amino acids of OSM that stabilize the binding events between the SMI-8 analogs and the protein. These experiments were accomplished using the University of California San-Francisco's Chimera program, used for the interactive visualization of proteins.[7] In addition, AutoDock Vina 4.2 and the ff14SB forcefield were used to calculate the free energy of binding (FEB) scores to predict how well the analogs bind to site III OSM.[8] For the ease

of reading, the complete set of free energy of binding scores is listed at the beginning of Chapter 3.

Panel A in Figure 2.5 shows the surface interactions between SMI-8 and site III of OSM, in which the FEB was predicted to be -6.5 kcal/mol. Panel B reveals which amino acids of OSM are predicted to stabilize the binding event. Panel C is a simplified, 2-dimensional representation of the stabilizing interactions that are predicted to occur. Overall, two basic types of interactions stabilize the binding event. These include hydrophobic interactions and hydrogen bond interactions. As seen in panel C, it is predicted that the bisthiazole of SMI-8 forms a hydrogen bond to the positively charged Lys163. In addition, one of the carboxylate groups of SMI-8 is predicted to hydrogen bond to Ser101 and Arg100, while the other carboxylate group is predicted to hydrogen bond to Asp41. It is hypothesized that the diene groups of SMI-8 wrap around a significant portion of site III and contribute to hydrophobic interactions that stabilize the binding event. One of the predicted interactions occurs between a diene group and a hydrophobic groove of OSM containing Leu40, Leu45, and Phe160. This is hypothesized to be an important interaction as Phe160 has been identified to be essential for OSM signaling.[2, 3] The other diene group is predicted to bury itself in a hydrophobic pocket containing Pro93, Leu88, and Ala159. The overall energy of binding contribution of these interactions is unknown, as these residues have not been identified in either *in vitro* or computational alanine scanning experiments.

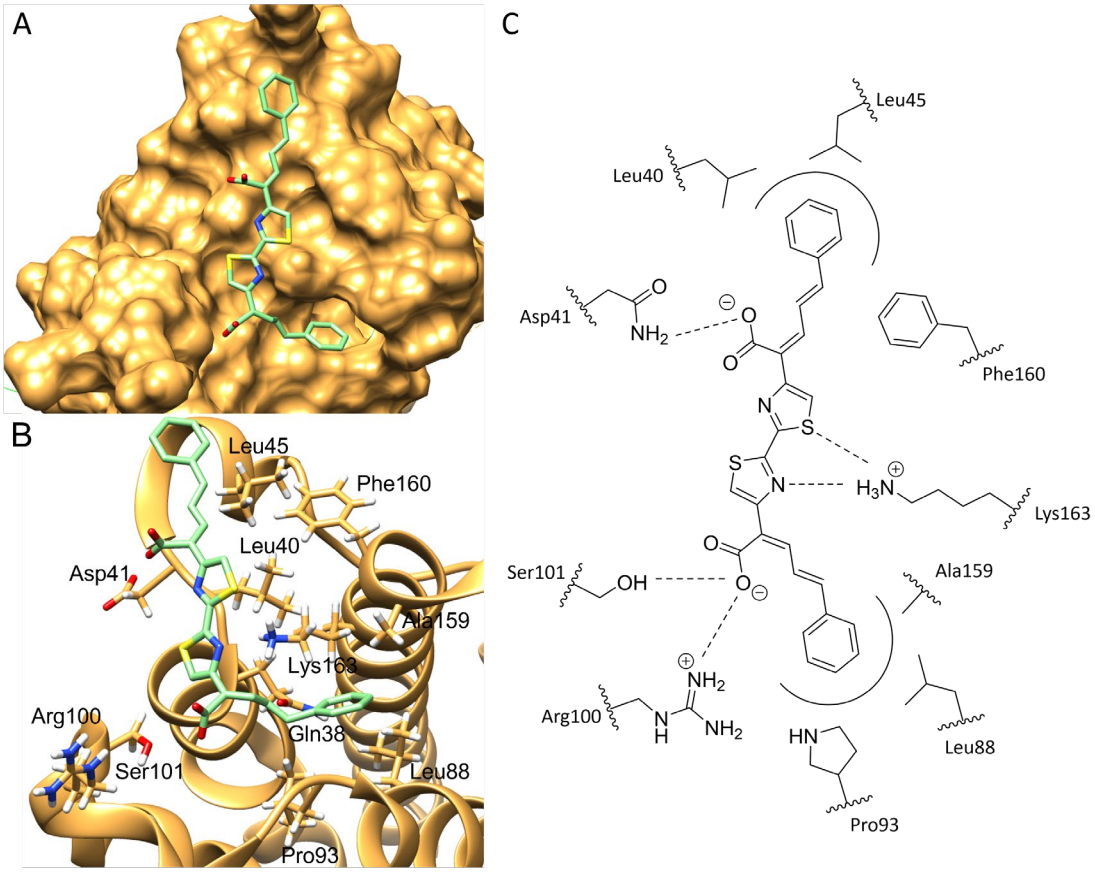


**Figure 2.5 Virtual docking of SMI-8 to OSM predicts key interactions**
(**A**) A top-down view of OSM shows SMI-8 bound to site III, with a FEB score of -6.5 kcal/mol. (**B**) Distinct amino acids shown are hypothesized to play a role in stabilizing the binding event between SMI-8 and OSM. (**C**) A simplified, 2-dimensional representation of SMI-8 interacting with specific amino acids at site III of OSM is illustrated. The semi-circles indicate hydrophobic pockets formed by non-polar amino acids, while the dashed lines indicate hydrogen bond interactions.

Although SMI-8 has proven to be a potent and consistent inhibitor of OSM-mediated JAK/STAT signaling, some significant issues regarding the physiochemical properties of the compound render it a poor substrate in both *in vitro* and *in vivo* experiments. For example, previous murine-based studies at BSU have used SMI-8 to inhibit breast cancer metastasis, but it has proven challenging to dissolve completely in a non-lethal vehicle. Therefore, it is worthwhile to use programs such as SwissADME to predict drug-like qualities of orally available small molecule drugs. Figure 2.6 depicts

some drug-like characteristics and pharmacokinetics of SMI-8 predicted by SwissADME.[9]

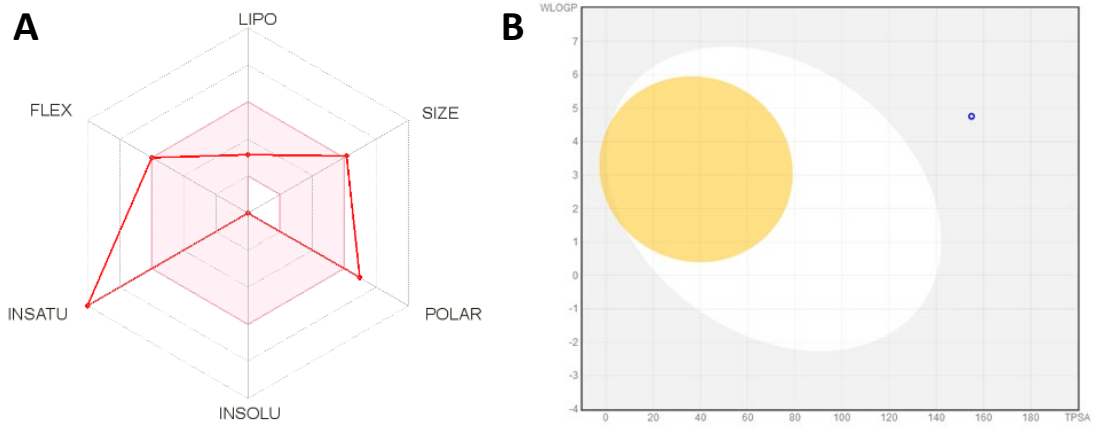


**Figure 2.6 SwissADME predicts physiochemical properties of SMI-8**
(**A**) SwissADME generates a bioavailability radar, which predicts several physiochemical properties of the SMI. These properties include lipophilicity (LIPO), size (SIZE), polarity (POLAR), solubility (INSOLU), flexibility (FLEX), and saturation (INSATU). (**B**) The BOILED-egg diagram shows the predicted lipophilicity and polarity of small molecules in a cleverly designed manner. The y-axis corresponds to lipophilicity (WLOGP) and the x-axis corresponds to polarity (TPSA). The blue dot indicates the predicted polarity and lipophilicity characteristics of the SMI.

According to SwissADME, SMI-8 is predicted to have poor drug-like qualities. There are six important physiochemical properties in drug discovery and design: lipophilicity (LIPO), size (SIZE), polarity (POLAR), solubility (INSOLU), flexibility (FLEX), and saturation (INSATU). According to the graph in panel A, if the red dot falls outside of the red-shaded area on the bioavailability radar, then the drug is considered to have a sub-optimal score for that physiochemical property. It is clear that SMI-8 exhibits unfavorable drug-like qualities when it comes to saturation and polarity. That being said, there are some physiochemical properties that can be argued to be less important. For example, one such rule states that the molecular weight of an orally available drug should be no more than 500 g/mol.[10] However, a paper published in 2014 identified at least 182 approved drugs have a molecular weight greater than 500 g/mol.[11] In contrast, one of the more important properties includes lipophilicity, which is experimentally measured as the

logarithm of the partition coefficient between n-octanol and water (log $P_{o/w}$).[12] Lipophilicity is a critical factor in the success of a drug, as this characteristic governs absorption, distribution, metabolism, excretion, and toxicity; these properties are referred to collectively by the acronym ADMET. Lipophilicity is considered to be the most predictive physiochemical property out of any of them when it comes to the future success of an oral drug.[13]

Panel B in Figure 2.6 shows the predicted gastro-intestinal solubility of an orally ingested compound in what is called a BOILED-Egg (Brain or intestinal estimated permeation method) diagram.[14] The yellow region of the egg shows the parameters in which the drug can pass through the blood-brain barrier. The white region shows the parameters in which the drug can be absorbed into the bloodstream through the intestines. The blue dot indicates the predicted polarity and lipophilicity characteristics of the small molecule. The diagram reveals that SMI-8 would not be well absorbed by the intestines if administered orally, as the blue dot representing the compound falls outside of the optimal parameters. Considering the reasons discussed in this section, there were changes that needed to be made to SMI-8 that would allow for more favorable drug-like properties.

### 2.4.2 Synthesis and Computational Modeling of SMI-8S

The first step in making a less toxic analog of SMI-8 was to replace the $sp^2$ hybridized carbons in the dienes with $sp^3$ hybridized carbons. Doing so would not only overcome the issues with the stereoselective synthesis of the dienes, but it would also do away with the undesired toxicity of the Michael acceptors. However, it introduces two new stereocenters, which results in the possibility of forming a total of three

stereoisomers, the (R,S) meso compound and the enantiomeric (R,R) and (S,S) pair. In spite of this, a saturated version of SMI-8, SMI-8S, was targeted. Molecular docking found favorable binding to the protein, and the synthesis was expected to be straightforward (Figure 2.7). In the first step of panel A, alkylation of the diketone was achieved in 68% yield using tetra-n-butylammonium iodide (TBAI) as a Finkelstein reaction catalyst, dimethoxyethane (DME) as the solvent, and 3-phenylpropyl bromide as the electrophile. The halogenation of the carbonyl α-carbon afforded the brominated intermediate, which was then heated with dithiooxamide in ethanol. The resulting bisthiazole was obtained in 59% yield and subsequently saponified to afford SMI-8S in 38% yield. It is unknown whether the compound was synthesized as the meso compound, as an enantiomeric mixture, or a combination of the three.

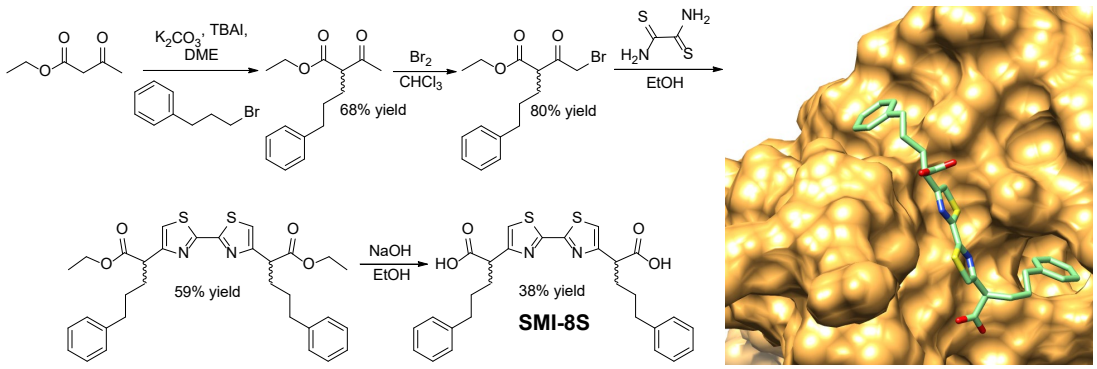


**Figure 2.7 Synthesis and docking of SMI-8S**

(**A**) SMI-8 was synthesized in 4 steps. (**B**) Virtual ligand docking predicted that SMI-8S binds to site III of OSM with a FEB of -6.3 kcal/mol. The meso compound is represented in this binding pose.

It was hypothesized that SMI-8S would still maintain structural features that allowed it to bind to OSM in the same fashion as SMI-8. According to panel B of Figure 2.7, it is predicted that SMI-8S participates in similar hydrogen bonding interactions and hydrophobic interactions that are observed in the virtual docking of SMI-8. The SMI-8S structure in panel B is depicted as the meso compound, which was calculated to have a

free energy of binding score of -6.3 kcal/mol. The (R,R) and (S,S) enantiomers were calculated to have binding scores of -6.0 kcal/mol and -6.2 kcal/mol, respectively. In contrast to the rigid diene structure of SMI-8, it is possible that the phenylpropyl side chains of SMI-8S can adapt to several different binding poses in site III; However, it is currently unknown which pose(s) of the side chains is/are most energetically favorable.

SwissADME was also used to analyze SMI-8S to predict its physiochemical properties and gastrointestinal absorption (Figure 2.8). Even though SMI-8S was predicted to be an overall worse drug in respect to physiochemical properties, the main goal of the synthesis was to determine if the dienes play a crucial role in binding SMI-8 to site III of OSM. As such, predicted physiochemical properties were not a significant concern at this point in the project. According to panel A in Figure 2.8, SMI-8S was predicted to be considerably worse in all categories besides saturation (INSATU). Saturation is simply the fraction of carbons that are $sp^3$ hybridized in the entire structure. According to SwissADME, an optimal saturation is that in which the small molecule contains no less than 25% of its carbons as being $sp^3$ hybridized. The lipophilicity of SMI-8 is predicted to be very poor as well. Since lipophilicity is the most critical factor in determining the success of an oral drug, SMI-8S is less likely to exhibit favorable ADMET qualities. The BOILED-Egg diagram in panel B predicts that SMI-8S would be poorly absorbed in the gastrointestinal tract, as the blue dot representing the compound does not fall within the acceptable parameters.

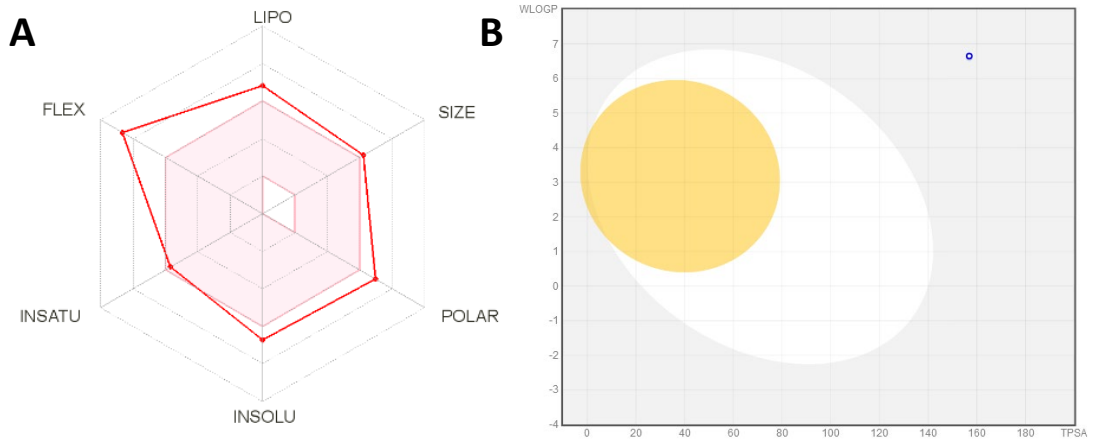


**Figure 2.8 SwissADME predicts physiochemical properties of SMI-8S**
(**A**) SwissADME generates a bioavailability radar, which predicts several physiochemical properties of the SMI being analyzed. (**B**) The BOILED-egg diagram shows the predicted lipophilicity and polarity of small molecules in a cleverly designed manner. The y-axis corresponds to lipophilicity (WLOGP) and the x-axis corresponds to polarity (TPSA). The blue dot indicates the predicted polarity and lipophilicity characteristics of the SMI.

## 2.4.3 A Potent Moiety is Identified

While efforts were focused on the design and synthesis of SMI-8 analogs, other researchers in the Warner lab synthesized potent SMIs based on the SMI-10 and SMI-26 structures seen in Figure 2.9. This work identified a potent aryl amide moiety, which contains a carboxylic acid at the 3-position of the benzene ring. In panel A, the only structure changing in the SMI-10 scaffold is the aryl amide group at the 2-position of the furan. From the fluorescence quenching data listed in accordance with the **Ar** groups, it is clear to see that the most potent inhibitor in the series of SMI-10 analogs includes this moiety ($K_D = 4 \pm 1$ μM). In panel B, the only structure changing in the SMI-26 scaffold is the aryl group at the 4-position of the quinoline core. Like SMI-10, SMI-26 is observed to bind to OSM with a greater affinity when this moiety is part of the structure ($K_D = 6 \pm 1$ μM). These trends observed from structurally different SMIs suggest that this specific aryl amide should be included in future analogs. Therefore, it was decided that this amide would be integrated into the rest of the SMI-8 analogs described after this point.

**A**

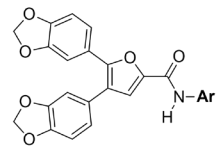


| SMI-10 Structures and $K_D$ Values | | | | | | | | |
|---|---|---|---|---|---|---|---|---|
| Ar | 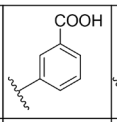 | 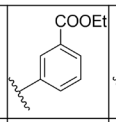 | 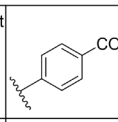 | 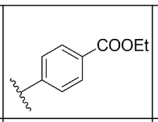 | 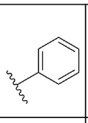 | 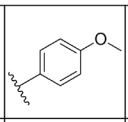 | 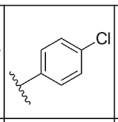 | 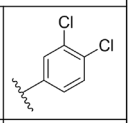 |
| $K_D$ (μM) | 4 ± 1 | 47 ± 6 | 20 ± 3 | 42 ± 15 | 51 ± 8 | 26 ± 3 | 13 ± 3 | 14 ± 3 |

**B**

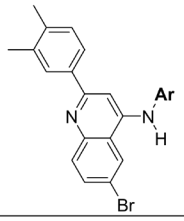


| SMI-26 Structures and $K_D$ Values | | | | | | | | | |
|---|---|---|---|---|---|---|---|---|---|
| Ar | 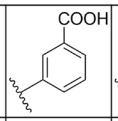 | 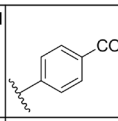 | 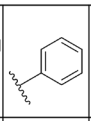 | 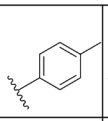 | 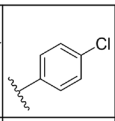 | 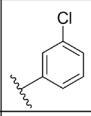 | 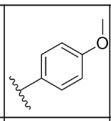 | 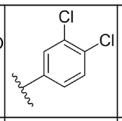 | 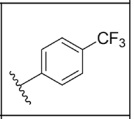 |
| $K_D$ (μM) | 6 ± 1 | 11 ± 2 | 23 ± 4 | 30 ± 2 | 19 ± 2 | 17 ± 2 | 18 ± 3 | 16 ± 3 | 23 ± 3 |

**Figure 2.9 Fluorescence quenching data reveals a potent moiety**
(A) $K_D$ values of SMI-10 analogs were found using a fluorescence quenching assay, where **Ar** = aryl. (B) $K_D$ values of SMI-26 analogs were found using a fluorescence quenching assay, where **Ar** = aryl.

## 2.4.4 Synthesis of SMI-8A4 Analogs

In order to explore non-branched bisthiazole analogs, three SMIs were synthesized. These new compounds varied from the original SMI-8 structure in 2 specific ways. First, they did not include any branching at the alpha carbon of the carbonyl group. Instead, these remained as methylene groups. This avoided the generation of stereocenters. Second, the carboxylic acids were replaced with substituted aryl amide moieties. It was hypothesized that simultaneous amidations would be relatively straightforward. Molecular modeling of the three compounds revealed free energy of binding scores that ranged from -6.6 to -7.7 kcal/mol.

The synthetic route of the bisthiazole analogs is shown in panel A of Figure 2.10, where elemental bromine and acetic acid were used to brominate the carbon at the 4-position of the ethyl acetoacetate starting material. The bromoalkene was then heated with dithiooxamide in ethanol to produce the bisthiazole intermediate. Afterward, the esters were saponified to produce the dicarboxylic acid. Attempts to make the reactive acid chloride intermediate with thionyl chloride proved unsuccessful as the dicarboxylic acid material was sparingly soluble in dichloromethane. In addition, previous attempts using ([(1-[Bis(dimethylamino)methylene]-1H-1,2,3-triazolo[4,5-b]pyridinium 3-oxide hexafluorophosphate]) (HATU) resulted in a blue/black solid that precipitated out of the DMF solvent. Finally, benzotriazol-1-yloxytris(dimethylamino)phosphonium hexafluorophosphate (BOP) was successfully used to form the reactive ester intermediate and install the aryl amide. Finally, panel B shows the saponification step that was unique to one of the three SMIs. All of the SMI-8A analogs prepared to date are presented in the next chapter in table 3.1.

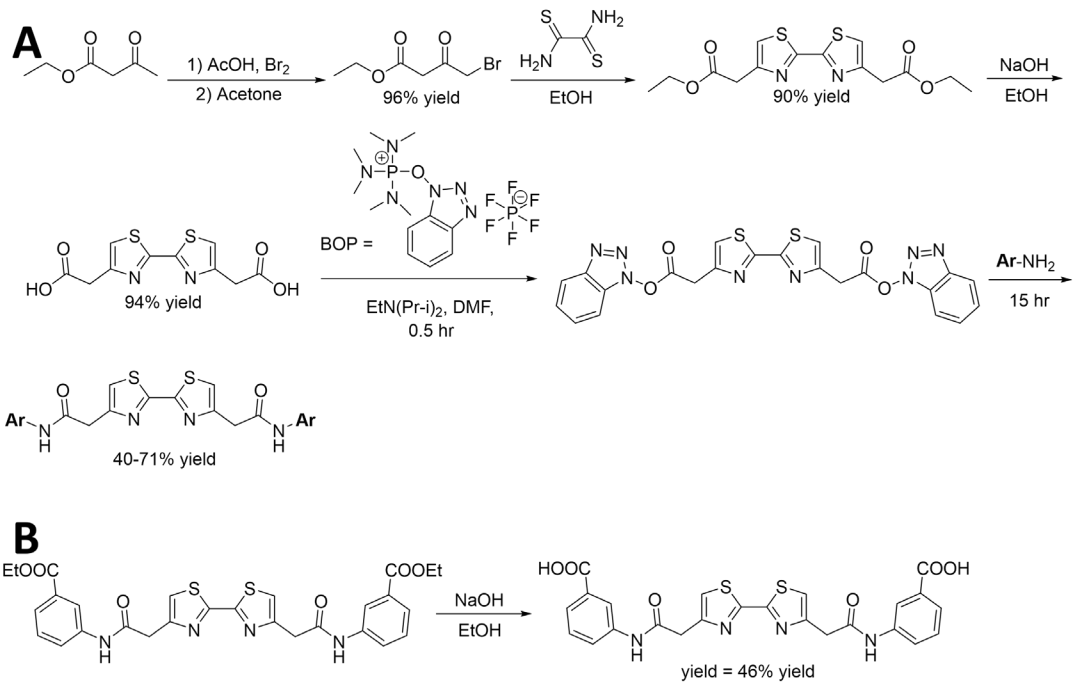


**Figure 2.10 General synthesis of SMI-8A4 analogs**

(**A**) Three bisthiazole compounds were constructed according to the general synthetic route, where "**Ar**" indicates the presence of a substituted aryl amide. (**B**) One of the three compounds synthesized was saponified.

2.4.5 Synthesis and Computational Modeling of SMI-8H Analogs

A new scaffold was designed that resembled half of SMI-8S while incorporating new fragments at the 2-position of the thiazole. This scaffold allowed for the generation of a small library consisting of twenty-two analogs. The general synthetic route can be seen in panel A of Figure 2.11. First, commercially available 2-aminothizole-4-carboxylic acid was treated with tert-butyl nitrite to form the diazonium intermediate, which reacts with Cu (II) bromide to form the 2-bromothizole-4-carboxylic acid. Next, an enolate alkylation was performed in order to form a new carbon-carbon bond at the α-carbon of the carbonyl. One equivalent of Hexamethylphosphoramide (HMPA) was introduced in the enolate alkylation reaction with the aim of improving the yield by sequestering the $Na^+$ cations and rendering the enolate more reactive.[15] Unfortunately, only an 8% increase in yield was observed when HMPA was added versus when it was

not. As a consequence of the non-enantioselective enolate alkylation, the intermediate was collected as a racemic mixture, which resulted in “intermediate C.” In the next step of the main synthetic scheme, saponification of the ester afforded the carboxylic acid. Similar in structure to BOP, 1-[bis(dimethylamino)methylene]-1H-1,2,3-triazolo[4,5-b]pyridinium 3-oxid hexafluorophosphate (HATU) was used to perform an amidation reaction to afford “intermediate E.” $\mathbf{R_1}$ groups were installed by Pd(0) catalyzed carbon-carbon coupling reactions to afford biaryl products, while $\mathbf{R_2}$ groups were installed by nucleophilic aromatic substitution to afford aryl amine products. As seen in panel B, the carbon-bromine bond in both intermediates C and E were reduced by Pd/C reduction in the presence of $H_2$ gas and then saponified. Acidification of the carboxylate groups afforded two separate SMIs. It should be noted that the product obtained after the reduction and subsequent saponification of intermediate C was named SMI-8S3 and is therefore not identified as an SMI-8H analog. All of the SMI-8H analogs prepared to date are presented in the next chapter in Figure 3.3.

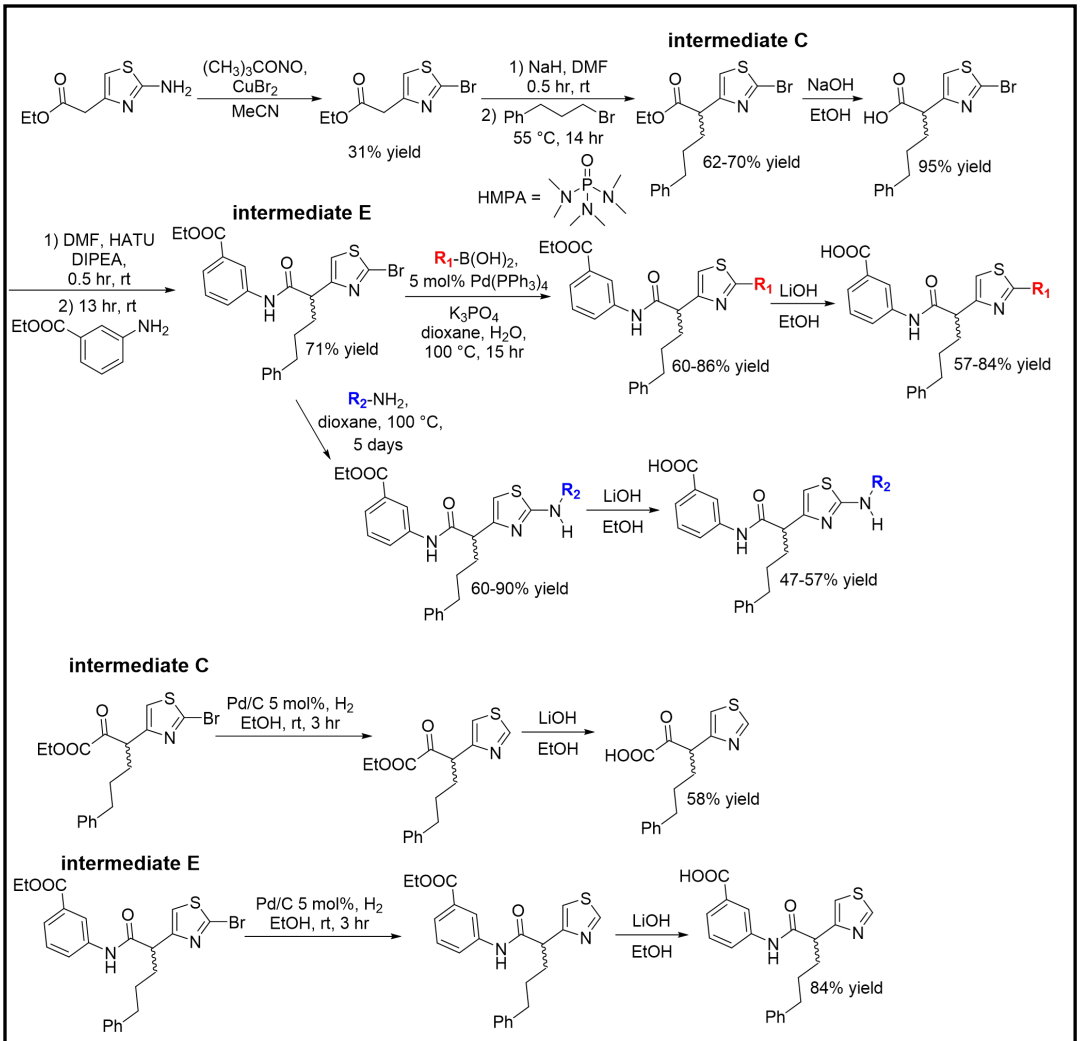


**Figure 2.11 General synthesis of SMI-8H analogs**

(**A**) $R_1$ groups were installed using Pd (0) carbon-carbon coupling, while $R_2$ groups were installed by nucleophilic aromatic substitution, where Ph = phenyl. Two SMIs were synthesized via catalytic hydrogenation of the brominated intermediate, followed by saponification.

According to the virtual docking experiments, the 8H analogs were consistently observed to have lower free energy of binding scores than SMI-8 and SMI-8S. While SMI-8 and SMI-8S exhibited free energy of binding (FEB) scores of -6.5 kcal/mol and -6.3 kcal/mol, respectively, the SMI-8H analogs were calculated to have FEB scores in the range of -6.1 to -8.0 kcal/mol when docked to site III of OSM. Even though this difference is not great, it suggests that the 8H analogs are predicted to bind to OSM just as well as SMI-8 and SMI-8S.

Although the new analogs were designed based on SMI-8 and contain a common thiazole moiety, their structural differences are such that they may bind to different amino acids at site III of OSM. In panel A of Figure 2.12, virtual docking experiments predicted that SMI-8H11 interacts with the same important residues as SMI-8 and SMI-8S. Panel B illustrates a simplified, two-dimensional interpretation of these binding interactions. A hydrogen bonding interaction can be observed between Lys163 of OSM and the nitrogen atom in the thiazole group of the SMI-8H11. The carboxylic acid on the aryl amide is predicted to bury itself in a hydrophobic pocket containing Arg91 and Arg162. Unlike SMI-8 or SMI-8S, SMI-8H11 is not observed to interact with as many hydrophobic side chains of OSM. However, it is plausible that the phenyl group at the 2-position of the thiazole and the Phe160 can still interact. Other fatty side-chain amino acids such as Ile37 and Leu98 were observed to form a hydrophobic groove to accommodate the phenylpropyl chain. Overall, virtual docking experiments suggest that SMI-8H analogs interact with the same critical residues as SMI-8 and SMI-8S.

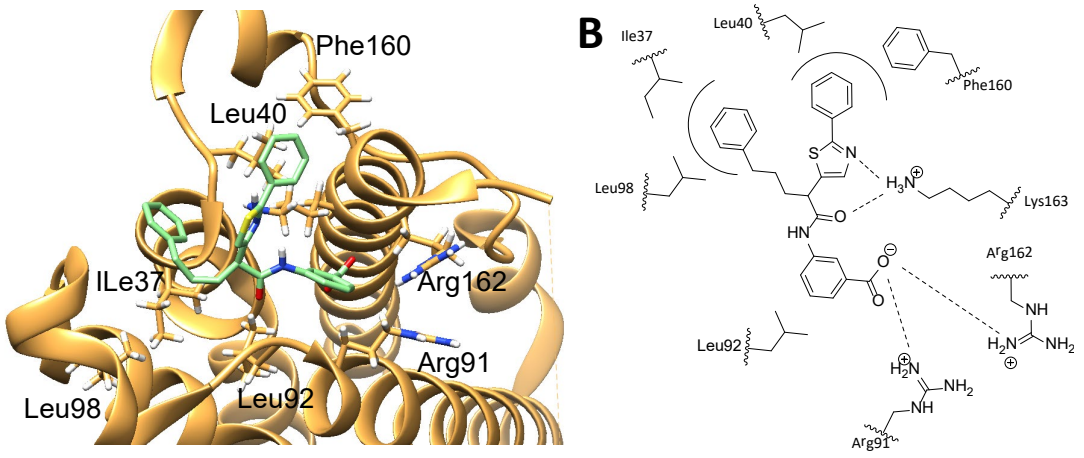


**Figure 2.12 Virtual docking of SMI-8H11 to OSM predicts key interactions**
(**A**) The amino acid that are predicted to stabilize the binding interaction between SMI-8H11 and site III of OSM are illustrated. (**B**) A simplified, 2-dimensional illustration shows SMI-8H11 interacting with specific amino acids. The semi-circles indicate hydrophobic pockets formed by non-polar amino acids, while the dashed lines indicate electrostatic/hydrogen-bond interactions.

2.4.6 Synthesis of 8M analogs

Rather than designing a scaffold from existing SMIs, the scaffold of SMI-8M was constructed using a diversity-oriented synthesis approach, where different structural moieties are changed to discover new lead compounds.[16] So, SMI-8M was designed to contain a thiazole as the core of the molecule, with the 2-position of the thiazole appended with a variety of substituted phenyl groups. Unlike the analogs previously discussed, the SMI-8M analogs exhibit minimal structural resemblance to SMI-8.

The SMI-8M analogs were constructed in three steps, as seen in Figure 2.13. First, commercially available 2-bromo-4-thiazolecarboxylic acid was reacted with Hünig's base and HATU to form the reactive ester intermediate. Nucleophilic attack by the 3-aminobenzoic acid afforded the amidation product in 69% yield. Next, Pd(0) catalyzed carbon-carbon coupling formed a new bond between the carbon on the 2-position of the thiazole and the according Ar group to give yields of 47-69%. Finally, saponification followed by acidification yielded the desired carboxylic acid final products in yields of 53-81%. All the SMI-8M analogs prepared to date are presented in the next chapter in Figure 3.2.

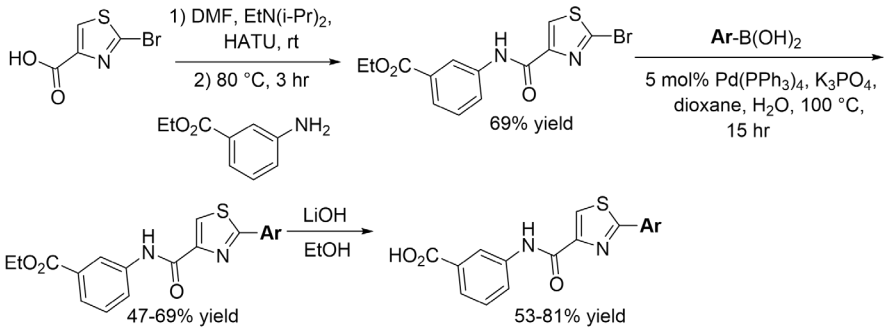


**Figure 2.13 General synthesis of SMI-8M analogs**

Seven compounds were constructed according to the general synthetic route, where "**Ar**" indicates the presence of a substituted aryl amide.

## 2.5 Summary of Chapter Two

Sites I, II, and III of OSM were independently identified as ligand binding sites on OSM. Targeting site III, a high throughput virtual screening was performed to identify SMI-8 as a lead compound. *In vitro* and *in silico* alanine scanning experiments exposed Tyr34, Arg36, Gln38, Leu40, Asp41, Val42, Leu45, Lys49, Arg100, Leu103, Phe160, Gln 161, and Lys163 as amino acids that participate in stabilizing interactions between OSM and one of its transmembrane receptors OSMRβ. In addition, computational docking studies and protein modeling revealed plausible binding interactions between the crystal structure of OSM and the virtually docked compounds. Upon synthesis and evaluation by ELISA experiments, SMI-8 was discovered to be a potent inhibitor of OSM signaling. The synthesis of SMI-8 and SMI-8S involved the generation of bisthiazoles through a proposed 5-exo-trig cyclization. However, the potential toxicity and lack of stereoselectivity of SMI-8 necessitated the design and synthesis of other analogs. Therefore, 34 SMIs were synthesized, 25 of which resemble the structure of SMI-8. The next chapter will contain a discussion of the several assessments used to determine the binding strength and properties of the SMIs to OSM.

## 2.6 Chapter Two References


1. Harris, R.; Olson, A. J.; Goodsell, D. S., Automated prediction of ligand-binding sites in proteins. *Proteins: structure, function, and bioinformatics* **2008,** *70* (4), 1506-1517.
2. Adrian-Segarra, J. M.; Schindler, N.; Gajawada, P.; Lörchner, H.; Braun, T.; Pöling, J., The AB loop and D-helix in binding site III of human Oncostatin M (OSM) are required for OSM receptor activation. *Journal of Biological Chemistry* **2018,** *293* (18), 7017-7029.
3. Deller, M. C.; Hudson, K. R.; Ikemizu, S.; Bravo, J.; Jones, E. Y.; Heath, J. K., Crystal structure and functional dissection of the cytostatic cytokine oncostatin M. *Structure* **2000,** *8* (8), 863-874.
4. Du, Q.; Qian, Y.; Xue, W., Molecular Simulation of Oncostatin M and Receptor (OSM–OSMR) Interaction as a Potential Therapeutic Target for Inflammatory Bowel Disease. *Frontiers in Molecular Biosciences* **2020,** *7* (29).
5. Goffin, V.; Bogorad, R. L.; Touraine, P., Identification of gain-of-function variants of the human prolactin receptor. *Methods in enzymology* **2010,** *484*, 329-355.
6. Krieger, F.; Möglich, A.; Kiefhaber, T., Effect of proline and glycine residues on dynamics and barriers of loop formation in polypeptide chains. *J Am Chem Soc* **2005,** *127* (10), 3346-52.
7. Pettersen, E. F.; Goddard, T. D.; Huang, C. C.; Couch, G. S.; Greenblatt, D. M.; Meng, E. C.; Ferrin, T. E., UCSF Chimera--a visualization system for exploratory research and analysis. *J Comput Chem* **2004,** *25* (13), 1605-12.
8. Maier, J. A.; Martinez, C.; Kasavajhala, K.; Wickstrom, L.; Hauser, K. E.; Simmerling, C., ff14SB: improving the accuracy of protein side chain and backbone parameters from ff99SB. *Journal of chemical theory and computation* **2015,** *11* (8), 3696-3713.
9. Daina, A.; Michielin, O.; Zoete, V., SwissADME: a free web tool to evaluate pharmacokinetics, drug-likeness and medicinal chemistry friendliness of small molecules. *Scientific Reports* **2017,** *7* (1), 42717.
10. Mullard, A., Re-assessing the rule of 5, two decades on. *Nature Reviews Drug Discovery* **2018,** *17* (11), 777-777.
11. Doak, Bradley C.; Over, B.; Giordanetto, F.; Kihlberg, J., Oral Druggable Space beyond the Rule of 5: Insights from Drugs and Clinical Candidates. *Chemistry & Biology* **2014,** *21* (9), 1115-1142.
12. Bannan, C. C.; Calabró, G.; Kyu, D. Y.; Mobley, D. L., Calculating Partition Coefficients of Small Molecules in Octanol/Water and Cyclohexane/Water. *Journal of Chemical Theory and Computation* **2016,** *12* (8), 4015-4024.
13. Arnott, J. A.; Planey, S. L., The influence of lipophilicity in drug discovery and design. *Expert Opinion on Drug Discovery* **2012,** *7* (10), 863-875.
14. Daina, A.; Zoete, V., A BOILED-Egg To Predict Gastrointestinal Absorption and Brain Penetration of Small Molecules. *ChemMedChem* **2016,** *11* (11), 1117-21.
15. Dykstra, R. R., Hexamethylphosphoric triamide. *Encyclopedia of reagents for organic synthesis* **2001**.

16. Galloway, W. R. J. D.; Isidro-Llobet, A.; Spring, D. R., Diversity-oriented synthesis as a tool for the discovery of novel biologically active small molecules. *Nature Communications* **2010,** *1* (1), 80.

# CHAPTER THREE: ASSESSMENT OF SMI-8 ANALOGS TARGETING OSM

## 3.1 Overview of Chapter Three

This chapter includes the nomenclature of the SMIs synthesized in the previous chapter, as well as the free energy of binding (FEB) scores calculated in the virtual ligand docking experiments, where lower FEB scores indicate better binding OSM-SMI. In addition, this chapter discusses the direct binding assays and cell-based inhibitory assays used to assess the small molecules. As OSM has been identified to induce the JAK/STAT pathway, levels of pSTAT3 expression in breast cancer cells can be measured to quantify the degree of OSM signaling. Therefore, the SMI-8 analogs were subject to an ELISA that measured their ability to inhibit OSM signaling in T47D human breast cancer cells. In addition, a Western blot assay was used to assess the ability of SMI-8 to inhibit OSM signaling in MDA-MB-231 human breast cancer cells. A fluorescence quenching assay was used to determine the direct binding affinity of SMI-8 and SMI-8S towards OSM. A chemical shift perturbation assay of SMI-8S was also accomplished to determine which amino acids closely interact with the compound upon binding. Finally, attempts were made to design a differential scanning fluorimetry experiment to rapidly determine relative binding affinities in a library of compounds.

## 3.2 Nomenclature and Computational Binding Scores of SMIs

### 3.2.1 SMI-8A4 analogs

The naming system for the bisthiazole based analogs is relatively crude and simple as a wide variety of structures were not synthesized. Therefore, unique names

were given to the compounds rather than developing a systematic naming convention more suitable for an extensive library. The “8A4” root of the analog name identifies that an acetamide moiety was installed on the 4-position of the thiazole rings. Figure 3.1 shows the three analogs labeled with their according names. The 8A4 analog was the first of its kind to be synthesized, so it was simply named as the basic root. The other two analogs include a “Cl” or an “OMe” in the name to signify the presence of a chlorine or methoxy group at the para position.

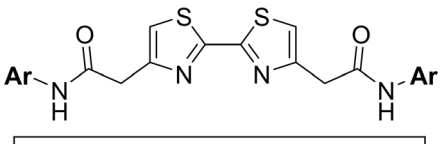


| Ar | | |
|---|---|---|
| 8A4 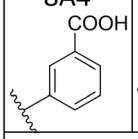 | A84Cl 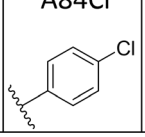 | 8A4OMe 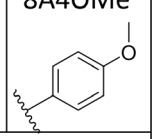 |
| FEB (kcal/mol) | | |
| -7.7 | -6.6 | -7.0 |

**Figure 3.1 Structure and binding scores of SMI-8H analogs**

The figure depicts SMI-8A4 analogs along with their FEB scores. AutoDock Vina 4.2 and the ff14SB forcefield were used to calculate the free energy of binding (FEB) scores.

3.2.2 SMI-8M analogs

The “M” in the base of the analog stands for the German word “Männchen,” which translates to “little/small men.” This was chosen because the 8M analogs are less massive than SMI-8. The analogs were designed so that only the 2-position on the thiazole was to be appended with different aryl groups. Therefore, the analogs are simply numbered, starting at number one. Also, this numbering system reflects the relative timeline in which the SMIs were successfully synthesized. For example, SMI-8M1 was

the first compound of its kind to be synthesized and isolated. These structures, with their according name and FEB scores, can be seen in Figure 3.2.

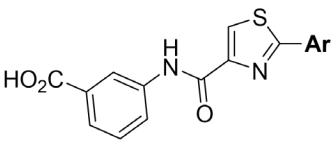


| Ar | | | | | | |
|---|---|---|---|---|---|---|
| 8M1 | 8M2 | 8M3 | 8M4 | 8M5 | 8M7 | 8M8 |
| FEB (kcal/mol) | | | | | | |
| -7.1 | -7.6 | -8.0 | -7.8 | -8.0 | -7.5 | -8.0 |

**Figure 3.2 Structure and binding scores of SMI-8M analogs**

The figure depicts the structures of the SMI-8M analogs along with their according FEB score.

3.2.3 SMI-8H analogs

The "H" portion in the base of the analog name stands for "half," which is used to describe its structure as being similar to half of SMI-8S. As the 2-position of the thiazole was the only portion of the molecule that varied among the analogs, a simple numbering system was used in order to differentiate them. Therefore, the analogs are numbered, starting at number one. This numbering system reflects the relative timeline in which the SMIs were successfully synthesized. For example, SMI-8H1 was the first compound of its kind to be synthesized and isolated. These structures and their according names can be seen in Figure 3.3.

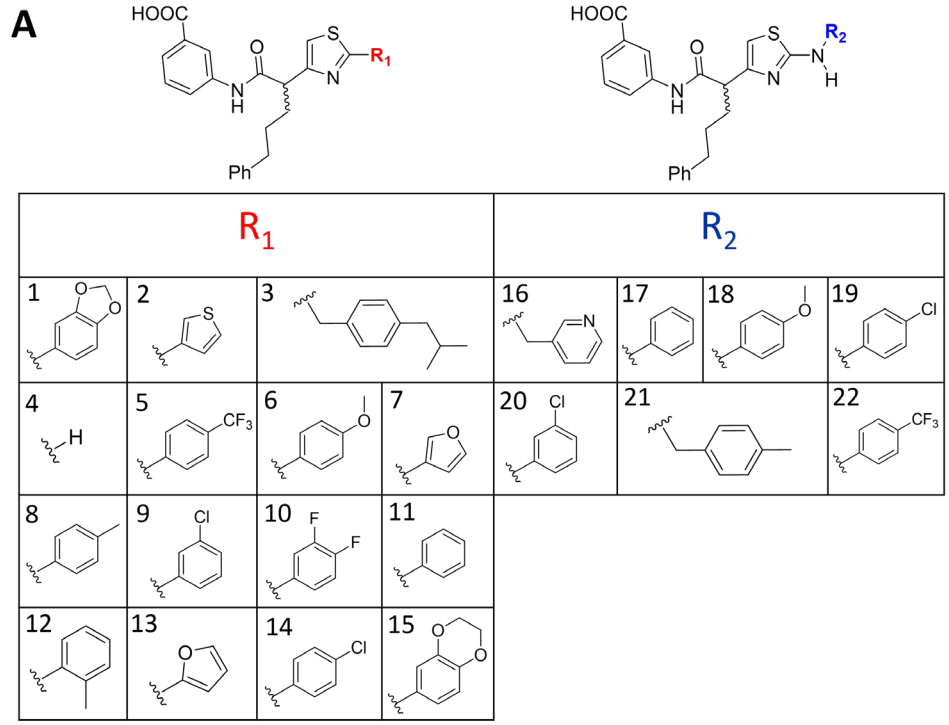


**B**

| FEB scores of SMI-8H Analogs | | | | | | | | | |
|---|---|---|---|---|---|---|---|---|---|
| **8HX** | **FEB** | **8HX** | **FEB** | **8HX** | **FEB** | **8HX** | **FEB** | **8HX** | **FEB** |
| 1 | -7.9 | 6 | -6.1 | 11 | -7.2 | 16 | -8.0 | 21 | -7.4 |
| 2 | -6.5 | 7 | -7.4 | 12 | -7.5 | 17 | -7.7 | 22 | -7.7 |
| 3 | -6.5 | 8 | -7.7 | 13 | -6.7 | 18 | -7.2 | | |
| 4 | -6.1 | 9 | -6.9 | 14 | -7.8 | 19 | -8.0 | | |
| 5 | -7.4 | 10 | -6.8 | 15 | -7.5 | 20 | -7.8 | | |

**Figure 3.3 Structure and binding scores of SMI-8H analogs**

(A) SMI-8H analogs were synthesized as either amines, or biaryl compounds. The numbers in the top left portion of the cells refer to the number of the analog. (**B**) The free energy of binding scores (FEB) are in units of kcal/mol and are listed to the right of the according compound.

## 3.3 Inhibitory Activity Studies

### 3.3.1 Enzyme-Linked Immunosorbent Assay

Introduced in the first chapter, phosphorylation of STAT proteins is an important mechanism that occurs in the JAK/STAT signaling pathway mediated by OSM.[1] Therefore, the quantity of pSTAT3 in cell lysates can serve as a metric for the degree of OSM signaling. Figure 3.4 shows the basic concept of the sandwich ELISA experiment

that was used to determine the relative expression of pSTAT3 in T47D breast cancer cell lysates.[2] To test the inhibitory effects of the SMIs, the wells of a 96-well plate are pre-coated with the pSTAT3 specific capture antibody (step 1). Next, the cell lysates are introduced into the wells, whereupon pSTAT3 binds to the capture antibody (step 2). Next, the primary antibody is introduced to "sandwich" the pSTAT3 protein between itself and the capture antibody (step 3). Next, a biotin-labeled secondary antibody is introduced into the wells where it binds to the primary antibody (step 4). Finally, streptavidin-horse radish peroxidase binds to the biotin and catalyzes a reaction that produces a specific color (step 5). The degree of coloring is then measured by probing the optical density of each well at 450 nm.

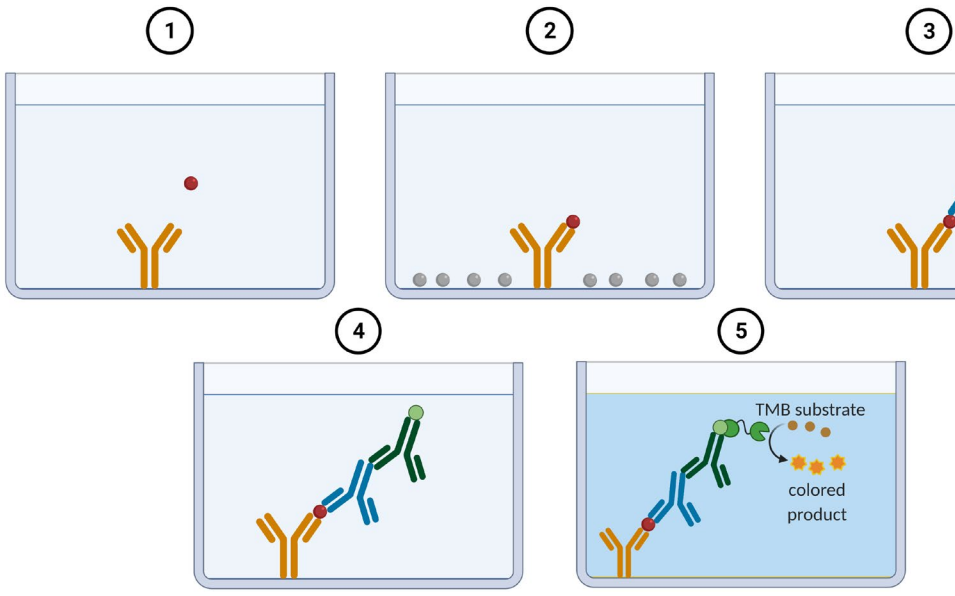


**Figure 3.4 Principles of a sandwich ELISA**

(**1**) The wells are pre-coated with the pSTAT3 specific capture antibody (yellow). (**2**) The capture antibody binds the specifically to pSTAT3 (red). (**3**) The primary STAT antibody (blue) then binds to the STAT protein, creating a "sandwich". (**4**) The biotin-labeled secondary antibody (green) is introduced, which binds to the primary antibody. (**5**) Finally, streptavidin-horse radish peroxidase is introduced and catalyzes a reaction that produces a blue color, which is measured by optical density.

As seen in Figure 3.5, several of the SMI-8H analogs were subjected to sandwich ELISA experiments where T47D breast cancer cells were treated with and without OSM. The cells that were treated with OSM induced a maximum level of pSTAT3 expression, and these levels were normalized to 1.0 (OSM, red). The pSTAT3 expression of cells that were not treated with OSM (NT, white) serves as a baseline value. Next, the cells were treated with the OSM and the SMIs to measure the extent of SMI-induced inhibition (blue). So, if an SMI was exceptionally efficient in inhibiting OSM signaling, it would lower the pSTAT3 expression level close or equal to that of the no treatment group.

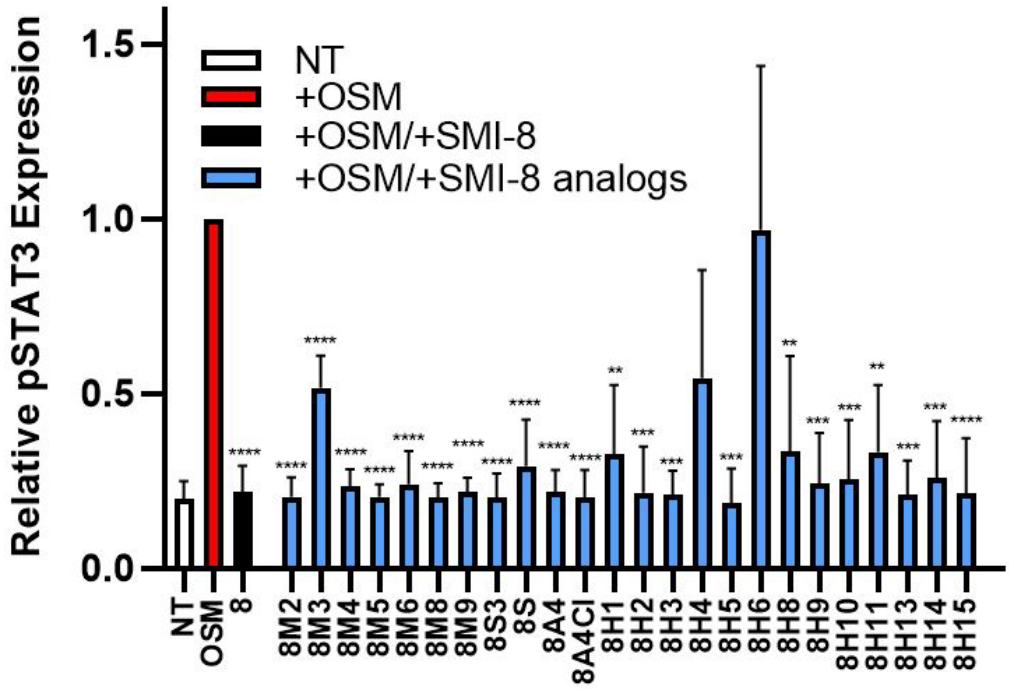


**Figure 3.5 ELISA of SMI-8 analogs**

OSM was treated with SMI-8 analogs (Blue) for 1 hour and then used to stimulate T47D cells for 30 minutes. Phosphorylated STAT3 was quantified in the resulting cell lysates. No treatment (white) refers to background levels of pSTAT3 in cells not treated with OSM. SMI-8 (black) is used as a positive control (n=3, mean ± SD by one-way ANOVA; ****p <0.0001 compared to +IP with Dunnett's multiple comparisons test). SMI-8H4 and SMI-8H6 do not yet have an n = 3, precluding statistical analysis

Not all the analogs synthesized have been subjected to an ELISA experiment, yet there are emerging structural activity relationships that can be identified. It is clear that SMI-8 and SMI-8S both reduce pSTAT3 expression in the cancer cells to the point of the

no treatment groups. The data suggest that the dienes are not critical for inhibiting OSM signaling. So, it is likely that the structural rigidity of the dienes in SMI-8 is not necessary. The 8M series of analogs was promising, as almost all performed as well or better than SMI-8. The only outlier was SMI-8M3, which was predicted to have one of the best FEB scores out of the series (-8.0 kcal/mol). Currently, there is not enough data to propose a rationale for this disagreement. Besides this, the ELISA results agree with the FEB scores of the SMI-8M analogs calculated by AutoDock Vina.

The inhibitory effects of the two 8A4 analogs are also comparable to SMI-8, as they were able to reduce the pSTAT3 expression values equal to that of the no treatment group. So, it is plausible that phenylpropyl groups in the structure might not be as necessary as previously thought. It is hypothesized that these SMIs can inhibit pSTAT3 expression effectively due to the bisthiazole core, which is predicted to hydrogen bond to Lys163. The ELISA results also agree with the results calculated by AutoDock Vina, as SMI-8A4, SMI-8A4Cl, and SMI-8AOMe have FEB scores of -7.7, -6.6, and -7.0 kcal/mol, respectively. More need to be synthesized and tested to determine any meaningful relationships between the structure and function of these analogs.

Since more SMI-8H analogs were synthesized and subjected to ELISA, it is easier to observe trends with this group of compounds. Based on FEB scores, it was hypothesized that an aryl group at the 2-position of the thiazole would increase ligand affinity towards site III of OSM compared to one that did not contain an aryl group. So, SMI-8H4 was synthesized to be negative control since it lacks an aryl group at the 2-position of the thiazole. SMI-8H4 and SMI-8H11 were computationally predicted to have FEB scores of -6.1 and -7.2 kcal/mol, respectively. The structures of both analogs can be

seen in Figure 3.6. In agreement with the hypothesis, SMI-8H4 was proven to be a less effective pSTAT3 inhibitor than SMI-8H11. This means that it is important for the 8H analogs to contain an aryl group at the 2-position of the thiazole (Figure 3.6). As a considerable amount of the analogs were within error of another in the ELISA experiments, it is difficult to draw definitive structural activity relationship (SAR) trends. However, the ELISA experiments tend to reflect the predicted binding scores of the compounds.

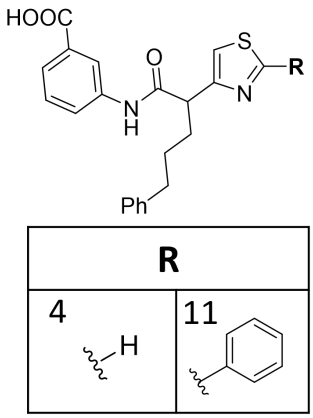


**Figure 3.6 Structures of SMI-8H4 and SMI-8H11**

3.3.2 Western Blot Assay of SMI-8

A Western blot assay is used to separate and identify a specific protein in a mixture of proteins.[3] A Western blot is performed by first separating the proteins by gel electrophoresis and transferring them to a membrane that produces a band for each protein present. The gel containing the bands is then incubated with specific antibodies that will attach to the protein so it can be visualized. The thickness of the band is often used to identify the concentration of the protein present when compared to a loading standard.[3] Western blot analyses were used to address two main concerns with the SMI project. First, other pro-inflammatory pathways can be induced by OSM. In addition to

the previously identified JAK/STAT pathway, OSM has been identified to induce the pJNK, pERK, and pAKT signaling pathways.[4] This is important to know, as the aforementioned ELISA experiments only measure the phosphorylation of STAT3. Second, pSTAT3 expression could be inhibited by a different mechanism that does not involve the SMI binding to OSM. To determine the downstream signaling effects of OSM inhibition and confirm that SMI-8 is binding to OSM to inhibit pSTAT3 expression, the Jorcyk lab conducted a Western blot assay in MDA-MB-231 human breast cancer cells treated with and without SMI-8 (Figure 3.7). The cells treated without OSM serve as a negative control (- lane), and the cells treated with OSM serve as a positive control (+ lane). The cancer cells we also treated with SMI-8 that was incubated with OSM for 1 hour (+SMI-8 lane). STAT3 and actin protein levels were used as internal loading controls. The Western blot shows that the OSM incubated with SMI-8 failed to induce the phosphorylation STAT3, JNK, ERK, and AKT as all the bands are gone or barely visible. This evidence supports the notion that other downstream pro-inflammatory signaling pathways are inhibited with the treatment of SMI-8. In addition, it also shows that pSTAT3 inhibition by an alternative mechanism is not likely, especially as the cells remain viable under experimental conditions.

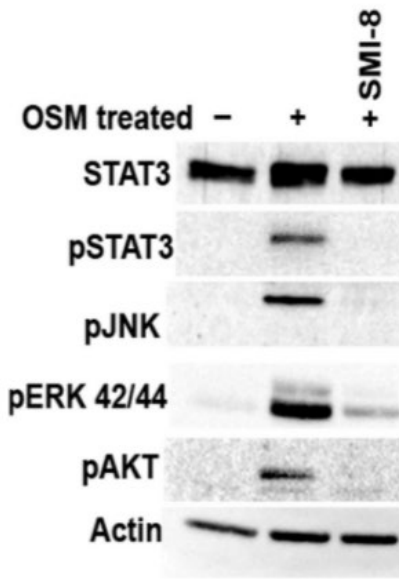


**Figure 3.7 SMI-8 Inhibits OSM signaling in human breast cancer cells**

MDA-MB-231 human breast cancer cells were stimulated with (+ lane) or without (- lane) OSM for 30 minutes. In addition, cells were treated with OSM incubated with SMI-8.

## 3.4 Direct Binding Assays of OSM-SMIs

### 3.4.1 Fluorescence Quenching Assays of SMI-8 and SMI-8S

Even though the ELISA results were promising, it is necessary to measure the binding affinities of the OSM-SMIs directly. Obtaining this information is essential as it discloses compound affinity for a specific substrate and verifies that a direct binding event is occurring. Obtaining $K_D$ values is a practical way to rank binding affinities for SMIs.[5] Researchers in the Warner group adopted a fluorescence quenching (FQ) assay used by Charlier and Plapp that relies on the intrinsic fluorescence of one or more tryptophan residues present in the protein.[6] A local change in the environment of the tryptophan residue can occur upon binding of the ligand. This change in environment can be caused by an SMI binding closely or far away from the tryptophan residue.[7] It was found that OSM has a tryptophan (Trp187), so the FQ was deemed appropriate. In the

experiment, a known amount of SMI is titrated into a cuvette containing a known amount of OSM in a buffered solution. The cuvette holding OSM is then subjected to a 280 nm wavelength of light, and fluorescence of the tryptophan is observed at 350 nm. Upon the binding of SMI to OSM, a reduction of the fluorescence intensity is observed. The fluorescence signal is then plotted against the SMI concentration added, and the data were fit to a modified Stern-Volmer function. The function is as follows: $\left(\frac{f}{f_o}\right) = \left(\frac{f_1}{1-\frac{[X]}{K_D}}\right) + (1 - f_1)$.

When subjected to the FQ assay, SMI-8 and SMI-8S returned $K_D$ values of 5 ± 1 μM and 14 ± 3 μM, respectively (Figure 3.8). $K_D$ is expressed as $\frac{[SMI]\,[OSM]}{[SMI \cdot OSM]}$, where [SMI] and [OSM] are the concentrations of ligand and receptor unbound, and where [SMI·OSM] is the concentration of ligand bound to the receptor. So, a smaller $K_D$ is favorable. These results help answer one of the most important questions posed at the inception of the SMI-8 project: do the dienes significantly contribute to the ability of parent-8 to bind to OSM? Considering that the $K_D$ values measured for SMI-8 and SMI-8S are close, the dienes are not critical. Therefore, future analogs based on SMI-8 should not include the dienes if structural changes can be made to make up for the observed slight loss in binding affinity.

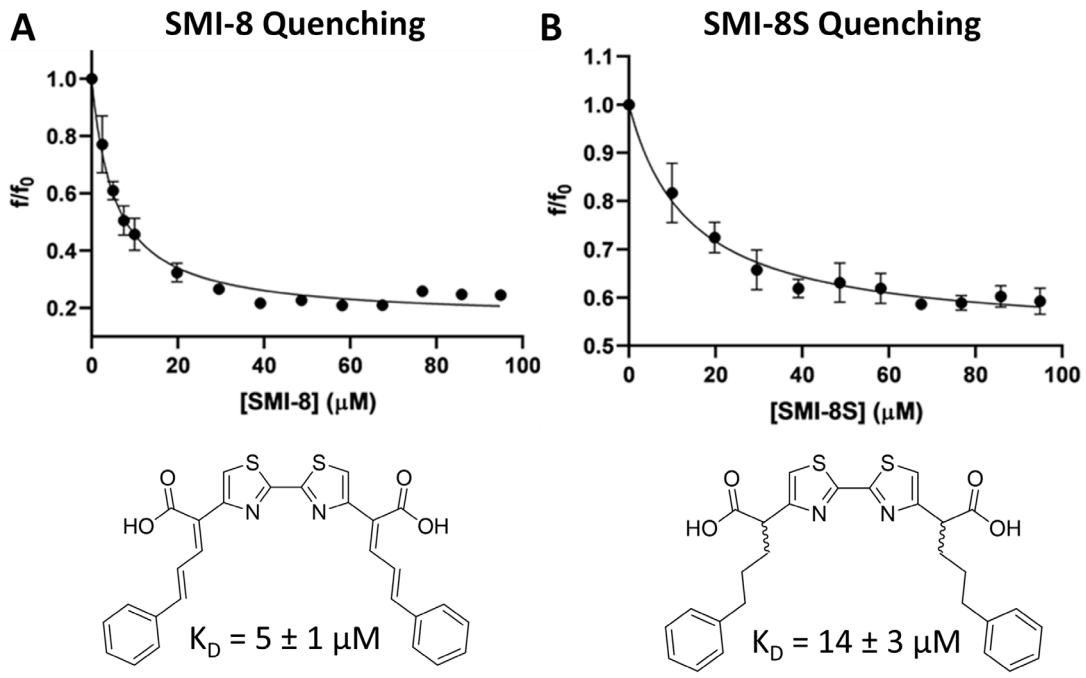


**Figure 3.8 Fluorescence quenching assays of SMI-8 and SMI-8S**

(**A**) Four separate polymethylmethacrylate cuvettes were filled with 750 μL protein/buffer solution containing 50 mM sodium phosphate, 100 mM sodium chloride, and 1.0 μM recombinant OSM (pH = 6.6). Three of the cuvettes were titrated with 0-100 μM SMI, while the fourth cuvette was titrated with DMSO to serve as a blank. The y-axis is the measured fluorescence signal of the sample containing SMI divided by the fluorescence signal of the DMSO blank ($f/f_o$) and the x axis is the concentration of SMI added. (**B**) SMI-8 and SMI-8S were measured to have $K_D$ values of 5 ± 1 μM and 14 ± 3 μM, respectively (n = 3).

Unfortunately, the remainder of the SMI-8H analogs could not successfully be tested by the FQ assay as they fluoresce at 350 nm once excited at 280 nm. Typically, subtractions can be made to the dataset to account for the addition of fluorescence observed by the small molecule, but corrections did not produce reliable results for the SMI-8H analogs. This is most likely due to a synergistic effect occurring between the SMI and the protein, where the OSM-SMI complex fluoresces at a higher wavelength in comparison to either the SMI-8H analog or the OSM protein alone. Unfortunately, these results demonstrated that an alternative method must be used to obtain binding affinities for these and other SMIs.

3.4.2 Chemical Shift Perturbation Experiment of SMI-8S

A Chemical shift perturbation (CSP) experiment is a two-dimensional NMR method of monitoring chemical shifts of amide protons in an isotopically enriched protein upon ligand addition. CSP experiments can reveal both the binding location on the protein and the affinity of the ligand.[8] This experiment is accomplished by obtaining a $^{15}N/^{1}H$ heteronuclear single quantum coherence (HSQC) NMR spectrum of the protein without any ligand added. Next, the protein solution in the NMR tube is titrated with a known ligand concentration, and an HSQC spectrum is obtained for multiple titration points. This results in an overlayed series of HSQC spectra that reveal which amino acids experience a change in their magnetic environment upon the addition of the SMI.

While CSP experiments provide rich binding information and can provide $K_D$ values, the cost associated with needing large quantities of 15N labeled protein precludes testing a complete library. As such, SMI-8 and SMI-8S, which have both successfully inhibited OSM in ELISA experiments and have $K_D$ values in the low micromolar range, were selected for CSP assays. Aaron Ajeti (Lisa Warner group) performed these titrations with protein obtained from the Biomolecular Research Center, using a protocol developed by Dr. Lisa Warner and coworkers.[2] Unfortunately, the CSP titration with SMI-8 was not successful as the SMI/OSM complex formed an orange-colored precipitate upon addition. As a result, the protein signal was diminished to the point where obtaining an accurate ppm shift was not possible.

The CSP titration with SMI-8S was a success as there were no solubility issues. An overlay of the HSQC spectra obtained in the SMI-8S CSP experiment can be seen in Figure 3.9. It was observed that the chemical shifts of several amino acids were perturbed

in the HSQC spectra upon the addition of increasing amounts of SMI-8S. By comparing the chemical shifts to a previously reported NMR spectrum of a glycosylated OSM construct,[9] three of the amino acids were tentatively identified as Gln90, Arg91, and Leu92 with chemical shifts at (7.4, 117), (7.3, 116), and (6.9, 117), respectively. Notably, these same amino acids were also perturbed when OSM was titrated with structurally unrelated SMIs that were also designed to bind to site III.[2] This is an important finding for two reasons. First, it validates the original computational modeling used to design structurally different molecules that specifically target site III of OSM. Second, the data suggest that the SMIs bind near Gln90, Arg91, and Leu92 at site III of OSM.[2]

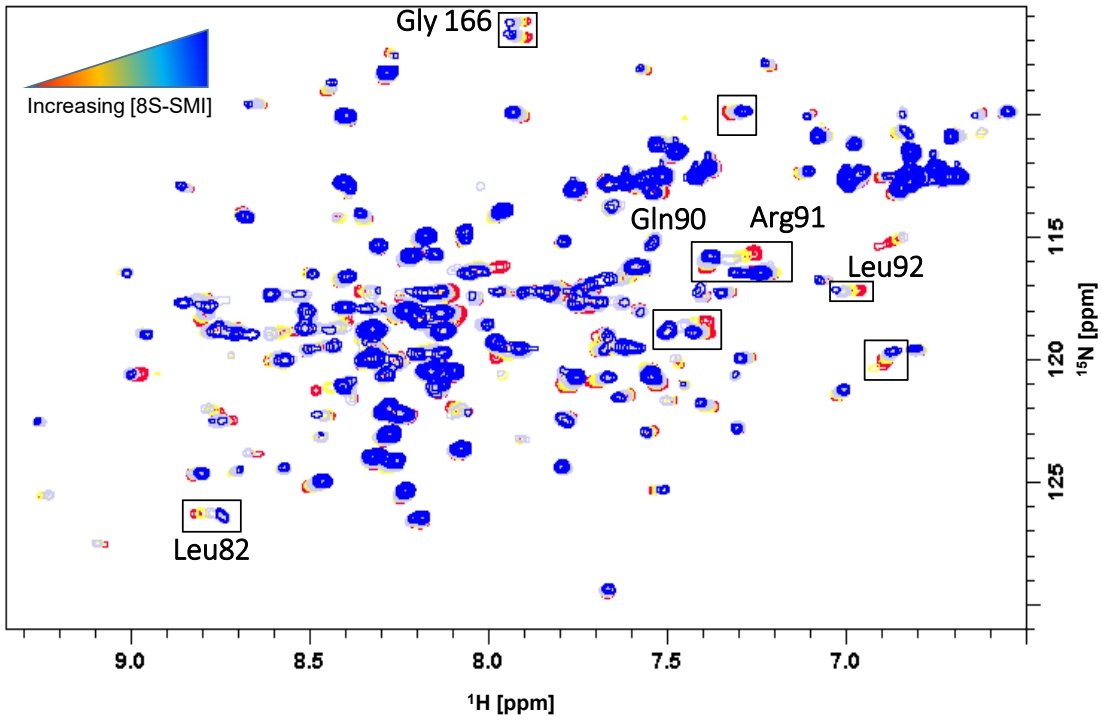


**Figure 3.9 Chemical shift perturbation assay of SMI-8S**

0-180.9 µM final concentrations of SMI-8S were added to an NMR tube containing the following components: 600 µL recombinant OSM, 100 µM OSM, 50 mM sodium phosphate, and 100 mM sodium chloride. In the figure, a red to blue shift indicates increasing SMI concentration. The spectral overlay shows cross peaks shifting red to blue with increasing 8S-SMI concentration. The 5 amino acids that have been identified include Leu92, Gln90, Arg91, and Gly166, with chemical shifts of (6.9, 117), (7.4, 117), (6.3, 116), and (6.9, 117) ppm, respectively.

Not all amino acid CSPs could be identified, as several of the observed shifts are not isolated enough to be compared to known chemical shift values. However, CSPs for Leu82 and Gly166 were identified at (8.7, 127) and (7.9, 111) ppm, respectively. This CSP observed for Leu82 is quite interesting, as Leu82 lies within the middle portion of the middle of the protein. It is hypothesized that some non-specific event binding might cause this perturbation as this amino acid is not located in site III of OSM, according to the crystal structure visualized in USCF Chimera.[10] In addition to consulting the previously known chemical shifts for a glycosylated construct of OSM, NMRFAM-SPARKY[11] was used to upload and visualize $^{1}H/^{15}N$ HSQC assignments for OSM. Known OSM $^{1}H/^{15}N$ HSQC assignments were retrieved from the Biological Magnetic Resonance Data Bank (OSM protein #4063) and overlayed with the experimental data to verify overlapping peaks.[12]

3.4.3 Differential Scanning Fluorimetry Experiments of SMI-8 Analogs

The thermal stability of a protein in solution is influenced by several different soluble components participating in non-specific binding events.[13] Notably, small molecule ligands have been reported to influence protein stability by increasing or decreasing the melting temperature ($T_M$) of a protein, which is indicative of a binding event.[14] Differential scanning fluorimetry (DSF) is a common drug discovery method that measures a protein's $T_M$ upon the presence and absence of a ligand.[14] Experiments by Holdgate and Ward show that the relative binding affinity of compounds with similar physicochemical properties can be determined by DSF.[15] Therefore, DSF was deemed to be an appropriate assay to determine the relative binding affinities of the SMI-8H analogs.

Figure 3.10 depicts the principles of a typical DSF experiment. As the stability of most proteins decreases with increasing temperature, they will start to melt (denature). The $T_M$ of a protein is identified as the inflection point of the curve where Gibbs free energy of the protein ($\Delta G_u$) becomes zero. At this point, the unfolded and folded protein population states are in equilibrium.[16] Upon protein unfolding, a dye called SYPRO Orange binds to the hydrophobic region of the protein, after which it fluoresces.[14] In the Figure, the black curve represents a hypothetical melting curve of OSM without any SMI, while the cyan curve represents a hypothetical melting curve of OSM that has been melted with SMI. The difference between the two melting points of the control and experimental group is what is referred to as a change in melting temperature, or thermal shift ($\Delta T_M$). Furthermore, ligands that bind to the protein in the native state and increase the $T_M$ are referred to as N-binders. In contrast, ligands that preferentially bind to the unfolded state of the protein are referred to as U-binders.[17] However, one should be aware of the limitations that exist when interpreting $\Delta T_M$ for purposes of calculating binding affinities. The magnitude of the $\Delta T_M$ can vary for different compounds with the same affinity. Therefore, DSF should be used in conjunction with other binding affinity experiments as it only identifies if the compound can or cannot bind to the protein in question.[14]

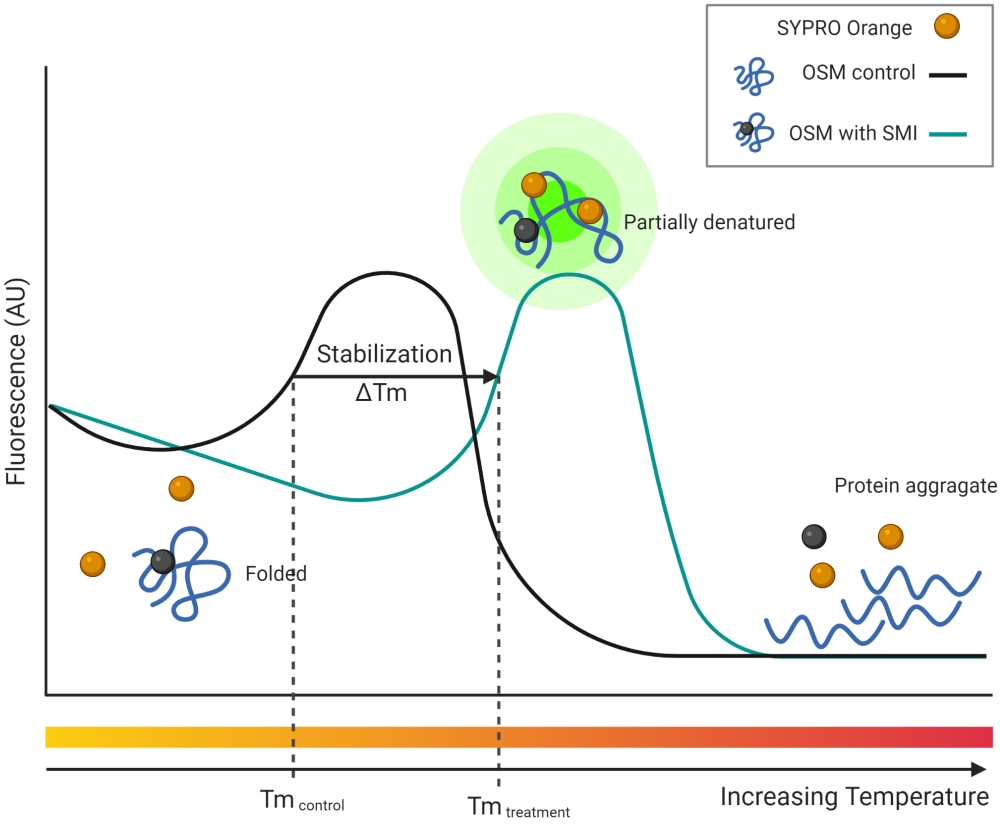


**Figure 3.10 Principles of DSF**

The black curve in represents a hypothetical melting curve of OSM without SMI (black sphere), while the cyan curve represents a hypothetical melting curve of OSM with SMI. Upon the unfolding of the protein in either curve, SYPRO Orange (orange sphere) binds to the hydrophobic portion of the protein and fluoresces. The melting temperature of the protein ($T_M$) is identified as the inflection point of the curve. A Shift in the $T_M$ of the protein ($\Delta T_M$) indicates a binding event.

In order to find a suitable concentration of OSM that would give a reliable fluorescence signal, a dilution series experiment was performed without any SMI. An adequate fluorescence signal was achieved using concentrations of OSM anywhere from 8-16 µM as concentrations of 2 and 4 µM of OSM were found to give a weak fluorescence signal. Preliminary experiments (data not shown) using a structurally unrelated SMI being studied in the Warner lab (SMI-10B)) at a final concentration of 1:1 SMI to OSM did not elicit an observable $\Delta T_M$, so an investigation using various concentrations of SMI-10B was conducted (Figure 3.11). Unfortunately, SMI-8 was not chosen as the compound was not soluble at the concentrations that needed to be tested.

Panel A shows the raw fluorescence obtained during the experiment as a function of temperature, while panel B shows the first derivative of the raw fluorescence as a function of temperature, in which the maximum y-value signifies the melting point of the protein.

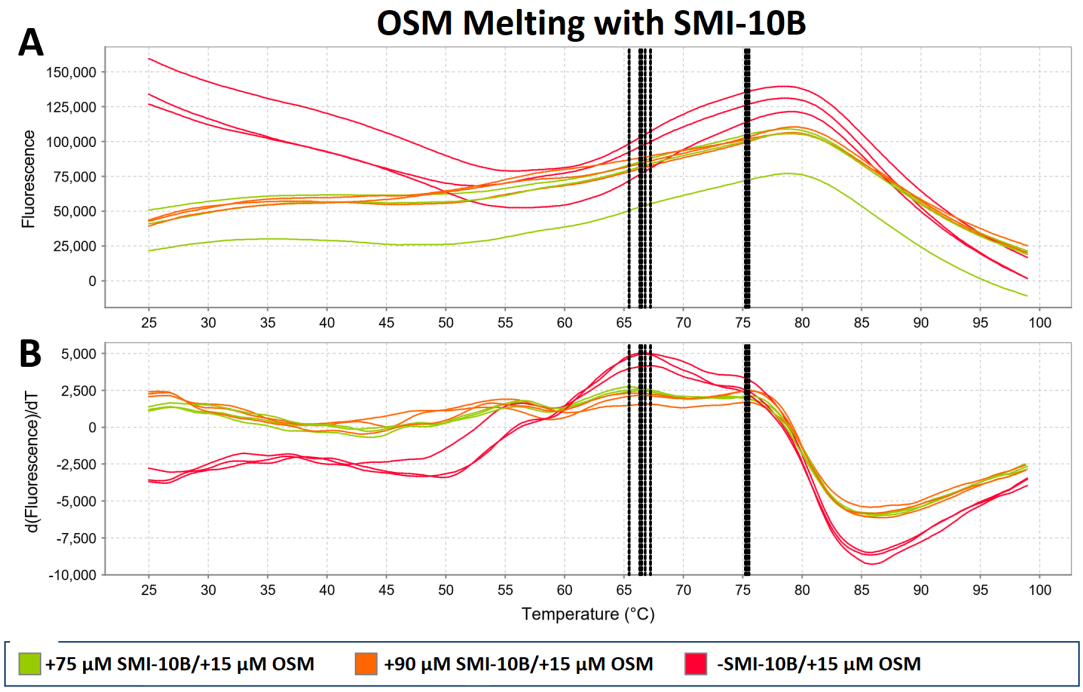


**Figure 3.11 SMI-10B stabilizes OSM**

SMI-10B was added at concentrations of 15, 30, 45, 60, 75, and 90 µM to an aqueous buffer solution containing 15 µM OSM, 50 mM sodium phosphate, and 100 mM sodium chloride. (**A**) The raw fluorescence was obtained as a function of temperature. The dashed black lines indicate the melting points for each specific replicate. (**B**) Graph B is the first derivative of the raw fluorescence as a function of temperature (n = 3).

Without any SMI-10B added, the OSM control group (red) experienced an average $T_M$ of 66.29 °C. Interestingly, the only concentration of 10B that seemed to cause a shift was 90 µM (orange), which shifted the average $T_M$ of OSM to 75.37 °C. This resulted in a calculated $\Delta T_M$ of +9.08 °C. As the measured $\Delta T_M$ is positive, this likely means that SMI-10B binds and stabilizes the native state of OSM, which classifies it as an N-ligand.[17] It seemed peculiar that any concentration lower than 90 µM did not elicit a shift in the $T_M$ of OSM. DSF experiments performed by Cimmperman and coworkers

describe a “saturation effect,” which can occur when a ligand does not elicit an expected $\Delta T_M$.[17] This can happen if the ligand is partially binding to the unfolded state of the protein, or it can be a result of ligand insolubility. Nevertheless, the data from this experiment suggested that SMIs should be subjected to DSF with no less than a 6:1 SMI to OSM ratio.

Figure 3.9 shows the DSF data that were obtained when SMI-8H3 and SMI-8H6 were heated with OSM in a DSF experiment. Without any SMI added, the OSM control group (red) experienced an average Tm of 69.46 °C. When OSM was treated with either SMI-8H3 or SMI-8H6, OSM experienced a negative shift in $T_M$. The average $T_M$ for OSM treated with SMI-8H3 was calculated to be 55.12 °C, which results in an $\Delta T_M$ of -14.34 °C. The average $T_M$ for OSM treated with SMI-8H6 was calculated to be 61.00 °C, which results in a $\Delta T_M$ of -8.46 °C. The larger magnitude shift observed for OSM treated with SMI-8H3 was expected as ELISA shows the compound effectively inhibits OSM signaling. It was hypothesized that a smaller $\Delta T_M$ would be observed for OSM treated with SMI-8H6, as it performed poorly in the ELISA experiments. These data also suggest that both SMI-8H3 and SMI-8H6 bind to the unfolded state of OSM, which classifies them as U-ligands.[17]

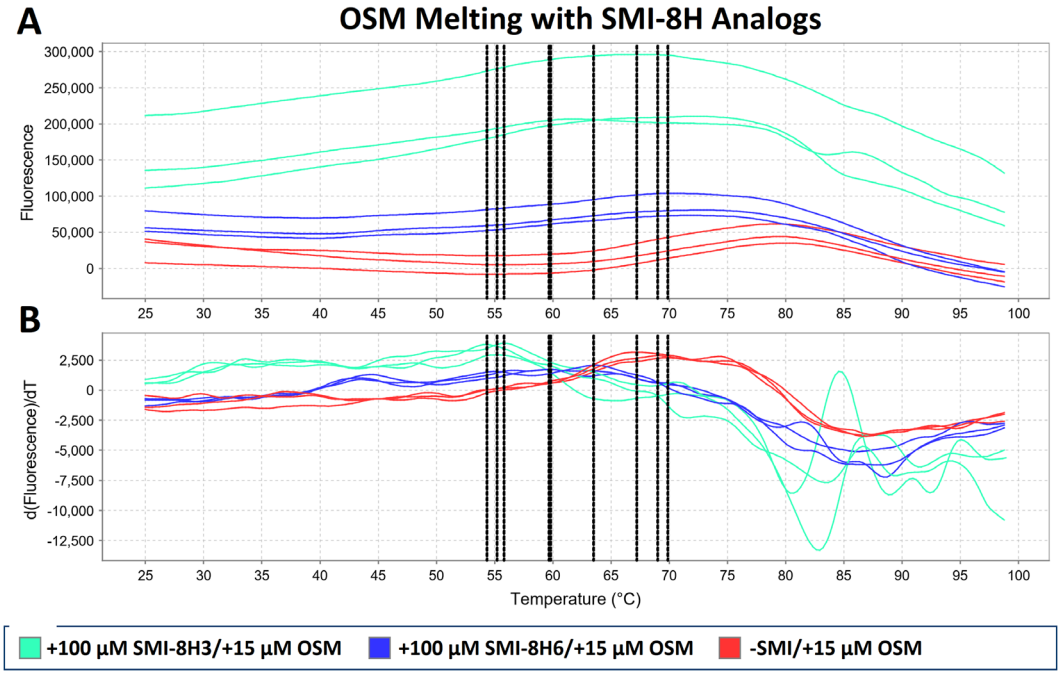


**Figure 3.12 SMI-8H analogs stabilize OSM**

100 µM concentrations of SMI-8H3 and SMI-8H6 were added to an aqueous buffer solution containing 15 µM OSM, 50 mM sodium phosphate, and 100 mM sodium chloride. (**A**) The raw fluorescence was obtained as a function of temperature. The dashed black lines indicate the melting temperature for each specific replicate. (**B**) Graph B is the first derivative of the raw fluorescence as a function of temperature (n = 3).

However, the melting curve of OSM looked irregular when compared to a published melting curve of OSM.[2] In the published OSM melting curve, there are few inflection points rather than many observed in Figure 3.2. It has been postulated that the multiple inflection points observed in the previous experiments suggest that OSM could be in a dimeric form or that there could be impurities in the solution.[18] Indeed, OSM has been identified to exist in solution as a dimer, connected by a disulfide bond between solvent exposes cysteine residues.[2] To test if the multiple inflection points were attributable to OSM dimers, Jayden Brandt (Lisa Warner lab) conducted a gel electrophoresis experiment to separate OSM treated with and without the reducing agent β-mercaptoethanol (BMe). If OSM exists in solution as a dimer, then treating it with a reducing agent, such as BMe, should afford monomeric OSM by reducing the disulfide

bonds. As seen in Figure 3.13, the OSM that was treated with the reducing agent (OSM +BMe) produced a strong band around 21 kDa, which corresponds to the monomer of OSM. When the reducing agent was not used (OSM -BMe), the dimer can be observed at approximately 40 kDa. This supports the idea that the OSM used in previous DSF experiments was several different forms of varying masses, including the original SMI-concentration experiments using SMI-10B.

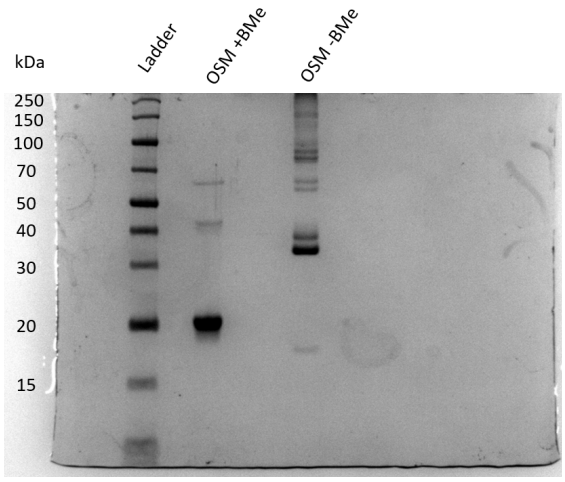


**Figure 3.13 OSM forms dimers.**
OSM was separated by gel electrophoresis after being treated (OSM +BMe) or not being treated (OSM +BMe). Image courtesy of Jayden Brandt.

Another DSF experiment was run to see if the addition of a reducing agent produced more consistent data. The samples were prepared in the same fashion as described in the previous experiment, but Tris(2-carboxyethyl)phosphine hydrochloride (TCEP) was introduced to all groups at a 1 mM concentration to afford monomeric OSM. Figure 3.11 shows the DSF data obtained when SMI-8H3 and SMI-8H6 were melted with OSM. Without any SMI added, the OSM control group (red) experienced an average $T_M$ of 66.05 °C. When OSM was treated with either SMI-8H3 or SMI-8H6, OSM experienced a negative shift in $T_M$. The average $T_M$ for OSM treated with SMI-8H3 was

calculated to be 63.08 °C, which results in a $\Delta T_M$ of -2.97 °C. The average $T_M$ for OSM treated with SMI-8H6 was calculated to be 65.01 °C, which results in a $\Delta T_M$ of -1.04 °C. The blank sample containing SYPRO, TCEP, and SMI did not fluoresce, so all fluorescence is due to protein-SYPRO binding interactions (data not shown). The data agree with the results from the ELISA experiments, where SMI-8H3 exhibits a stronger binding affinity for OSM, causing a larger magnitude in a $\Delta T_M$.

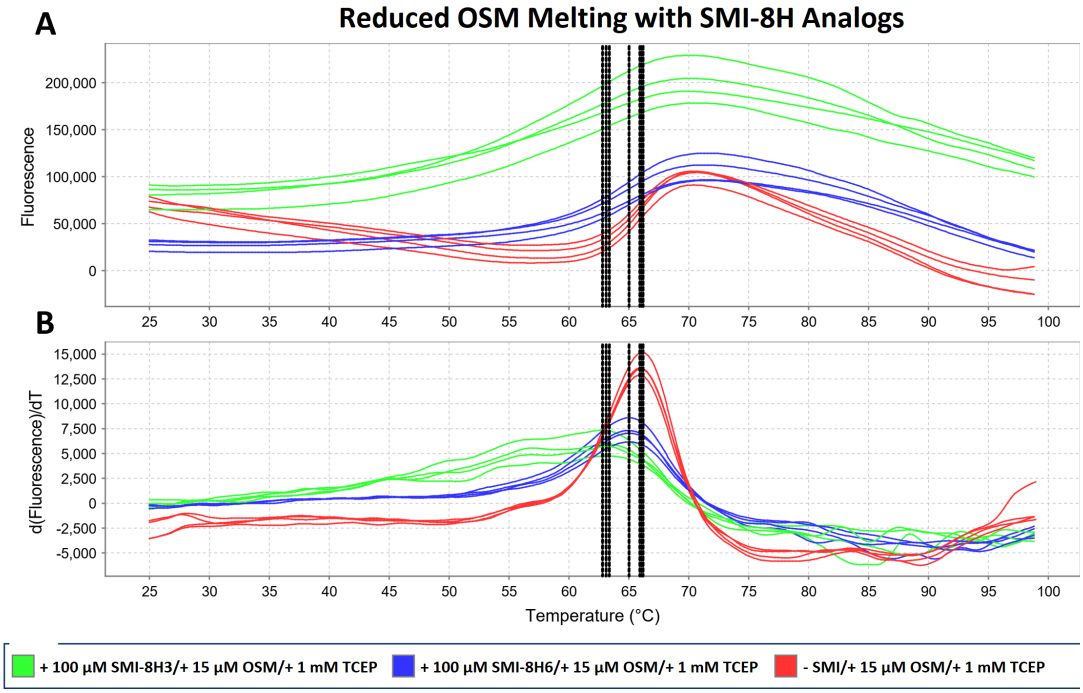


**Figure 3.14 SMI-8H analogs stabilize the OSM monomer**

100 µM concentrations of SMI-8H3 and SMI-8H6 were added to an aqueous buffer solution containing 15 µM OSM, 50 mM sodium phosphate, and 100 mM sodium chloride, and 1 mM TCEP. (**A**) The raw fluorescence was obtained as a function of temperature. The dashed black line indicates Tm for each specific replicate. (**B**) Graph B is the first derivative of the raw fluorescence as a function of temperature (n = 4).

Since previous data obtained for SMI-8H and SMI-8H3 were promising, a total of 13 SMI-8H analogs were subjected to DSF with monomeric OSM to observe trends amongst a larger group of compounds (Figure 3.15). Unfortunately, there is no discernable trend among the SMI-induced $\Delta T_M$ values that collectively agree with the ELISA data. For example, SMI-8H5 performed as well as SMI-8H13 in the ELISA, yet

the SMI-8H5 barely caused a shift in melting temperature. It is possible that the lack of trends observed in DSF is due to the difference in aqueous solubility among the SMI-8H analogs. The only definitive conclusion that can be made so far is that the SMI-8H analogs do bind to OSM, but their relative binding affinities have yet to be identified.

| SMI-8HX | ΔTm (°C) | SMI-8HX | ΔTm (°C) |
|---|---|---|---|
| 1 | -0.51 | 8 | -1.13 |
| 2 | -0.51 | 9 | -1.43 |
| 3 | -2.97 | 10 | -1.28 |
| 4 | -0.48 | 11 | -1.39 |
| 5 | -1.09 | 12 | -2.87 |
| 6 | -1.04 | 13 | -0.65 |
| 7 | -0.43 | | |

**Figure 3.15 $\Delta T_M$ values for SMI-8H analogs**

$T_M$ values were calculated by averaging the mean of the four replicates for each sample. $\Delta T_M$ values were calculated by subtracting the average OSM $T_M$ value from the experimental $T_M$ value.

3.4.4 A Cost-Benefit Analysis of Binding Assays

It is an expensive and laborious process to express and purify OSM. So, it is necessary to perform a cost-benefit analysis of each current and prospective binding assay. We have the expertise available to use isothermal calorimetric titrations, chemical shift perturbation, and saturation transfer difference-nuclear magnetic resonance experiments to measure $K_D$ values for SMIs binding to OSM. Even though isothermal calorimetric titrations have been used to measure $K_D$ values of a structurally different OSM-SMI analog, they are extremely sensitive to errors in concentrations, and they do not serve as a high-throughput assay.[19, 20] CSP experiments are also not ideal as the expression of the $^{15}N/^{1}H$ OSM is expensive. Finally, STD-NMR does not serve as a high-throughput assay either as NMR-based experiments lack sensitivity in comparison to

other analytical methods.[21] However, FQ, DSF, and SPR binding experiments will be discussed as they offer moderate to high-throughput methods of obtaining binding data. This breakdown will only factor in the cost of specialty reagents and expensive consumables used. The usage of protein will be discussed as one of the main determining factors of the costs associated with the experiments, as it is the most expensive consumable material used.

The FQ assay was the first accurate and reproducible experiment used to measure $K_D$ values for SMIs binding to OSM. The only expensive reagent required in the FQ assay is the reducing agent TCEP (1g/$80.50, Thermo Fisher). The most obvious benefit is that accurate and reliable $K_D$ values can be obtained. Another advantage is that the assays are relatively easy to run and only require protein and SMI. However, there are some serious drawbacks. The biggest problem occurs when the SMI absorbs and/or fluoresces near or at 350nm. In addition, the mass of OSM used to obtain a $K_D$ value for one SMI is 66.4 μg, while DSF uses 11.8 μg. Therefore, this assay is currently the most expensive when considering just the consumption of OSM. In theory, smaller cells could be used that would reduce the amount needed. However, the nature of the experiment requires mixing, which was problematic in the micro cells. Finally, FQ assays are not high-throughput enough to assess an extensive library of compounds since an experiment to obtain a $K_D$ value for a single SMI in triplicate requires approximately 30 minutes.

DSF experiments have been investigated as an approach to rapidly screen large libraries of compounds. As previously discussed, in our hands, the DSF experiments cannot be used to obtain dependable $K_D$ values based on just the $\Delta T_M$ of the protein. Given that all SMI-8H analogs that performed well by ELISA caused a $\Delta T_M$ shift, the

DSF assay may be better suited as a method to identify compounds that bind to OSM and compounds that do not. The most obvious benefit to using DSF is that many SMIs can be assessed at once using a 96-well plate. In addition, DSF requires less OSM per experiment. Considering that the wells in the qPCR plate contain 20 microliters of sample, It is possible to prepare a single experimental sample in triplicate using 11.8 μg while still obtaining a good fluorescence signal.

SPR experiments can possibly serve as a high-throughput and accurate method of determining binding affinities of OSM-SMIs. As seen in Figure 3.16, the experiment begins with choosing an appropriate sensor chip (grey) to immobilize the protein of interest (purple).[22] Once the protein is successfully immobilized to the sensor chip, a baseline reading is obtained by shining light through a high refractive index prism onto the backside of the sensor chip and then capturing the reflected light with a detector. When the dissolved ligand is injected across the surface of the sensor chip, the ligand can bind to the protein adhered to the sensor chip. As a result of a binding event, the angle of the reflected light will change, which causes a shift in the minimum intensity of the reflected light. Most importantly, it is possible to plot SPR response vs. time to obtain dissociation constants.

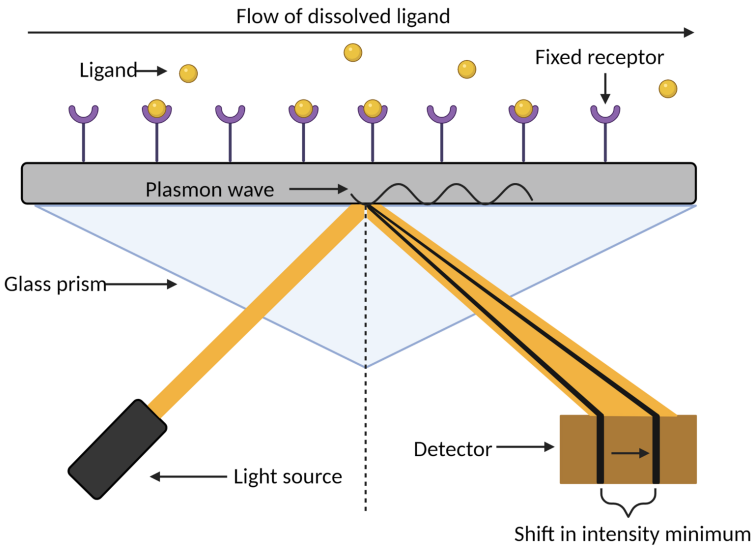


**Figure 3.16 Principles of SPR**

The protein of choice is adhered to a planar sensor chip (grey), which specifically or non-specifically binds the protein (purple). SPR response is recorded with and without ligand flowing across the sensor chip. Upon ligand binding, the detector measures a change in the SPR response is recorded as well as a shift in intensity minimum of the reflected light.

Since SPR experiments have not been successfully accomplished with OSM-SMIs, it is difficult to know the exact cost of determining the binding affinity of a single SMI. An estimation of the cost of materials will have to serve as a substitute. The most considerable benefit to using SPR is that $K_D$ values can be obtained in a high-throughput manner, as Boise State University has a Themofinnagen Surveyor autosampler that can hold 200 sample vials. Also, the amount of protein necessary to run an SPR binding experiment is considerably less than both FQ and DSF assays. According to previous experiments at Boise State University that involved OSM, only 100 µL of 20 µg/mL was used to adhere OSM to the sensor chip surface.[23] This translates to a total mass of 2.0 µg OSM being used to prepare a single sensor chip. It is currently unknown how many different samples can be analyzed using the same gold sensor chip. This is an important factor, as the planar polyethylene glycol/carboxyl sensor chips (Reichert part #13206061) previously used for OSM are currently $66.94/sensor chip. So, the economic feasibility

of this assay will ultimately depend on the ability of the OSM to stay bound to the sensor chip. As the instrumentation can run up to 200 samples, the limiting factor will most likely be the ability of the protein to stay bound to the sensor chip.

In conclusion, SPR would be the best choice as it can collect gather binding data in a high-throughput manner. However, this is assuming that OSM stays adhered to the hydrophobic sensor chip after several wash cycles. The cost of the chips also might make SPR expensive if used as an initial screening tool. It is imaginable that both DSF and SPR could be used together in a simple workflow. Even though DSF does not reveal relative binding affinities, the experiments discussed show they identify protein-ligand binding. So, it is conceivable that extensive libraries of compounds can be screened by DSF as it is relatively inexpensive. Once specific molecules are identified to cause shifts in the $T_M$ of OSM, they could be further subjected to analysis by SPR to obtain direct binding data. If both DSF and SPR are proven to give accurate and reproducible results in future experiments, then it is possible that the FQ methodology can exist as the least desirable option of the three binding assays.

### 3.5 Conclusions and Future Work

Collectively, 35 individual SMIs were synthesized according to five unique reaction pathways and characterized using standard methods. The linear synthesis of both SMI-8 and SMI-8S called for the planning of new synthetic routes that produced compounds resembling SMI-8. These pathways used common medicinal chemistry reactions, such as Pd (0) catalyzed carbon-carbon coupling, nucleophilic aromatic substitution, amide formations, basic ester hydrolysis, heterocycle formation, and reactions with diazonium intermediates.[24] Notably, the SMI-8H analog series was the

most amenable to functionalization as enolate formation at the α-carbon allows for branching via an alkylation reaction, and the electrophilic carbon at the 2-position of the thiazole can be exploited by Suzuki-Miyaura couplings and nucleophilic aromatic substitutions. In addition, the synthesis of structurally different compounds teased out whether specific structures were necessary for the success of SMI-8. For example, SMI-8 and SMI-8S were measured to have $K_D$ values of 5 ± 1 μM and 14 ± 3 μM, respectively. The ELISA also shows that the dienes are not needed, as SMI-8S performed just as well as SMI-8.

The CSP and FQ experiments support the argument that SMI-8S directly binds to OSM, while the ELISA data show that most SMI-8 analogs inhibit OSM signaling in T47D breast cancer cells. However, a considerable amount of the SMI-8H analogs were within error of another in the ELISA experiments, making it difficult to establish definitive SAR trends. The DSF experiments reveal that OSM becomes stabilized or destabilized upon ligand binding, as evidenced by the proteins shift in $T_M$. Unfortunately, the results from DSF experiments of the SMI-8H analogs do not agree with the overall trends observed in the ELISA. Therefore, it is uncertain whether this assay can be of any practical use in ranking relative binding affinities. Finally, the perturbations of the $^{15}N/^{1}H$ HSQC chemical shifts observed for Gln90, Arg91, and Leu92 in the CSP experiment suggest that SMI-8S directly binds to site III of OSM and further validates the initial high throughput virtual screening.

The most consistent interaction that the virtual docking experiments have predicted is the hydrogen bonding interaction between the Lys166 and the thiazole(s) of the SMI-8 analogs. It would be worthwhile to determine if replacing the bisthiazole core

of SMI-8 and SMI-8S with a bisoxazole would prove to be beneficial. When the bisthiazole groups were substituted with bisoxazole groups in virtual docking studies, the binding scores were slightly lower ( -0.5 kcal/mol). Unfortunately, this is another linear synthesis that would not afford an extensive library of compounds. However, it would work to identify if the bisthiazole can be replaced in SMI-8 and still maintain or increase its affinity for OSM. If this is the case, it is conceivable that a library of analogs structurally similar to SMI-8 could be synthesized with oxazoles instead.

One of the most important questions considering the SMI-8H analogs has yet to be answered: which enantiomer of the SMI-8H analogs is more potent? At this point in the project, it is unknown whether the R or S enantiomer of the analogs has a greater binding affinity. This question can be answered by taking two important steps. Step one involves isolating the specific enantiomers of a small selection of SMI-8H compounds via chiral chromatography and subjecting them to an adequate assay that will determine their binding affinity. Step two involves planning a synthetic route that selectively produces the more potent enantiomer. This can be accomplished by the use of chiral auxiliary groups, which are temporarily incorporated into the structure to determine the stereoselective outcome of the products.

Oxazolidinones are known to be useful chiral auxiliary groups in the context of enolate alkylation reactions. Chiral directing groups, such as Evans' oxazolidinones, have proven to afford either the R or S isomer in enantiomeric excess of 98%.[25] Figure 3.17 shows a proposed pathway in which the S enantiomer can be synthesized with high selectivity. The first step of the synthesis involves installing the oxazolidinone directing group using DCC as a peptide coupling reagent.[26] Next, the formation of the enolate can

be accomplished using lithium diisopropylamide (LDA).[25] Nucleophilic attack of the electrophile by the pi electrons is expected to occur from the *si* face of the prochiral group, resulting in the formation of an S stereocenter. Finally, the oxazolidinone directing group is removed under oxidative conditions.[25] The choice to use an S or and R oxazolidinone will depend on which enantiomer is identified to be the most potent.

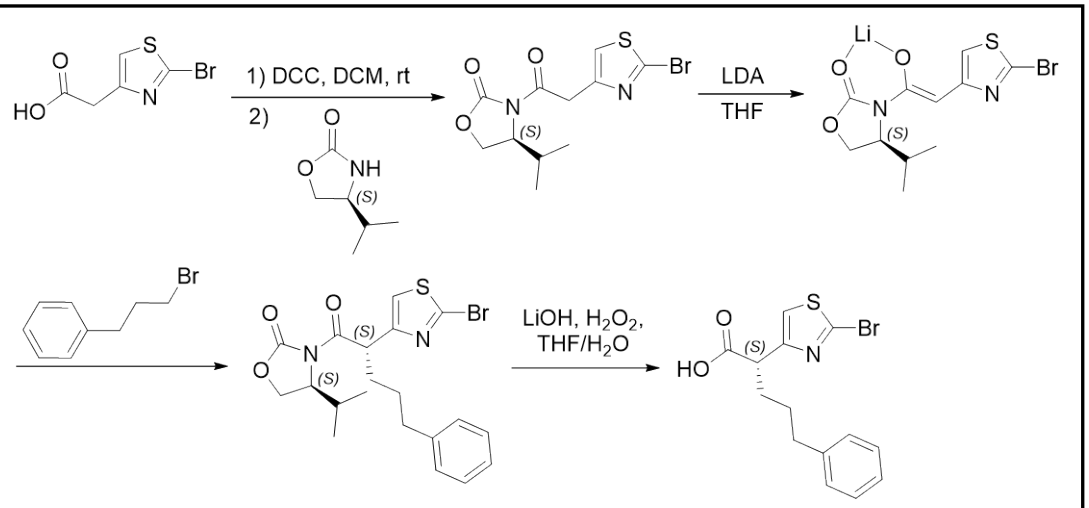


**Figure 3.17 Proposed enantioselective enolate alkylation**

The solubility of the SMI-8 has complicated *in vitro* and *in vivo* experiments. In addition, SwissADME has predicted that all the SMI-8H analogs have poor solubility. A fundamental strategy used in medicinal chemistry to overcome solubility problems is to integrate what is known as an isostere. Isosteres are simply surrogate structures that can be used to replace functional groups that are problematic while maintaining the same electronic features.[27] Therefore, it might be advantageous to integrate certain isosteres in these structures to increase the solubility of the compounds. The first proposed change to the analogs includes the addition of a tetrazole isostere as a replacement for carboxylic acid functional groups.[28] It is hypothesized that the introduction of a tetrazole to the SMI-8H analog structure will improve solubility in aqueous media, as Lassalass and

coworkers determined that tetrazole derivatives participate in stronger hydrogen-bond interactions than their corresponding amino acids.[27]

Virtual ligand docking experiments have guided the synthesis of the SMI-8 analogs, but a more robust method is needed. Therefore, it is proposed that a structure-activity relationship be created to help guide future students working on the project. This can be accomplished with a three-dimensional quantitative structural activity relationship (3D QSAR) model with as little as twenty compounds.[29] Roger Vuong (Don Warner lab) has developed a 3DQSAR model of SMI-26, as seen in Figure 3.18. To create the contour map seen in panel B, twenty-four SMI-26 analogs were aligned using Open3DALIGN and imported Into 3DQSAR[30] along with their respective $K_D$ values. These data were then used to visualize a contour map in PyMOL.

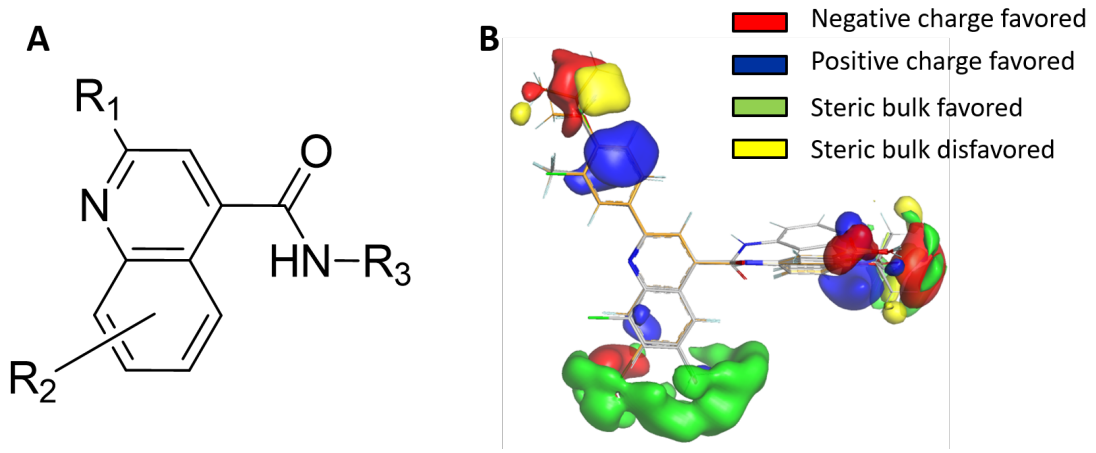


**Figure 3.18 A 3DQSAR model of SMI-26**

(**A**) The SMI-26 scaffold is a quinoline core in which the $R_1$, $R_2$, and $R_3$ groups have been appended with different groups. (**B**) A contour map of SMI-26 was generated using 3DQSAR to observe favorable interactions.

In panel B, several trends can be identified. For example, favored groups at the $R_1$ substitution site include phenyl groups with small, negatively charged substituents at the ortho position, while positively charged groups seem to be favored at the meta position. In respect to the $R_2$ substitution site, it is overwhelmingly clear that steric bulk is

preferred at the bottom portion of the quinoline ring. The substituent favorability at the $R_3$ substitution site remains ambiguous. Creating a model as described will undoubtedly help guide future students in their goals of optimizing SMI-8 analogs.

The inability of the SMI-8H analogs to be subjected to FQ assays has been a serious obstacle in determining the direct binding affinities to OSM. So, the next logical step in the SMI-8 project is to develop a high-throughput binding assay to assess the compound's affinities towards OSM. As previously discussed, it is conceivable that SPR can be used to determine direct binding affinities of the SMI-8H analogs. This approach is promising, as other research groups at Boise State University have obtained binding affinities of extracellular matrix and neutralizing OSM antibodies towards OSM using a published approach.[31] Not only will this allow reliable SAR trends of the SMI-8H analogs to be identified, but it will also greatly expand the scope of the SMI project as a whole.

## 3.6 Chapter Three References


1. Tanaka, M.; Miyajima, A., Oncostatin M, a multifunctional cytokine. *Rev Physiol Biochem Pharmacol* **2003,** *149*, 39-52.
2. Mass, O. A.; Tuccinardi, J.; Woodbury, L.; Wolf, C. L.; Grantham, B.; Holdaway, K.; Pu, X.; King, M. D.; Warner, D. L.; Jorcyk, C. L.; Warner, L. R., Bioactive recombinant human oncostatin M for NMR-based screening in drug discovery. *Scientific Reports* **2021,** *11* (1), 16174.
3. Mahmood, T.; Yang, P. C., Western blot: technique, theory, and trouble shooting. *N Am J Med Sci* **2012,** *4* (9), 429-34.
4. Dey, G.; Radhakrishnan, A.; Syed, N.; Thomas, J. K.; Nadig, A.; Srikumar, K.; Mathur, P. P.; Pandey, A.; Lin, S.-K.; Raju, R.; Prasad, T. S. K., Signaling network of Oncostatin M pathway. *J Cell Commun Signal* **2013,** *7* (2), 103-108.
5. Jarmoskaite, I.; AlSadhan, I.; Vaidyanathan, P. P.; Herschlag, D., How to measure and evaluate binding affinities. *Elife* **2020,** *9*, e57264.
6. Charlier, H. A., Jr.; Plapp, B. V., Kinetic cooperativity of human liver alcohol dehydrogenase gamma(2). *J Biol Chem* **2000,** *275* (16), 11569-75.
7. Yammine, A.; Gao, J.; Kwan, A. H., Tryptophan Fluorescence Quenching Assays for Measuring Protein-ligand Binding Affinities: Principles and a Practical Guide. *Bio Protoc* **2019,** *9* (11), e3253.
8. Williamson, M. P., Using chemical shift perturbation to characterise ligand binding. *Prog Nucl Magn Reson Spectrosc* **2013,** *73*, 1-16.
9. Hoffman, R. C.; Moy, F. J.; Price, V.; Richardson, J.; Kaubisch, D.; Frieden, E. A.; Krakover, J. D.; Castner, B. J.; King, J.; March, C. J.; Powers, R., Resonance assignments for Oncostatin M, a 24-kDa alpha-helical protein. *J Biomol NMR* **1996,** *7* (4), 273-82.
10. Pettersen, E. F.; Goddard, T. D.; Huang, C. C.; Couch, G. S.; Greenblatt, D. M.; Meng, E. C.; Ferrin, T. E., UCSF Chimera--a visualization system for exploratory research and analysis. *J Comput Chem* **2004,** *25* (13), 1605-12.
11. Lee, W.; Tonelli, M.; Markley, J. L., NMRFAM-SPARKY: enhanced software for biomolecular NMR spectroscopy. *Bioinformatics* **2015,** *31* (8), 1325-7.
12. Ulrich, E. L.; Akutsu, H.; Doreleijers, J. F.; Harano, Y.; Ioannidis, Y. E.; Lin, J.; Livny, M.; Mading, S.; Maziuk, D.; Miller, Z.; Nakatani, E.; Schulte, C. F.; Tolmie, D. E.; Kent Wenger, R.; Yao, H.; Markley, J. L., BioMagResBank. *Nucleic Acids Research* **2007,** *36* (suppl_1), D402-D408.
13. Zbacnik, T. J.; Holcomb, R. E.; Katayama, D. S.; Murphy, B. M.; Payne, R. W.; Coccaro, R. C.; Evans, G. J.; Matsuura, J. E.; Henry, C. S.; Manning, M. C., Role of Buffers in Protein Formulations. *J Pharm Sci* **2017,** *106* (3), 713-733.
14. Niesen, F. H.; Berglund, H.; Vedadi, M., The use of differential scanning fluorimetry to detect ligand interactions that promote protein stability. *Nature Protocols* **2007,** *2* (9), 2212-2221.
15. Holdgate, G. A.; Ward, W. H., Measurements of binding thermodynamics in drug discovery. *Drug Discov Today* **2005,** *10* (22), 1543-50.
16. Schellman, J. A., Temperature, stability, and the hydrophobic interaction. *Biophys J* **1997,** *73* (6), 2960-4.

17. Cimmperman, P.; Baranauskiene, L.; Jachimoviciūte, S.; Jachno, J.; Torresan, J.; Michailoviene, V.; Matuliene, J.; Sereikaite, J.; Bumelis, V.; Matulis, D., A quantitative model of thermal stabilization and destabilization of proteins by ligands. *Biophysical journal* **2008,** *95* (7), 3222-3231.
18. Warner, L., Boise State University, Boise, ID. Personal communication, 2021.
19. Dutta, A. K.; Rösgen, J.; Rajarathnam, K., Using isothermal titration calorimetry to determine thermodynamic parameters of protein-glycosaminoglycan interactions. *Methods Mol Biol* **2015,** *1229*, 315-24.
20. Torres, F. E.; Recht, M. I.; Coyle, J. E.; Bruce, R. H.; Williams, G., Higher throughput calorimetry: opportunities, approaches and challenges. *Curr Opin Struct Biol* **2010,** *20* (5), 598-605.
21. Ardenkjaer-Larsen, J.-H.; Boebinger, G. S.; Comment, A.; Duckett, S.; Edison, A. S.; Engelke, F.; Griesinger, C.; Griffin, R. G.; Hilty, C.; Maeda, H.; Parigi, G.; Prisner, T.; Ravera, E.; van Bentum, J.; Vega, S.; Webb, A.; Luchinat, C.; Schwalbe, H.; Frydman, L., Facing and Overcoming Sensitivity Challenges in Biomolecular NMR Spectroscopy. *Angewandte Chemie (International ed. in English)* **2015,** *54* (32), 9162-9185.
22. Tang, Y.; Zeng, X.; Liang, J., Surface Plasmon Resonance: An Introduction to a Surface Spectroscopy Technique. *J Chem Educ* **2010,** *87* (7), 742-746.
23. Ryan, R. E.; Martin, B.; Mellor, L.; Jacob, R. B.; Tawara, K.; McDougal, O. M.; Oxford, J. T.; Jorcyk, C. L., Oncostatin M binds to extracellular matrix in a bioactive conformation: implications for inflammation and metastasis. *Cytokine* **2015,** *72* (1), 71-85.
24. Brown, D. G.; Boström, J., Analysis of Past and Present Synthetic Methodologies on Medicinal Chemistry: Where Have All the New Reactions Gone? *Journal of Medicinal Chemistry* **2016,** *59* (10), 4443-4458.
25. Heravi, M. M.; Zadsirjan, V.; Farajpour, B., Applications of oxazolidinones as chiral auxiliaries in the asymmetric alkylation reaction applied to total synthesis. *RSC advances* **2016,** *6* (36), 30498-30551.
26. Shen, X. Method for preparing intermediate of PARP-1 (poly(adenosine diphosphate-ribose) polymerase-1) inhibitor Niraparib. 2018.
27. Lassalas, P.; Gay, B.; Lasfargeas, C.; James, M. J.; Tran, V.; Vijayendran, K. G.; Brunden, K. R.; Kozlowski, M. C.; Thomas, C. J.; Smith III, A. B., Structure property relationships of carboxylic acid isosteres. *Journal of medicinal chemistry* **2016,** *59* (7), 3183-3203.
28. Ballatore, C.; Huryn, D. M.; Smith, A. B., 3rd, Carboxylic acid (bio)isosteres in drug design. *ChemMedChem* **2013,** *8* (3), 385-95.
29. McKinney, J. D.; Richard, A.; Waller, C.; Newman, M. C.; Gerberick, F., The Practice of Structure Activity Relationships (SAR) in Toxicology. *Toxicological Sciences* **2000,** *56* (1), 8-17.
30. Tosco, P.; Balle, T., Open3DQSAR: a new open-source software aimed at high-throughput chemometric analysis of molecular interaction fields. *Journal of molecular modeling* **2011,** *17* (1), 201-208.
31. Jorcyk, C. L.; Holzer, R. G.; Ryan, R. E., Oncostatin M induces cell detachment and enhances the metastatic capacity of T-47D human breast carcinoma cells. *Cytokine* **2006,** *33* (6), 323-36.

# APPENDIX A

## Materials and Methods

Biological Based Evaluations

***General procedure for enzyme-linked immunosorbent assays:*** Inhibition of pSTAT3 expression was determined by an ELISA using T47D human breast cancer cell lines. The breast cancer cells were serum-starved for 4 hours to halt the growth and further development of the cell. The SMI-8 analogs (10 μM in DMSO) were then incubated with recombinant hOSM at a 10 ng/ml concentration in a serum-free RPMI-1640 growth medium at 37 °C and 5% $CO_2$ for 1 hour. Following the incubation period, the SMI-8 analogs and recombinant hOSM mixture stimulated the serum-starved cells for 30 minutes. Afterward, the cells were then lysed using a 1x PathScan Sandwich ELISA lysis buffer (CST #7018S) for 15 minutes. After lysis was completed, the cell lysates were collected and stored at -20 °C. The collected lysates were warmed to room temperature, then analyzed for levels of pSTAT3 expression using a human/mouse DuoSet® IC ELISA sandwich ELISA antibody pair kit (R&D Systems). This was accomplished by transferring the lysates to a 96 well plate and measuring with absorbance at 450 nm. Next, pSTAT3 levels were quantified by relative comparison to OSM-induced levels of pSTAT3 expression.

***General Procedure for fluorescence quenching assays:*** SMIs were prepared as a 1.875 mM DMSO solution by diluting a previously prepared 10 mM stock solution in DMSO. In four separate polymethylmethacrylate cuvettes was added 750 μL of a stock solution containing 1.0 μM recombinant hOSM, 0.1 mM tris(2-carboxyethyl)phosphine (TCEP), 50 mM sodium phosphate, and 100 mM NaCl (pH = 6.6). Three of the cuvettes were titrated with 0-100 μM SMI, while the fourth cuvette was titrated with DMSO to serve as a blank. A total of 11 titration points are collected, which includes the initial excitation of

OSM without adding any SMI. At no point does the DMSO exceed 5% of the total solution (v/v). The wavelength emission of the fluorimeter was set to 280 nm, while the fluorescence intensity of OSM was observed at 350 nm. The slit width was set to 4nm, and the photomultiplier voltage was set to 700V. Each titration point obtained from the experimental group was normalized to the fluorescence intensity of the OSM control group in the absence of a small molecule. The samples run in triplicate values are then averaged to yield a single value for each titration point. These averaged values at each titration point are then plotted against the concentration of SMI delivered and fit to a modified Stern-Volmer function, $\left(\frac{f}{f_o}\right) = \left(\frac{f_1}{1-\frac{[X]}{K_d}}\right) + (1 - f_1)$, where $\left(\frac{f}{f_o}\right)$ is the measured fluorescence signal of the sample containing SMI divided by the fluorescence signal of the DMSO blank, $f_1$ is the fraction of fluorescence quenched, [X] is the concentration of SMI, and $K_D$ is the binding affinity of the SMI towards OSM.[1] $K_D$ values were calculated from the fitting routine, and the errors for each titration point were reported as the standard error of the fit with a symmetrical 95% confidence interval. The raw data were analyzed using Microsoft Excel, and the curve fitting analysis was accomplished in GraphPad Prism 8.[2]

***General Procedure for Differential Scanning Fluorimetry Assays***: The assay buffer was prepared as a DI $H_2O$-based solution containing 100 mM NaCl and 50 mM NaPi (pH = 6.8). All samples were prepared in this buffer. Before diluting the stock solution of SYPRO orange to a manageable volume, the small tube containing the 5,000X stock concentrated solution was brought to room temperature and spun down on a mini centrifuge for 10 seconds to ensure homogeneity. The concentration of OSM was kept constant, as well as the concentrations of ligands used. In order to prepare samples in

triplicate, control groups and experimental groups were all prepared in 1.5 mL Eppendorf tubes with a final volume of 100 µL, where the final target concentration of OSM was 15 µL, the final DMSO concentration did not exceed 2% (v/v), the final SYPRO Orange concentration was 10X, the final SMI concentration in the Eppendorf tube was 100 µM, and the final concentration of TCEP was 1 mM. The TCEP was added to the samples last and allowed to sit at room temperature for 30 minutes. Once the 150 µL stock solutions were prepared in the Eppendorf tubes, 4 x 20 µL aliquots were pipetted from the 150 µL Eppendorf solutions into a 96 well qPCR plate to run both control and experimental groups in quadruplicate. A sealable plastic covering was placed atop the 96 well plate and centrifuged at 500 x g for 1 minute to get rid of any air bubbles in the wells. The data were collected on a QuantStudio3 qPCR instrument (Applied Biosystems). The samples were equilibrated at 25 °C for 2 minutes before being gradually heated up to 99 °C, where fluorescence measurements were recorded at intervals of approximately 0.05 °C increments. The data were analyzed using Protein Thermal Shift software (ThermoFisher Scientific). The $T_M$ values were calculated as an average value for the replicates and identified as the maximum y-value of the first derivative of the raw fluorescence data vs. temperature.

***General Procedure for chemical shift perturbation experiments:*** The HSQC sample was prepared as a 600µL protein/buffer solution containing 100 µM $^{15}N/^{1}H$ recombinant human OSM, 50 mM sodium phosphate, 100 mM sodium chloride, and 5% $D_2O$. (pH = 6.6). 5 mM NMR tubes were used. The titration series was performed by pipetting 1.5, 3.0, or 6.0 µL aliquots of a 4.2 mM SMI-8S solution prepared in DMSO into the protein/buffer solution. Overall, 10 titration points were collected, which correspond to

SMI-8S concentrations of 0-180.9 μM. Spectra were obtained at 298K on a Bruker AVANCE III 600 MHz spectrometer equipped with a 5 mm TCI cryoprobe with z-axis gradients. HSQC spectra were obtained with the *hsqcfpf3gpphwg* preset Bruker sequence. The resulting spectra were processed using Topspin 3.2.

Computational Modeling

***General procedure for computational docking studies:*** The virtual docking studies referenced in this document were performed using AutoDock Vina 4.2 using the ff14SB force feild.[3, 4] The crystal structure of hOSM was uploaded to University of California San-Francisco Chimera 1.14 using the protein data bank (PDB) code 1EVS. The protein was then prepared for docking interactions by using the "Dock Prep" action. Next, the small molecule ligand under investigation was drawn in ChemDraw 16.0 and imported into Chimera as a SMILES code. Both small molecule minimization and addition of net charges were accomplished by using the Antechamber module, which uses the default ff14SB force field—opening the "AutoDock Vina" tab located in the tools section allowed small molecule docking parameters to be set. The center docking coordinates were assigned to (10, 35, 25), and the size coordinates were assigned to (30,30,30). No further manipulation of the molecule and/or protein was done after the AutoDock Vina function was run.

Instrumental Analysis

***General information regarding methods of Instrumentation:*** Both $^{1}H$ and $^{13}C$ spectroscopic data were obtained using a Bruker AVANCE III 600 MHz spectrometer equipped with a 5 mm TCI cryoprobe with z-axis gradients or a Bruker AVANCE III 300 MHz spectrometer. All spectra of intermediates and final compounds were obtained at

298K using reagent grade $CDCl_3$ (99.9% D atom) or DMSO-d6 (99.9% D atom). Both deuterated reagents were stored under 3Å molecular sieves. In addition to the DMSO-d6 being stored over molecular sieves, it was also stored in a container filled with calcium chloride. The $CDCl_3$ residual $CHCl_3$ signal at δ(H) = 7.26 ppm and the central resonance signal of the $CDCl_3$ triplet signal at δ(C) = 77.20 ppm were used to reference $^{1}H$ and $^{13}C$, respectfully. The residual DMSO-H6 signal at δ(H) = 2.50 ppm and the residual signal at δ(C) = 39.52 ppm were used to reference $^{1}H$ and $^{13}C$, respectively. The HNMR data were recorded as follows: chemical shift (δ), multiplicity, coupling constant(s) J (Hz), relative integral, where the multiplicity is denoted as s = singlet; d = doublet; t = triplet; q = quartet; hept = heptet; sept = septet; m = multiplet or a combination of multiplets. 5mm NMR tubes were used for sample preparation with either deuterated solvent previously discussed. The original free induction decay data from spectra were originally transformed and observed using Bruker Topspin. Afterward, the data were plotted and analyzed MestReNova version 14.2.1. The reverse-phase high-pressure liquid chromatography (HPLC) analyses were accomplished using an Agilent 1100 series HPLC equipped with a Phenomenex Synergi Fusion C18 column. The mobile phase consisted of a 95:5 mixture containing 95 parts acetonitrile and 5 parts 0.1% aqueous trifluoroacetic acid. The instrument was also equipped with a diode array detector in order to determine specific absorbance. The area under the peaks was automatically integrated by the software. Samples were sent to the Biological Research Center at Boise State University for high-resolution mass spectroscopy (HRMS). Mass spectra were obtained in positive ion mode using a Bruker Daltonics MaXis-Time of flight mass spectrometer. Melting points for all final compounds were observed using a Vernier Melt

Station MLT-BTA as uncorrected results. DSF experiments were run using a QuantStudio3 qPCR instrument, and the data were analyzed using Protein Thermal Shift software.

Synthetic Chemistry

***General information regarding glassware and reagents:*** The reagents used in the synthesis were purchased directly from chemical suppliers as the highest purity possible unless otherwise noted. All glassware used was either oven-dried, or flame dried using a propane torch. After being flame dried or oven-dried, the glassware was cooled under an inert $N_2$ atmosphere using direct in and out gas lines. All reactions were stirred by a magnetic stir bar placed in the reaction vessels. Any solvents used in the syntheses were either distilled to be anhydrous or purchased as anhydrous and kept under 3Å molecular sieves in round bottom flasks with Teflon caps. The reactions were monitored by glass-backed TLC plates coated with 250 mm silica gel. Ultraviolet light active compounds were visualized on the TLC plate using a 240 nm light. $KMnO_4$, ninhydrin stain, and curcumin stains were all used in conjunction with subsequent heating in order to identify the consumption and formation of compounds with specific functional groups. Unless otherwise noted, all reactions were either performed under inert Argon or $N_2$ gas atmosphere. Flash column chromatography was used in order to separate compounds. All columns were packed as a slurry using 60Å, 230-400 mesh silica gel.

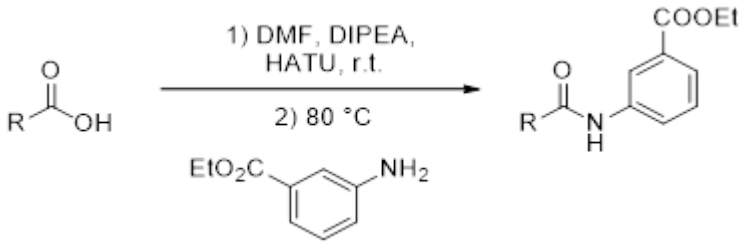


***General procedure for HATU mediated amidations:*** To a round bottom flask was added 1.0 eq. of carboxylic acid starting material, which was dissolved in dimethylformamide (~0.2M). Once dissolved, 1.0 eq. of HATU [(1-[Bis(dimethylamino)methylene]-1H-1,2,3-triazolo[4,5-b]pyridinium 3-oxide hexafluorophosphate] was transferred to the reaction flask and dissolved with continuous magnetic stirring. After the HATU was dissolved, the flask was capped with a rubber septum and purged with $N_2$ gas. 1.3 eq. of N,N-Diisopropylethylamine (DIPEA) was added via syringe, and the reaction solution was allowed to stir for 1.0 hours at room temperature under $N_2$ gas. After stirring at room temperature, 1.0 eq. of m-carboxyaniline was added to the flask, and the reaction mixture was heated to 80 °C for 3 hours under $N_2$. The flask was cooled to room temperature, then the contents were dissolved in ethyl acetate (~25 mL), washed with an aqueous 1N HCl solution (2 x 15 mL), aqueous 1N NaOH solution (2 x 15 mL), and then washed with DI $H_2O$ (5 x 15 mL). The organic layer was dried over anhydrous $MgSO_4$ and filtered through a fritted glass funnel. The filtered organic layer was concentrated under reduced pressure to afford a white/yellow solid. The solid was then further purified by flash column chromatography. The appropriate fractions were collected and concentrated under reduced pressure.

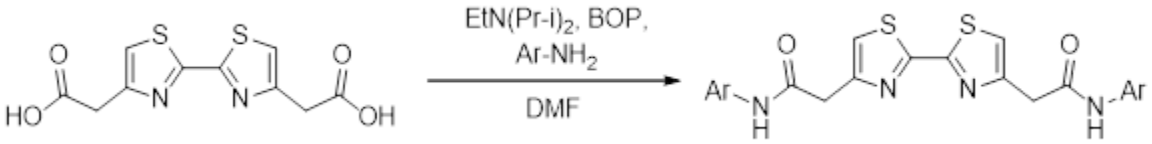


***General procedure for BOP mediated amidations:*** To a flask was added 1 eq. of bisthiazole, 2.4 eq. of substituted aniline, and 2.4 eq. BOP [benzotriazol-1-yloxytris(dimethylamino)phosphonium hexafluorophosphate)]. Dimethylformamide was then added to the mixture of reagents in the flask (~0.05M). The flask was capped with a rubber septum and purged with $N_2$ atmosphere. Once the solids were dissolved, 3 eq. of N,N-Diisopropylethylamine (DIPEA) were added via syringe. The reaction mixture was stirred for 14 hours under $N_2$ gas. After the 14-hour mark, a white precipitate was observed. The white solid was filtered out using vacuum filtration. The white solid was washed on the Hirsch funnel with ~25 mL of DI $H_2O$. The solids were transferred to small vials and triturated with dichloromethane until a fine suspension was achieved. The white suspension was then filtered on a Hirsch funnel to dry. Trace dichloromethane was removed by subjecting the solids to vacuum overnight.

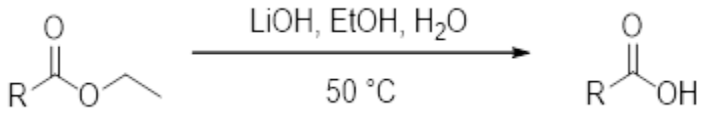


***General procedure for saponification of esters:*** 1 eq. of the ethyl ester was added to an appropriately sized round bottom flask and dissolved in ethanol (~0.1M). 2 eq. of lithium hydroxide. To increase the solubility of the LiOH, DI $H_2O$ was added to the ethanol so that the reaction mixture was 90 parts EtOH and 10 parts $H_2O$ (v:v). A Liebig condenser was attached to the round bottom flask joint and capped with a rubber septum. The apparatus was flushed with $N_2$ gas and heated to 50 °C for 3 hours, or until the reaction was observed to be complete by TLC. Once complete, the flask was cooled to room temperature, and the solvent was removed under reduced pressure and light heating in a water bath. The resulting solid or oil was taken up into ~20 mL of $H_2O$ and acidified to pH 2-3, where the free acid precipitated out of water. The solid was then filtered by vacuum filtration to afford the saponified product.

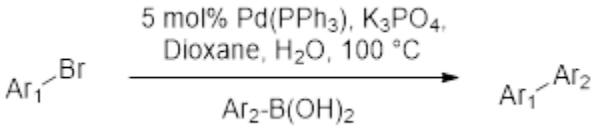


***General procedure for Pd catalyzed carbon-carbon coupling:*** To a round bottom flask was added 1 eq. aryl bromide material, 1.5 eq. of appropriate boronic acid, and 2 eq. of $K_3PO_4$. Dioxane was then added to the flask via syringe (~0.2M). DI $H_2O$ was added to the flask afterward so that the reaction mixture was 90 parts dioxane and 10 parts $H_2O$ (v:v). A Liebig condenser was placed on top of the round bottom flask and the top of the Liebig condenser was capped with a rubber septum. The reflux apparatus was purged with $N_2$ gas for ~3 minutes. Once purged, palladium triphenylphosphine was weighed out in the open air as quickly as possible and put into the flask. The apparatus was purged again with $N_2$ and then heated to 100 °C for a minimum duration of 15 hours. During the heating, the contents of the reaction apparatus were kept under static $N_2$. After 15 hours, the round bottom flask was allowed to cool to room temperature, and the dioxane solvent was removed by reduced pressure and a hot water bath. The crude organic matter was taken up into dichloromethane (~20 mL), washed with DI $H_2O$ (5 x 10 mL), an aqueous 1N solution of NaOH (~15 mL), and saturated brine solution (~10 mL). The organic layer was dried with anhydrous $MgSO_4$ and vacuum filtered through a sintered glass funnel. The organic layer was reduced under negative pressure to produce a black oil. The oil was then purified by flash column chromatography, and the appropriate fractions were collected.

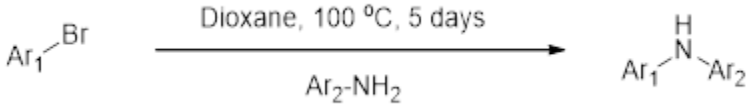


***General procedure for nucleophilic aromatic substitutions:*** To a round bottom flask was added 1 eq. of the aryl bromide starting material and 1 eq. of substituted aniline. The contents of the flask were then dissolved in dioxane (~0.2M). A Liebig condenser was attached to the round bottom in preparation for reflux. The top of the Liebig condenser was capped with a rubber septum and purged with $N_2$, and the reaction mixture was refluxed for 2 days under a static pressure of $N_2$ gas. After 48 hours, the starting material was observed to still be present. 3 more eq. of the substituted aniline was added to the reaction flask and refluxed for another 3 days under a static pressure of $N_2$ gas. Once the flask was cooled to room temperature, the contents were reduced under negative pressure and a heated water bath. The resulting oil was taken up in ~15 mL of dichloromethane, washed with DI $H_2O$ (5 x 15 mL), 15 mL of an aqueous solution of 1N HCl, and 15 mL of an aqueous 1N solution of NaOH. The solids obtained from the nucleophilic aromatic substitution were either triturated, recrystallized, or separated by column chromatography to produce solids.

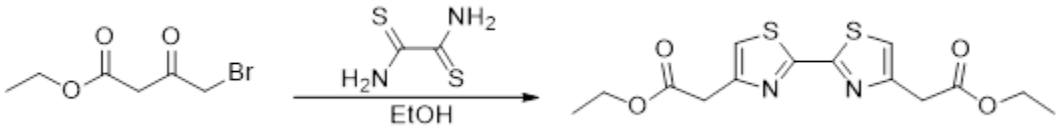


***General Procedure for the Hantzsch thiazole synthesis:*** To an appropriately sized round bottom flask were added 2.1 eq. of 4-bromo ethyl acetoacetate and 1.0 eq. of dithiooxamide. Ethanol was used to dissolve the contents of the flask (~0.30 M). A Liebig condenser was attached to the round bottom flask to construct a reflux apparatus. The top of the reflux condenser was capped with a rubber septum, and the apparatus was purged with $N_2$ gas. The reaction was refluxed at 80 °C for a minimum of 14 hours. After reflux, the round bottom flask was cooled to room temperature. The ethanol in the flask was reduced by negative pressure to yield a flaky yellow solid. The solid was taken up in ~25 mL dichloromethane. The organic layer was washed with 15 mL 1N aqueous solution HCl, and 15 mL 1N aqueous solution NaOH, and ~20 mL DI $H_2O$. The organic layer was then dried with $MgSO_4$ and vacuum filtered to produce a dark black liquid in dichloromethane. The dichloromethane was removed under reduced pressure to afford a brown/tan flaky solid. The brown/tan solid was then recrystallized in an EtOH/hexanes solvent system and vacuum filtered to afford thin golden-colored crystals.

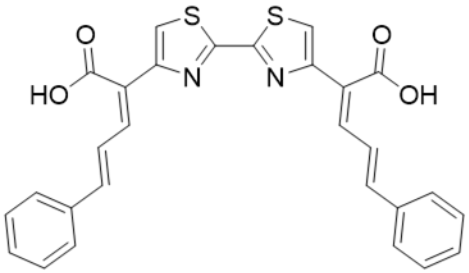


**SMI-8**

***(2Z/E,2'Z,4E,4'E)-2,2'-([2,2'-bithiazole]-4,4'-diyl)bis(5-phenylpenta-2,4-dienoic acid)***

Prepared according to the general saponification procedure to afford a bright yellow solid (54% yield). $^{1}$H NMR (600 MHz, DMSO) δ 13.09 (s, 2H), 8.12 (d, *J* = 12.3 Hz, 1H), 7.98 (d, *J* = 7.9 Hz, 1H), 7.92 – 7.76 (m, 1H), 7.77 – 7.60 (m, 3H), 7.57 (dd, *J* = 7.8, 5.7 Hz, 4H), 7.46 – 7.38 (m, 4H), 7.37 – 7.30 (m, 2H), 7.24 (dd, *J* = 15.5, 5.2 Hz, 1H), 7.18 (dd, *J* = 15.2, 6.5 Hz, 1H). $^{13}$C NMR (151 MHz, DMSO) δ 119.97, 120.09, 123.35, 123.50, 124.29, 124.41, 125.10, 125.36, 126.54, 126.68, 127.15, 127.41, 128.96, 129.02, 129.06, 129.25, 136.26, 136.39, 136.86, 136.98, 140.01, 141.14, 141.80, 150.42, 152.27, 158.93, 159.31, 159.79, 160.16, 167.59, 167.62, 167.73, 167.75. HPLC: $T_R$ = 4.352 min, peak area = 92.3%. MP: 266.5-270.8 °C. HRMS m/z: $[M + Na]^+$ Calcd. for $C_{28}H_{20}N_2O_4S_2$ 535.0757; Found 535.0759, Error 0.4 ppm.

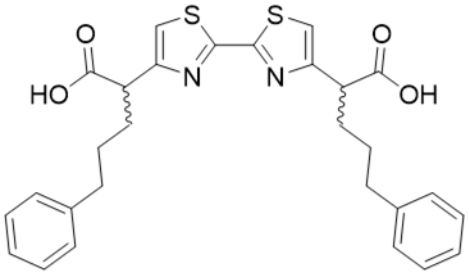


**SMI-8S**

***2,2'-([2,2'-bithiazole]-4,4'-diyl)bis(5-phenylpentanoic acid)***

Prepared to the general saponification procedure to afford a bright white solid (38% yield). $^{1}$H NMR (300 MHz, DMSO) δ 12.56 (s, 2H), 7.65 (s, 2H), 7.26 (t, *J* = 7.4 Hz, 4H), 7.16 (d, *J* = 7.2 Hz, 6H), 3.87 (t, *J* = 7.4 Hz, 2H), 2.60 (t, *J* = 7.6 Hz, 4H), 1.93 (ddt, *J* = 29.8, 14.2, 5.7 Hz, 4H), 1.73 – 1.39 (m, 4H).$^{13}$C NMR (75 MHz, DMSO) δ 29.23, 31.33, 35.18, 47.54, 118.85, 126.16, 128.72, 142.31, 156.01, 160.37, 173.92. HPLC: $T_R$ = 4.377 min, peak area = 98.1%. MP: 188.8-191.3 °C. HRMS m/z: $[M + H]^+$ Calcd. for $C_{28}H_{28}N_2O_4S_2$ 521.1563; Found 521.1556, Error -1.4 ppm.

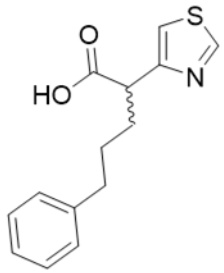


**SMI-8S3**

***5-phenyl-2-(thiazol-4-yl)pentanoic acid***

Prepared to the general saponification procedure to afford a bright white solid (58% yield). $^{1}$H NMR (600 MHz, $CDCl_3$) δ 12.07 (s, 1H), 8.85 (d, *J* = 2.0 Hz, 1H), 7.26 (t, *J* = 7.5 Hz, 2H), 7.22 – 7.10 (m, 4H), 4.01 (t, *J* = 7.5 Hz, 1H), 2.69 – 2.58 (m, 2H), 2.16 (dddd, *J* = 13.1, 10.4, 7.4, 5.5 Hz, 1H), 2.07 – 1.97 (m, 1H), 1.78 – 1.53 (m, 2H). $^{13}$C NMR (151 MHz, $CDCl_3$) δ 29.06, 32.04, 35.52, 47.55, 115.47, 125.89, 128.38, 128.42, 141.85, 153.45, 153.88, 176.97. HPLC: $T_R$ = 5.540 min, peak area = 47.6%. MP: 83.2-84.0 °C. HRMS m/z: $[M + H]^+$ Calcd. for $C_{14}H_{15}NO_2S$ 262.0896; Found 262.0899, Error 1.0 ppm.

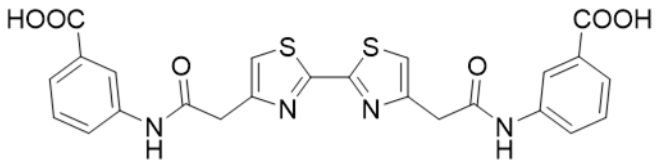


**SMI-8A4**

***3,3'-((2,2'-([2,2'-bithiazole]-4,4'-diyl)bis(acetyl))bis(azanediyl))dibenzoic acid***

Prepared to the general saponification procedure to afford a bright yellow solid (46% yield). $^{1}$H NMR (600 MHz, DMSO) δ 12.91 (s, 2H), 10.42 (s, 2H), 8.26 (s, 2H), 7.84 (d, *J* = 8.3 Hz, 2H), 7.68 (s, 2H), 7.63 (d, *J* = 7.7 Hz, 2H), 7.44 (t, *J* = 7.9 Hz, 2H), 3.93 (s, 4H). $^{13}$C NMR (151 MHz, DMSO) δ 119.35, 119.88, 123.21, 124.11, 128.99, 131.30, 139.22, 151.48, 159.85, 167.05, 167.72. HPLC: $T_R$ = 3.540 min, peak area = 96.7%. MP: >303.6 °C. HRMS m/z: $[M + Na]^+$ Calcd. for $C_{24}H_{18}N_4O_6S_2$ 545.0560; Found 545.0582, Error 4.0 ppm.

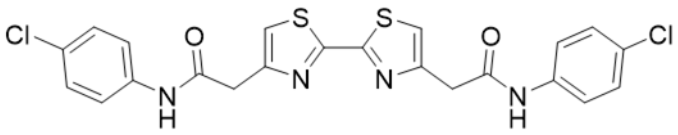

**SMI-8A4Cl**

***2,2'-([2,2'-bithiazole]-4,4'-diyl)bis(N-(4-chlorophenyl)acetamide)***

Prepared according to the general BOP mediated amidation procedure to afford a bright white solid (46% yield). $^{1}$H NMR (300 MHz, DMSO) δ 10.40 (s, 2H), 7.81 – 7.55 (m, 6H), 7.48 – 7.28 (m, 4H), 3.91 (s, 4H). $^{13}$C NMR (151 MHz, DMSO) δ 119.51, 120.69, 126.91, 128.73, 138.05, 151.53, 159.91, 167.71 . HPLC: $T_R$ = 4.002 min, peak area = 96.2%. MP: > 303.6 °C. HRMS m/z: $[M + H]^+$ Calcd. for $C_{22}H_{16}Cl_2N_4O_2S_2$ 503.0165; Found 503.0178, Error 2.6 ppm.

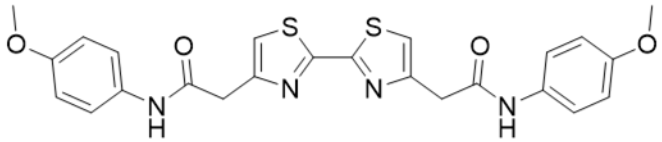

**SMI-8A4OMe**

***2,2'-([2,2'-bithiazole]-4,4'-diyl)bis(N-(4-methoxyphenyl)acetamide)***

Prepared according to the general BOP mediated amidation procedure to afford a bright white solid (44% yield). $^{1}$H NMR (600 MHz, DMSO) δ 10.07 (s, 2H), 7.65 (s, 2H), 7.55 – 7.49 (m, 4H), 6.91 – 6.85 (m, 4H), 3.86 (s, 4H), 3.72 (s, 6H). $^{13}$C NMR (75 MHz, DMSO) δ 55.61, 114.34, 119.70, 121.13, 132.70, 152.35, 155.71, 160.31, 167.41. HPLC: $T_R$ = 3.763 min, peak area = 97.6%. MP: > 303.6 °C. HRMS m/z: $[M + H]^+$ Calcd. for $C_{24}H_{22}N_4O_4S_2$ 495.115; Found 495.1178, Error 4.6 ppm.

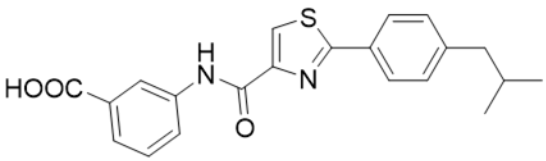


**SMI-8M1**

***3-(2-(4-isobutylphenyl)thiazole-4-carboxamido)benzoic acid***

Prepared to the general saponification procedure to afford a bright white solid (70% yield). $^{1}$H NMR (600 MHz, DMSO) δ 13.18 (s, 1H), 10.42 (s, 1H), 8.47 (d, *J* = 9.8 Hz, 2H), 8.12 – 8.05 (m, 3H), 7.71 (dt, *J* = 7.7, 1.3 Hz, 1H), 7.49 (t, *J* = 7.9 Hz, 1H), 7.37 – 7.33 (m, 2H), 2.54 (d, *J* = 7.2 Hz, 2H), 1.89 (dt, *J* = 13.5, 6.8 Hz, 1H), 0.89 (d, *J* = 6.6 Hz, 6H). $^{13}$C NMR (151 MHz, DMSO) δ 22.55, 30.05, 44.77, 121.80, 125.10, 125.19, 125.61, 127.01, 129.34, 130.18, 130.54, 131.71, 139.12, 144.89, 150.51, 159.70, 167.64, 167.95. HPLC: $T_R$ = 4..594 min, peak area = 98.6%. MP: 224.3-225.7 °C. HRMS m/z: $[M + H]^+$ Calcd. for $C_{21}H_{20}N_2O_3S$ 381.1267; Found 381.1254, Error -3.4 ppm.

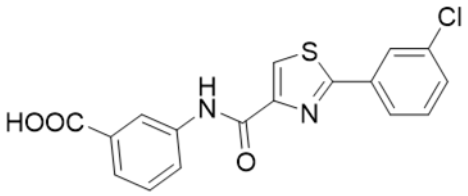


**SMI-8M2**

***3-(2-(3-chlorophenyl)thiazole-4-carboxamido)benzoic acid***

Prepared to the general saponification procedure to afford a bright white solid (53% yield). $^{1}$H NMR (600 MHz, DMSO) δ 13.02 (s, 1H), 10.49 (s, 1H), 8.55 (s, 1H), 8.50 (t, *J* = 1.9 Hz, 1H), 8.35 (t, *J* = 1.8 Hz, 1H), 8.16 – 8.11 (m, 1H), 8.07 (dt, *J* = 7.5, 1.5 Hz, 1H), 7.72 (dt, *J* = 7.8, 1.3 Hz, 1H), 7.64 – 7.56 (m, 2H), 7.51 (t, *J* = 7.9 Hz, 1H). $^{13}$C NMR (151 MHz, DMSO) δ 121.51, 124.74, 124.81, 125.49, 126.03, 126.33, 128.84, 130.54, 131.14, 131.40, 134.12, 134.24, 138.57, 150.22, 159.06, 165.56, 167.18. HPLC: $T_R$ = 4.151 min, peak area = 95.1%. MP: 269.5-272.3 °C. HRMS m/z: $[M + H]^+$ Calcd. for $C_{17}H_{11}ClN_2O_3S$ 359.0252; Found 359.0239, Error -3.5 ppm.

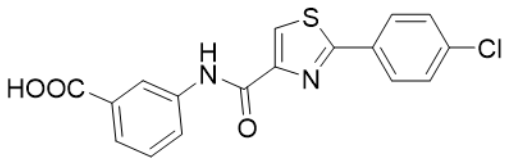


**SMI-8M3**

***3-(2-(4-chlorophenyl)thiazole-4-carboxamido)benzoic acid***

Prepared to the general saponification procedure to afford a bright white solid (81% yield). $^{1}$H NMR (300 MHz, DMSO) δ 12.98 (s, 1H), 10.47 (s, 1H), 8.52 (s, 1H), 8.49 (t, *J* = 1.9 Hz, 1H), 8.23 – 8.17 (m, 2H), 8.13 (ddd, *J* = 8.2, 2.3, 1.1 Hz, 1H), 7.72 (dt, *J* = 7.9, 1.3 Hz, 1H), 7.69 – 7.54 (m, 2H), 7.50 (t, *J* = 7.9 Hz, 1H). $^{13}$C NMR (151 MHz, DMSO) δ 121.44, 124.68, 124.83, 126.10, 128.48, 128.95, 129.33, 131.27, 131.39, 135.52, 138.67, 150.26, 159.16, 166.04, 167.27. HPLC: $T_R$ = 4.191 min, peak area = 90.6%. MP: 259.6-274.1 °C. HRMS m/z: $[M + H]^+$ Calcd. for $C_{17}H_{11}ClN_2O_3S$ 359.0252; Found 359.0247, Error -1.3 ppm.

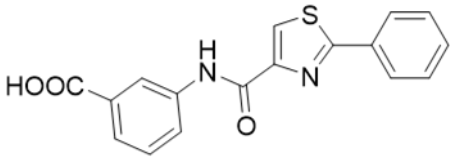


**SMI-8M4**

***3-(2-phenylthiazole-4-carboxamido)benzoic acid***

Prepared to the general saponification procedure to afford a bright white solid (76% yield). $^{1}$H NMR (600 MHz, DMSO) δ 12.61 (s, 1H), 10.45 (s, 2H), 8.51 (s, 2H), 8.25 – 8.14 (m, 2H), 8.15 – 8.04 (m, 1H), 7.72 (d, *J* = 7.7 Hz, 1H), 7.65 – 7.51 (m, 2H), 7.50 (t, *J* = 7.9 Hz, 1H). $^{13}$C NMR (151 MHz, DMSO) δ 121.48, 124.58, 124.85, 125.66, 126.77, 128.89, 129.30, 130.97, 131.81, 132.43, 138.65, 150.26, 159.27, 167.43, 167.70. HPLC: $T_R$ = 4.058 min, peak area = 96.9%. MP: 242.1-245.8 °C. HRMS m/z: $[M + H]^+$ Calcd. for $C_{17}H_{12}N_2O_3S$ 325.0641; Found 325.0630, Error -3.5 ppm.

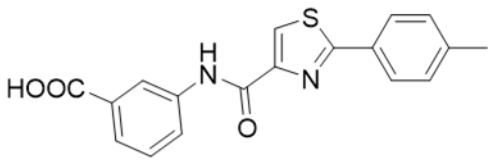


**SMI-8M5**

***3-(2-(p-tolyl)thiazole-4-carboxamido)benzoic acid***

Prepared to the general saponification procedure to afford a bright white solid (78% yield). $^{1}$H NMR (300 MHz, DMSO) δ 12.96 (s, 1H), 10.42 (s, 1H), 8.50 (t, *J* = 1.9 Hz, 1H), 8.46 (s, 1H), 8.13 (dt, *J* = 8.0, 1.6 Hz, 1H), 8.10 – 8.04 (m, 2H), 7.71 (dt, *J* = 7.7, 1.3 Hz, 1H), 7.50 (t, *J* = 7.9 Hz, 1H), 7.38 (d, *J* = 8.0 Hz, 2H), 2.39 (s, 3H). $^{13}$C NMR (151 MHz, DMSO) δ 21.08, 121.45, 124.63, 124.82, 125.15, 126.69, 128.90, 129.81, 129.84, 131.63, 138.69, 140.91, 150.12, 159.30, 167.55. HPLC: $T_R$ = 4.170 min, peak area = 99.2%. MP: 257.2-259.2 °C. HRMS m/z: $[M + H]^+$ Calcd. for $C_{18}H_{14}N_2O_3S$ 339.0798; Found 339.0783, Error -4.4 ppm.

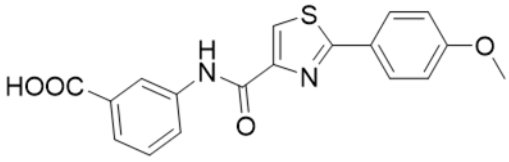


**SMI-8M7**

***3-(2-(4-methoxyphenyl)thiazole-4-carboxamido)benzoic acid***

Prepared to the general saponification procedure to afford a bright white solid (63% yield). $^{1}$H NMR (600 MHz, DMSO) δ 13.03 (s, 1H), 10.42 (s, 1H), 8.50 (d, *J* = 1.9 Hz, 1H), 8.41 (s, 1H), 8.12 (dd, *J* = 7.3, 5.0 Hz, 3H), 7.71 (d, *J* = 7.6 Hz, 1H), 7.50 (t, *J* = 7.9 Hz, 1H), 7.11 (d, *J* = 8.7 Hz, 2H), 3.85 (s, 3H). $^{13}$C NMR (151 MHz, DMSO) δ 55.50, 114.58, 121.40, 124.62, 124.71, 124.78, 125.22, 128.43, 128.94, 131.31, 138.73, 149.98, 159.34, 161.39, 167.25, 167.34. HPLC: $T_R$ = 4.076 min, peak area = 97.3%. MP: 267.8-269.0 °C. HRMS m/z: $[M + H]^+$ Calcd. for $C_{18}H_{14}N_2O_4S$ 355.0747 ; Found 355.0730, Error -4.8 ppm.

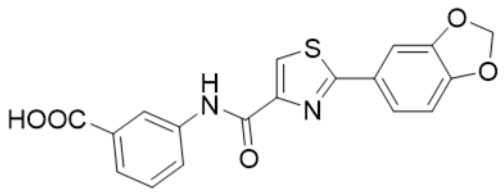


**SMI-8M8**

***3-(2-(benzo[d][1,3]dioxol-5-yl)thiazole-4-carboxamido)benzoic acid***

Prepared to the general saponification procedure to afford a bright white solid (75% yield). $^{1}$H NMR (600 MHz, DMSO) δ 13.03 (s, 1H), 10.41 (s, 1H), 8.49 (t, *J* = 2.0 Hz, 1H), 8.41 (s, 1H), 8.15 – 8.11 (m, 1H), 7.87 (d, *J* = 1.7 Hz, 1H), 7.71 (d, *J* = 7.7 Hz, 1H), 7.64 (dd, *J* = 8.2, 1.8 Hz, 1H), 7.51 (t, *J* = 7.9 Hz, 1H), 7.08 (d, *J* = 8.1 Hz, 1H), 6.15 (s, 2H). $^{13}$C NMR (151 MHz, DMSO) δ 101.92, 106.71, 108.82, 121.43, 121.62, 124.77, 124.82, 124.87, 126.81, 128.94, 128.96, 131.31, 138.70, 148.20, 149.57, 149.75, 159.23, 167.06, 167.25. HPLC: $T_R$ = 3.893 min, peak area = 96.9%. MP: 279.7-281.0 °C. HRMS m/z: $[M + H]^+$ Calcd. for $C_{18}H_{12}N_2O_5S$ 369.0540; Found 369.0533, Error -1.8 ppm.

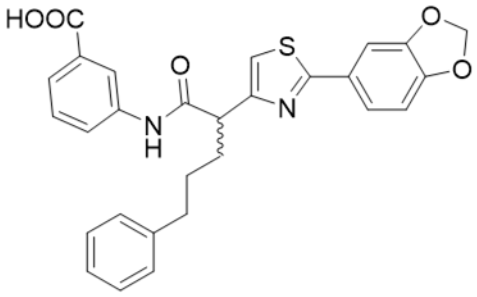


**SMI-8H1**

***3-(2-(2-(benzo[d][1,3]dioxol-5-yl)thiazol-4-yl)-5-phenylpentanamido)benzoic acid***

Prepared to the general saponification procedure to afford a bright white solid (61% yield).$^{1}$H NMR (600 MHz, DMSO) δ 12.99 (s, 1H), 10.45 (s, 1H), 8.30 (s, 1H), 7.84 (dd, *J* = 8.0, 2.1 Hz, 1H), 7.63 (d, *J* = 7.7 Hz, 1H), 7.42 (td, *J* = 7.8, 4.1 Hz, 4H), 7.25 (t, *J* = 7.5 Hz, 2H), 7.21 – 7.09 (m, 3H), 7.01 (d, *J* = 8.1 Hz, 1H), 6.10 (s, 2H), 4.03 (dd, *J* = 8.9, 6.1 Hz, 1H), 2.65 (td, *J* = 7.4, 4.0 Hz, 2H), 2.12 – 2.02 (m, 1H), 1.92 (dq, *J* = 13.8, 7.1 Hz, 1H), 1.62 (p, *J* = 7.6 Hz, 2H). $^{13}$C NMR (151 MHz, DMSO) δ 29.22, 31.58, 34.87, 49.09, 101.78, 105.92, 108.90, 114.79, 120.03, 120.71, 123.37, 124.24, 125.76, 127.44, 128.33, 129.10, 131.35, 139.30, 141.96, 148.07, 149.00, 155.62, 166.10, 167.18, 170.79. HPLC: $T_R$ = 3.880 min, peak area = 100.0%. MP: 206.5-208.4 °C. HRMS m/z: $[M + H]^+$ Calcd. for $C_{28}H_{24}N_2O_5S$ 501.1479; Found 504.1467, Error -2.3 ppm.

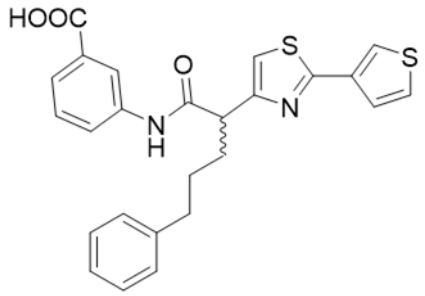


**SMI-8H2**

***3-(5-phenyl-2-(2-(thiophen-3-yl)thiazol-4-yl)pentanamido)benzoic acid***

Prepared to the general saponification procedure to afford a bright white solid (83% yield). $^{1}$H NMR (600 MHz, $CDCl_3$) δ 8.15 – 8.10 (m, 23H), 7.90 (dt, *J* = 2.8, 1.1 Hz, 10H), 7.78 (dt, *J* = 7.7, 1.3 Hz, 11H), 7.56 (dq, *J* = 5.2, 1.2 Hz, 11H), 7.50 – 7.35 (m, 22H), 7.25 – 7.22 (m, 19H), 7.20 – 7.10 (m, 44H), 4.26 – 3.64 (m, 12H), 3.07 – 2.46 (m, 24H), 2.26 (dddd, *J* = 12.9, 10.5, 7.2, 5.4 Hz, 11H), 2.03 (tq, *J* = 13.3, 6.3 Hz, 11H), 1.75 (dddd, *J* = 15.1, 11.1, 9.0, 5.8 Hz, 11H), 1.71 – 1.59 (m, 8H). $^{13}$C NMR (151 MHz, $CDCl_3$) δ 29.30, 33.27, 35.50, 50.11, 114.65, 121.11, 124.43, 124.71, 125.31, 125.79, 126.10, 127.18, 128.29, 128.37, 129.23, 130.31, 134.48, 138.68, 141.79, 154.65, 164.16, 170.24, 170.58. HPLC: $T_R$ = 3.898 min, peak area = 99.5%. MP: 82.0-83.9 °C. HRMS m/z: $[M + H]^+$ Calcd. for $C_{25}H_{22}N_2O_3S_2$ 463.1145; Found 463.1127, Error -3.8 ppm.

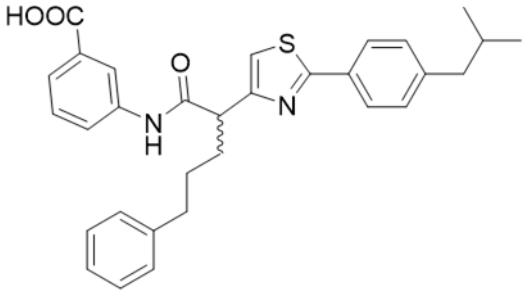


**SMI-8H3**

***3-(2-(2-(4-isobutylphenyl)thiazol-4-yl)-5-phenylpentanamido)benzoic acid***

Prepared to the general saponification procedure to afford a bright white solid (65% yield). $^{1}$H NMR (600 MHz, $CDCl_3$) δ 9.64 (s, 1H), 8.15 (s, 1H), 8.11 – 7.98 (m, 1H), 7.87 (d, *J* = 7.9 Hz, 2H), 7.81 – 7.72 (m, 1H), 7.41 (t, *J* = 7.9 Hz, 1H), 7.27 (s, 1H), 7.25 – 7.22 (m, 3H), 7.15 (dd, *J* = 9.1, 7.3 Hz, 3H), 7.10 (s, 1H), 3.91 (t, *J* = 7.6 Hz, 1H), 2.89 – 2.58 (m, 2H), 2.53 (d, *J* = 7.2 Hz, 2H), 2.41 – 2.17 (m, 1H), 2.07 (dtd, *J* = 15.5, 8.6, 5.1 Hz, 1H), 1.90 (dq, *J* = 13.5, 6.8 Hz, 1H), 1.83 – 1.48 (m, 2H), 0.92 (d, *J* = 6.6 Hz, 6H).

$^{13}$C NMR (151 MHz, $CDCl_3$) δ 22.30, 29.32, 30.13, 33.43, 35.50, 45.20, 50.53, 115.17, 121.12, 124.60, 125.37, 125.79, 126.42, 128.30, 128.38, 129.20, 129.85, 130.16, 130.34, 138.63, 141.82, 144.79, 154.56, 169.63, 170.64, 170.67. HPLC: $T_R$ = 4.709 min, peak area = 99.8%. MP: 175.6-176.5 °C. HRMS m/z: $[M + H]^+$ Calcd. for $C_{31}H_{32}N_2O_3S$ 513.2206; Found 513.2226, Error 3.8 ppm.

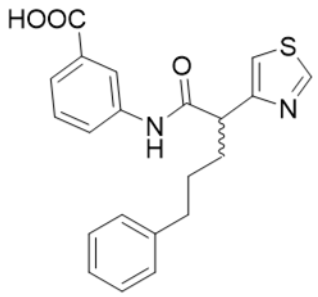


**SMI_8H4**

***3-(5-phenyl-2-(thiazol-4-yl)pentanamido)benzoic acid***

Prepared to the general saponification procedure to afford an off-white solid (84% yield). $^1$H NMR (300 MHz, DMSO) δ 12.97 (s, 1H), 10.41 (s, 1H), 9.04 (d, *J* = 2.0 Hz, 1H), 8.27 (t, *J* = 1.9 Hz, 1H), 7.83 (ddd, *J* = 8.1, 2.3, 1.1 Hz, 1H), 7.62 (dt, *J* = 7.8, 1.3 Hz, 1H), 7.50 (d, *J* = 2.0 Hz, 1H), 7.41 (t, *J* = 7.9 Hz, 1H), 7.34 – 7.21 (m, 2H), 7.20 – 6.99 (m, 3H), 4.06 (dd, *J* = 8.9, 6.1 Hz, 1H), 2.63 (t, *J* = 7.6 Hz, 2H), 1.97 (dtd, *J* = 50.5, 13.8, 7.5 Hz, 2H), 1.58 (p, *J* = 7.6 Hz, 2H). $^{13}$C NMR (75 MHz, DMSO) δ 29.15, 31.50, 34.84, 48.85, 114.98, 119.96, 123.29, 124.15, 125.73, 128.27, 128.30, 129.02, 131.32, 139.27, 141.92, 153.66, 155.65, 167.14, 170.82. HPLC: $T_R$ = 3.904 min, peak area = 97.2%. MP: 173.2-175.7 °C. HRMS m/z: $[M + H]^+$ Calcd. for $C_{21}H_{20}N_2O_3S$ 381.1267; Found 381.1269, Error 0.4 ppm.

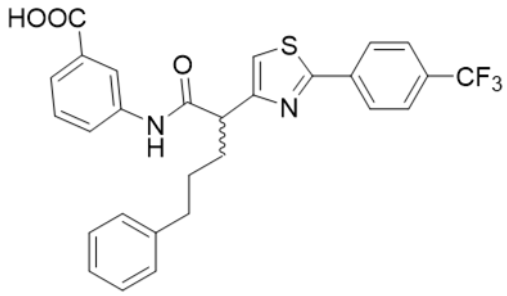


**SMI-8H5**

***3-(5-phenyl-2-(2-(4-(trifluoromethyl)phenyl)thiazol-4-yl)pentanamido)benzoic acid***

Prepared to the general saponification procedure to afford a bright white solid (61% yield). $^{1}$H NMR (600 MHz, DMSO) δ 13.00 (s, 1H), 10.50 (s, 1H), 8.31 (d, *J* = 1.9 Hz, 1H), 8.11 (d, *J* = 8.2 Hz, 2H), 7.88 – 7.83 (m, 4H), 7.76 – 7.55 (m, 2H), 7.43 (t, *J* = 7.9 Hz, 1H), 7.25 (t, *J* = 7.5 Hz, 2H), 7.20 – 6.96 (m, 4H), 4.11 (dd, *J* = 8.9, 6.2 Hz, 1H), 2.71 – 2.60 (m, 2H), 2.16 – 2.06 (m, 1H), 2.02 – 1.79 (m, 1H), 1.63 (p, *J* = 7.7 Hz, 2H). $^{13}$C NMR (151 MHz, DMSO) δ 29.20, 31.65, 34.86, 49.07, 117.29, 120.04, 123.14, 123.38, 124.28, 124.95, 125.77, 126.25, 126.27, 126.30, 126.32, 126.74, 128.32, 129.10, 129.57, 129.78, 130.00, 130.21, 131.35, 136.53, 139.26, 141.92, 156.52, 164.58, 167.16, 170.65. HPLC: $T_R$ = 4.062 min, peak area = 98.9%. MP: 143.4-145.2 °C. HRMS m/z: $[M + H]^+$ Calcd. for $C_{28}H_{23}F_3N_2O_3S$ 525.1454; Found 525.1428, Error -5.0 ppm.

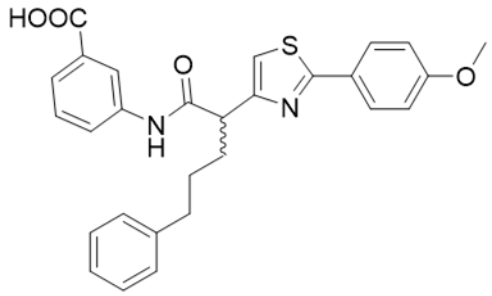


**SMI-8H6**

***3-(2-(2-(4-methoxyphenyl)thiazol-4-yl)-5-phenylpentanamido)benzoic acid***

Prepared to the general saponification procedure to afford an off-white solid (60% yield). $^{1}$H NMR (300 MHz, DMSO) δ 12.98 (s, 1H), 10.46 (s, 1H), 8.30 (t, *J* = 1.9 Hz, 1H), 7.84 (d, *J* = 8.8 Hz, 3H), 7.63 (dt, *J* = 7.8, 1.3 Hz, 1H), 7.54 – 7.33 (m, 2H), 7.25 (dd, *J* = 8.1, 6.7 Hz, 2H), 7.21 – 7.10 (m, 3H), 7.03 (d, *J* = 8.8 Hz, 2H), 4.05 (dd, *J* = 8.9, 6.0 Hz, 1H), 3.80 (s, 3H), 2.65 (dd, *J* = 8.7, 6.5 Hz, 2H), 2.07 (dt, *J* = 15.7, 8.1 Hz, 1H), 1.94 (dt, *J* = 13.7, 6.5 Hz, 1H), 1.62 (p, *J* = 7.6 Hz, 2H). $^{13}$C NMR (151 MHz, DMSO) δ 29.24, 31.58,

34.88, 49.11, 55.39, 114.42, 114.59, 120.01, 123.33, 124.22, 125.76, 125.90, 127.63, 128.33, 129.08, 131.41, 139.31, 141.97, 155.71, 160.81, 166.34, 167.21, 170.83. HPLC: $T_R$ = 4.027 min, peak area = 100.0%. MP: 174.9-176.8 °C. HRMS m/z: $[M + H]^+$ Calcd. for $C_{28}H_{26}N_2O_4S$ 487.1686; Found 487.1677, Error -1.9 ppm.

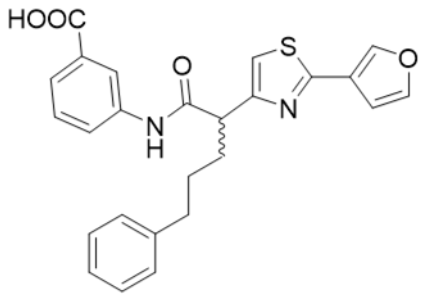


**SMI-8H7**

***3-(2-(2-(furan-3-yl)thiazol-4-yl)-5-phenylpentanamido)benzoic acid***

Prepared to the general saponification procedure to afford a slightly yellow-white solid (15% yield). $^1$H NMR (600 MHz, DMSO) δ 12.98 (s, 1H), 10.47 (s, 1H), 8.28 (t, *J* = 1.9 Hz, 1H), 7.86 (dd, *J* = 1.8, 0.8 Hz, 1H), 7.83 (ddd, *J* = 8.2, 2.3, 1.1 Hz, 1H), 7.62 (dt, *J* = 7.8, 1.3 Hz, 1H), 7.48 (s, 1H), 7.42 (t, *J* = 7.9 Hz, 1H), 7.25 (dd, *J* = 8.0, 7.1 Hz, 2H), 7.22 – 7.11 (m, 3H), 7.04 (dd, *J* = 3.5, 0.8 Hz, 1H), 6.68 (dd, *J* = 3.5, 1.8 Hz, 1H), 4.04 (dd, *J* = 9.0, 6.0 Hz, 1H), 2.64 (td, *J* = 7.3, 5.4 Hz, 2H), 2.14 – 1.98 (m, 1H), 1.99 – 1.81 (m, 1H), 1.60 (p, *J* = 7.6 Hz, 2H). $^{13}$C NMR (151 MHz, DMSO) δ 29.21, 31.63, 34.83, 48.97, 109.12, 112.62, 114.78, 119.96, 123.32, 124.23, 125.76, 128.31, 128.33, 129.10, 131.31, 139.25, 141.93, 144.76, 148.18, 155.95, 156.46, 167.13, 170.65. HPLC: $T_R$ = 4.433 min, peak area = 99.3%. MP: 90.0-93.2 °C. HRMS m/z: $[M + H]^+$ Calcd. for $C_{25}H_{22}N_2O_4S$ 447.1373; Found 447.1377, Error 0.9 ppm.

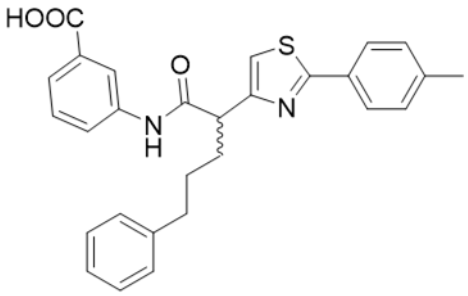


**SMI-8H8**

***3-(5-phenyl-2-(2-(p-tolyl)thiazol-4-yl)pentanamido)benzoic acid***

Prepared to the general saponification procedure to afford a bright white solid (57% yield). $^{1}$H NMR (600 MHz, $CDCl_3$) δ 9.66 (s, 1H), 8.15 (s, 1H), 8.06 – 8.04 (m, 1H), 7.84 (d, *J* = 8.1 Hz, 2H), 7.78 (dd, *J* = 7.7, 1.1 Hz, 1H), 7.40 (t, *J* = 7.9 Hz, 1H), 7.28 (d, *J* = 7.9 Hz, 2H), 7.26 – 7.22 (m, 2H), 7.19 – 7.12 (m, 3H), 7.11 (s, 1H), 4.28 – 3.86 (m, 1H), 2.82 – 2.54 (m, 2H), 2.40 (s, 3H), 2.37 – 2.21 (m, 1H), 2.06 (dddd, *J* = 13.4, 10.2, 8.3, 5.1 Hz, 1H), 1.83 – 1.56 (m, 2H). $^{13}$C NMR (151 MHz, $CDCl_3$) δ 21.44, 29.32, 33.40, 35.50, 50.51, 115.15, 121.09, 124.55, 125.35, 125.79, 126.54, 128.30, 128.38, 129.20, 129.81, 130.10, 130.14, 138.63, 140.98, 141.82, 154.59, 169.60, 170.64. HPLC: $T_R$ = 4.811 min, peak area = 100.0%. MP: 179.1-182.3 °C. HRMS m/z: $[M + H]^+$ Calcd. for $C_{28}H_{26}N_2O_3S$ 471.1737; Found 471.1719, Error -3.8 ppm.

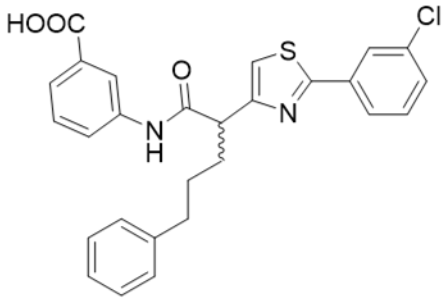


**SMI-8H9**

***3-(2-(2-(3-chlorophenyl)thiazol-4-yl)-5-phenylpentanamido)benzoic acid***

Prepared to the general saponification procedure to afford an off-white solid (50% yield). $^{1}$H NMR (600 MHz, $CDCl_3$) δ 11.92 (s, 1H), 9.39 (s, 1H), 8.12 (s, 1H), 8.08 – 8.01 (m, 1H), 7.96 (s, 1H), 7.93 – 7.70 (m, 2H), 7.48 – 7.36 (m, 3H), 7.26 – 7.23 (m, 2H), 7.19 (s, 1H), 7.18 – 7.12 (m, 3H), 3.98 – 3.92 (m, 1H), 2.73 – 2.62 (m, 2H), 2.32 – 2.24 (m, 1H), 2.11 – 2.02 (m, 1H), 1.83 – 1.71 (m, 1H), 1.70 – 1.62 (m, 1H). $^{13}$C NMR (75 MHz, DMSO) δ 29.14, 31.59, 34.82, 49.03, 116.66, 120.03, 123.35, 124.24, 124.82, 125.30,

125.74, 128.29, 129.06, 129.88, 131.25, 131.36, 133.96, 134.88, 139.23, 141.91, 156.15, 164.56, 167.13, 170.64. HPLC: $T_R$ = 4.274 min, peak area = 96.7%. HRMS m/z: [M + H]$^+$ Calcd. for $C_{27}H_{23}ClN_2O_3S$ 491.1191; Found 491.1183, Error -1.6 ppm.

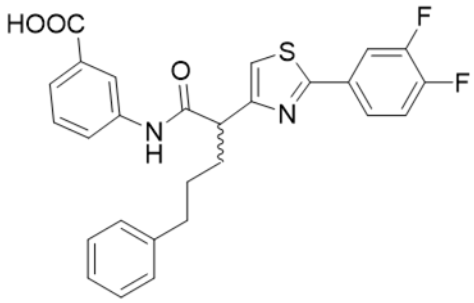


**SMI-8H10**

***3-(2-(2-(3,4-difluorophenyl)thiazol-4-yl)-5-phenylpentanamido)benzoic acid***

Prepared to the general saponification procedure to afford a bright white solid (67% yield). $^1$H NMR (600 MHz, DMSO) δ 13.26 – 12.57 (m, 1H), 10.46 (s, 1H), 8.29 (s, 1H), 8.02 – 7.88 (m, 1H), 7.84 (d, *J* = 8.1 Hz, 1H), 7.81 – 7.71 (m, 1H), 7.62 (d, *J* = 7.7 Hz, 1H), 7.56 (d, *J* = 13.7 Hz, 2H), 7.42 (t, *J* = 8.0 Hz, 1H), 7.25 (t, *J* = 7.5 Hz, 2H), 7.23 – 7.10 (m, 3H), 4.07 (t, *J* = 7.3 Hz, 1H), 2.66 (t, *J* = 5.8 Hz, 2H), 2.08 (dq, *J* = 15.5, 8.1 Hz, 1H), 1.94 (dq, *J* = 14.0, 7.0 Hz, 1H), 1.62 (p, *J* = 7.7 Hz, 2H). $^{13}$C NMR (151 MHz, DMSO) δ 29.18, 31.61, 34.85, 40.06, 49.02, 114.94, 115.06, 116.72, 118.54, 118.65, 120.04, 123.22, 123.26, 123.29, 123.33, 124.26, 125.77, 128.32, 129.07, 130.58, 130.62, 130.64, 131.44, 139.24, 141.93, 148.94, 149.02, 149.65, 149.73, 150.57, 150.66, 151.30, 151.39, 156.10, 163.95, 167.22, 170.65. HPLC: $T_R$ = 4.741 min, peak area = 100.0%. MP: 177.0-180.0 °C. HRMS m/z: [M + H]$^+$ Calcd. for $C_{27}H_{22}F_2N_2O_3S$ 493.1392; Found 493.1370, Error -4.5 ppm.

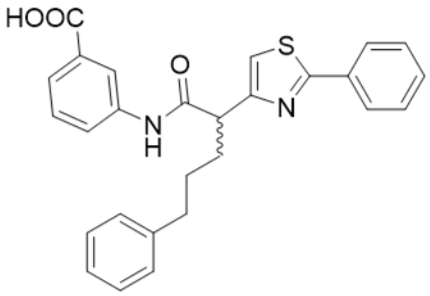


**SMI-8H11**

***3-(5-phenyl-2-(2-phenylthiazol-4-yl)pentanamido)benzoic acid***

Prepared to the general saponification procedure to afford a bright white solid (74% yield). $^{1}$H NMR (600 MHz, $CDCl_3$) δ 9.57 (s, 1H), 8.14 (t, *J* = 1.9 Hz, 1H), 8.02 (ddd, *J* = 8.3, 2.3, 1.1 Hz, 1H), 8.00 – 7.91 (m, 2H), 7.78 (dt, *J* = 7.7, 0.8 Hz, 1H), 7.56 – 7.44 (m, 3H), 7.41 (t, *J* = 7.9 Hz, 1H), 7.24 (d, *J* = 7.4 Hz, 2H), 7.19 – 7.06 (m, 4H), 4.16 – 3.69 (m, 1H), 2.89 – 2.52 (m, 2H), 2.48 – 2.17 (m, 1H), 2.21 – 1.96 (m, 1H), 1.92 – 1.53 (m, 2H). $^{13}$C NMR (151 MHz, $CDCl_3$) δ 29.32, 33.42, 35.49, 50.55, 115.68, 121.08, 124.62, 125.44, 125.81, 126.61, 128.31, 128.38, 129.14, 129.22, 130.13, 130.60, 132.74, 138.58, 141.80, 154.78, 169.39, 170.60, 170.65. HPLC: $T_R$ = 4.083 min, peak area = 99.7%. MP: 156.5-158.8 °C. HRMS m/z: $[M + H]^+$ Calcd. for $C_{27}H_{24}N_2O_3S$ 457.1580; Found 457.1576, Error -1.0 ppm.

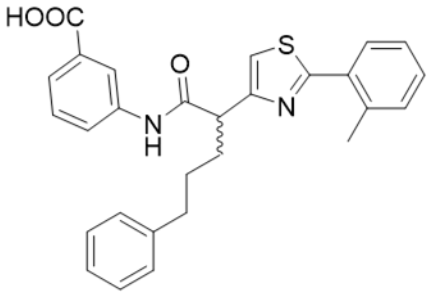


**SMI-8H12**

***3-(5-phenyl-2-(2-(o-tolyl)thiazol-4-yl)pentanamido)benzoic acid***

Prepared to the general saponification procedure to afford a bright white solid (62% yield). $^{1}$H NMR (300 MHz, $CDCl_3$) δ 9.50 (s, 1H), 8.41 – 7.96 (m, 2H), 7.96 – 7.59 (m, 2H), 7.46 – 7.27 (m, 5H), 7.26 – 7.10 (m, 5H), 4.10 (s, 1H), 2.88 – 2.59 (m, 2H), 2.56 (s, 3H), 2.44 – 2.21 (m, 1H), 2.15 – 1.99 (m, 1H), 1.86 – 1.60 (m, 2H). $^{13}$C NMR (151 MHz, DMSO) δ 21.16, 29.19, 31.35, 34.90, 49.04, 115.93, 120.03, 123.37, 124.19, 125.75, 126.41, 128.32, 129.06, 129.41, 129.53, 131.30, 131.61, 132.35, 135.83, 139.33, 141.96, 155.28, 166.06, 167.16, 170.79. HPLC: $T_R$ = 4.728 min, peak area = 100.0%. MP: 126.5-

130.1 °C. HRMS m/z: $[M + H]^+$ Calcd. for $C_{28}H_{26}N_2O_3S$ 471.1737; Found 471.1733, Error -0.8 ppm.

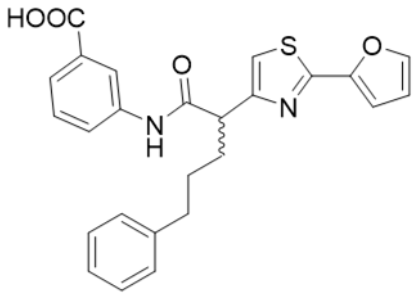


**SMI-8H13**

***3-(2-(2-(furan-2-yl)thiazol-4-yl)-5-phenylpentanamido)benzoic acid***

Prepared to the general saponification procedure to afford a bright white solid (99% yield). $^1$H NMR (300 MHz, $CDCl_3$) δ 9.55 (s, 1H), 8.21 (d, *J* = 8.6 Hz, 1H), 8.14 (t, *J* = 1.8 Hz, 1H), 8.02 – 7.68 (m, 1H), 7.70 – 7.47 (m, 1H), 7.41 (t, *J* = 7.9 Hz, 1H), 7.24 (d, *J* = 7.2 Hz, 1H), 7.21 – 7.13 (m, 4H), 7.10 (dd, *J* = 3.5, 0.7 Hz, 1H), 6.56 (dd, *J* = 3.5, 1.8 Hz, 1H), 4.07 (t, *J* = 7.6 Hz, 1H), 2.67 (q, *J* = 7.2 Hz, 2H), 2.25 (dt, *J* = 13.0, 6.0 Hz, 1H), 1.85 – 1.58 (m, 2H). $^{13}$C NMR (151 MHz, DMSO) δ 29.22, 31.64, 34.84, 48.98, 109.12, 112.62, 114.77, 119.98, 123.33, 124.25, 125.76, 128.31, 128.33, 129.10, 131.32, 139.26, 141.93, 144.75, 148.19, 155.96, 156.48, 167.15, 170.66. HPLC: $T_R$ = 3.914 min, peak area = 95.9%. MP: 91.0-94.2 °C. HRMS m/z: $[M + H]^+$ Calcd. for $C_{25}H_{22}N_2O_4S$ 447.1373; Found 447.1356, Error -3.8 ppm.

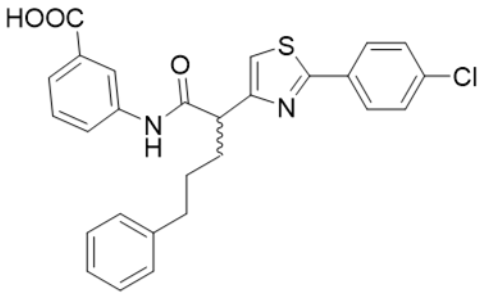


**SMI-8H14**

***3-(2-(2-(4-chlorophenyl)thiazol-4-yl)-5-phenylpentanamido)benzoic acid***

Prepared to the general saponification procedure to afford a white solid (56% yield). $^{1}$H NMR (600 MHz, $CDCl_3$) δ 11.70 (s, 1H), 9.40 (s, 1H), 8.11 (d, *J* = 2.0 Hz, 1H), 8.03 (d, *J* = 8.1 Hz, 1H), 7.88 (d, *J* = 8.4 Hz, 2H), 7.79 (dt, *J* = 7.8, 1.2 Hz, 1H), 7.45 (d, *J* = 8.5 Hz, 2H), 7.41 (t, *J* = 8.0 Hz, 1H), 7.24 (d, *J* = 7.5 Hz, 2H), 7.17 (s, 1H), 7.16 – 7.09 (m, 3H), 3.94 (t, *J* = 7.6 Hz, 1H), 3.03 – 2.50 (m, 2H), 2.33 – 2.22 (m, 1H), 2.06 (dddd, *J* = 13.5, 10.4, 8.3, 5.2 Hz, 1H), 1.81 – 1.61 (m, 2H). $^{13}$C NMR (151 MHz, DMSO) δ 29.50, 33.51, 35.68, 50.79, 116.18, 121.28, 124.86, 125.70, 126.04, 128.01, 128.53, 128.58, 129.49, 129.58, 130.23, 131.47, 136.79, 138.69, 141.95, 155.24, 168.20, 170.63, 170.76. HPLC: $T_R$ = 4.195 min, peak area = 89.2%. MP: 172.0-177.4 °C. HRMS m/z: $[M + H]^+$ Calcd. for $C_{27}H_{23}ClN_2O_3S$ 491.1191; Found 491.1176, Error -3.0 ppm.

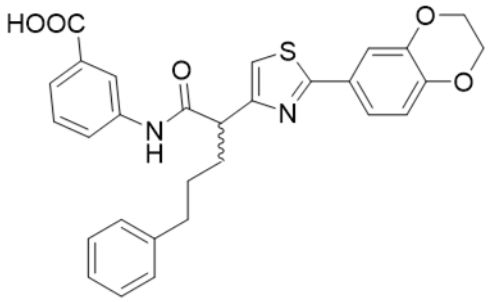


**SMI8H15**

***3-(2-(2-(2,3-dihydrobenzo[b][1,4]dioxin-6-yl)thiazol-4-yl)-5-phenylpentanamido)benzoic acid***

Prepared to the general saponification procedure to afford a bright white solid (79% yield). $^{1}$H NMR (600 MHz, $CDCl_3$) δ 12.72 (s, 1H), 9.76 (s, 1H), 8.19 (s, 1H), 8.04 (d, *J* = 8.0 Hz, 1H), 7.79 (d, *J* = 7.8 Hz, 1H), 7.52 (d, *J* = 2.2 Hz, 1H), 7.45 – 7.42 (m, 1H), 7.40 (t, *J* = 7.9 Hz, 1H), 7.24 (t, *J* = 7.6 Hz, 2H), 7.21 – 7.12 (m, 3H), 7.08 (s, 1H), 6.94

(d, *J* = 8.4 Hz, 1H), 4.30 (s, 4H), 3.93 (s, 1H), 3.05 – 2.51 (m, 2H), 2.52 – 2.16 (m, 1H), 2.05 (dddd, *J* = 13.4, 10.3, 8.3, 5.1 Hz, 1H), 1.96 – 1.51 (m, 2H). $^{13}$C NMR (151 MHz, $CDCl_3$) δ 29.30, 33.42, 35.48, 50.45, 64.28, 64.55, 114.91, 115.57, 117.92, 120.13, 121.07, 124.50, 125.32, 125.79, 126.28, 128.30, 128.37, 129.19, 130.15, 138.61, 141.81, 143.92, 145.90, 154.24, 169.03, 170.60, 170.86. HPLC: $T_R$ = 3.972 min, peak area = 99.2%. MP: 86.4-88.2 °C. HRMS m/z: $[M + H]^+$ Calcd. for $C_{29}H_{26}N_2O_5S$ 515.1635; Found 515.1629, Error -1.2 ppm.

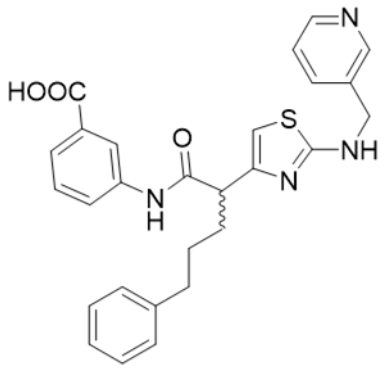


**SMI-8H16**

***3-(5-phenyl-2-(2-((pyridin-3-ylmethyl)amino)thiazol-4-yl)pentanamido)benzoic acid***

Prepared to the general saponification procedure to afford a yellow solid (47% yield). $^1$H NMR (300 MHz, DMSO) δ 10.16 (s, 1H), 8.56 (s, 1H), 8.44 (d, *J* = 4.3 Hz, 1H), 8.24 (s, 1H), 8.11 (s, 1H), 7.92 – 7.61 (m, 3H), 7.33 (s, 1H), 7.30 – 7.20 (m, 3H), 7.16 (d, *J* = 7.3 Hz, 3H), 6.36 (s, 1H), 4.42 (d, *J* = 5.8 Hz, 2H), 3.66 (dd, *J* = 8.7, 6.1 Hz, 1H), 2.60 (t, *J* = 7.6 Hz, 2H), 1.84 (ddd, *J* = 31.2, 13.3, 6.0 Hz, 2H), 1.56 (q, *J* = 7.6 Hz, 2H). $^{13}$C NMR (151 MHz, DMSO) δ 29.21, 30.89, 34.90, 45.32, 49.23, 101.38, 119.90, 123.24, 123.38, 124.04, 125.71, 128.30, 129.01, 131.29, 134.62, 135.45, 139.38, 142.02, 148.26, 149.10, 150.51, 167.19, 168.08, 170.95. HPLC: $T_R$ = 4.463 min, peak area = 65.8%. MP: 155.8-160.0 °C. HRMS m/z: $[M + H]^+$ Calcd. for $C_{27}H_{26}N_4O_3S$ 487.1798; Found 487.1798, Error 0.0 ppm.

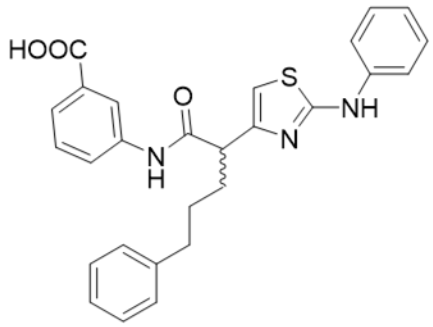


**SMI-H17**

***3-(5-phenyl-2-(2-(phenylamino)thiazol-4-yl)pentanamido)benzoic acid***

Prepared to the general saponification procedure to afford a yellow solid (57% yield). $^{1}$H NMR (600 MHz, DMSO) δ 10.31 (s, 1H), 10.17 (s, 1H), 8.22 (s, 1H), 7.82 (dt, *J* = 8.1, 1.6 Hz, 1H), 7.59 (t, *J* = 7.2 Hz, 3H), 7.37 (t, *J* = 7.9 Hz, 1H), 7.29 – 7.22 (m, 4H), 7.21 – 7.18 (m, 2H), 7.18 – 7.13 (m, 1H), 6.90 (t, *J* = 7.3 Hz, 1H), 6.60 (s, 1H), 3.81 (dd, *J* = 9.2, 5.8 Hz, 1H), 2.65 (td, *J* = 7.4, 3.9 Hz, 2H), 2.05 – 1.96 (m, 1H), 1.91 – 1.83 (m, 1H), 1.62 (p, *J* = 7.7 Hz, 2H). $^{13}$C NMR (151 MHz, DMSO) δ 29.18, 30.52, 34.89, 49.18, 102.90, 116.72, 119.96, 121.06, 123.29, 124.08, 125.74, 128.32, 128.89, 129.04, 131.30, 139.41, 141.23, 142.00, 150.64, 162.87, 167.18, 170.87. HPLC: $T_R$ = 3.999 min, peak area = 93.6%. MP: 222.2-225.6 °C. HRMS m/z: $[M + H]^+$ Calcd. for $C_{27}H_{25}N_3O_3S$ 472.1689; Found 472.1685, Error -0.9 ppm.

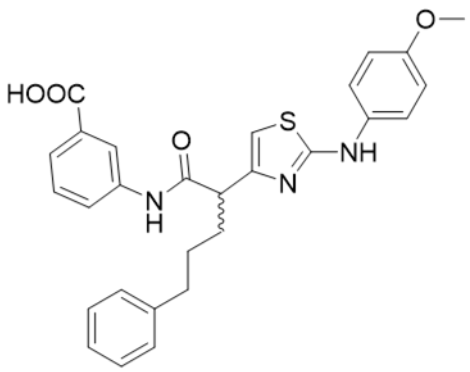


**SMI-8H18**

***3-(2-(2-((4-methoxyphenyl)amino)thiazol-4-yl)-5-phenylpentanamido)benzoic acid***

Prepared to the general saponification procedure to afford a bright white solid (47% yield). $^{1}$H NMR (600 MHz, DMSO) δ 13.04 (s, 1H), 10.32 (s, 1H), 9.94 (s, 1H), 8.26 (t, *J* = 2.0 Hz, 1H), 7.93 – 7.80 (m, 1H), 7.61 (dt, *J* = 7.7, 1.4 Hz, 1H), 7.52 – 7.46 (m, 2H),

7.40 (t, *J* = 7.9 Hz, 1H), 7.26 (t, *J* = 7.6 Hz, 2H), 7.23 – 7.18 (m, 2H), 7.18 – 7.13 (m, 1H), 6.84 – 6.78 (m, 2H), 6.53 – 6.50 (m, 1H), 3.77 (dd, *J* = 9.1, 5.8 Hz, 1H), 3.69 (s, 3H), 2.65 (td, *J* = 7.3, 4.4 Hz, 2H), 2.04 – 1.95 (m, 1H), 1.90 – 1.81 (m, 1H), 1.61 (p, *J* = 7.3 Hz, 2H). $^{13}$C NMR (151 MHz, DMSO) δ 29.20, 30.45, 34.91, 40.06, 49.20, 55.18, 102.05, 114.09, 118.60, 119.95, 123.21, 124.05, 125.73, 128.32, 129.00, 134.76, 139.43, 142.02, 150.59, 153.99, 163.62, 170.90. HPLC: $T_R$ = 4.074 min, peak area = 98.6%. MP: 258.0-259.8 °C. HRMS m/z: $[M + H]^+$ Calcd. for $C_{28}H_{27}N_3O_4S$ 502.1795; Found 502.1792, Error -0.6 ppm.

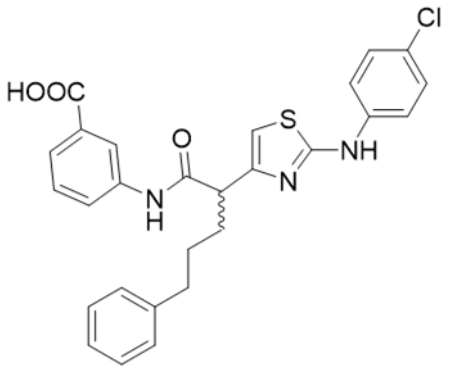


**SMI-8H19**

***3-(2-(2-((4-chlorophenyl)amino)thiazol-4-yl)-5-phenylpentanamido)benzoic acid***

Prepared to the general saponification procedure to afford a white solid (49% yield).$^1$H NMR (600 MHz, DMSO) δ 13.00 (s, 1H), 10.36 (s, 1H), 10.31 (s, 1H), 8.28 (d, *J* = 2.2 Hz, 1H), 8.00 – 7.77 (m, 1H), 7.78 – 7.55 (m, 3H), 7.43 (t, *J* = 7.9 Hz, 1H), 7.26 (dd, *J* = 8.2, 5.8 Hz, 4H), 7.22 – 7.18 (m, 2H), 7.17 – 7.13 (m, 1H), 6.65 (s, 1H), 3.81 (dd, *J* = 9.2, 5.8 Hz, 1H), 2.65 (q, *J* = 7.1 Hz, 2H), 2.17 – 1.95 (m, 1H), 1.94 – 1.79 (m, 1H), 1.62 (p, *J* = 7.7 Hz, 2H). $^{13}$C NMR (151 MHz, DMSO) δ 29.18, 30.52, 34.90, 49.17, 103.45, 118.16, 119.97, 123.32, 124.10, 124.32, 125.74, 128.32, 128.67, 129.06, 131.31, 139.41, 140.15, 142.00, 150.67, 162.49, 167.19, 170.82. HPLC: $T_R$ = 4.664 min, peak area = 98.1%. MP: 262.0-263.5 °C. HRMS m/z: $[M + H]^+$ Calcd. for $C_{27}H_{24}ClN_3O_3S$ 506.1300; Found 506.1286, Error -2.7 ppm.

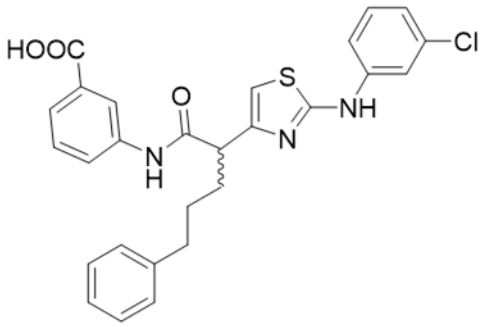


**SMI-8H20**

***3-(2-(2-((3-chlorophenyl)amino)thiazol-4-yl)-5-phenylpentanamido)benzoic acid***

Prepared to the general saponification procedure to afford a bright white solid (47% yield). $^{1}$H NMR (600 MHz, DMSO) δ 10.42 (s, 1H), 10.33 (s, 1H), 8.20 (s, 1H), 7.86 (s, 1H), 7.82 (d, *J* = 8.0 Hz, 1H), 7.59 (d, *J* = 7.6 Hz, 1H), 7.44 (dd, *J* = 8.3, 2.1 Hz, 1H), 7.34 (t, *J* = 7.9 Hz, 1H), 7.25 (dd, *J* = 8.9, 7.5 Hz, 3H), 7.21 – 7.11 (m, 2H), 7.17 – 7.05 (m, 1H), 6.93 (dd, *J* = 8.0, 2.0 Hz, 1H), 6.68 (s, 1H), 3.84 (dd, *J* = 9.1, 5.8 Hz, 1H), 3.44 (s, 1H), 2.66 (q, *J* = 7.2 Hz, 2H), 2.06 – 1.95 (m, 1H), 1.92 – 1.83 (m, 1H), 1.62 (p, *J* = 7.6 Hz, 2H). $^{13}$C NMR (75 MHz, DMSO) δ 29.12, 30.49, 34.88, 49.05, 103.77, 115.07, 116.01, 120.02, 120.51, 123.30, 124.08, 125.72, 128.29, 128.97, 130.41, 131.32, 133.39, 139.35, 141.96, 142.52, 150.75, 162.26, 167.17, 170.82. HPLC: $T_R$ = 3.957 min, peak area = 97.9%. MP: 258.9-259.7 °C. HRMS m/z: $[M + H]^+$ Calcd. for $C_{27}H_{24}ClN_3O_3S$ 506.1300; Found 506.1289, Error -2.1 ppm.

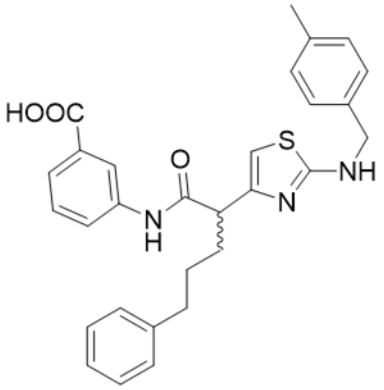


**SMI-8H21**

***3-(5-phenyl-2-(2-(p-tolylamino)thiazol-4-yl)pentanamido)benzoic acid***

Prepared to the general saponification procedure to afford an off-white solid (60% yield).$^{1}$H NMR (600 MHz, DMSO) δ 10.18 (s, 1H), 8.18 (s, 1H), 8.04 (t, *J* = 5.9 Hz, 1H), 7.74 (dd, *J* = 8.0, 2.2 Hz, 1H), 7.59 (d, *J* = 7.6 Hz, 1H), 7.33 (t, *J* = 7.9 Hz, 1H), 7.26 (t, *J* = 7.5 Hz, 2H), 7.21 (d, *J* = 7.8 Hz, 2H), 7.19 – 7.13 (m, 3H), 7.05 (d, *J* = 7.7 Hz, 2H), 6.32 (s, 1H), 4.32 (dd, *J* = 6.0, 2.8 Hz, 2H), 3.66 (dd, *J* = 9.0, 6.0 Hz, 1H), 2.61 (td, *J* = 7.5, 3.9 Hz, 2H), 2.24 (s, 3H), 1.92 (dtd, *J* = 13.2, 8.8, 6.4 Hz, 1H), 1.83 – 1.74 (m, 1H), 1.56 (p, *J* = 7.1 Hz, 2H). $^{13}$C NMR (151 MHz, DMSO) δ 20.70, 29.22, 30.86, 34.90, 47.59, 49.27, 100.90, 119.89, 119.96, 123.16, 124.01, 125.71, 127.61, 128.30, 128.79, 128.97, 131.43, 135.98, 136.03, 139.39, 142.04, 150.49, 167.22, 168.39, 170.98. HPLC: $T_R$ = 4.422 min, peak area = 42.2%. MP: 160.9-163.0 °C. HRMS m/z: $[M + H]^+$ Calcd. for $C_{29}H_{29}N_3O_3S$ 500.2002; Found 2009, Error 1.3 ppm.

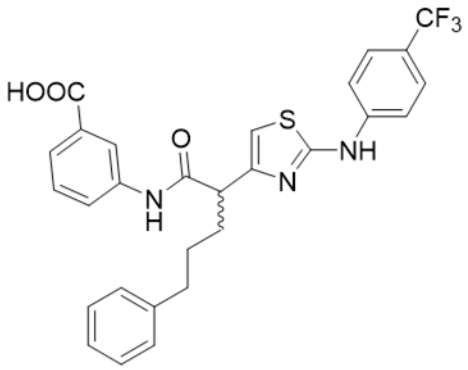


**SMI-8H22**

***3-(5-phenyl-2-(2-((4-(trifluoromethyl)phenyl)amino)thiazol-4-yl)pentanamido)benzoic acid***

Prepared to the general saponification procedure to afford a yellow solid (38% yield). $^{1}$H NMR (300 MHz, DMSO) δ 10.60 (s, 1H), 10.40 (s, 1H), 8.32 (s, 1H), 7.83 (t, *J* = 8.4 Hz, 3H), 7.69 (d, *J* = 8.7 Hz, 2H), 7.63 (d, *J* = 7.7 Hz, 1H), 7.43 (t, *J* = 7.9 Hz, 1H), 7.23 (dq, *J* = 16.1, 7.9 Hz, 5H), 6.74 (s, 1H), 3.86 (t, *J* = 7.4 Hz, 1H), 2.67 (t, *J* = 7.5 Hz, 2H), 2.26 – 1.79 (m, 2H), 1.69 – 1.58 (m, 2H). $^{13}$C NMR (75 MHz, DMSO) δ 29.15, 30.64, 34.89, 49.09, 104.36, 115.77, 119.98, 122.66, 123.26, 124.12, 125.73, 128.31, 128.33, 129.00, 130.68, 131.42, 139.40, 142.00, 145.01, 150.82, 162.01, 167.08, 170.83. HPLC: $T_R$ = 4.216 min, peak area = 74.1%. MP: 231.2-237.2 °C. HRMS m/z: $[M + Na]^+$ Calcd. for $C_{28}H_{24}F_3N_3O_3S$ 562.1383; Found 532.1368, Error -2.6 ppm.

## Materials And Methods References

1. Charlier, H. A., Jr.; Plapp, B. V., Kinetic cooperativity of human liver alcohol dehydrogenase gamma(2). *J Biol Chem* **2000,** *275* (16), 11569-75.
2. Motulsky, H. *Analyzing Data with GraphPad Prism*; 1999.
3. Pettersen, E. F.; Goddard, T. D.; Huang, C. C.; Couch, G. S.; Greenblatt, D. M.; Meng, E. C.; Ferrin, T. E., UCSF Chimera--a visualization system for exploratory research and analysis. *J Comput Chem* **2004,** *25* (13), 1605-12.
4. Maier, J. A.; Martinez, C.; Kasavajhala, K.; Wickstrom, L.; Hauser, K. E.; Simmerling, C., ff14SB: improving the accuracy of protein side chain and backbone parameters from ff99SB. *Journal of chemical theory and computation* **2015,** *11* (8), 3696-3713.

# APPENDIX B

## $^{1}$H spectra, $^{13}$C spectra, and HPLC Chromatograms

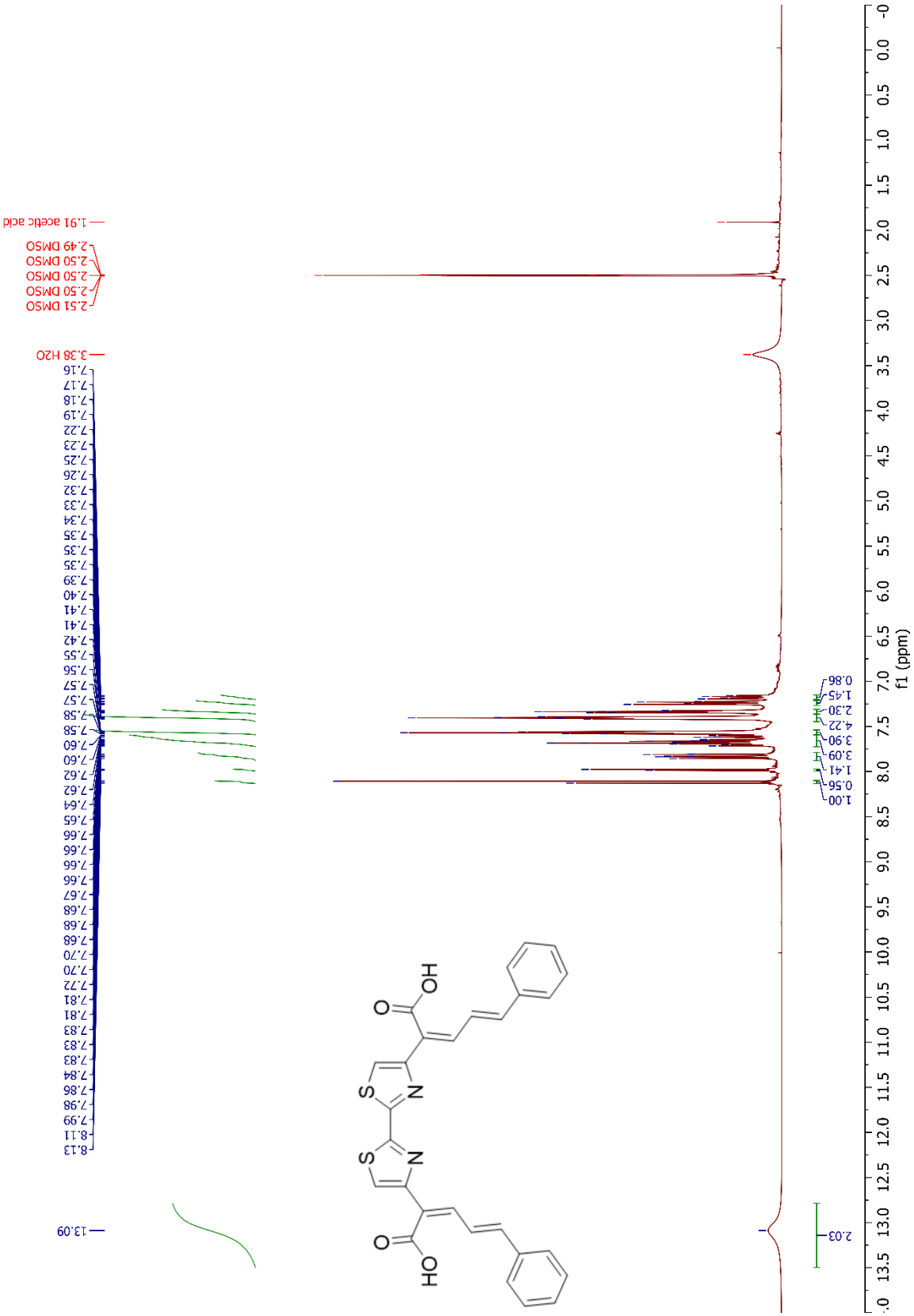
1.91 acetic acid
2.49 DMSO
2.50 DMSO
2.50 DMSO
2.50 DMSO
2.51 DMSO
3.38 H2O
7.16
7.17
7.18
7.19
7.22
7.23
7.25
7.26
7.32
7.33
7.34
7.35
7.35
7.35
7.39
7.40
7.41
7.41
7.42
7.55
7.56
7.57
7.57
7.58
7.58
7.60
7.60
7.62
7.62
7.64
7.65
7.66
7.66
7.66
7.66
7.67
7.68
7.68
7.68
7.70
7.70
7.72
7.81
7.81
7.83
7.83
7.83
7.84
7.86
7.98
7.99
8.11
8.13
13.09
1.00
0.56
1.41
3.09
3.90
4.22
2.30
1.45
0.86
2.03
HO
O
S
N
S
N
O
HO
f1 (ppm)

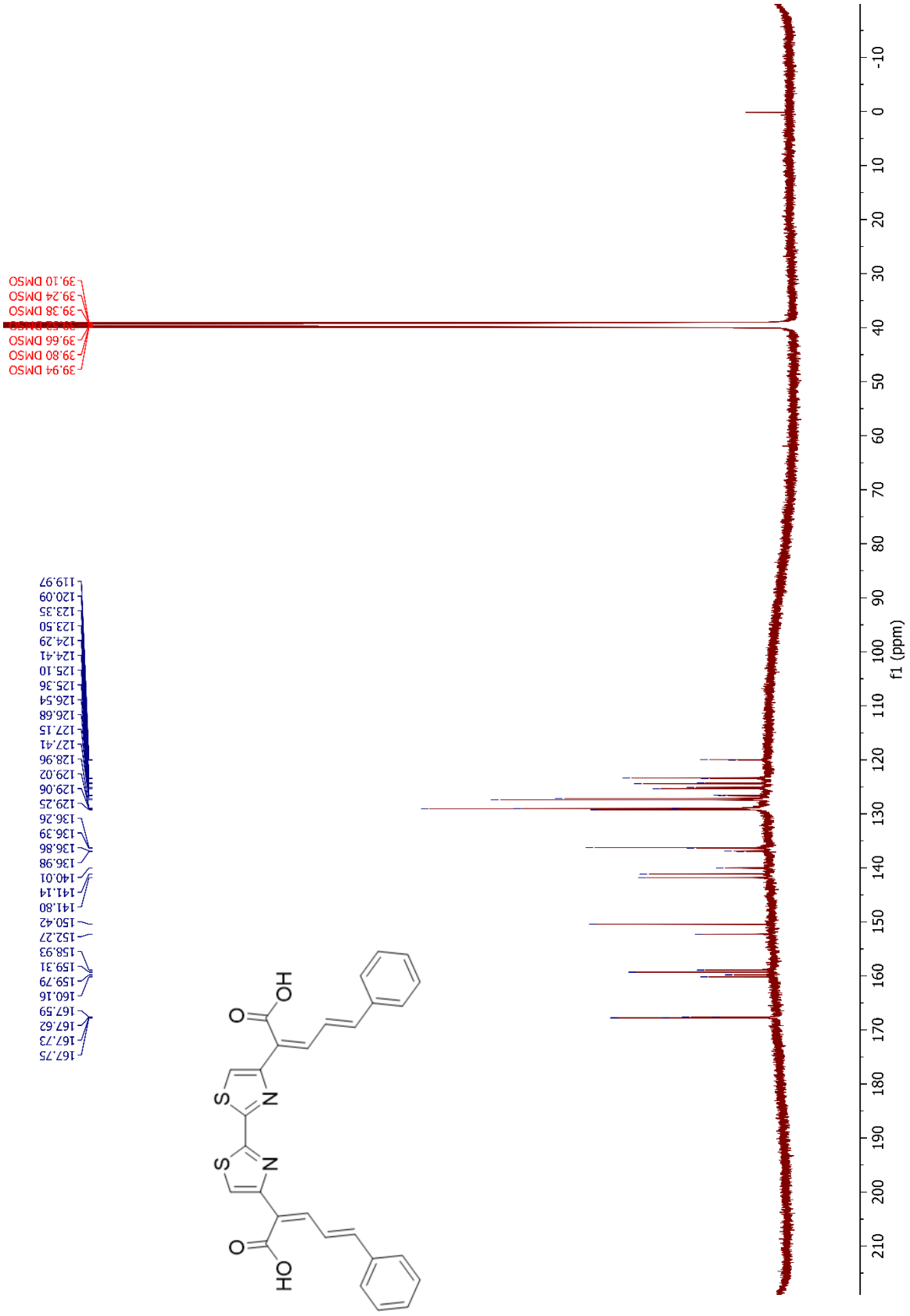
39.94 DMSO
39.80 DMSO
39.66 DMSO
39.38 DMSO
39.24 DMSO
39.10 DMSO
119.97
120.09
123.35
123.50
124.29
124.41
125.10
125.36
126.54
126.68
127.15
127.41
128.96
129.02
129.06
129.25
136.26
136.39
136.86
136.98
140.01
141.14
141.80
150.42
152.27
158.93
159.31
159.79
160.16
167.59
167.62
167.73
167.75
HO
O
S
N
S
N
O
HO
f1 (ppm)

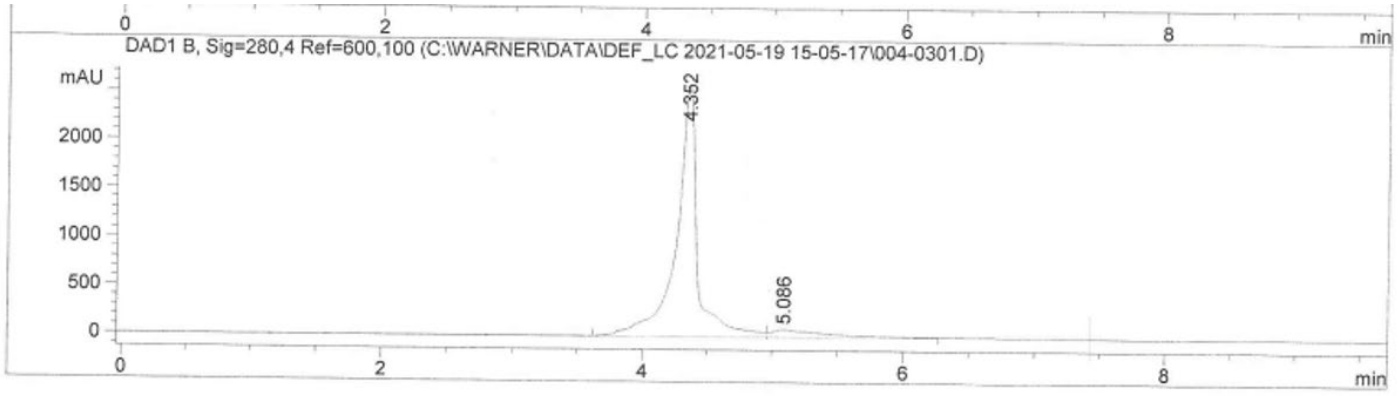


Signal 2: DAD1 B, Sig=280,4 Ref=600,100

| Peak # | RetTime [min] | Type | Width [min] | Area [mAU*s] | Height [mAU] | Area % |
|---|---|---|---|---|---|---|
| 1 | 4.352 | BV | 0.1591 | 2.96189e4 | 2595.85938 | 92.3015 |
| 2 | 5.086 | VV | 0.3877 | 2470.39990 | 80.57047 | 7.6985 |
| Totals : | | | | 3.20893e4 | 2676.42984 | |

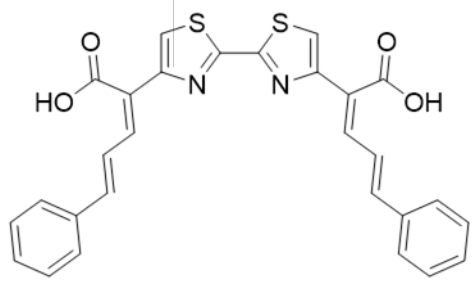

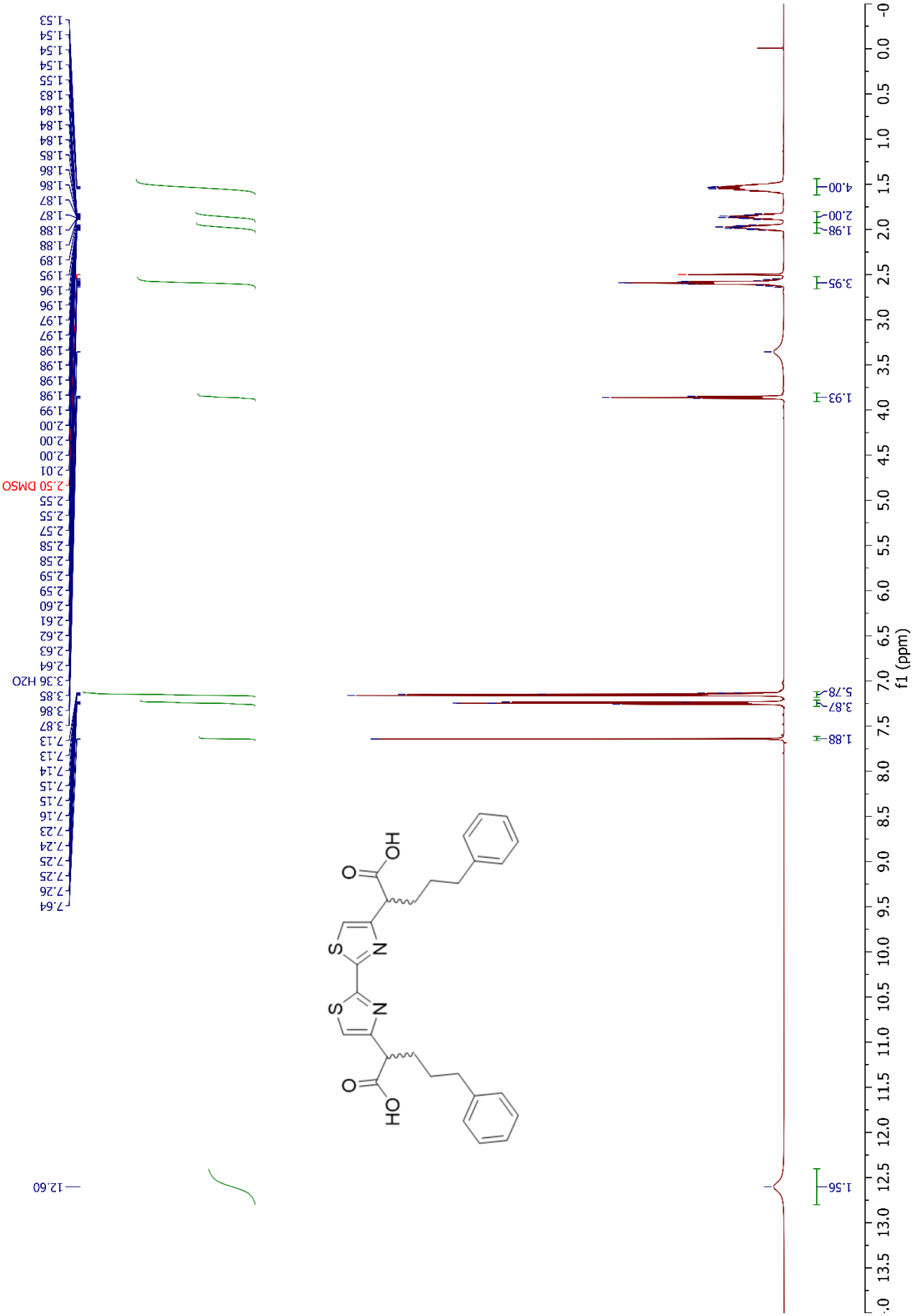
12.60
7.64
7.26
7.25
7.25
7.24
7.23
7.16
7.15
7.15
7.14
7.13
7.13
3.87
3.86
3.85
3.36 H2O
2.64
2.63
2.62
2.61
2.60
2.59
2.59
2.58
2.58
2.57
2.55
2.55
2.50 DMSO
2.01
2.00
2.00
2.00
1.99
1.98
1.98
1.98
1.97
1.97
1.96
1.96
1.95
1.89
1.88
1.88
1.87
1.87
1.86
1.86
1.85
1.84
1.84
1.84
1.83
1.55
1.54
1.54
1.54
1.53
OH
O
S
N
S
N
O
HO
1.56
1.88
3.87
5.78
1.93
3.95
1.98
2.00
4.00
f1 (ppm)

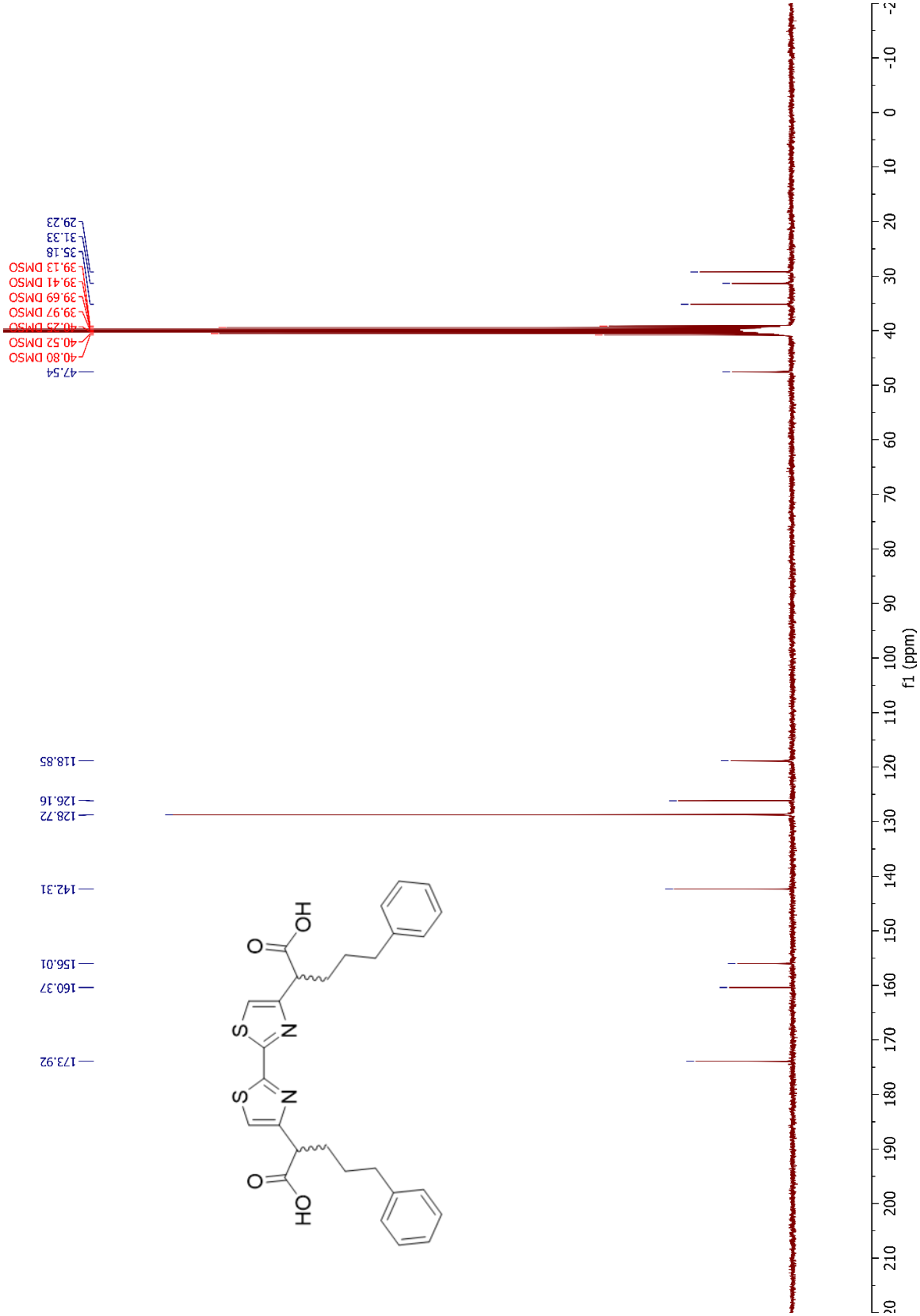
173.92
160.37
156.01
142.31
128.72
126.16
118.85
47.54
40.80 DMSO
40.52 DMSO
40.25 DMSO
39.97 DMSO
39.69 DMSO
39.41 DMSO
39.13 DMSO
35.18
31.33
29.23
f1 (ppm)

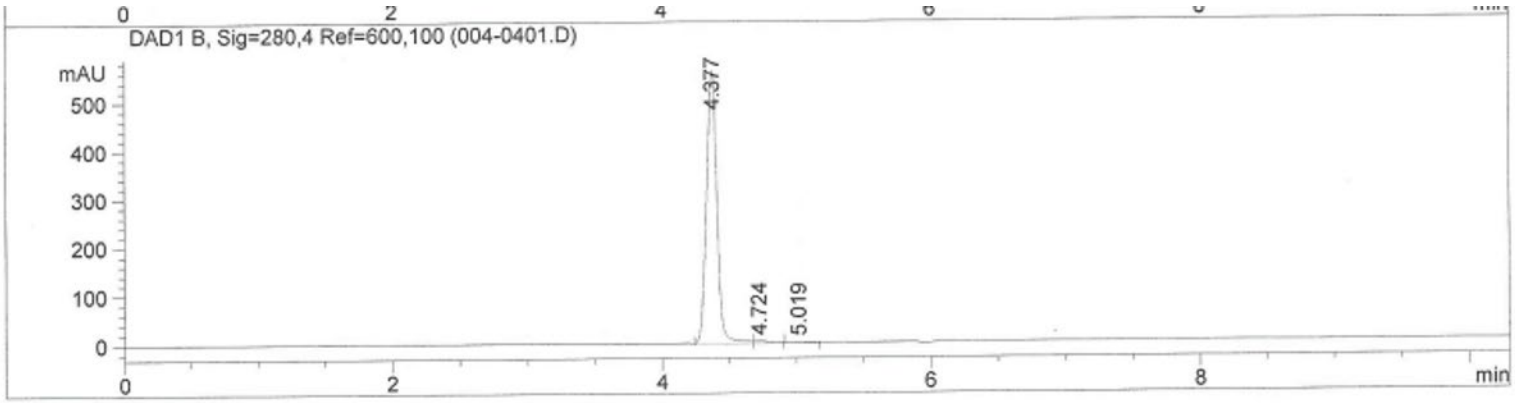


Signal 2: DAD1 B, Sig=280,4 Ref=600,100

| Peak # | RetTime [min] | Type | Width [min] | Area [mAU*s] | Height [mAU] | Area % |
|---|---|---|---|---|---|---|
| 1 | 4.377 | BV | 0.0827 | 3036.11963 | 564.82996 | 98.1445 |
| 2 | 4.724 | VB | 0.1270 | 39.43226 | 4.30029 | 1.2747 |
| 3 | 5.019 | BB | 0.1521 | 17.96833 | 1.61183 | 0.5808 |
| Totals : | | | | 3093.52022 | 570.74208 | |

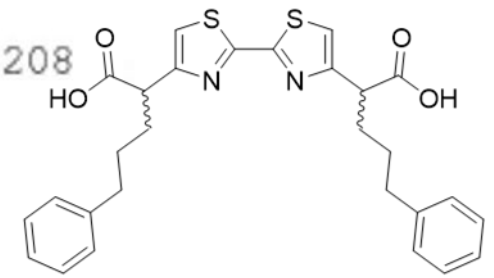

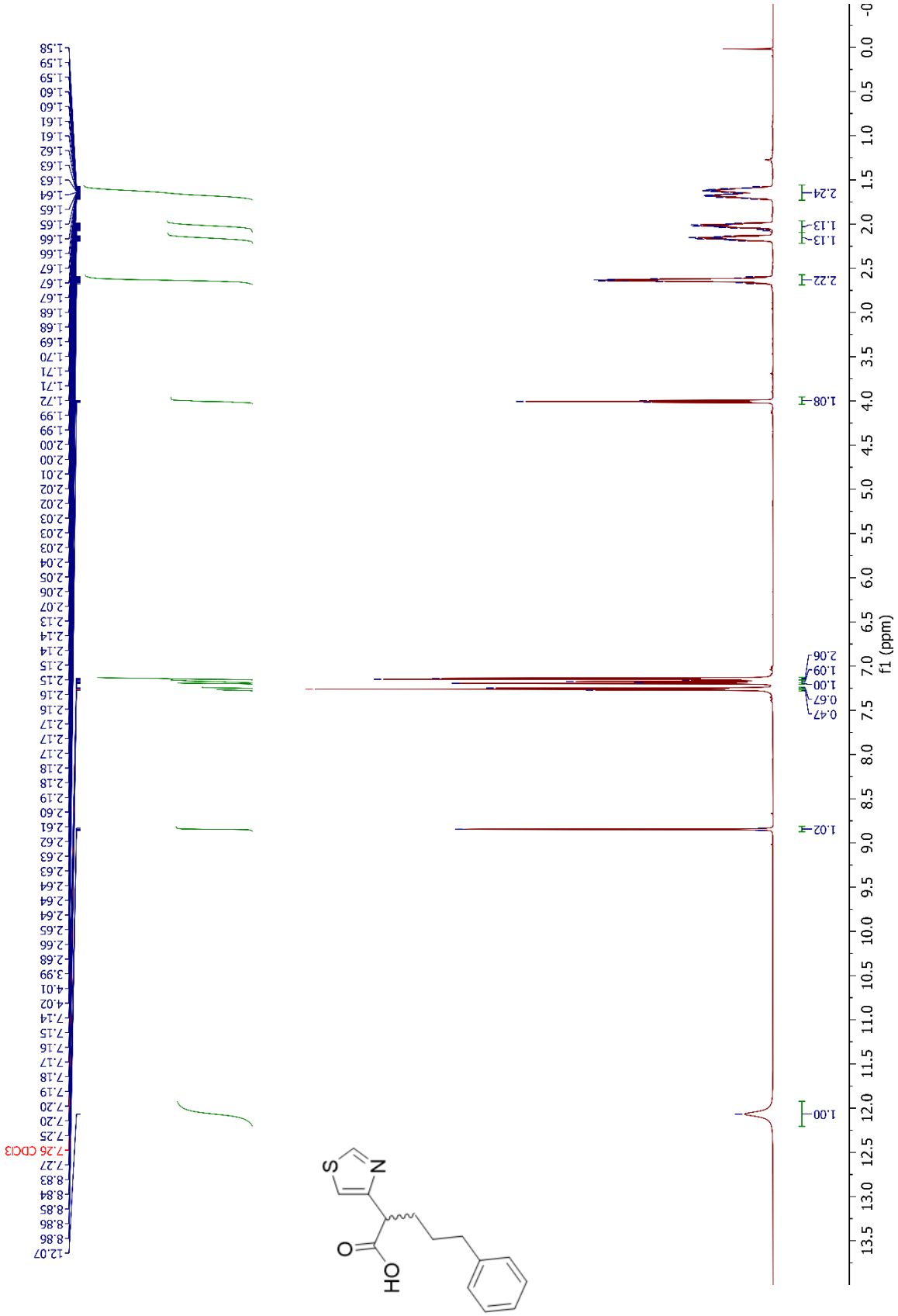
f1 (ppm)
7.26 CDCl3
1.00
1.02
0.47
0.67
1.00
1.09
2.06
1.08
2.22
1.13
1.13
2.24
S
N
O
OH

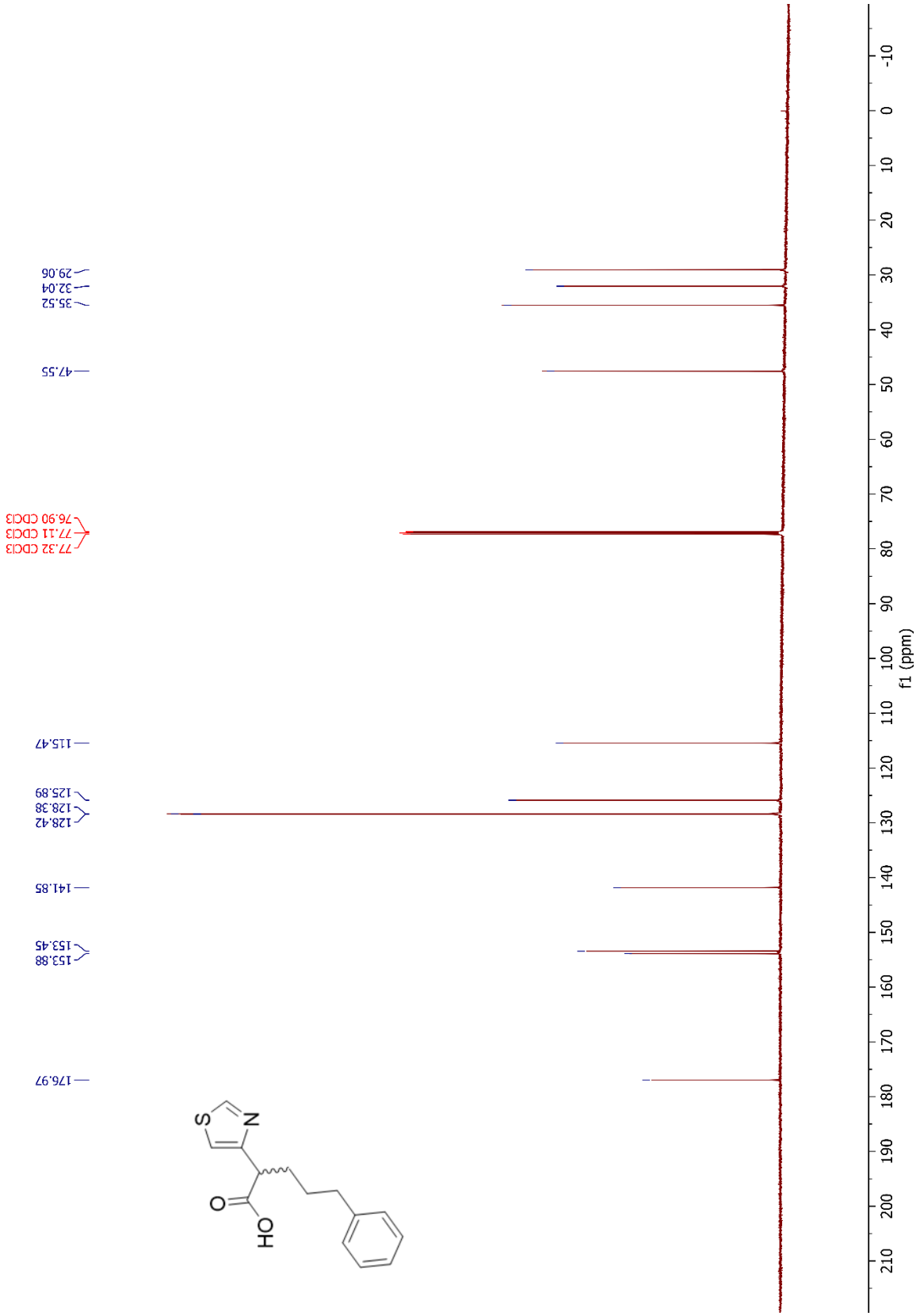
176.97
153.88
153.45
141.85
128.42
128.38
125.89
115.47
77.32 CDCl3
77.11 CDCl3
76.90 CDCl3
47.55
35.52
32.04
29.06
S
N
O
OH
f1 (ppm)

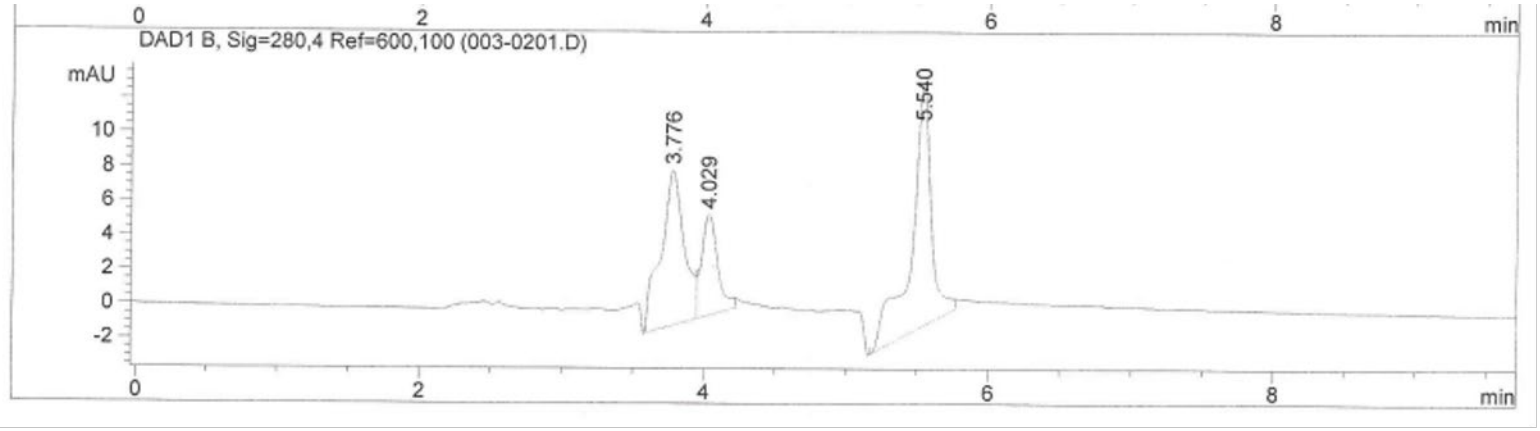


Signal 2: DAD1 B, Sig=280,4 Ref=600,100

| Peak # | RetTime [min] | Type | Width [min] | Area [mAU*s] | Height [mAU] | Area % |
|---|---|---|---|---|---|---|
| 1 | 3.776 | BV | 0.1607 | 102.97849 | 9.05617 | 35.9274 |
| 2 | 4.029 | VB | 0.1218 | 47.29840 | 5.88536 | 16.5016 |
| 3 | 5.540 | BB | 0.1332 | 136.35231 | 14.30476 | 47.5710 |

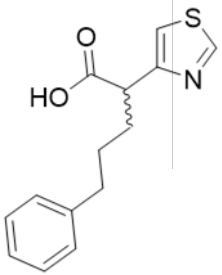

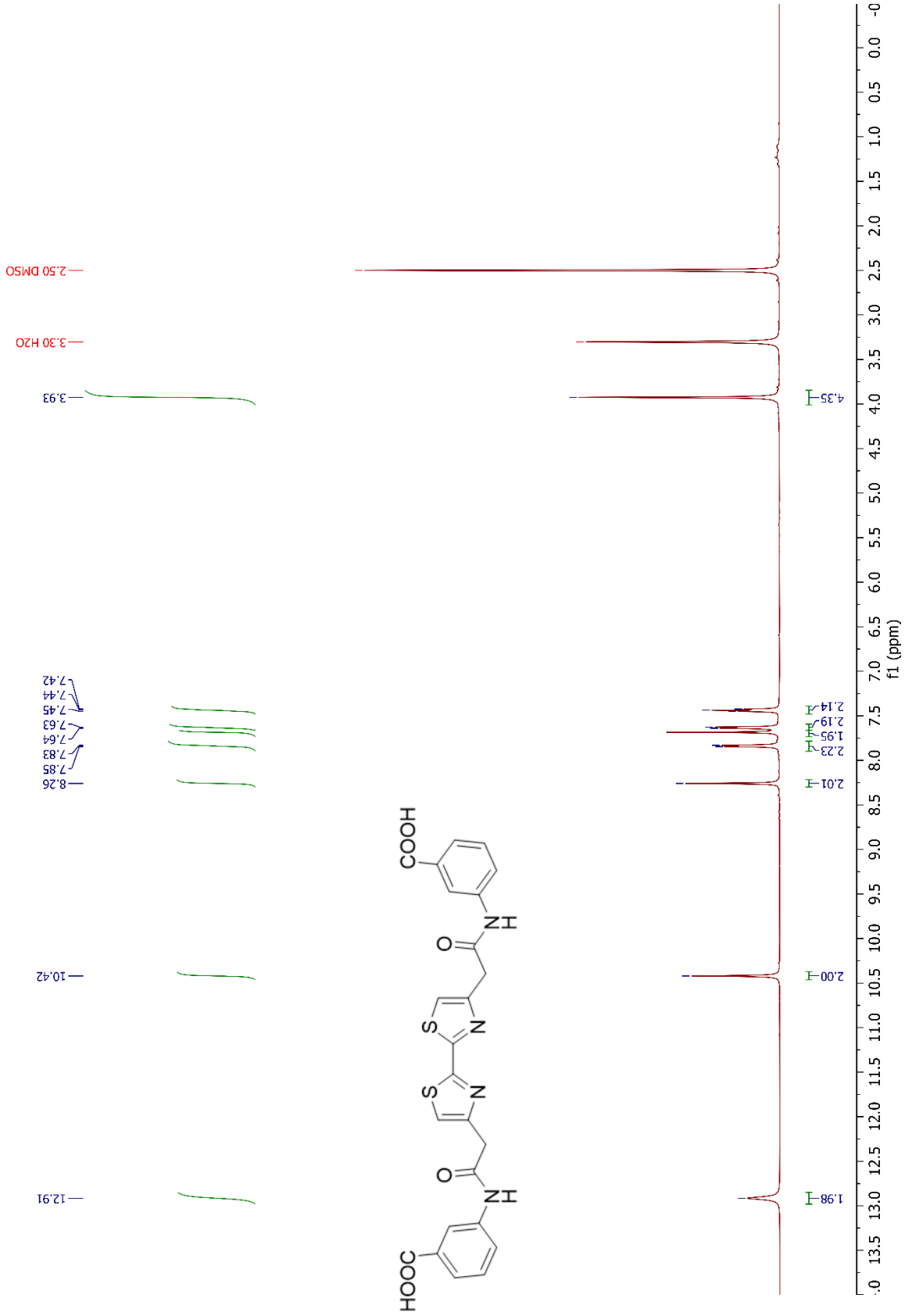
12.91
10.42
8.26
7.85
7.83
7.64
7.63
7.45
7.44
7.42
3.93
3.30 H2O
2.50 DMSO
1.98
2.00
2.01
2.14
2.19
1.95
2.23
4.35
f1 (ppm)

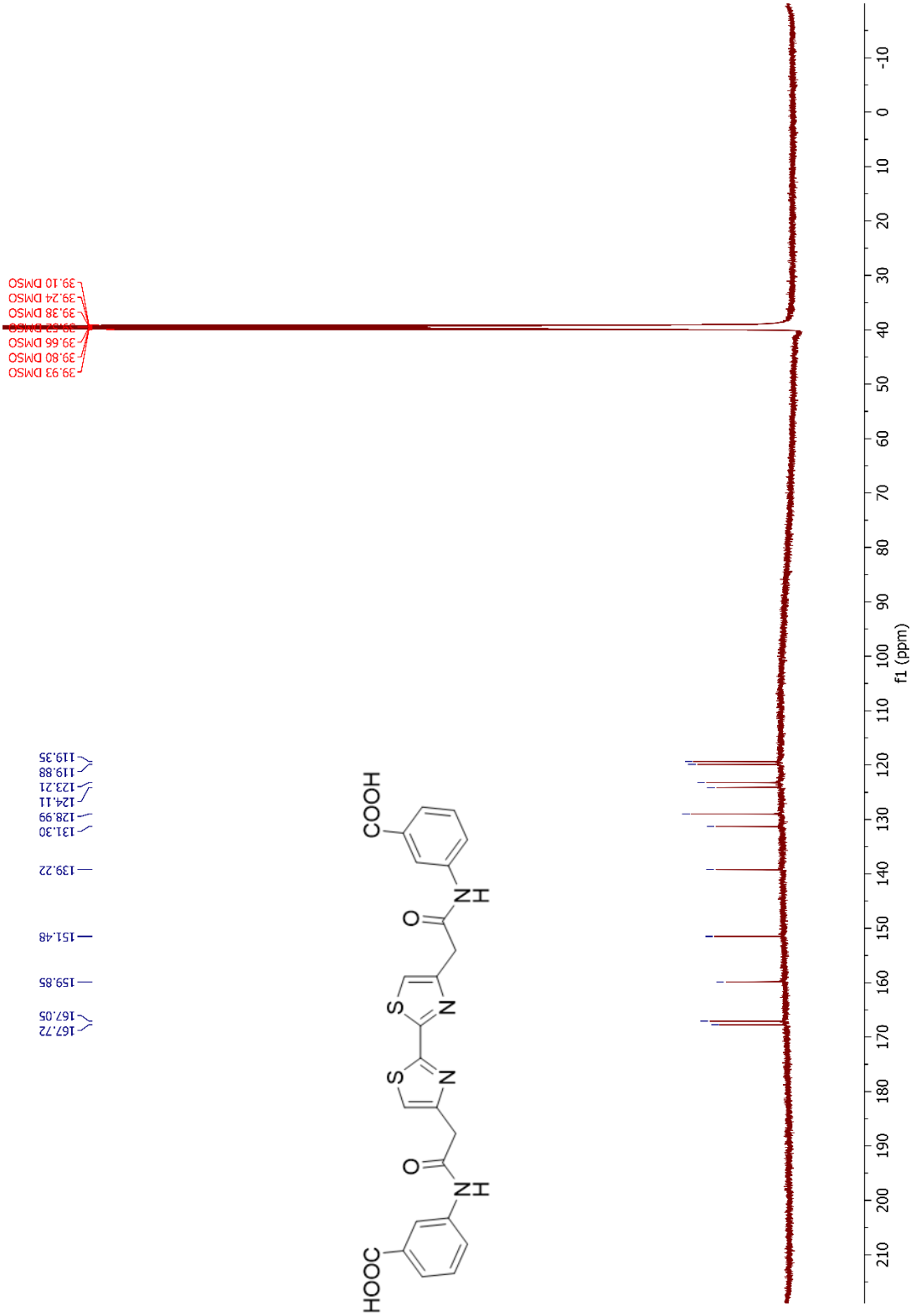
39.10 DMSO
39.24 DMSO
39.38 DMSO
39.52 DMSO
39.66 DMSO
39.80 DMSO
39.93 DMSO
119.35
119.88
123.21
124.11
128.99
131.30
139.22
151.48
159.85
167.05
167.72
COOH
HN
O
S
N
S
N
O
NH
HOOC
f1 (ppm)

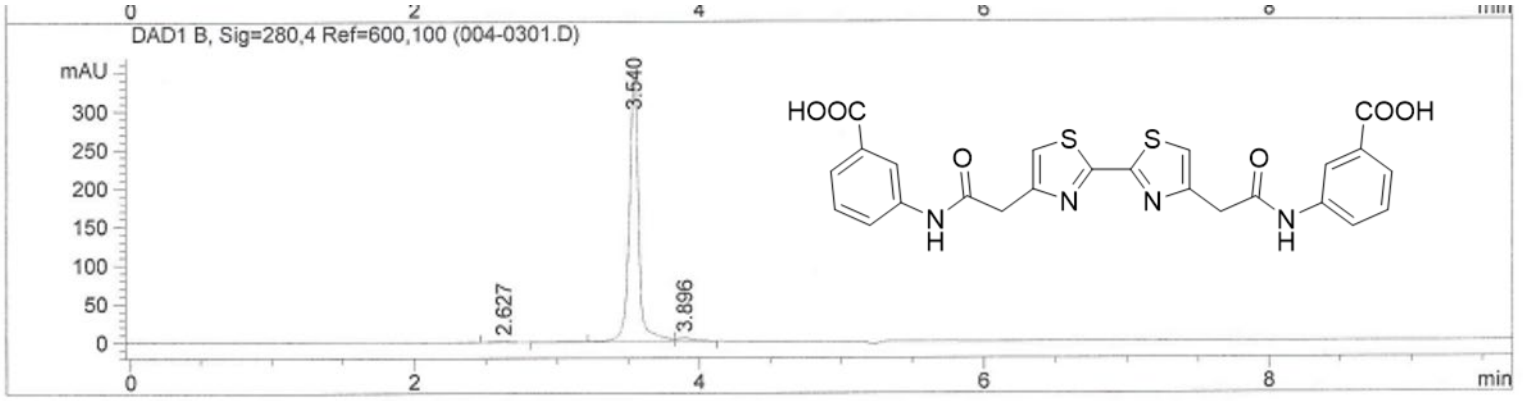


Signal 2: DAD1 B, Sig=280,4 Ref=600,100

| Peak # | RetTime [min] | Type | Width [min] | Area [mAU*s] | Height [mAU] | Area % |
|---|---|---|---|---|---|---|
| 1 | 2.627 | BB | 0.1020 | 9.17031 | 1.18928 | 0.5583 |
| 2 | 3.540 | BV | 0.0666 | 1587.88831 | 352.01788 | 96.6706 |
| 3 | 3.896 | VB | 0.1379 | 45.51830 | 4.58117 | 2.7712 |
| Totals : | | | | 1642.57692 | 357.78834 | |

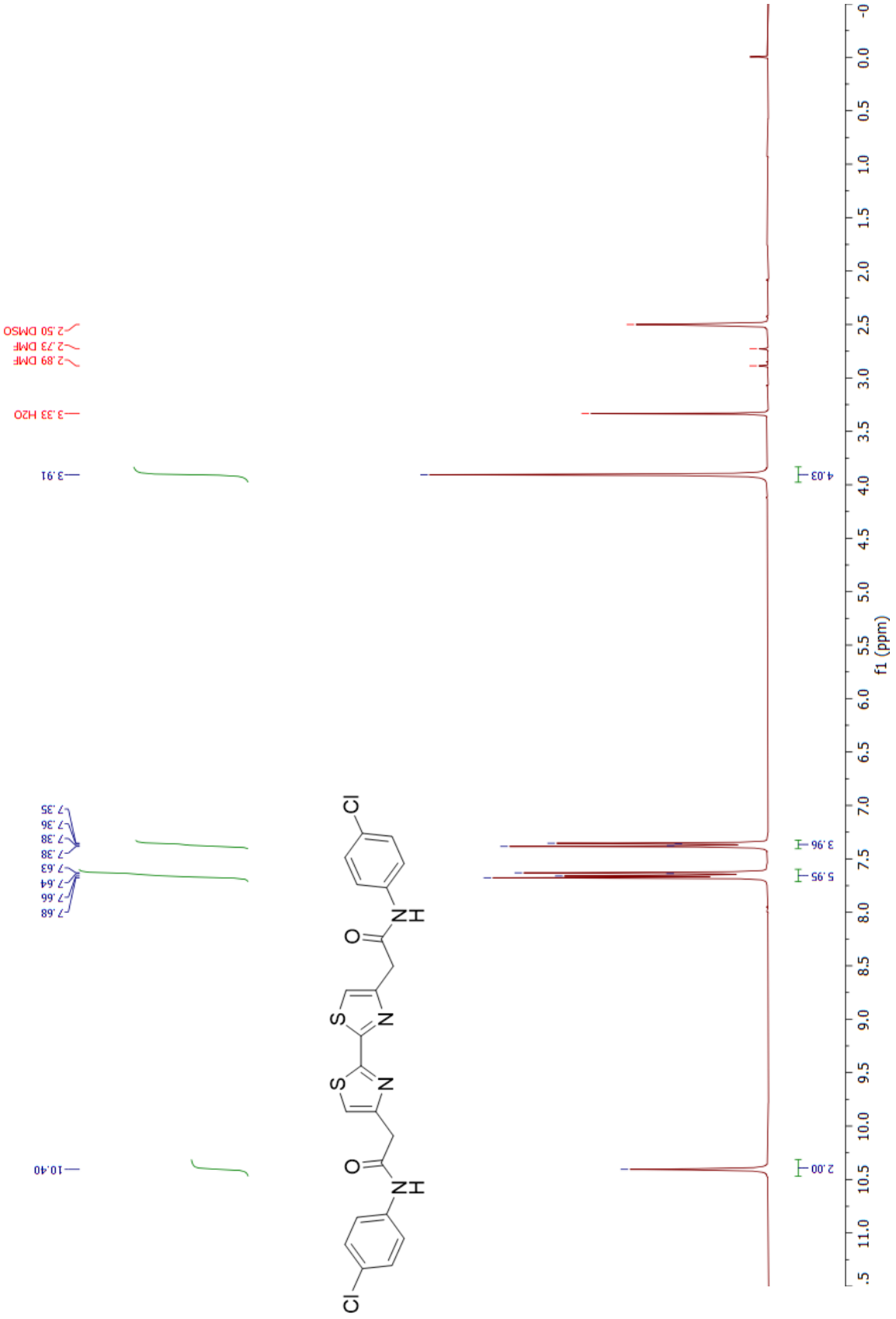
10.40
7.68
7.66
7.64
7.63
7.38
7.38
7.36
7.35
3.91
3.33 H2O
2.89 DMF
2.73 DMF
2.50 DMSO
2.00
3.96
5.95
4.03
f1 (ppm)

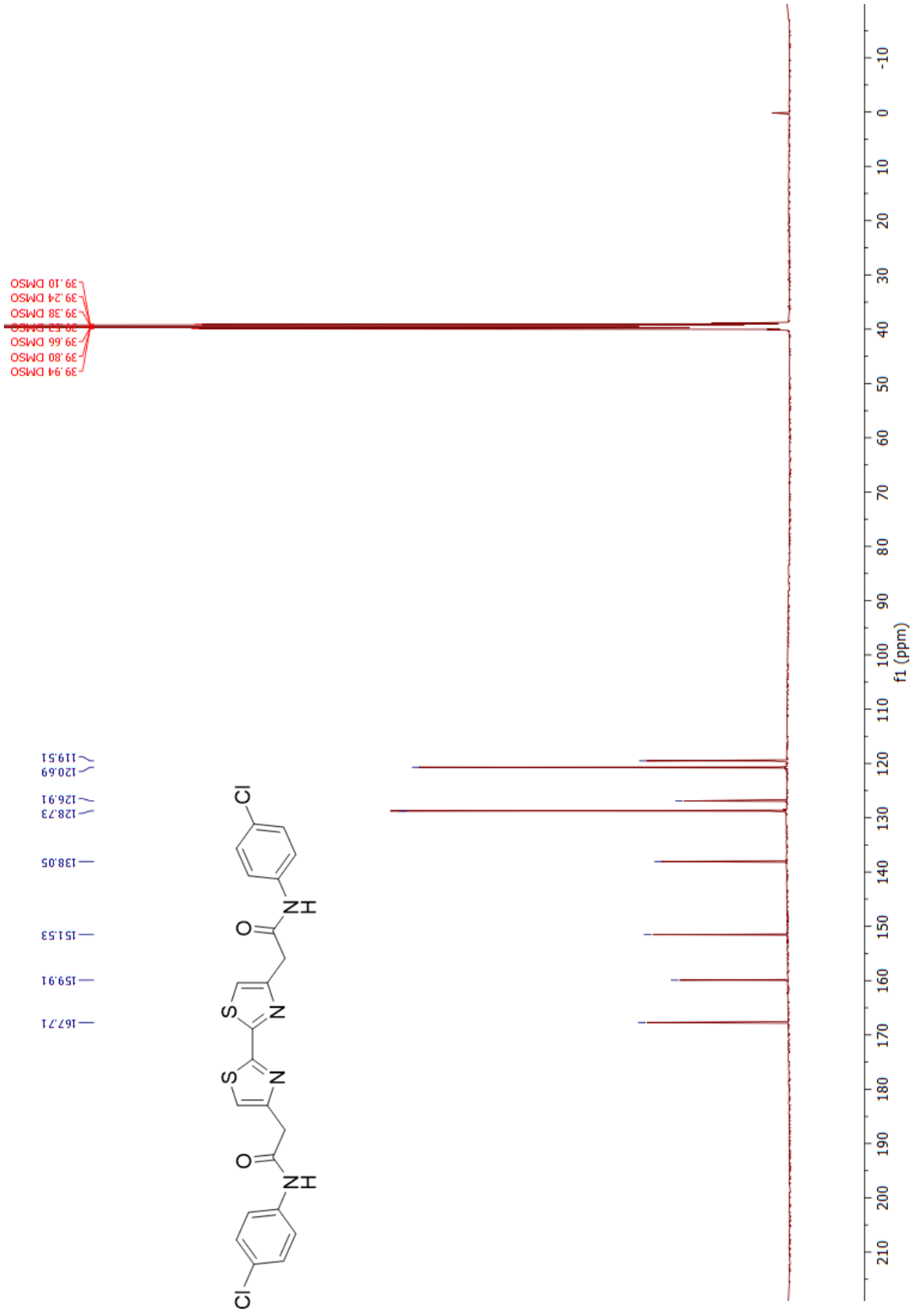
39.10 DMSO
39.24 DMSO
39.38 DMSO
39.52 DMSO
39.66 DMSO
39.80 DMSO
39.94 DMSO
119.51
120.69
126.91
128.73
138.05
151.53
159.91
167.71
Cl
HN
O
S
N
S
N
O
HN
Cl
f1 (ppm)

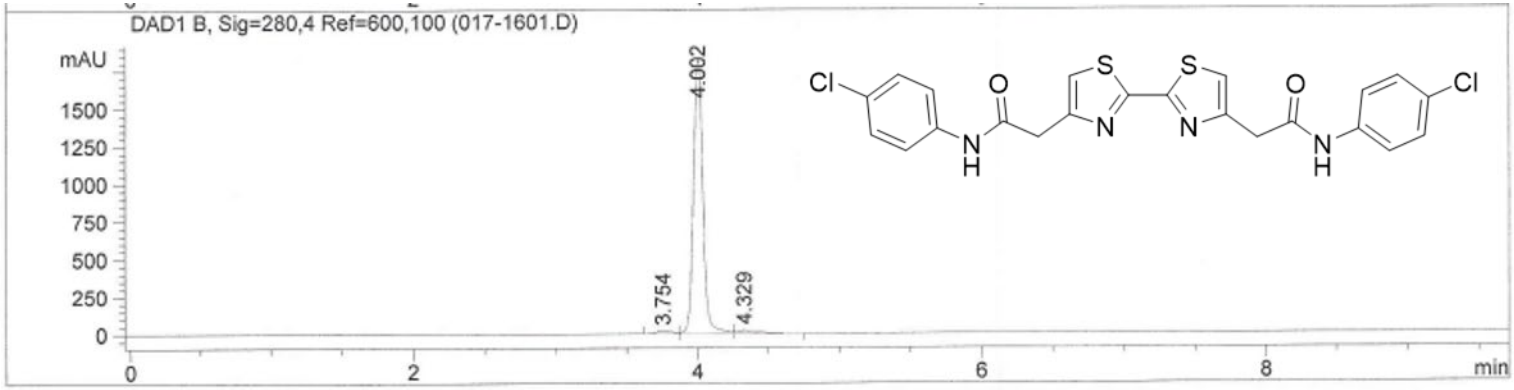


Signal 2: DAD1 B, Sig=280,4 Ref=600,100

| Peak # | RetTime [min] | Type | Width [min] | Area [mAU*s] | Height [mAU] | Area % |
|---|---|---|---|---|---|---|
| 1 | 3.754 | BV | 0.1350 | 139.54594 | 17.12988 | 1.5983 |
| 2 | 4.002 | VV | 0.0716 | 8402.96582 | 1828.14807 | 96.2430 |
| 3 | 4.329 | VB | 0.1264 | 188.48161 | 19.91366 | 2.1588 |
| Totals : | | | | 8730.99338 | 1865.19162 | |

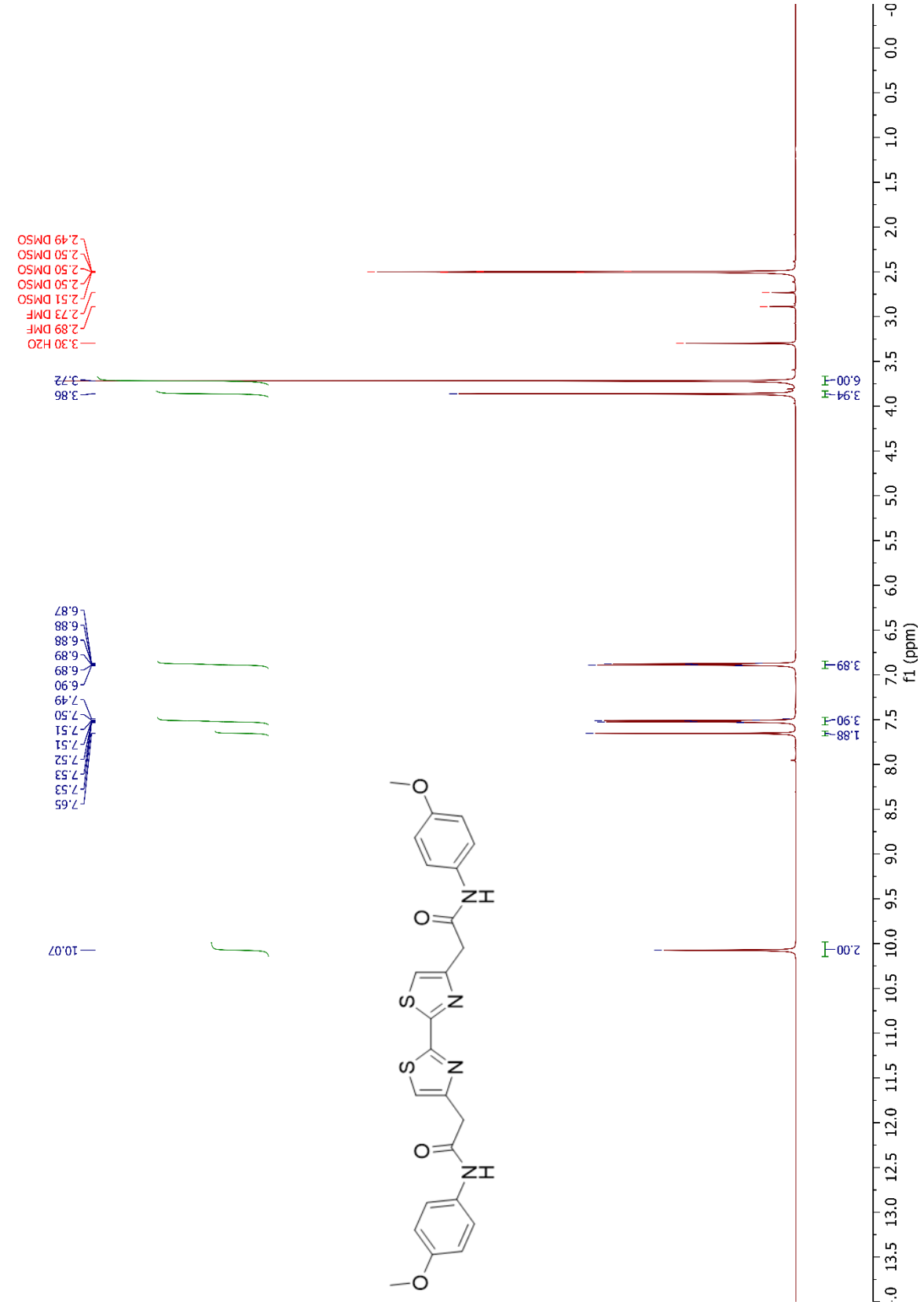
10.07
7.65
7.53
7.53
7.52
7.51
7.51
7.50
7.49
6.90
6.89
6.89
6.88
6.88
6.87
3.86
3.72
3.30 H2O
2.89 DMF
2.73 DMF
2.51 DMSO
2.50 DMSO
2.50 DMSO
2.50 DMSO
2.49 DMSO
2.00
3.89
3.90
1.88
3.94
6.00
f1 (ppm)

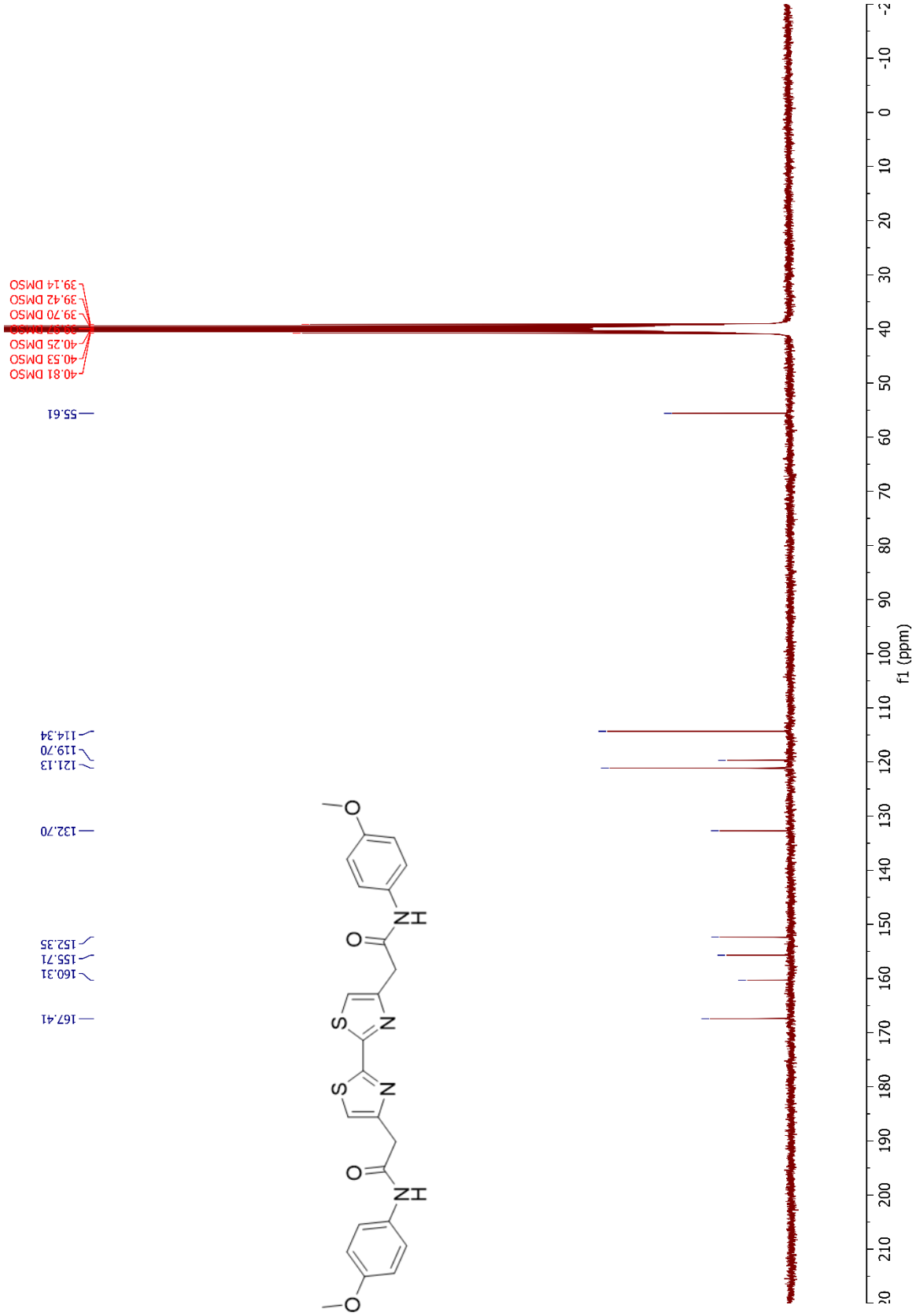
39.14 DMSO
39.42 DMSO
39.70 DMSO
40.25 DMSO
40.53 DMSO
40.81 DMSO
55.61
114.34
119.70
121.13
132.70
152.35
155.71
160.31
167.41
O
NH
S
N
S
N
O
NH
O
f1 (ppm)

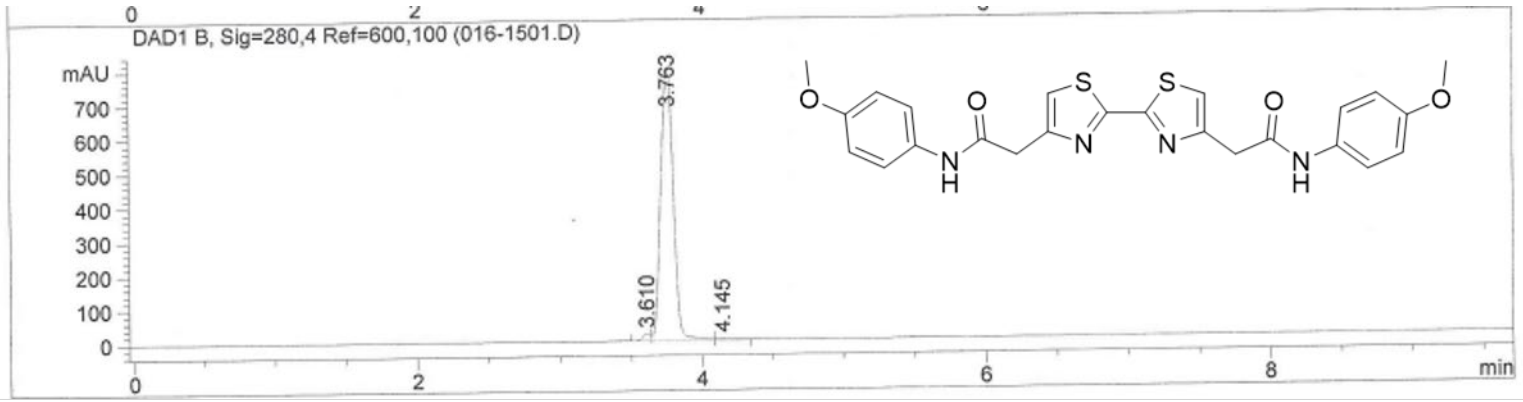


Signal 2: DAD1 B, Sig=280,4 Ref=600,100

| Peak # | RetTime [min] | Type | Width [min] | Area [mAU*s] | Height [mAU] | Area % |
|---|---|---|---|---|---|---|
| 1 | 3.610 | BV | 0.0601 | 79.04633 | 20.89510 | 1.5718 |
| 2 | 3.763 | VV | 0.0995 | 4909.46338 | 800.97833 | 97.6201 |
| 3 | 4.145 | VB | 0.1003 | 40.64161 | 5.76411 | 0.8081 |
| Totals : | | | | 5029.15133 | 827.63755 | |

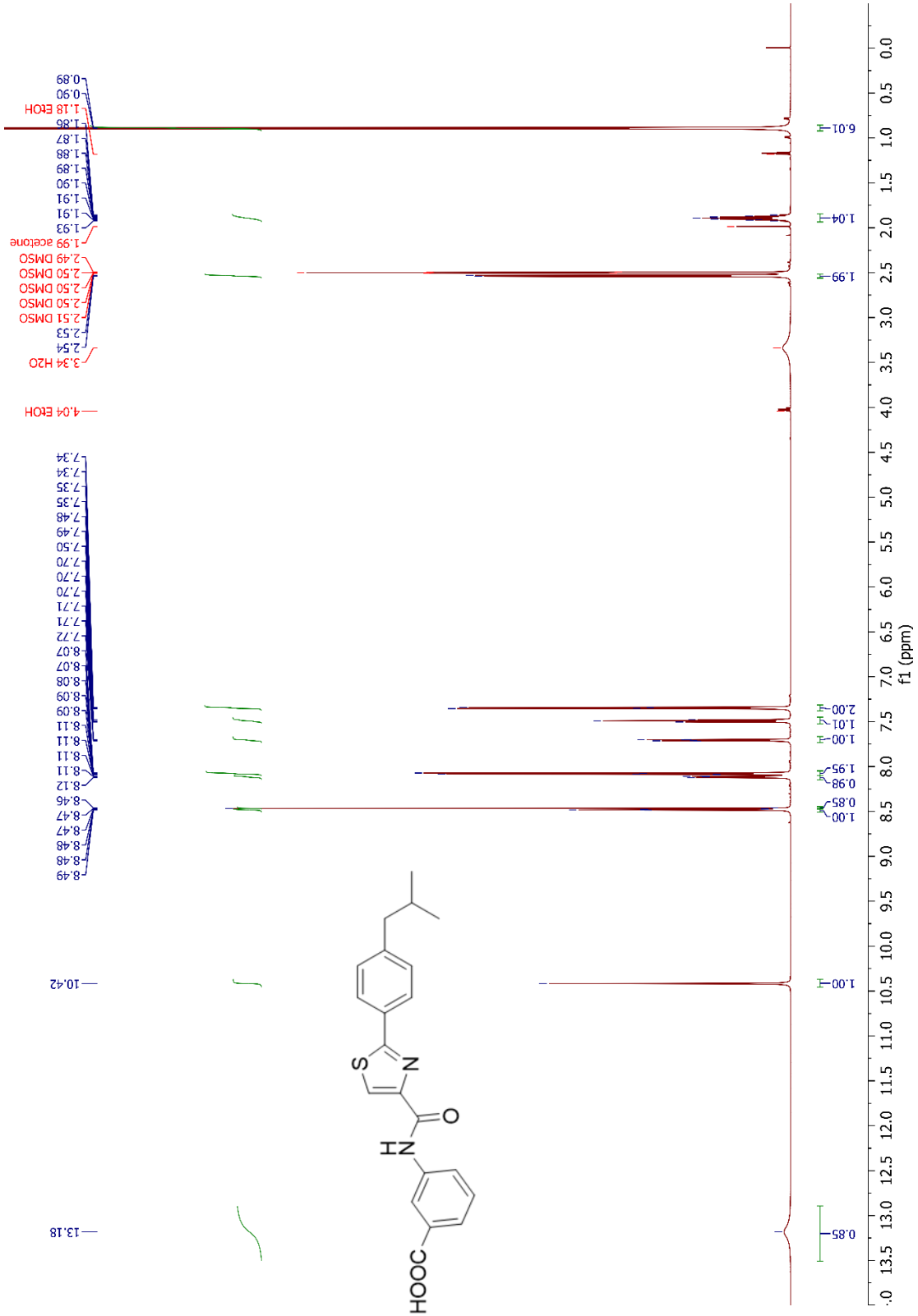
HOOC
HN
O
N
S
f1 (ppm)

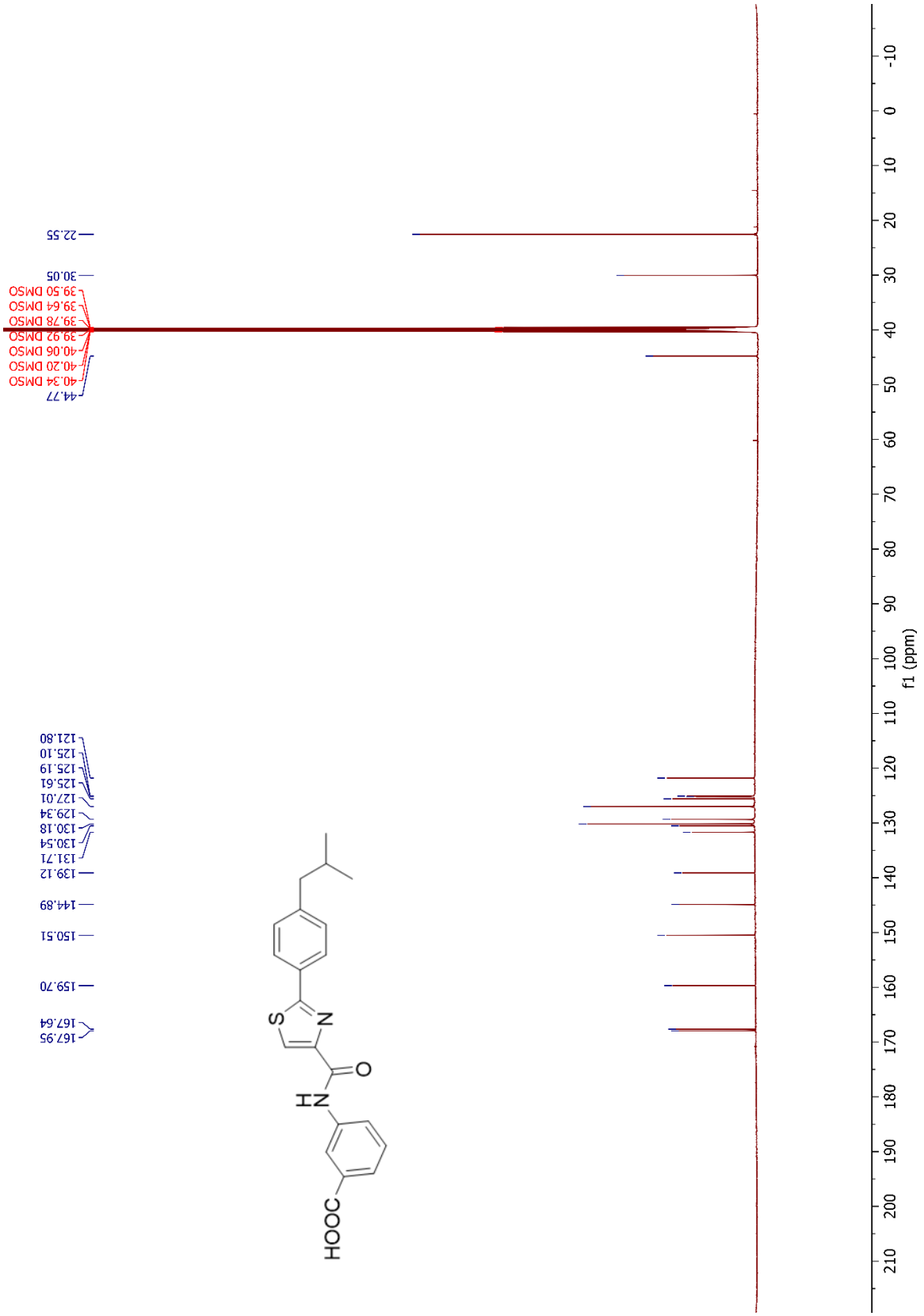
22.55
30.05
39.50 DMSO
39.64 DMSO
39.78 DMSO
39.92 DMSO
40.06 DMSO
40.20 DMSO
40.34 DMSO
44.77
121.80
125.10
125.19
125.61
127.01
129.34
130.18
130.54
131.71
139.12
144.89
150.51
159.70
167.64
167.95
S
N
O
NH
HOOC
-10
0
10
20
30
40
50
60
70
80
90
100
110
120
130
140
150
160
170
180
190
200
210
f1 (ppm)

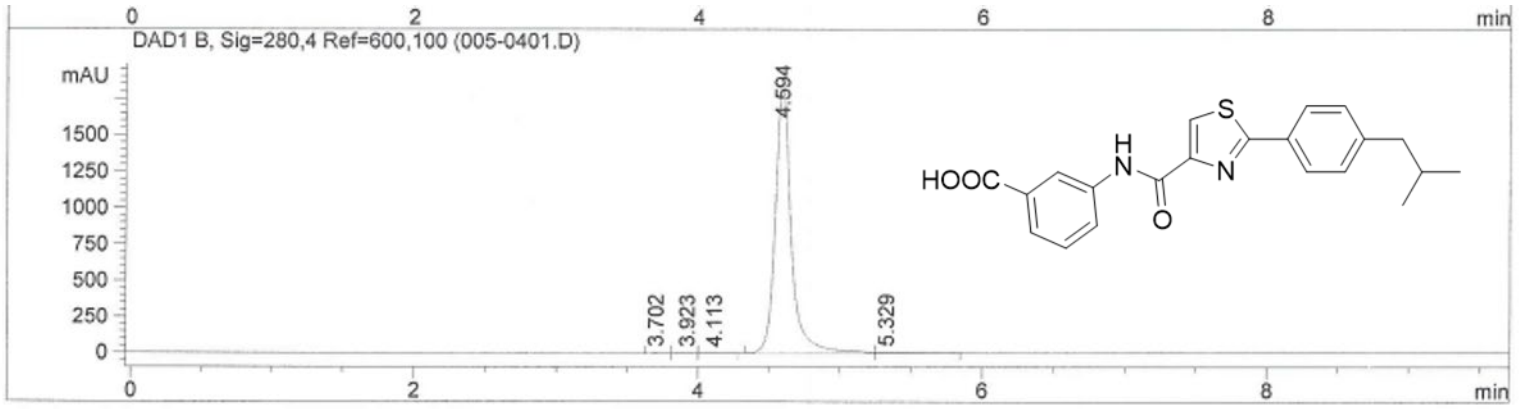


Signal 2: DAD1 B, Sig=280,4 Ref=600,100

| Peak # | RetTime [min] | Type | Width [min] | Area [mAU*s] | Height [mAU] | Area % |
|---|---|---|---|---|---|---|
| 1 | 3.702 | BV | 0.1074 | 32.77112 | 4.58397 | 0.2214 |
| 2 | 3.923 | VV | 0.1419 | 28.98550 | 2.77525 | 0.1958 |
| 3 | 4.113 | VB | 0.1838 | 33.16177 | 2.27890 | 0.2240 |
| 4 | 4.594 | BV | 0.1140 | 1.45953e4 | 1891.97961 | 98.5990 |
| 5 | 5.329 | VB | 0.2608 | 112.46149 | 5.49466 | 0.7597 |
| Totals : | | | | 1.48026e4 | 1907.11239 | |

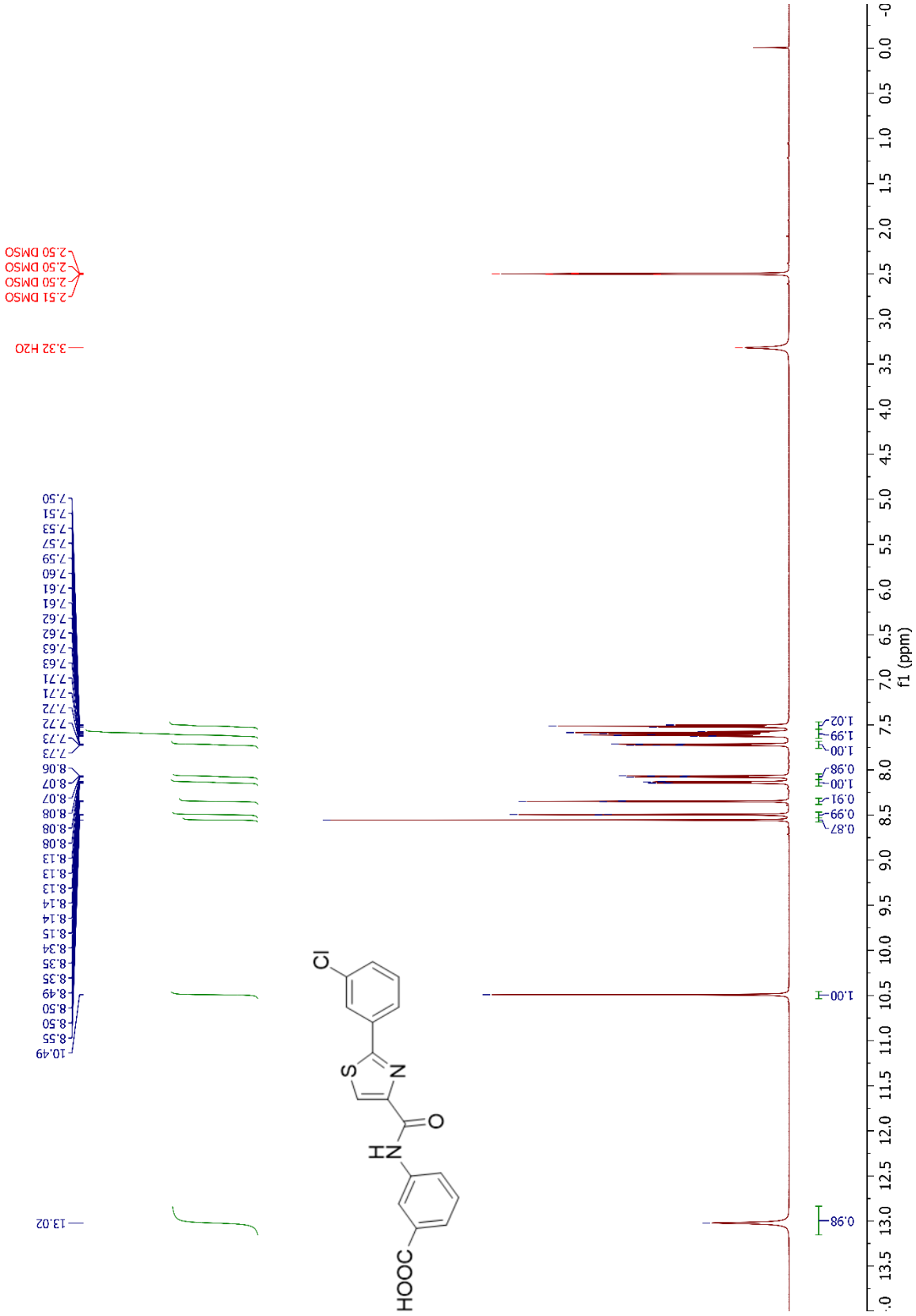
2.51 DMSO
2.50 DMSO
2.50 DMSO
2.50 DMSO
3.32 H2O
13.02
10.49
8.55
8.50
8.50
8.49
8.35
8.35
8.34
8.15
8.14
8.14
8.13
8.13
8.13
8.08
8.08
8.08
8.07
8.07
8.06
7.73
7.73
7.72
7.72
7.71
7.71
7.63
7.63
7.62
7.62
7.61
7.61
7.60
7.59
7.57
7.53
7.51
7.50
0.87
0.99
0.91
1.00
0.98
1.00
1.99
1.02
0.98
1.00
Cl
S
N
O
NH
HOOC
f1 (ppm)

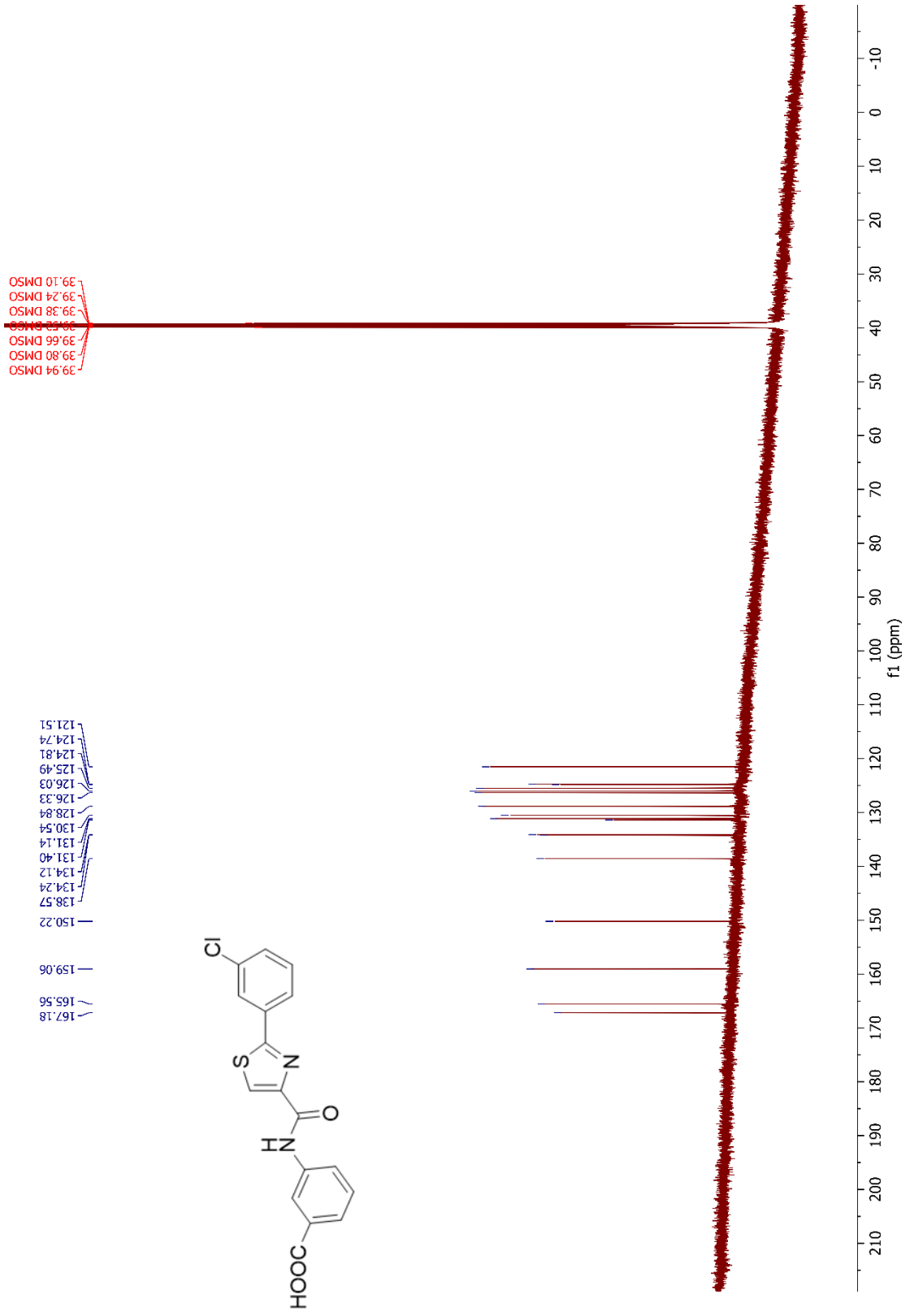
39.10 DMSO
39.24 DMSO
39.38 DMSO
39.52 DMSO
39.66 DMSO
39.80 DMSO
39.94 DMSO
121.51
124.74
124.81
125.49
126.03
126.33
128.84
130.54
131.14
131.40
134.12
134.24
138.57
150.22
159.06
165.56
167.18
Cl
S
N
O
NH
HOOC
f1 (ppm)

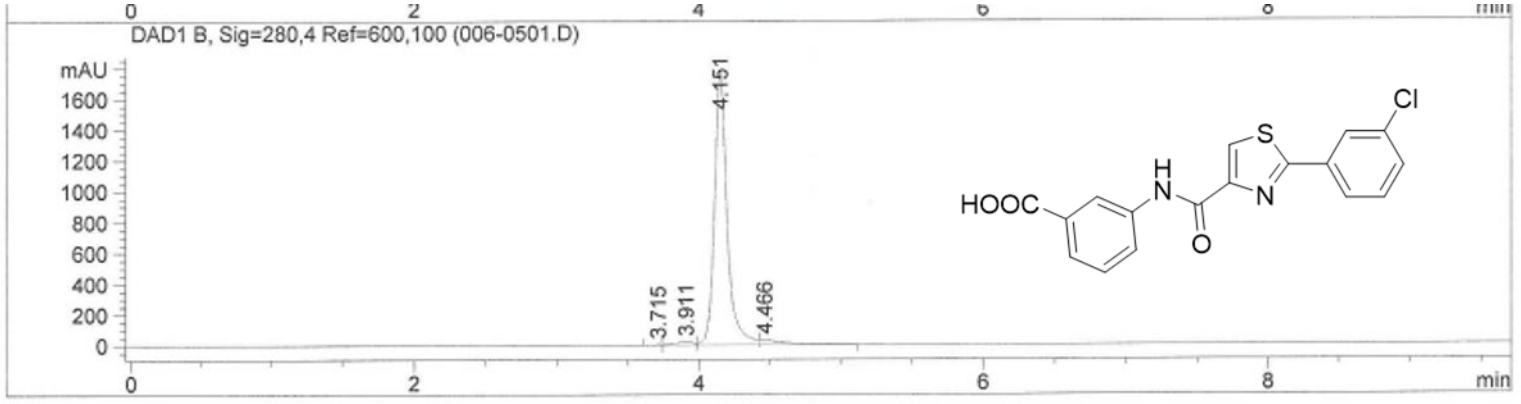


Signal 2: DAD1 B, Sig=280,4 Ref=600,100

| Peak # | RetTime [min] | Type | Width [min] | Area [mAU*s] | Height [mAU] | Area % |
|---|---|---|---|---|---|---|
| 1 | 3.715 | BV | 0.0493 | 5.32970 | 2.27598 | 0.0457 |
| 2 | 3.911 | VV | 0.1302 | 170.41899 | 20.24973 | 1.4612 |
| 3 | 4.151 | VV | 0.0923 | 1.10953e4 | 1790.34644 | 95.1301 |
| 4 | 4.466 | VB | 0.1605 | 392.24283 | 32.57600 | 3.3630 |
| Totals : | | | | 1.16633e4 | 1845.44815 | |

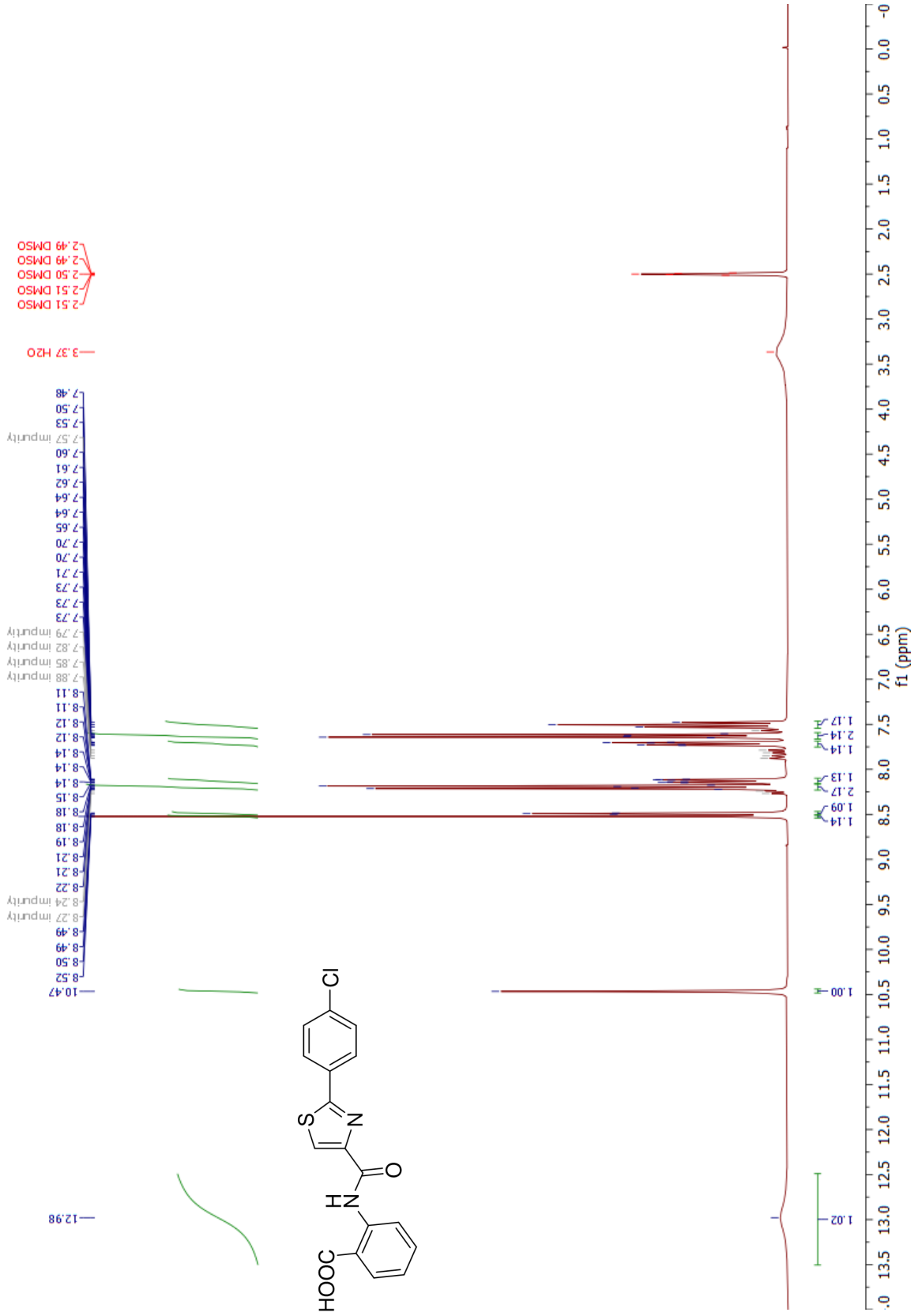
f1 (ppm)
Cl
S
N
O
NH
HOOC
2.51 DMSO
2.50 DMSO
2.49 DMSO
3.37 H2O
7.48
7.50
7.53
7.57 impurity
7.60
7.61
7.62
7.64
7.64
7.65
7.70
7.70
7.71
7.73
7.73
7.79 impurity
7.82 impurity
7.85 impurity
7.88 impurity
8.11
8.11
8.12
8.12
8.14
8.14
8.14
8.15
8.18
8.18
8.19
8.21
8.21
8.22
8.24 impurity
8.27 impurity
8.49
8.49
8.50
8.52
10.47
12.98
1.17
2.14
1.14
1.13
2.17
1.09
1.14
1.00
1.02

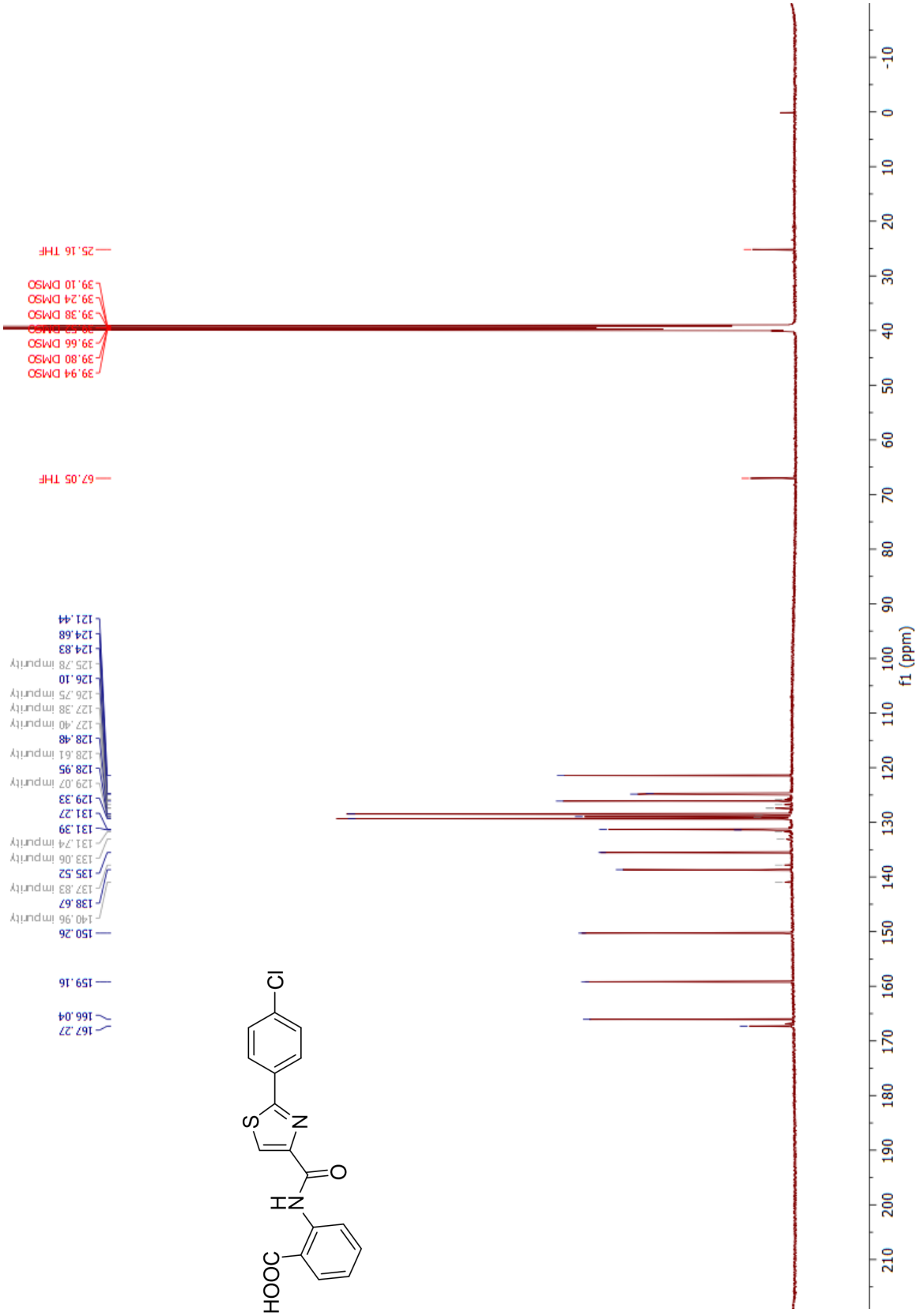
25.16 THF
39.10 DMSO
39.24 DMSO
39.38 DMSO
39.66 DMSO
39.80 DMSO
39.94 DMSO
67.05 THF
121.44
124.68
124.83
125.78 impurity
126.10
126.75 impurity
127.38 impurity
127.40 impurity
128.48
128.61 impurity
128.95
129.07 impurity
129.33
131.27
131.39
131.74 impurity
133.06 impurity
135.52
137.83 impurity
138.67
140.96 impurity
150.26
159.16
166.04
167.27
Cl
S
N
O
NH
HOOC
f1 (ppm)

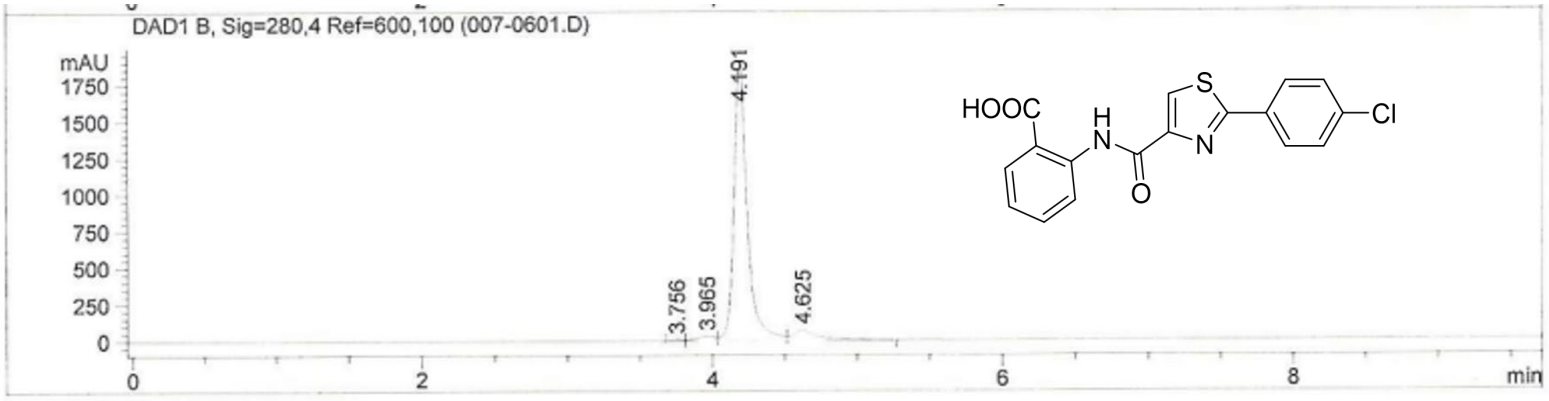


Signal 2: DAD1 B, Sig=280,4 Ref=600,100

| Peak # | RetTime [min] | Type | Width [min] | Area [mAU*s] | Height [mAU] | Area % |
|---|---|---|---|---|---|---|
| 1 | 3.756 | BV | 0.0724 | 52.90156 | 10.56174 | 0.3936 |
| 2 | 3.965 | VV | 0.1273 | 281.54266 | 32.41135 | 2.0945 |
| 3 | 4.191 | VV | 0.0943 | 1.21773e4 | 1911.98206 | 90.5908 |
| 4 | 4.625 | VV | 0.1713 | 930.35004 | 73.69817 | 6.9212 |
| Totals : | | | | 1.34421e4 | 2028.65331 | |

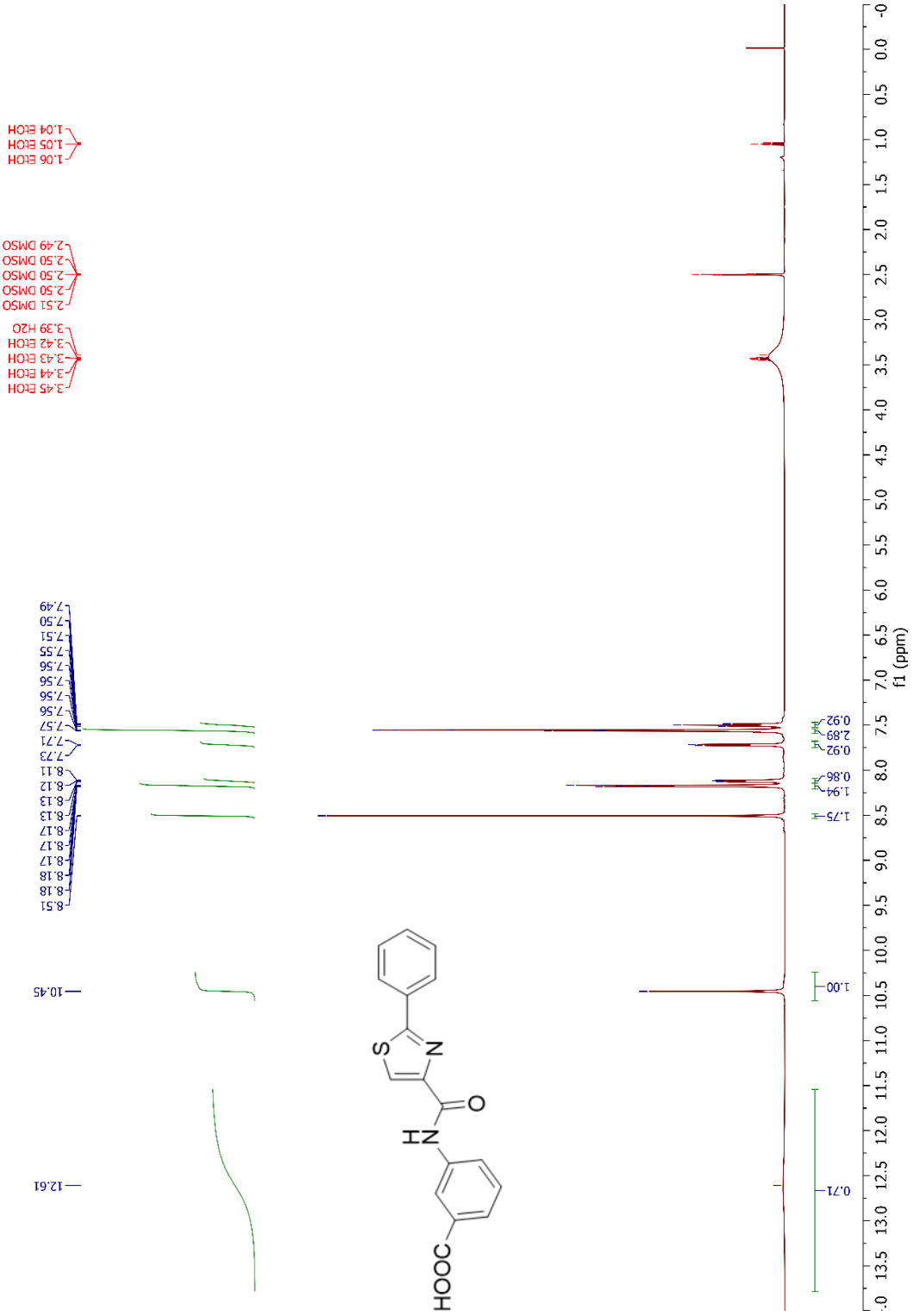
f1 (ppm)
HOOC
S
N
O
NH
1.00
0.71
1.75
1.94
0.86
2.89
0.92
0.92
10.45
12.61
8.51
8.18
8.18
8.17
8.17
8.17
8.17
8.13
8.13
8.12
8.11
7.73
7.71
7.57
7.56
7.56
7.56
7.55
7.51
7.50
7.49
3.45 EtOH
3.44 EtOH
3.43 EtOH
3.42 EtOH
3.39 H2O
2.51 DMSO
2.50 DMSO
2.50 DMSO
2.50 DMSO
2.49 DMSO
1.06 EtOH
1.05 EtOH
1.04 EtOH

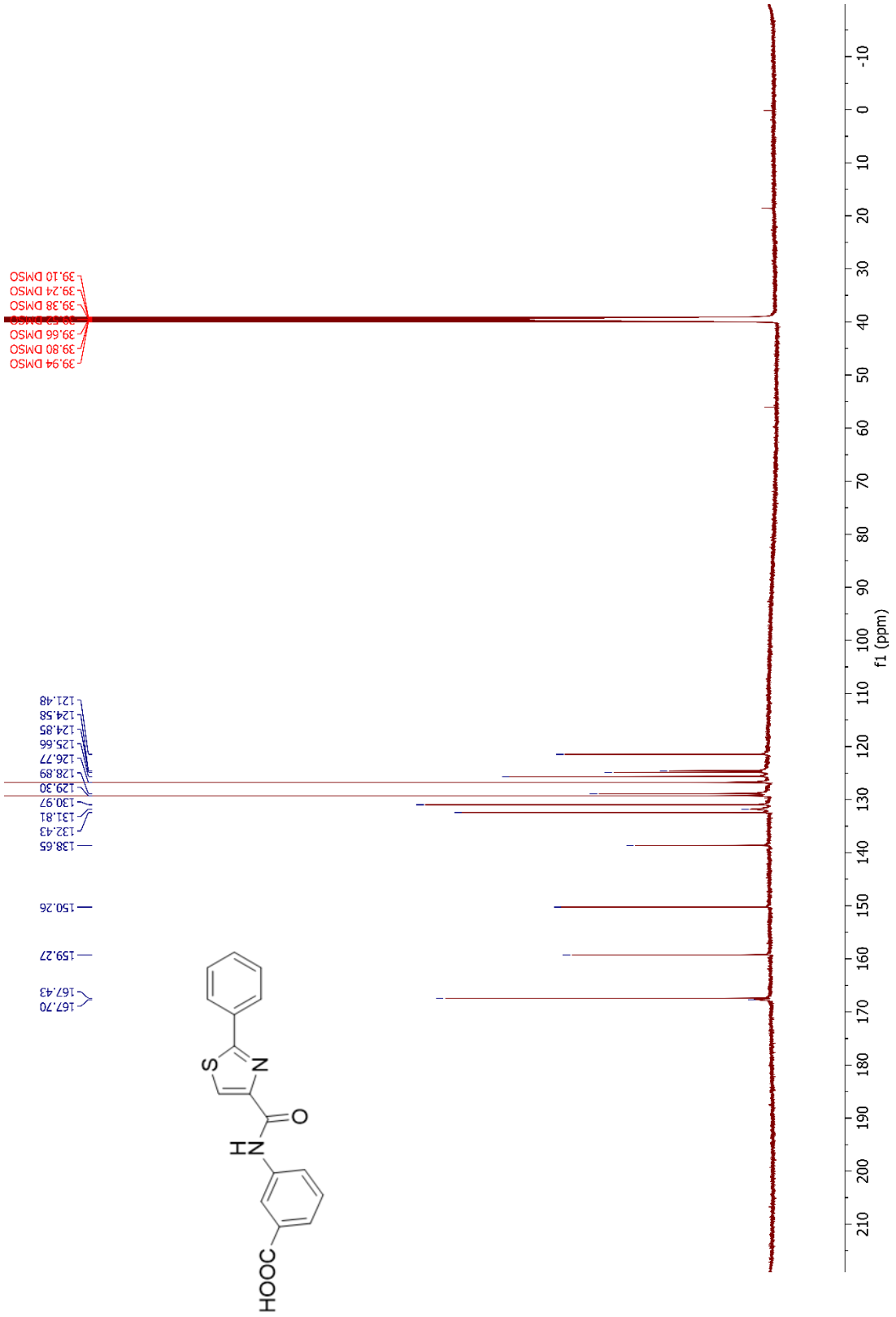
39.10 DMSO
39.24 DMSO
39.38 DMSO
39.66 DMSO
39.80 DMSO
39.94 DMSO
121.48
124.58
124.85
125.66
126.77
128.89
129.30
130.97
131.81
132.43
138.65
150.26
159.27
167.70
167.43
HOOC
NH
O
N
S
f1 (ppm)

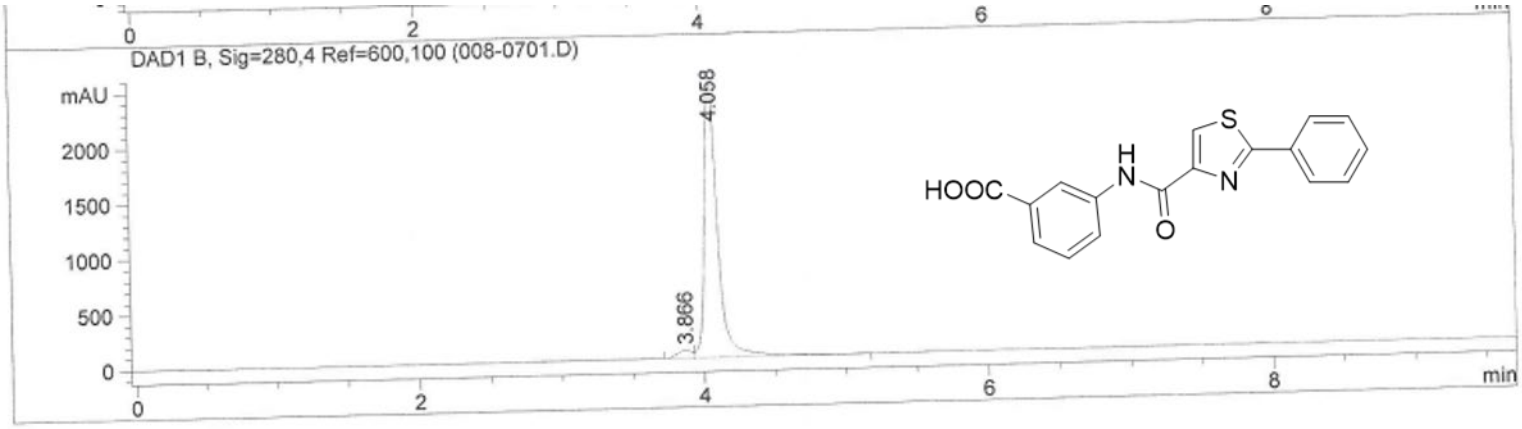


Signal 2: DAD1 B, Sig=280,4 Ref=600,100

| Peak # | RetTime [min] | Type | Width [min] | Area [mAU*s] | Height [mAU] | Area % |
|---|---|---|---|---|---|---|
| 1 | 3.866 | BV | 0.1162 | 525.45404 | 72.84534 | 3.1139 |
| 2 | 4.058 | VB | 0.1005 | 1.63490e4 | 2494.81299 | 96.8861 |
| Totals : | | | | 1.68745e4 | 2567.65833 | |

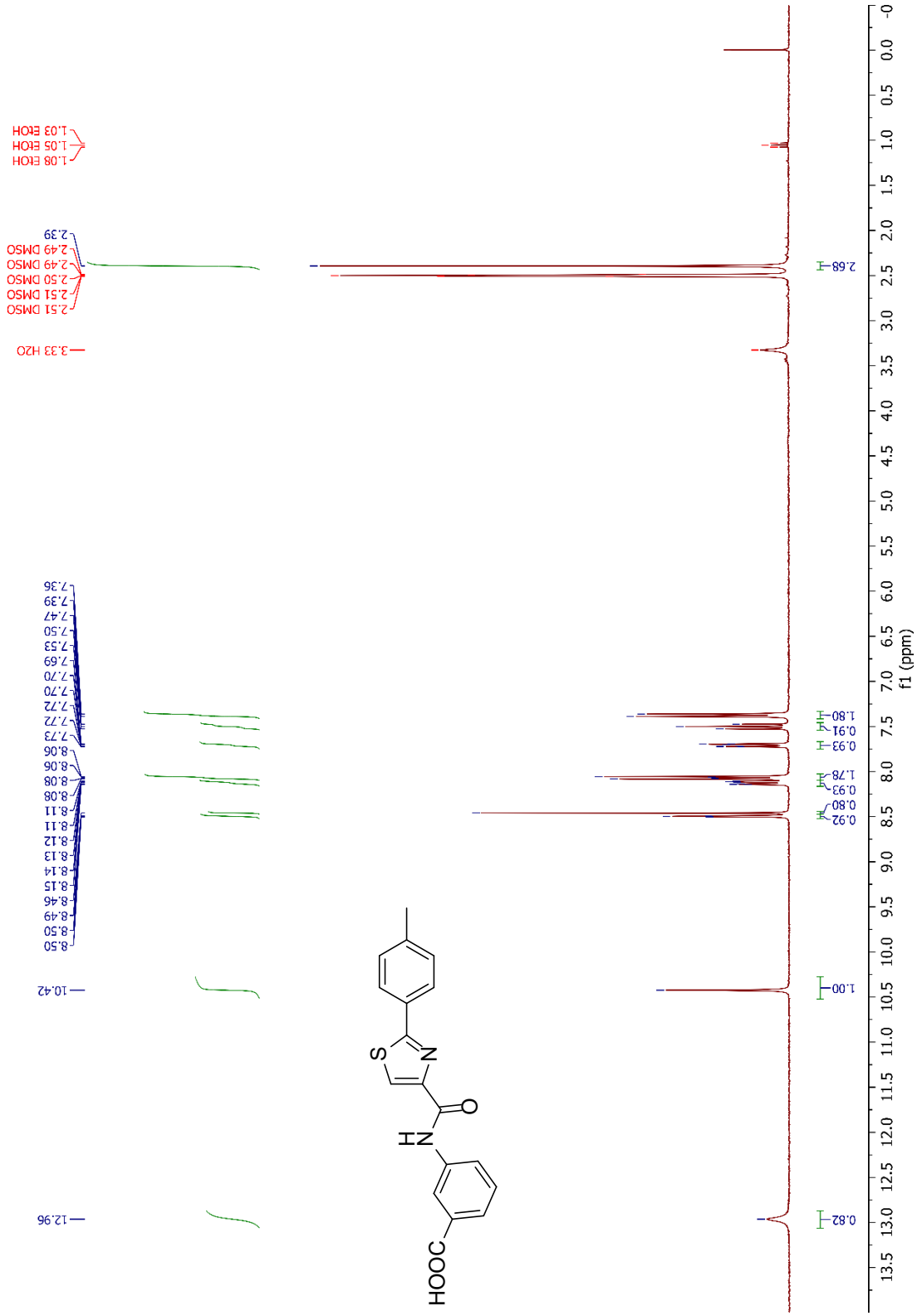
f1 (ppm)
HOOC
HN
O
N
S
2.68
1.80
0.91
0.93
1.78
0.93
0.92
0.80
1.00
0.82
10.42
12.96
3.33 H2O
2.51 DMSO
2.50 DMSO
2.49 DMSO
2.49 DMSO
2.39
1.08 EtOH
1.05 EtOH
1.03 EtOH

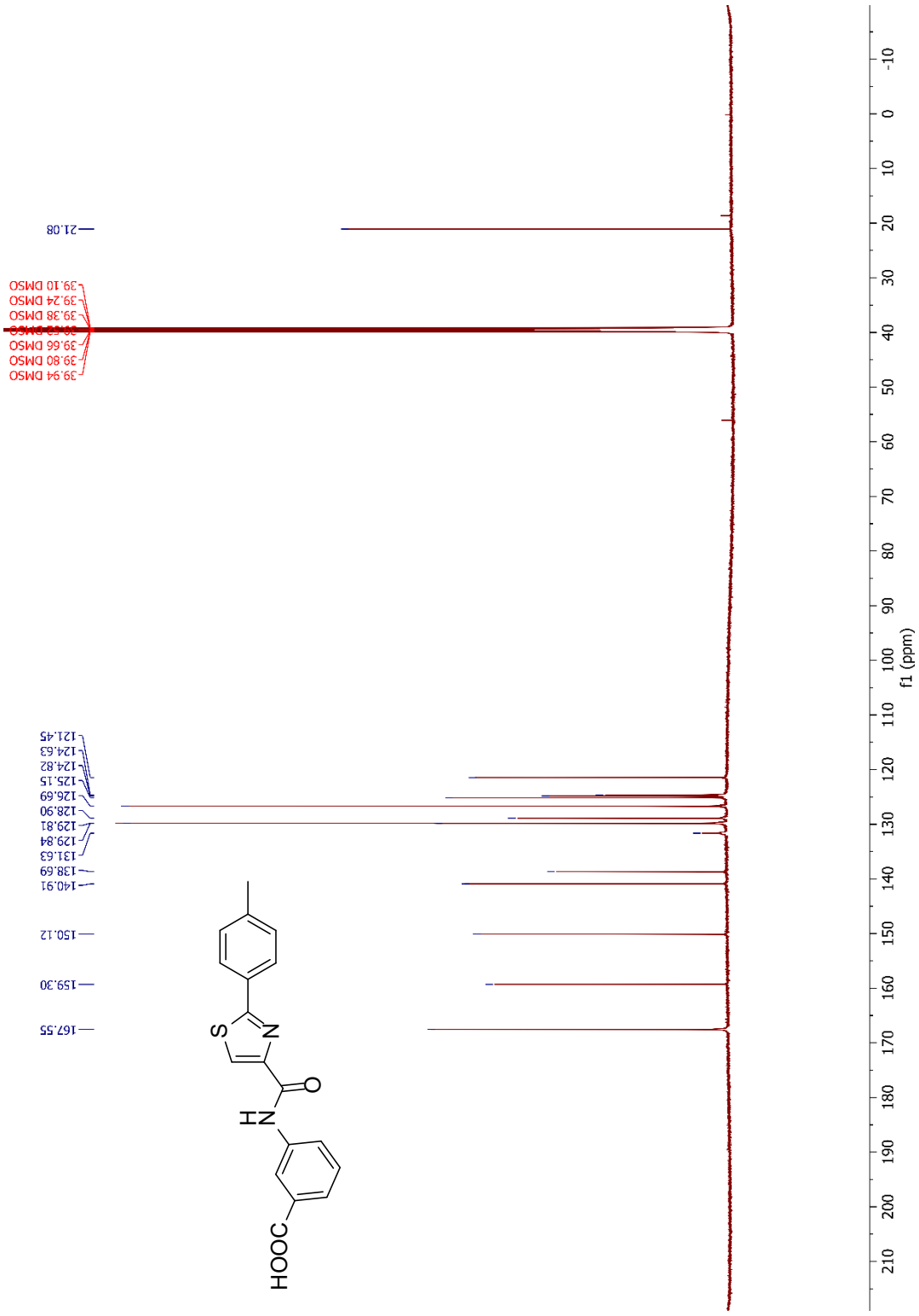
21.08
39.10 DMSO
39.24 DMSO
39.38 DMSO
39.52 DMSO
39.66 DMSO
39.80 DMSO
39.94 DMSO
121.45
124.63
124.82
125.15
126.69
128.90
129.81
129.84
131.63
138.69
140.91
150.12
159.30
167.55
S
N
O
NH
HOOC
f1 (ppm)

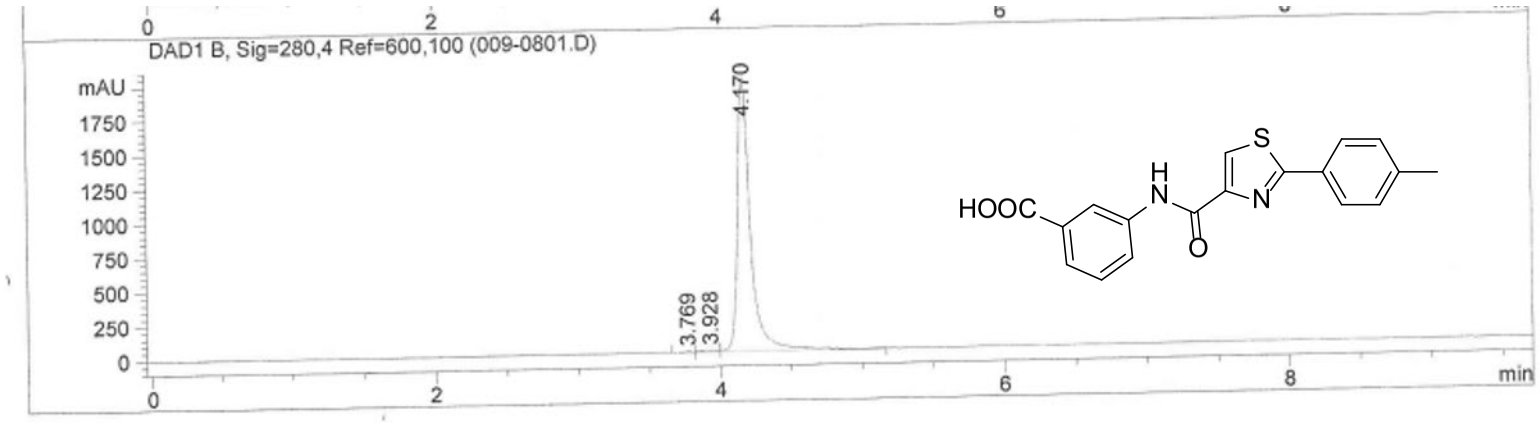


Signal 2: DAD1 B, Sig=280,4 Ref=600,100

| Peak # | RetTime [min] | Type | Width [min] | Area [mAU*s] | Height [mAU] | Area % |
|---|---|---|---|---|---|---|
| 1 | 3.769 | BV | 0.0818 | 15.20615 | 3.29958 | 0.1175 |
| 2 | 3.928 | VV | 0.1132 | 90.52567 | 11.57707 | 0.6993 |
| 3 | 4.170 | VB | 0.0946 | 1.28388e4 | 2007.39038 | 99.1832 |
| Totals : | | | | 1.29445e4 | 2022.26703 | |

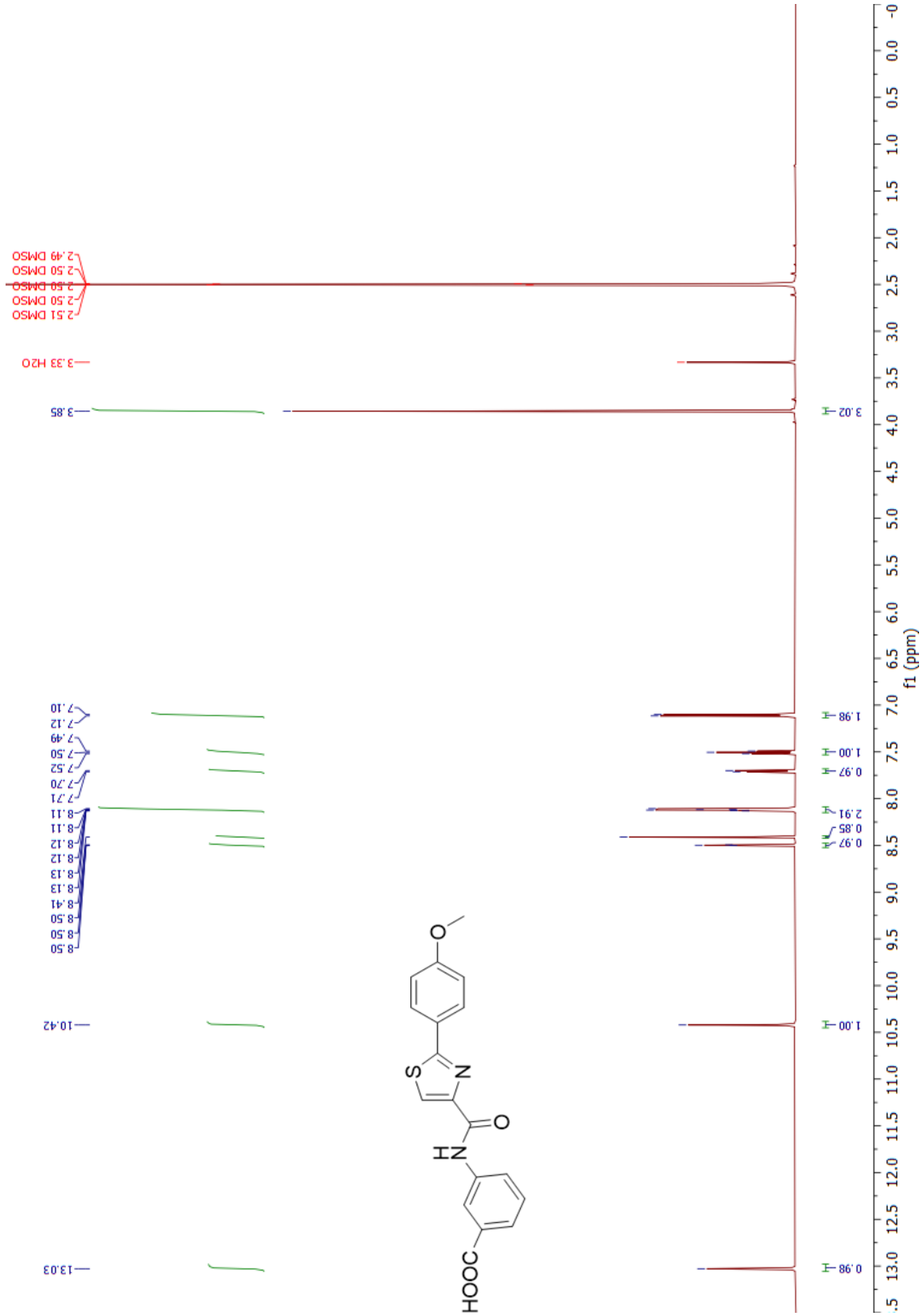
2.51 DMSO
2.50 DMSO
2.50 DMSO
2.50 DMSO
2.49 DMSO
3.33 H2O
3.85
8.50
8.50
8.41
8.13
8.13
8.12
8.12
8.11
8.11
7.71
7.70
7.52
7.50
7.49
7.12
7.10
10.42
13.03
3.02
1.98
1.00
0.97
2.91
0.85
0.97
1.00
0.98
HOOC
NH
N
S
O
O
f1 (ppm)

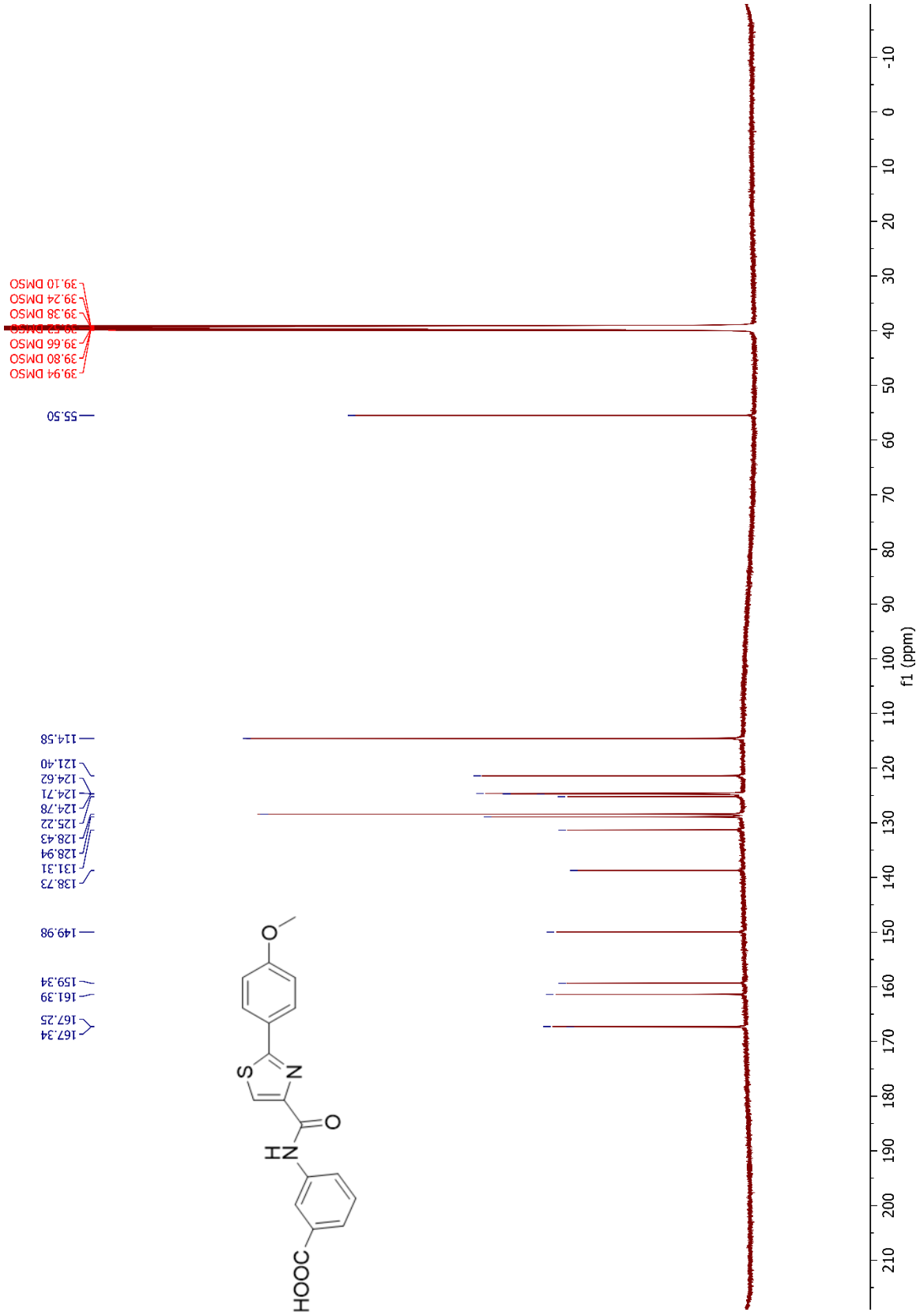
39.10 DMSO
39.24 DMSO
39.38 DMSO
39.66 DMSO
39.80 DMSO
39.94 DMSO
55.50
114.58
121.40
124.62
124.71
124.78
125.22
128.43
128.94
131.31
138.73
149.98
159.34
161.39
167.25
167.34
O
S
N
O
NH
HOOC
f1 (ppm)

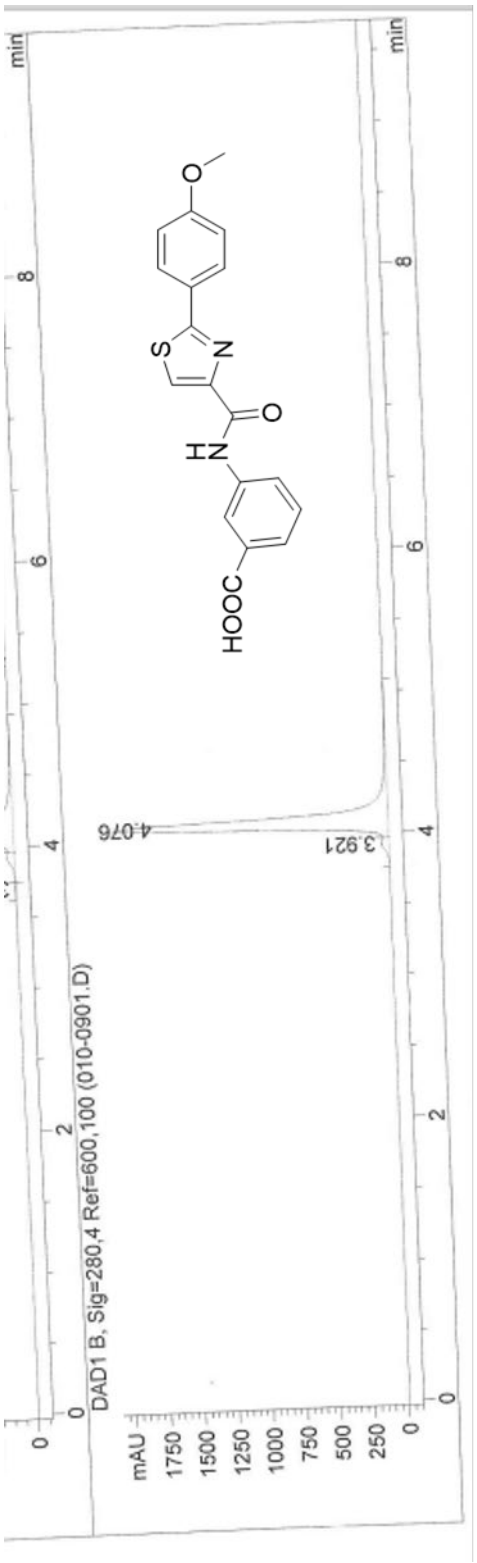


Signal 2: DAD1 B, Sig=280,4 Ref=600,100

| Peak # | RetTime [min] | Type | Width [min] | Area [mAU*s] | Height [mAU] | Area % |
|---|---|---|---|---|---|---|
| 1 | 3.921 | BV | 0.0864 | 311.76288 | 54.77051 | 2.6707 |
| 2 | 4.076 | VB | 0.0843 | 1.13619e4 | 1999.23145 | 97.3293 |
| Totals : | | | | 1.16736e4 | 2054.00195 | |

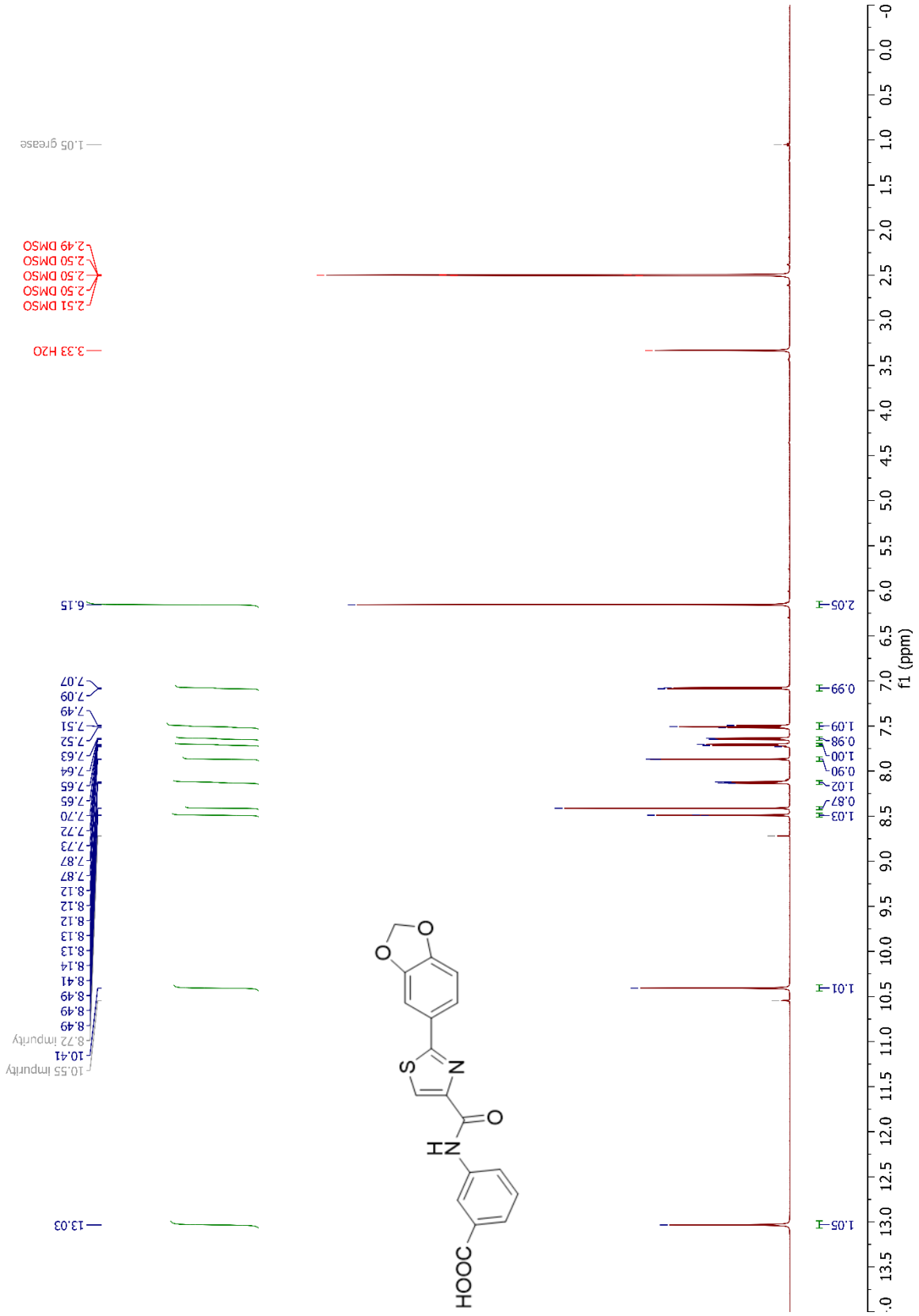
1.05 grease
3.33 H2O
2.51 DMSO
2.50 DMSO
2.50 DMSO
2.50 DMSO
2.49 DMSO
6.15
7.07
7.09
7.49
7.51
7.52
7.63
7.64
7.65
7.65
7.70
7.72
7.73
7.87
7.87
8.12
8.12
8.12
8.13
8.13
8.14
8.41
8.49
8.49
8.49
8.72 impurity
10.41
10.55 impurity
13.03
2.05
0.99
1.09
0.98
1.00
0.90
1.02
0.87
1.03
1.01
1.05
HOOC
NH
f1 (ppm)

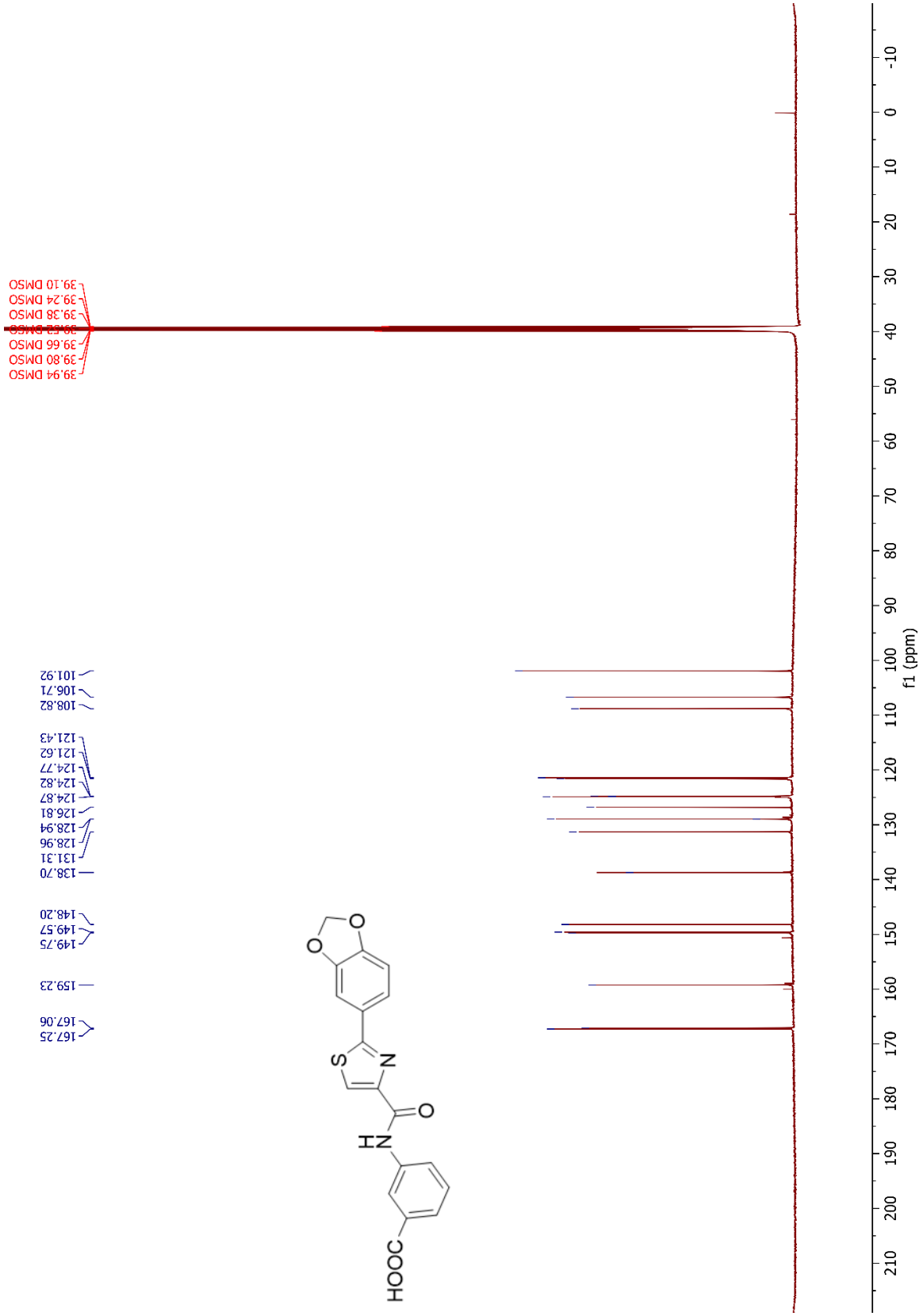
39.10 DMSO
39.24 DMSO
39.38 DMSO
39.52 DMSO
39.66 DMSO
39.80 DMSO
39.94 DMSO
101.92
106.71
108.82
121.43
121.62
124.77
124.82
124.87
126.81
128.94
128.96
131.31
138.70
148.20
149.57
149.75
159.23
167.06
167.25
HOOC
NH
S
N
O
O
O
f1 (ppm)

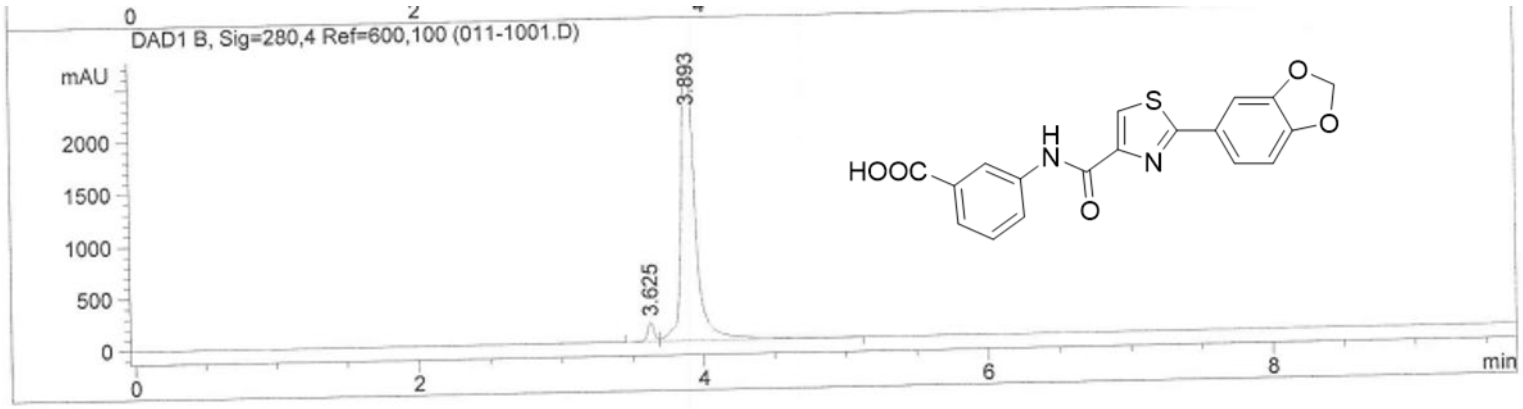


Signal 2: DAD1 B, Sig=280,4 Ref=600,100

| Peak # | RetTime [min] | Type | Width [min] | Area [mAU*s] | Height [mAU] | Area % |
|---|---|---|---|---|---|---|
| 1 | 3.625 | BV | 0.0490 | 596.15405 | 187.79315 | 3.0802 |
| 2 | 3.893 | VB | 0.1091 | 1.87580e4 | 2633.95752 | 96.9198 |
| Totals : | | | | 1.93541e4 | 2821.75067 | |

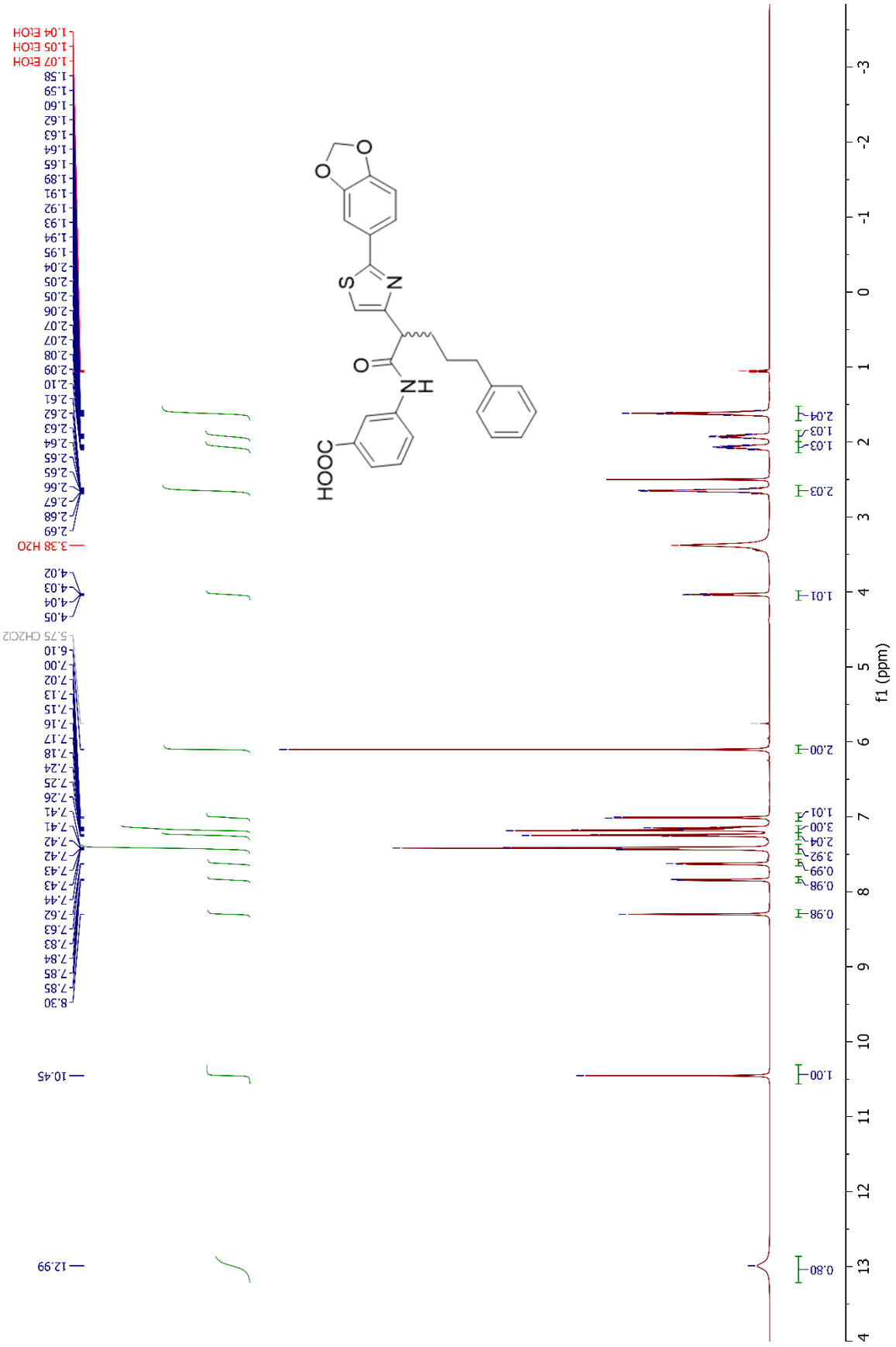
HOOC
f1 (ppm)

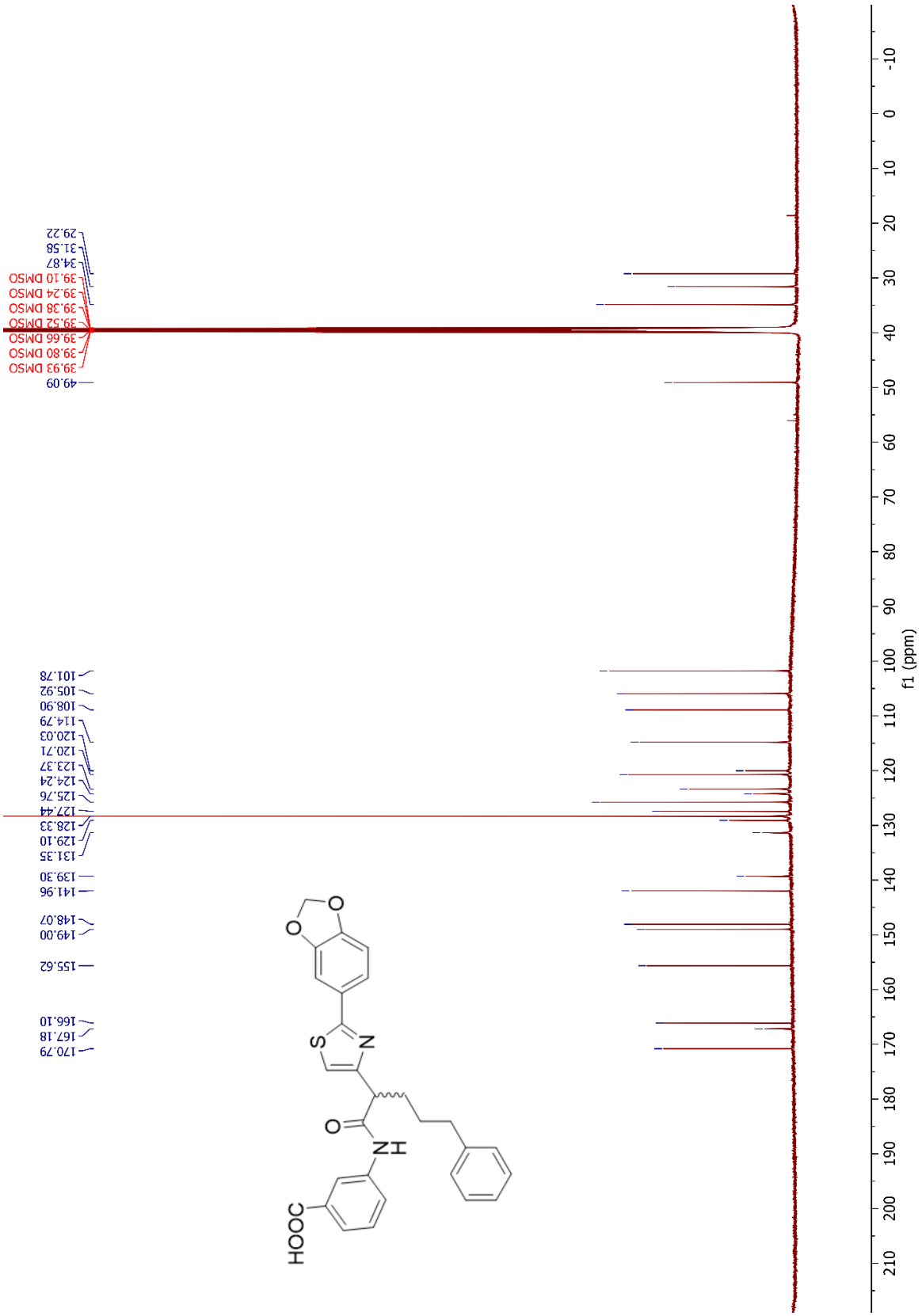
29.22
31.58
34.87
39.10 DMSO
39.24 DMSO
39.38 DMSO
39.52 DMSO
39.66 DMSO
39.80 DMSO
39.93 DMSO
49.09
101.78
105.92
108.90
114.79
120.03
120.71
123.37
124.24
125.76
127.44
128.33
129.10
131.35
139.30
141.96
148.07
149.00
155.62
166.10
167.18
170.79
HOOC
HN
O
S
N
O
O
f1 (ppm)

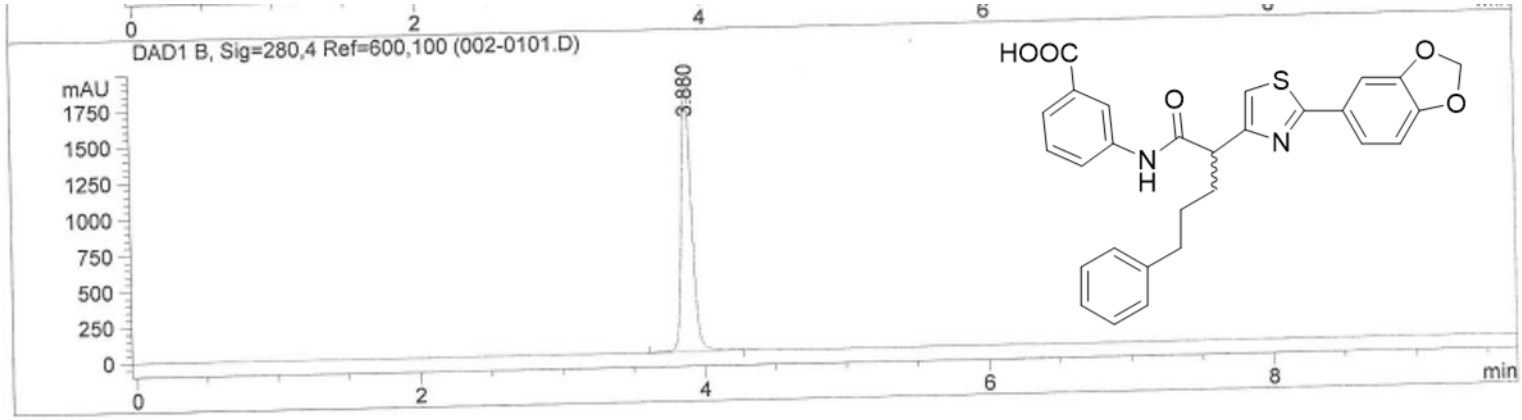


Signal 2: DAD1 B, Sig=280,4 Ref=600,100

| Peak # | RetTime [min] | Type | Width [min] | Area [mAU*s] | Height [mAU] | Area % |
|---|---|---|---|---|---|---|
| 1 | 3.880 | BB | 0.0758 | 9455.29004 | 1907.93628 | 100.0000 |
| Totals : | | | | 9455.29004 | 1907.93628 | |

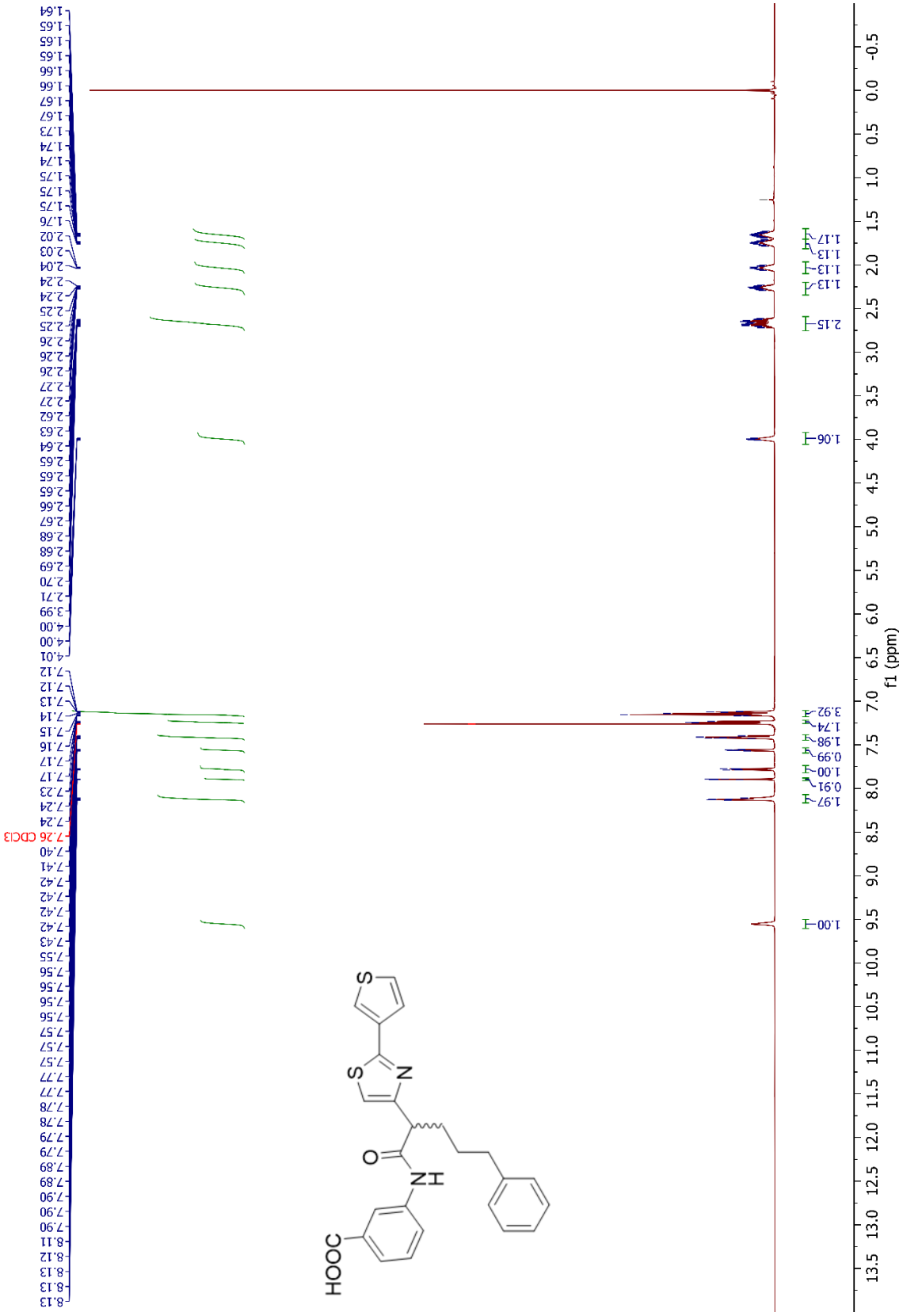
f1 (ppm)
CDCl3
HOOC
O
NH
S
N

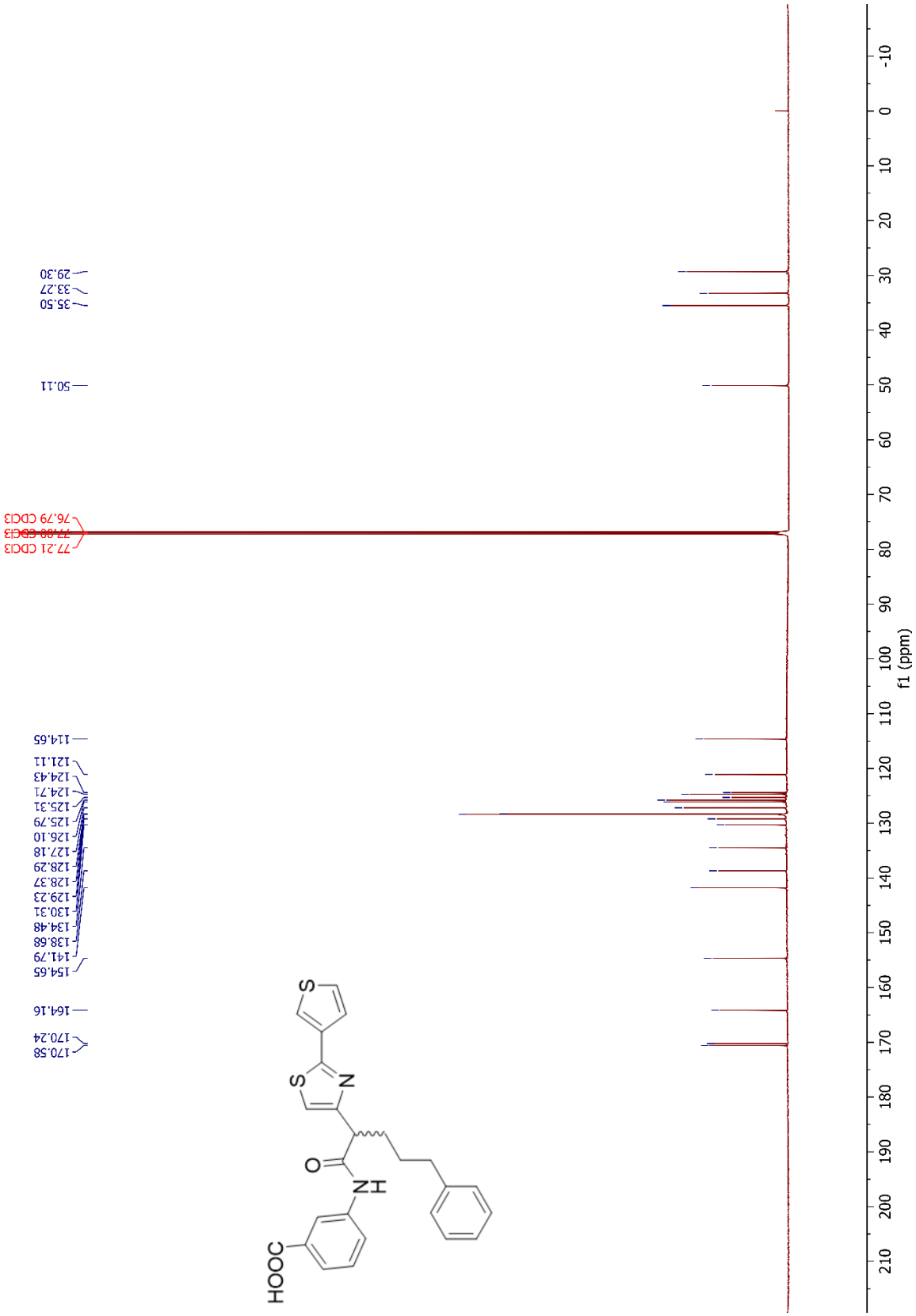
29.30
33.27
35.50
50.11
76.79 CDCl3
77.00 CDCl3
77.21 CDCl3
114.65
121.11
124.43
124.71
125.31
125.79
126.10
127.18
128.29
128.37
129.23
130.31
134.48
138.68
141.79
154.65
164.16
170.24
170.58
HOOC
O
HN
N
S
S
f1 (ppm)

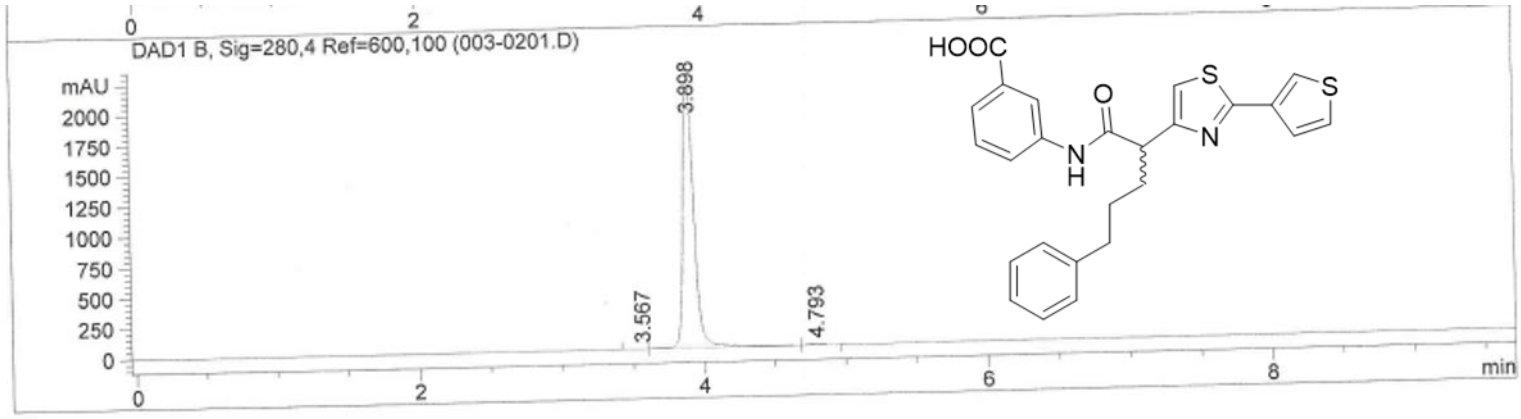


Signal 2: DAD1 B, Sig=280,4 Ref=600,100

| Peak # | RetTime [min] | Type | Width [min] | Area [mAU*s] | Height [mAU] | Area % |
|---|---|---|---|---|---|---|
| 1 | 3.567 | BV | 0.0722 | 8.19277 | 1.53612 | 0.0684 |
| 2 | 3.898 | VV | 0.0817 | 1.19216e4 | 2255.19604 | 99.4999 |
| 3 | 4.793 | VB | 0.0949 | 51.72743 | 8.05692 | 0.4317 |
| Totals : | | | | 1.19815e4 | 2264.78909 | |

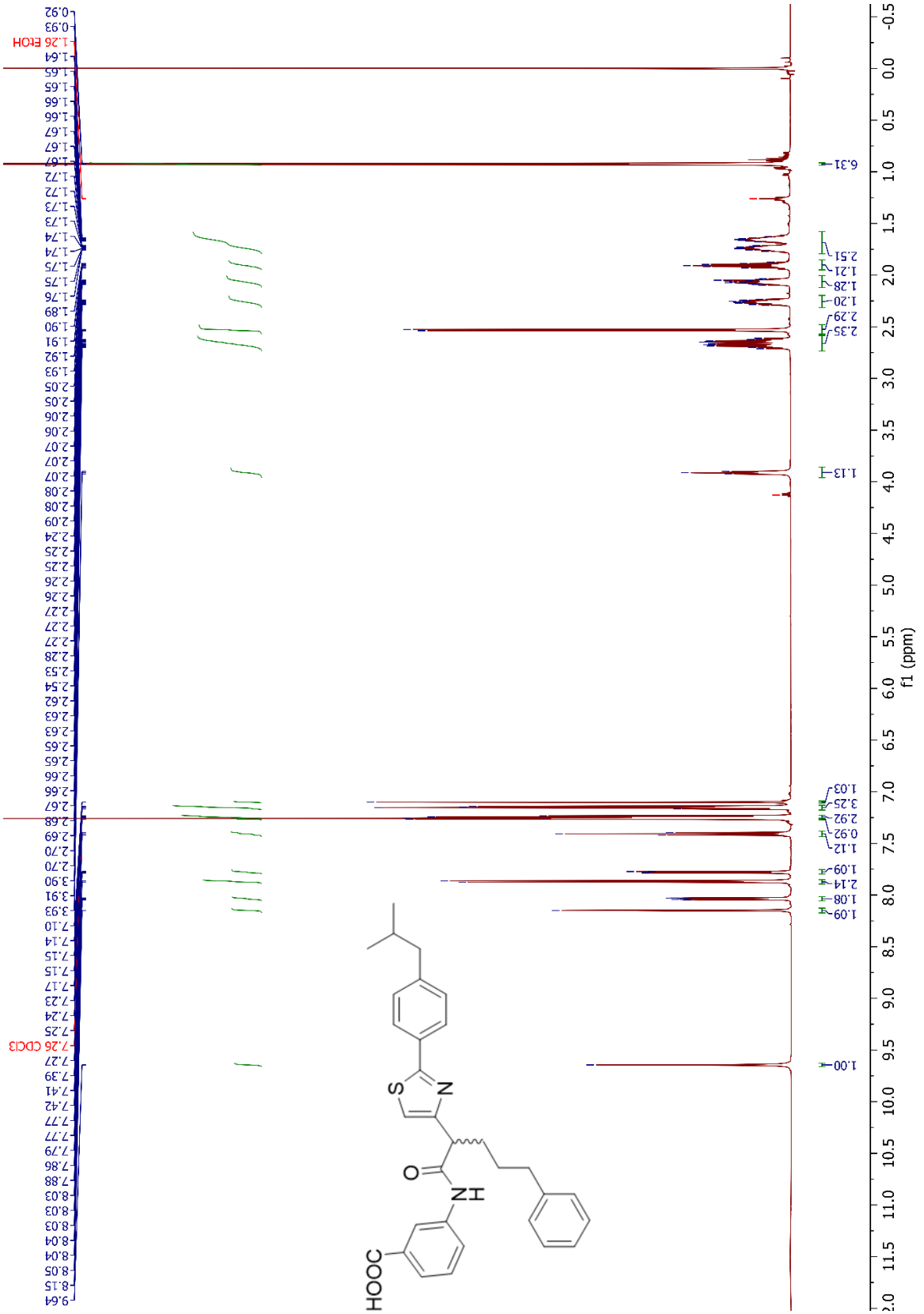
1.26 EtOH
7.26 CDCl3
HOOC
HN
O
N
S
f1 (ppm)

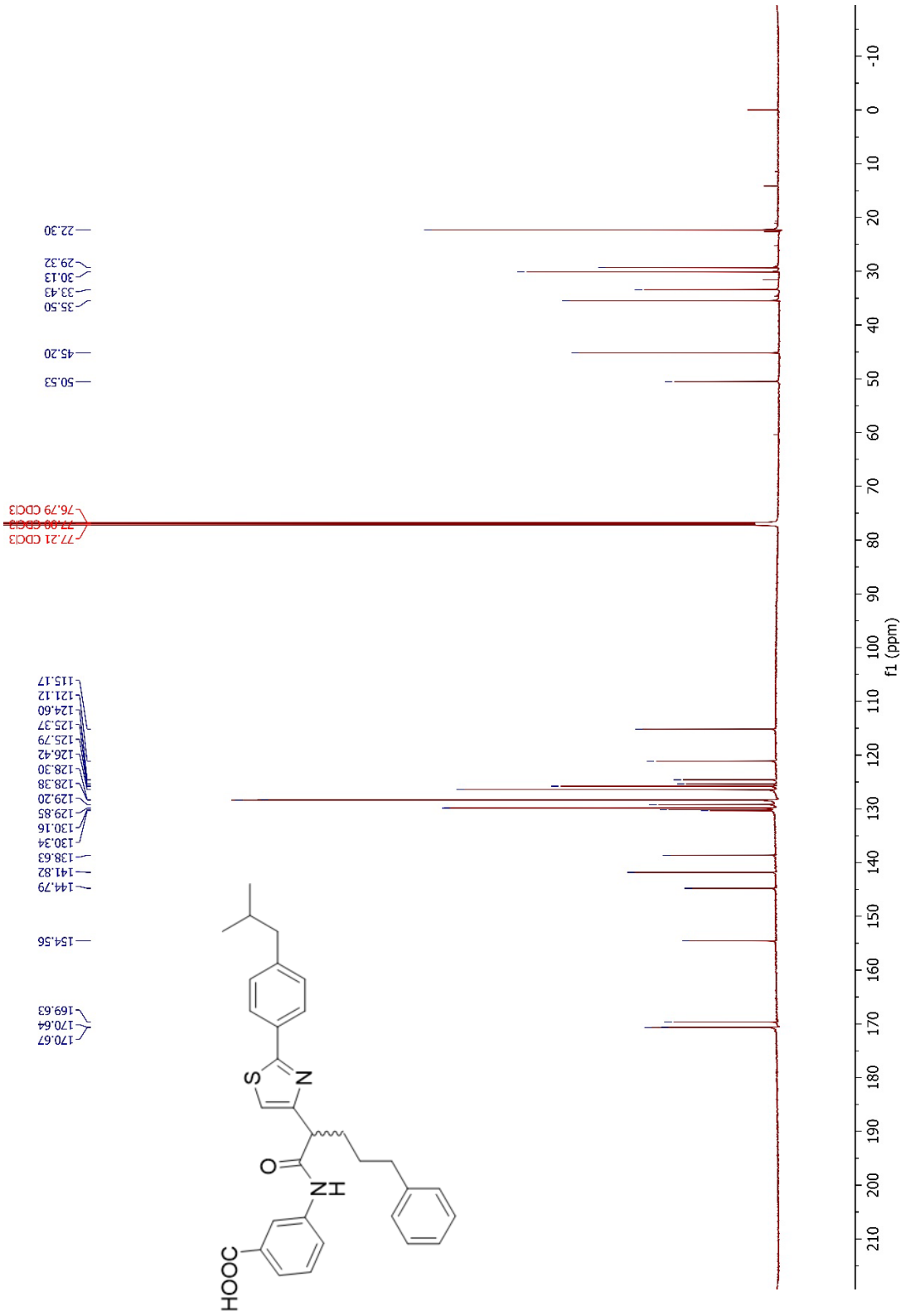
22.30
29.32
30.13
33.43
35.50
45.20
50.53
76.79 CDCl3
77.00 CDCl3
77.21 CDCl3
115.17
121.12
124.60
125.37
125.79
126.42
128.30
128.38
129.20
129.85
130.16
130.34
138.63
141.82
144.79
154.56
169.63
170.64
170.67
HOOC
HN
O
N
S
f1 (ppm)

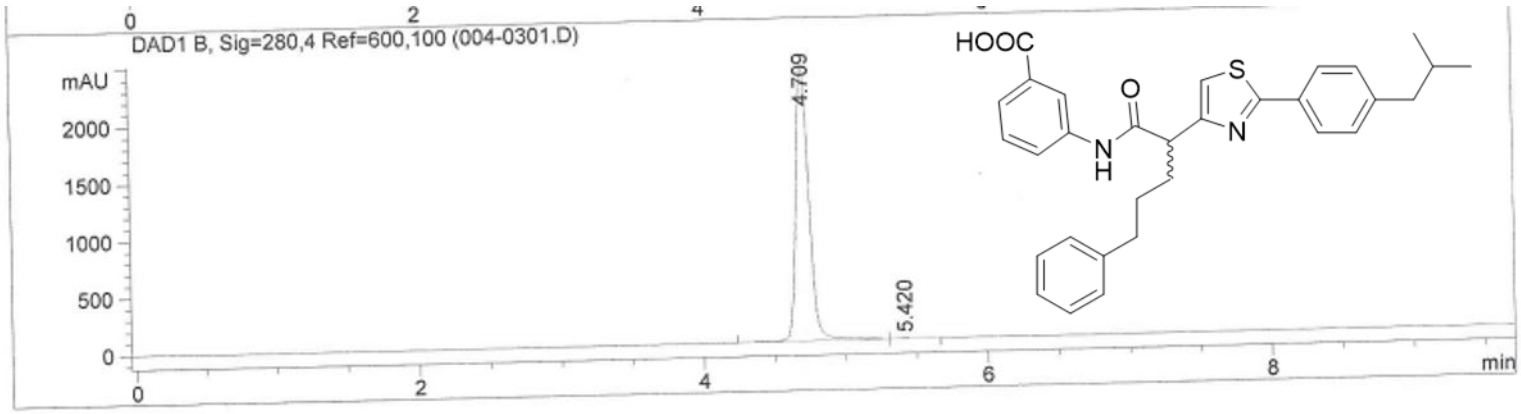


Signal 2: DAD1 B, Sig=280,4 Ref=600,100

| Peak # | RetTime [min] | Type | Width [min] | Area [mAU*s] | Height [mAU] | Area % |
|---|---|---|---|---|---|---|
| 1 | 4.709 | VV | 0.1011 | 1.54712e4 | 2402.83911 | 99.7942 |
| 2 | 5.420 | VB | 0.1767 | 31.90016 | 2.43776 | 0.2058 |
| Totals : | | | | 1.55031e4 | 2405.27687 | |

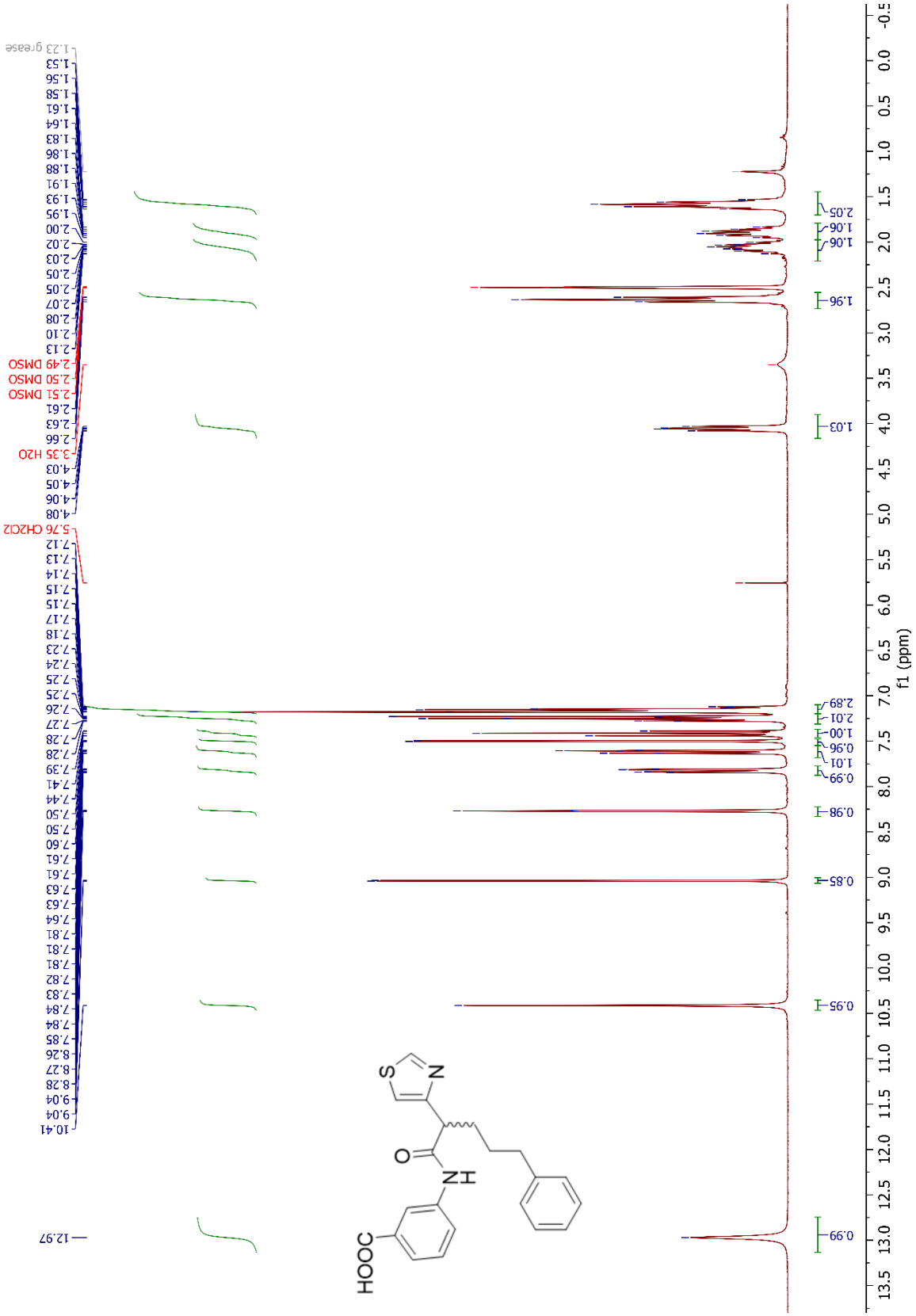
f1 (ppm)
HOOC
HN
O
S
N

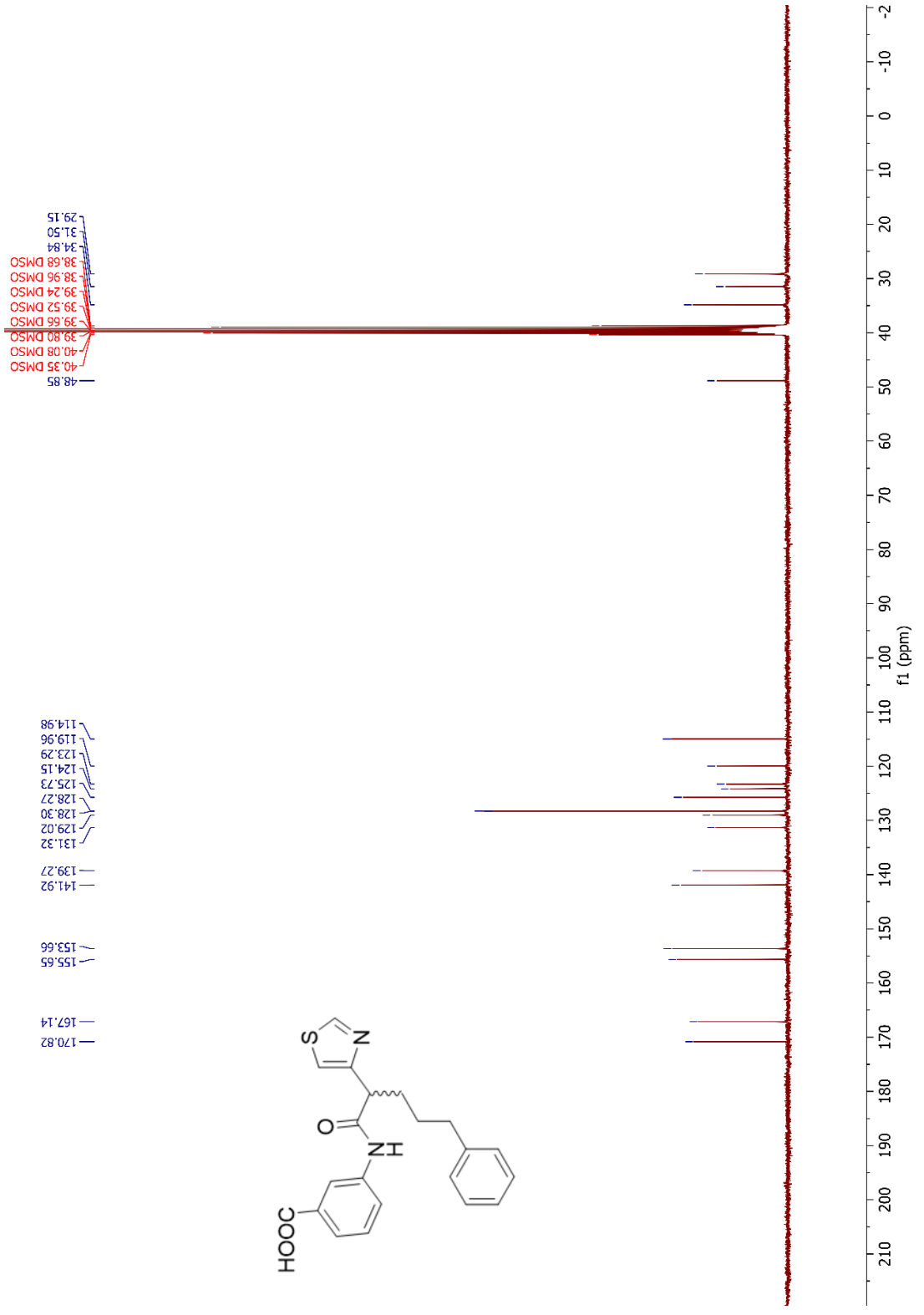
29.15
31.50
34.84
38.68 DMSO
38.96 DMSO
39.24 DMSO
39.52 DMSO
39.66 DMSO
39.80 DMSO
40.08 DMSO
40.35 DMSO
48.85
114.98
119.96
123.29
124.15
125.73
128.27
128.30
129.02
131.32
139.27
141.92
153.66
155.65
167.14
170.82
HOOC
HN
O
S
N
f1 (ppm)

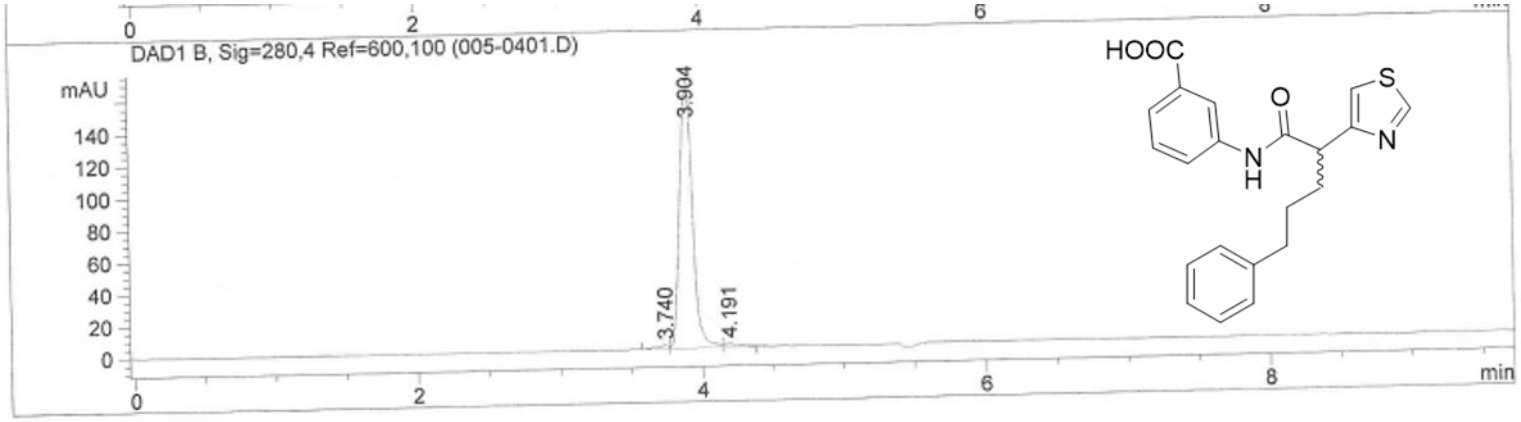


Signal 2: DAD1 B, Sig=280,4 Ref=600,100

| Peak # | RetTime [min] | Type | Width [min] | Area [mAU*s] | Height [mAU] | Area % |
|---|---|---|---|---|---|---|
| 1 | 3.740 | BV | 0.0852 | 13.79842 | 2.14023 | 1.2765 |
| 2 | 3.904 | VV | 0.1026 | 1050.46130 | 168.77782 | 97.1793 |
| 3 | 4.191 | VB | 0.1027 | 16.69147 | 2.19577 | 1.5441 |
| Totals : | | | | 1080.95120 | 173.11382 | |

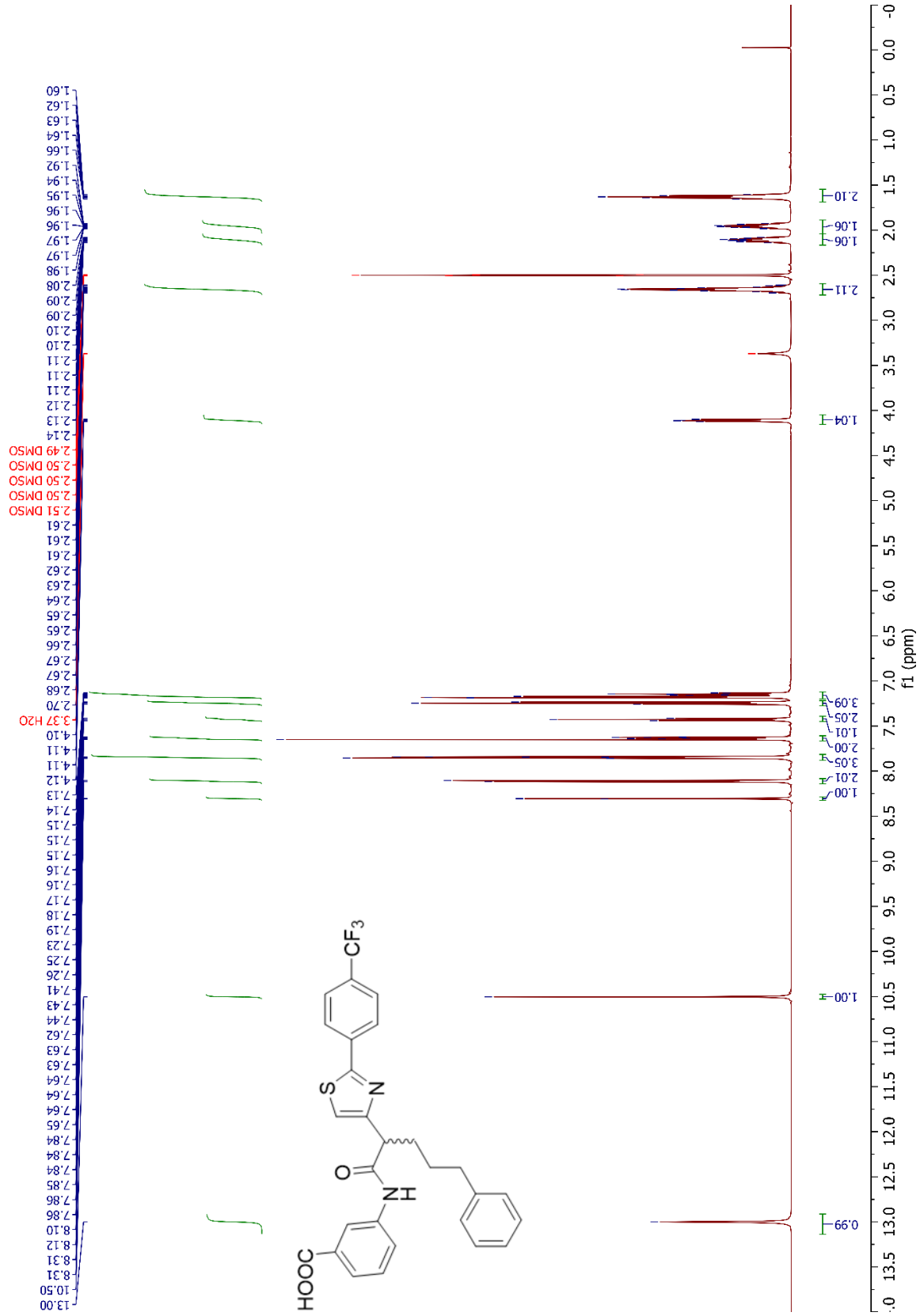
f1 (ppm)
2.10
1.06
1.06
2.11
1.04
3.09
2.05
1.01
2.00
3.05
2.01
1.00
1.00
0.99
2.49 DMSO
2.50 DMSO
2.50 DMSO
2.50 DMSO
2.51 DMSO
3.37 H2O
CF3
S
N
O
NH
HOOC

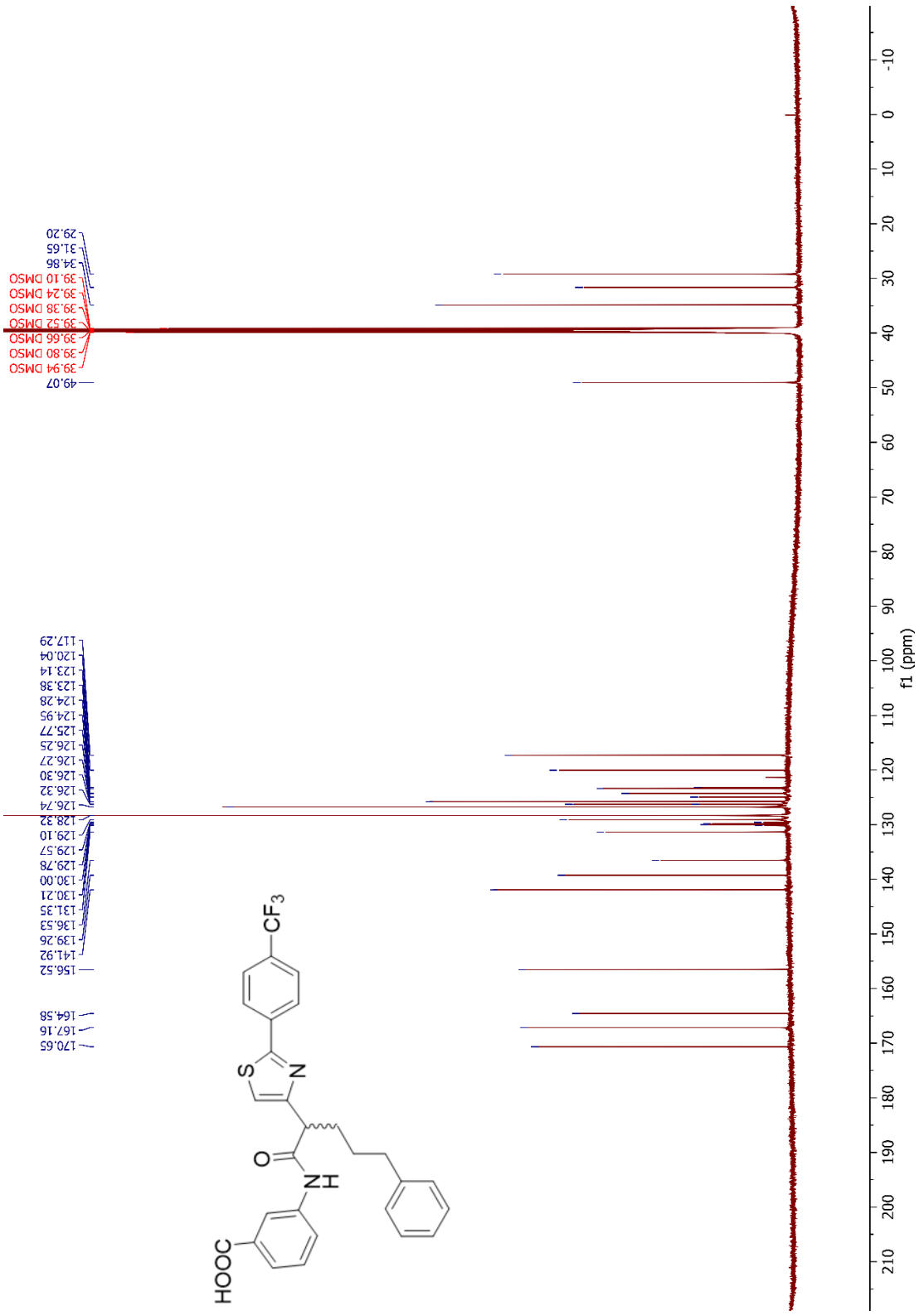
29.20
31.65
34.86
39.10 DMSO
39.24 DMSO
39.38 DMSO
39.52 DMSO
39.66 DMSO
39.80 DMSO
39.94 DMSO
49.07
117.29
120.04
123.14
123.38
124.28
124.95
125.77
126.25
126.27
126.30
126.32
126.74
128.32
129.10
129.57
129.78
130.00
130.21
131.35
136.53
139.26
141.92
156.52
164.58
167.16
170.65
CF3
S
N
O
NH
HOOC
f1 (ppm)

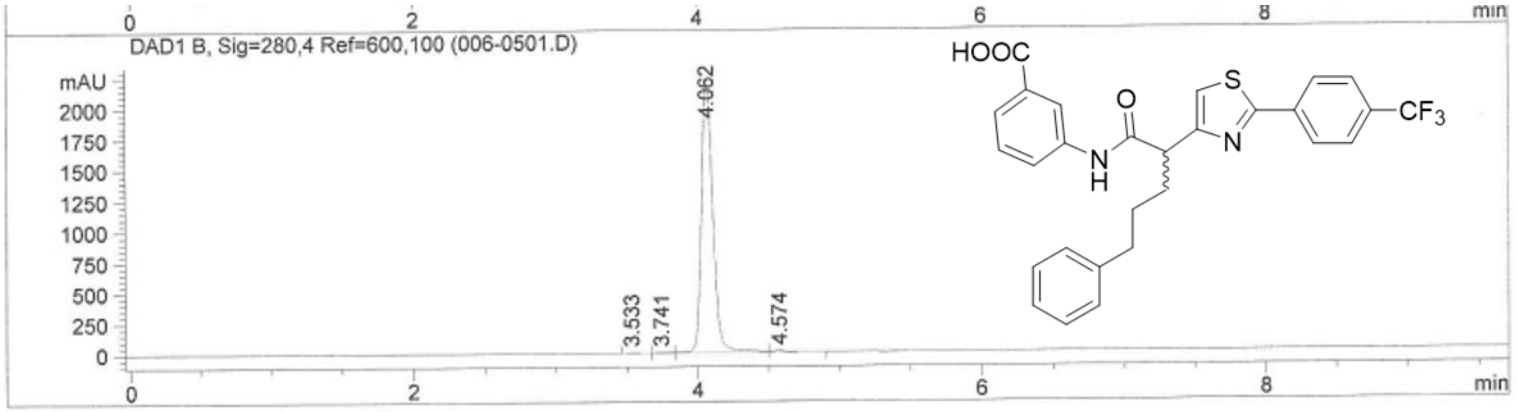


Signal 2: DAD1 B, Sig=280,4 Ref=600,100

| Peak # | RetTime [min] | Type | Width [min] | Area [mAU*s] | Height [mAU] | Area % |
|---|---|---|---|---|---|---|
| 1 | 3.533 | BV | 0.1105 | 18.52796 | 2.19373 | 0.1473 |
| 2 | 3.741 | VV | 0.1021 | 29.01798 | 4.33427 | 0.2307 |
| 3 | 4.062 | VV | 0.0871 | 1.24399e4 | 2230.73730 | 98.8799 |
| 4 | 4.574 | VB | 0.1380 | 93.36695 | 9.22827 | 0.7421 |
| Totals : | | | | 1.25809e4 | 2246.49357 | |

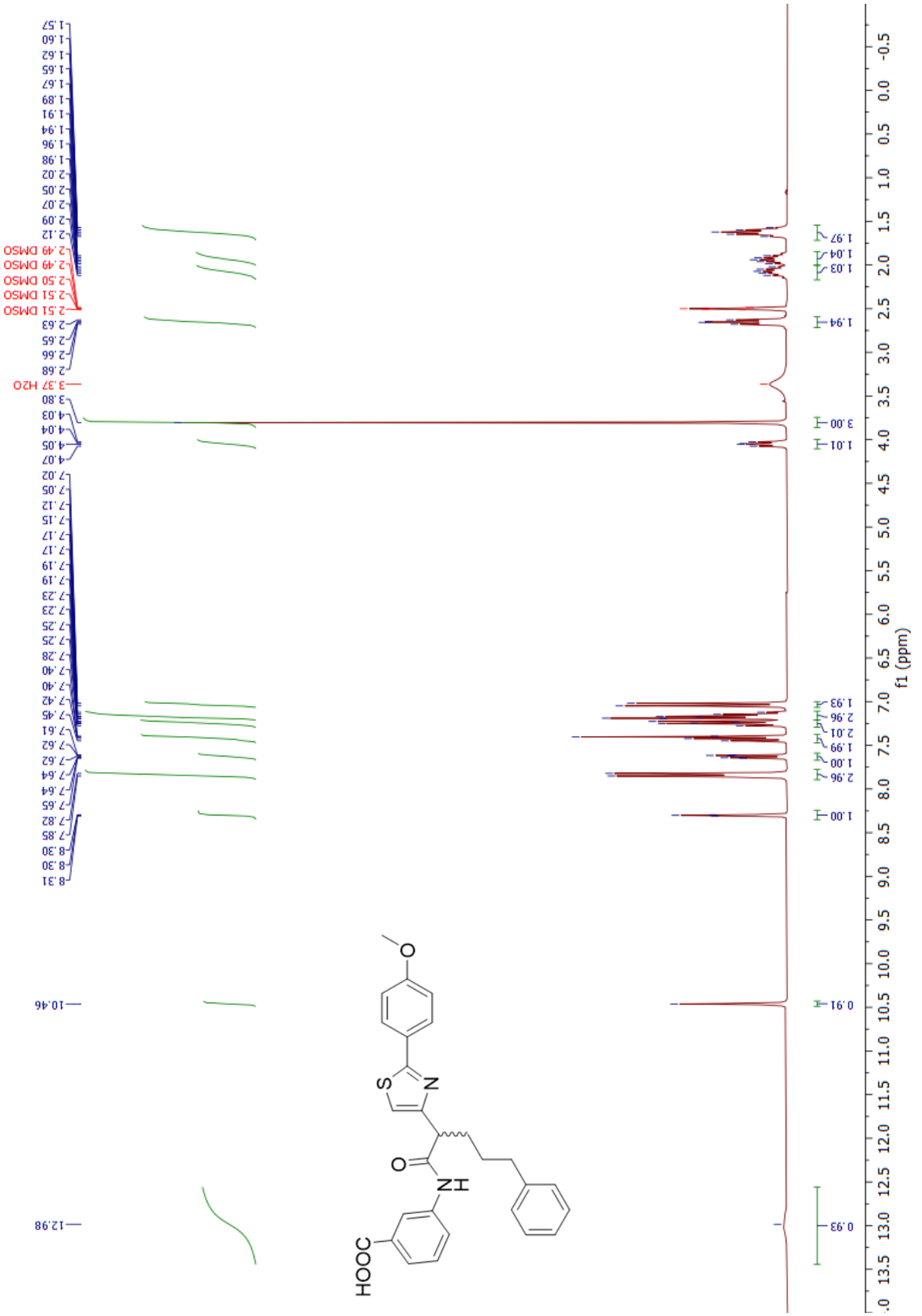
HOOC
HN
O
S
N
O
f1 (ppm)

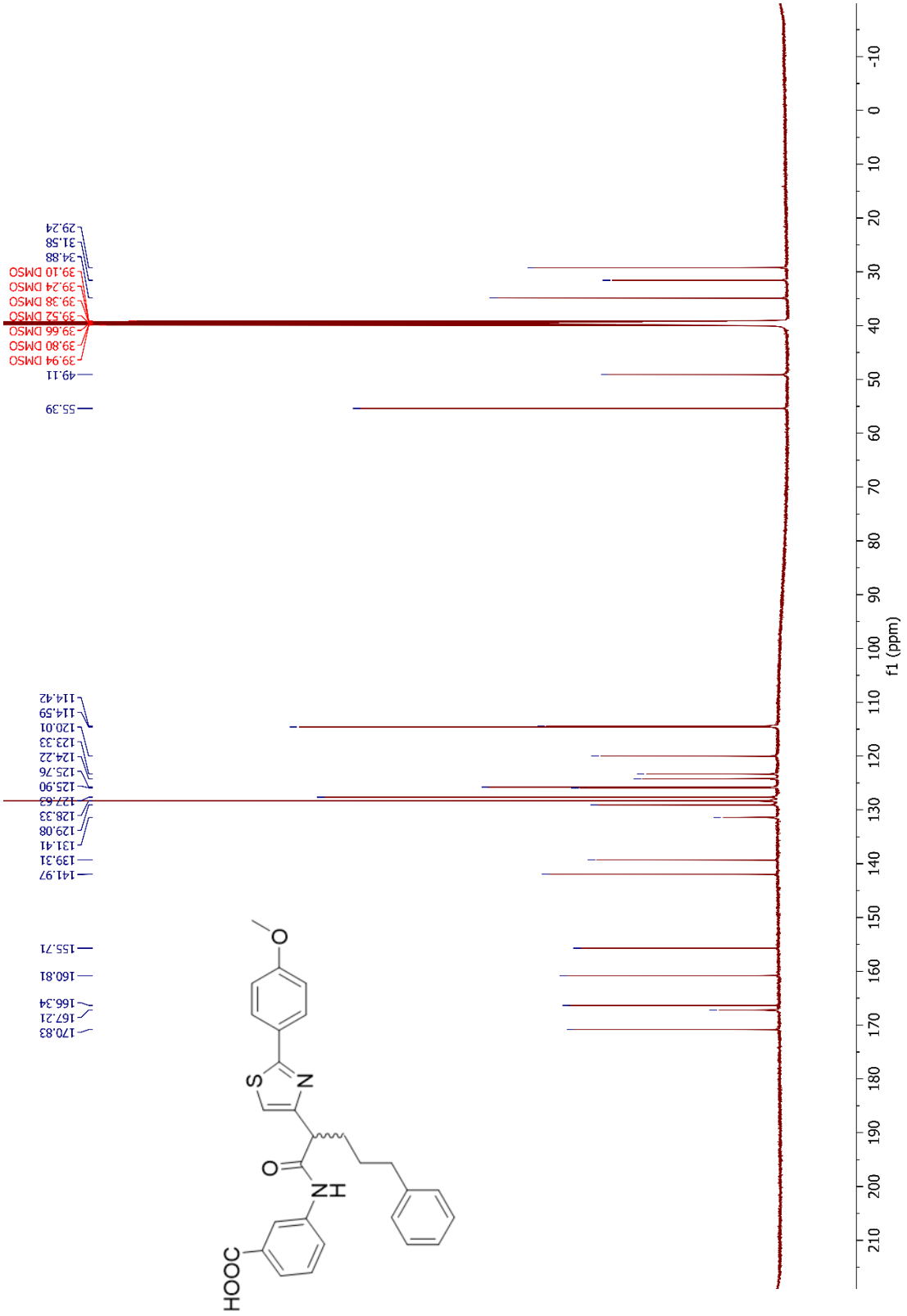
29.24
31.58
34.88
39.10 DMSO
39.24 DMSO
39.38 DMSO
39.52 DMSO
39.66 DMSO
39.80 DMSO
39.94 DMSO
49.11
55.39
114.42
114.59
120.01
123.33
124.22
125.76
125.90
127.63
128.33
129.08
131.41
139.31
141.97
155.71
160.81
166.34
167.21
170.83
HOOC
HN
O
S
N
O
f1 (ppm)

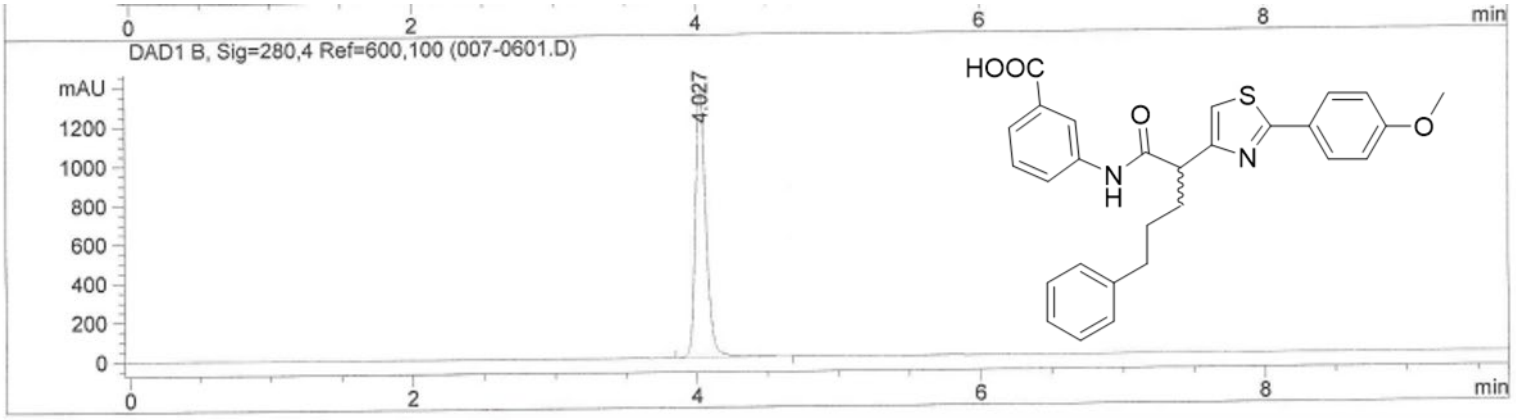


Signal 2: DAD1 B, Sig=280,4 Ref=600,100

| Peak # | RetTime [min] | Type | Width [min] | Area [mAU*s] | Height [mAU] | Area % |
|---|---|---|---|---|---|---|
| 1 | 4.027 | VB | 0.0777 | 7165.24707 | 1399.41467 | 100.0000 |
| Totals : | | | | 7165.24707 | 1399.41467 | |

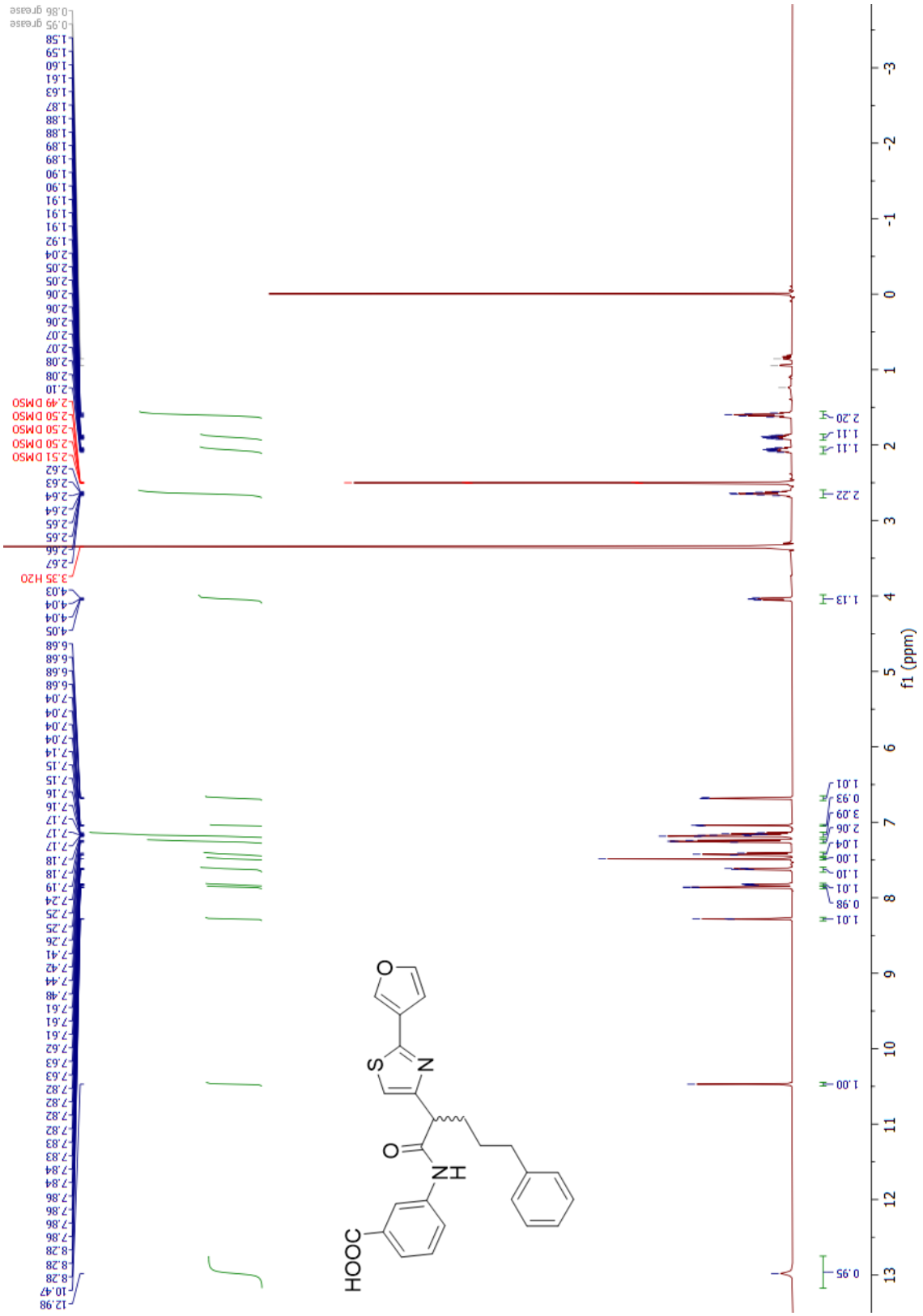
f1 (ppm)
HOOC
HN
O
S
N
O
3.35 H2O
2.49 DMSO
2.50 DMSO
2.51 DMSO

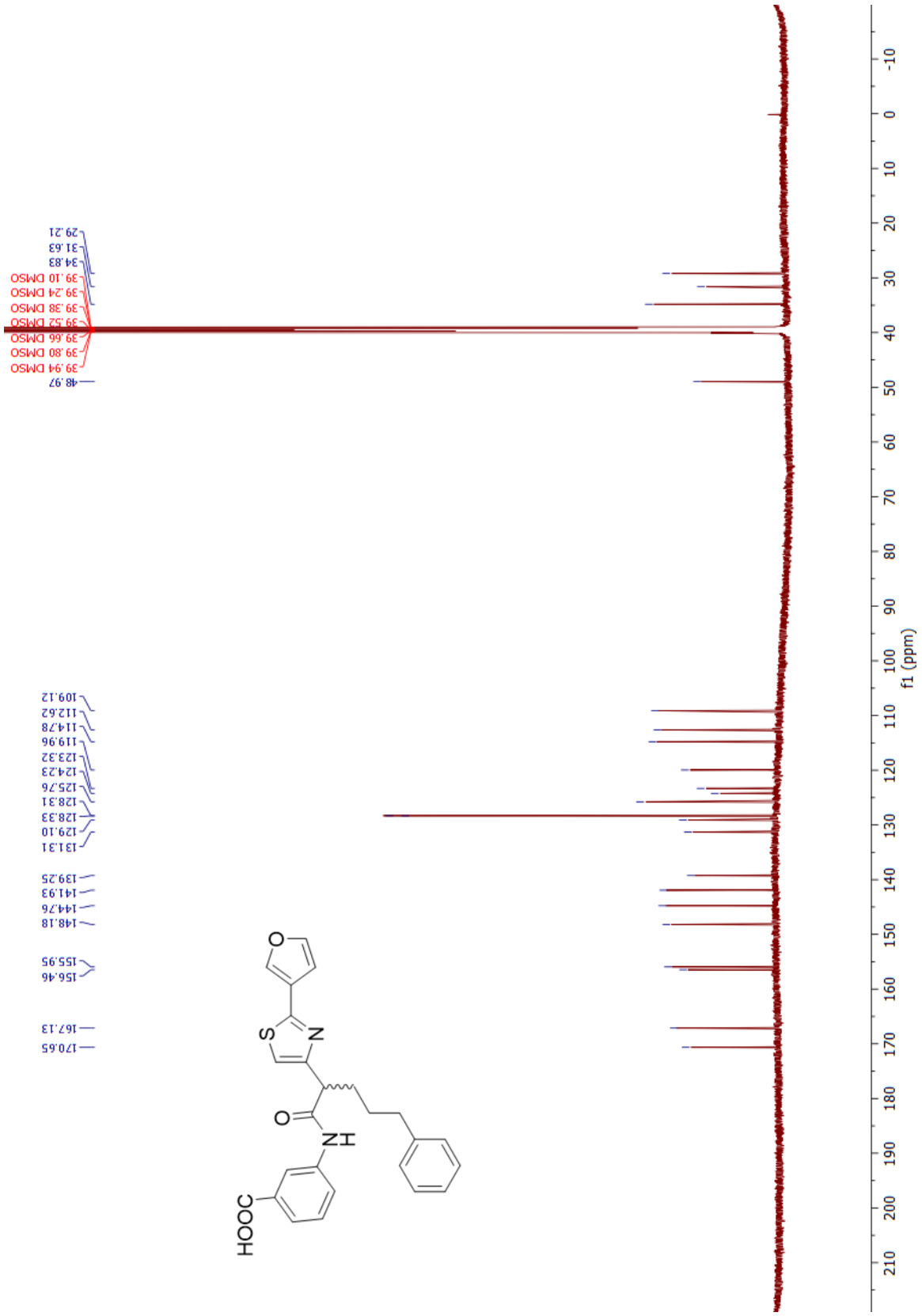
29.21
31.63
34.83
39.10 DMSO
39.24 DMSO
39.38 DMSO
39.52 DMSO
39.66 DMSO
39.80 DMSO
39.94 DMSO
48.97
109.12
112.62
114.78
119.96
123.32
124.23
125.76
128.31
128.33
129.10
131.31
139.25
141.93
144.76
148.18
155.95
156.46
167.13
170.65
O
S
N
O
HN
HOOC
-10
0
10
20
30
40
50
60
70
80
90
100
110
120
130
140
150
160
170
180
190
200
210
f1 (ppm)

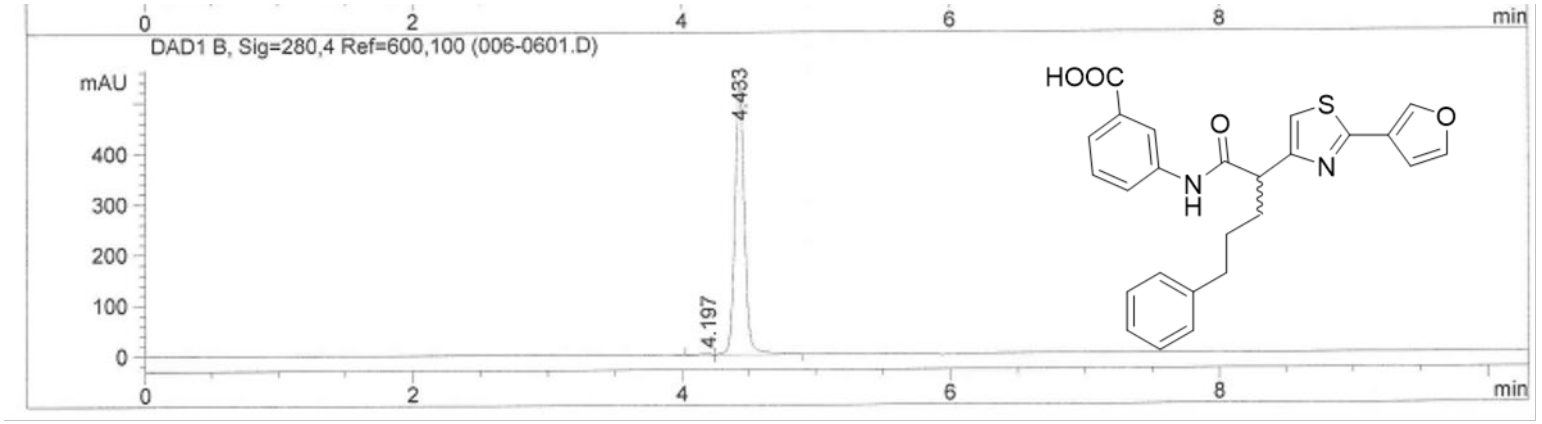


Signal 2: DAD1 B, Sig=280,4 Ref=600,100

| Peak # | RetTime [min] | Type | Width [min] | Area [mAU*s] | Height [mAU] | Area % |
|---|---|---|---|---|---|---|
| 1 | 4.197 | BV | 0.1013 | 18.09385 | 2.41715 | 0.6611 |
| 2 | 4.433 | VB | 0.0768 | 2718.97217 | 539.87805 | 99.3389 |
| Totals : | | | | 2737.06602 | 542.29520 | |

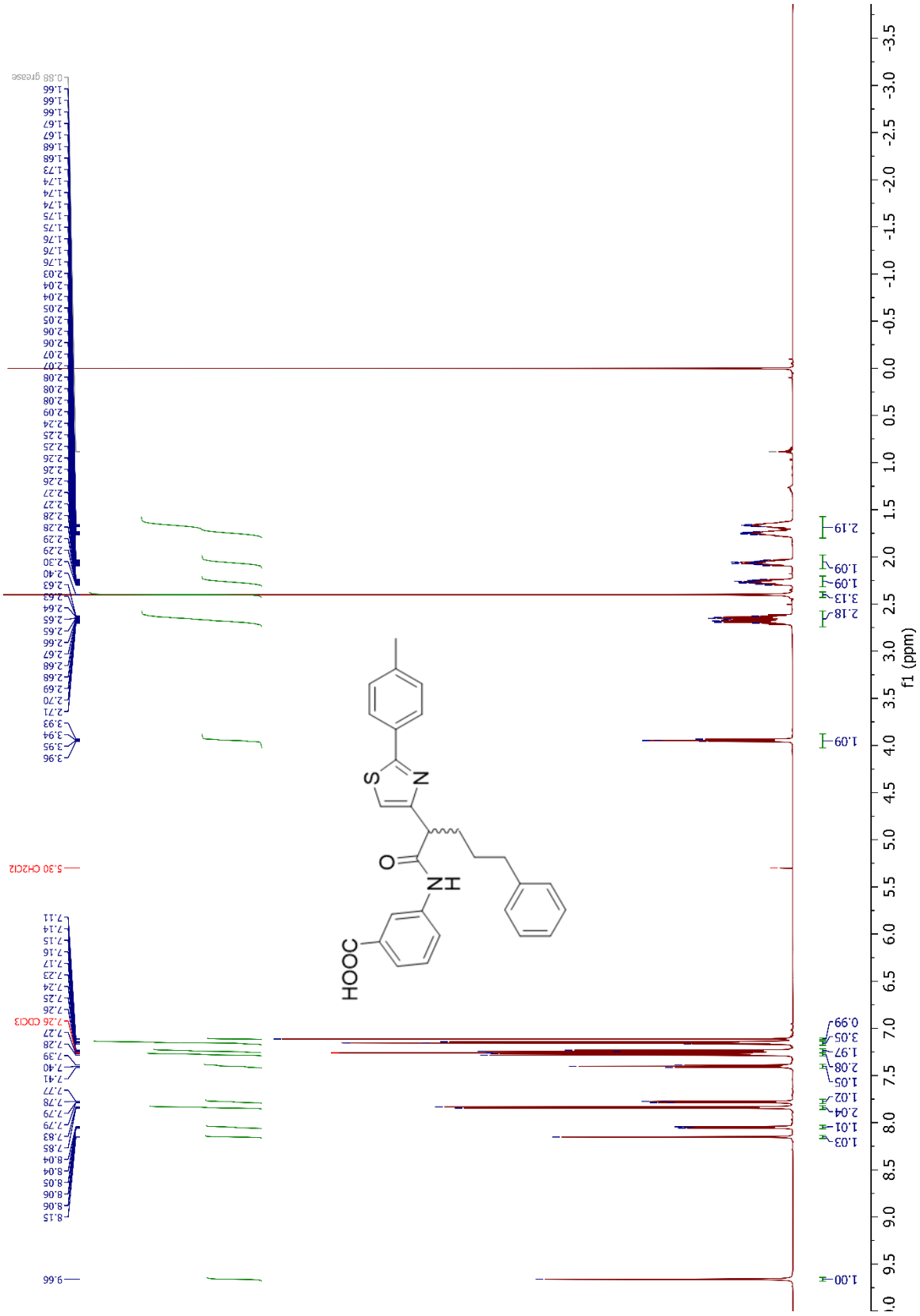
f1 (ppm)
HOOC
S
N
O
NH
5.30 CH2Cl2
7.26 CDCl3
0.88 grease

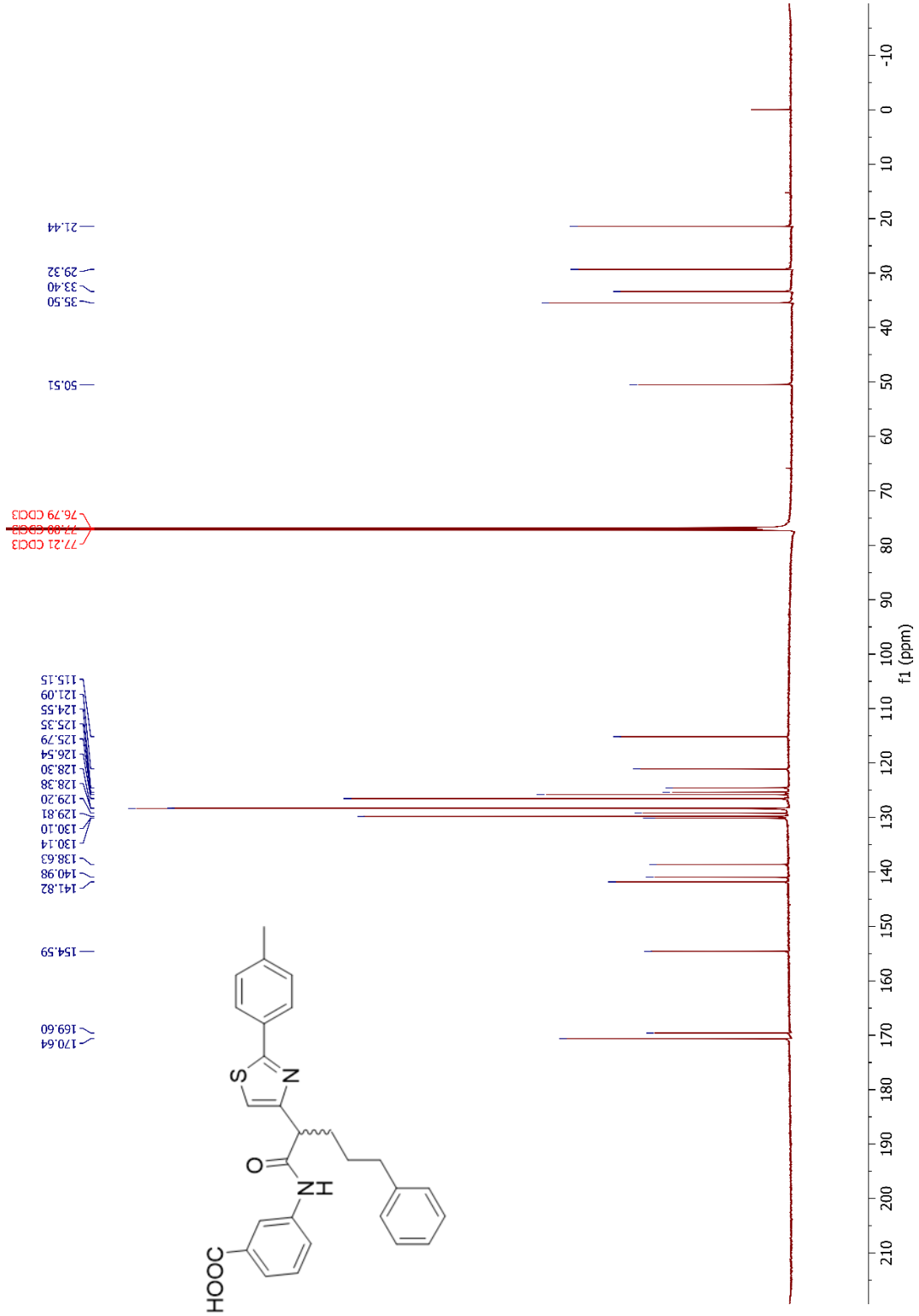
21.44
29.32
33.40
35.50
50.51
76.79 CDCl3
77.08 CDCl3
77.21 CDCl3
115.15
121.09
124.55
125.35
125.79
126.54
128.30
128.38
129.20
129.81
130.10
130.14
138.63
140.98
141.82
154.59
169.60
170.64
HOOC
NH
O
N
S
f1 (ppm)

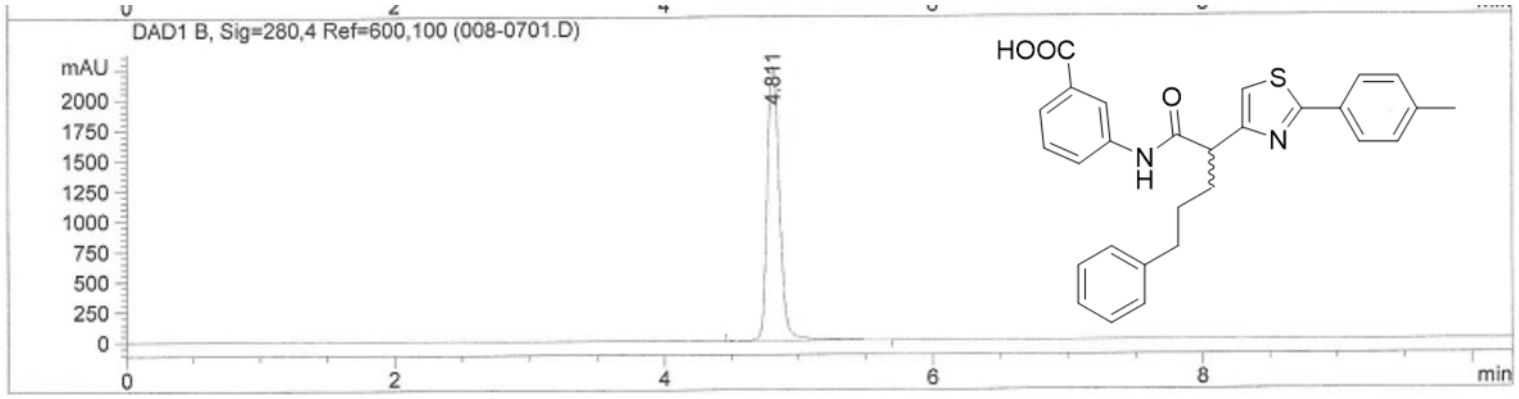


Signal 2: DAD1 B, Sig=280,4 Ref=600,100

| Peak # | RetTime [min] | Type | Width [min] | Area [mAU*s] | Height [mAU] | Area % |
|---|---|---|---|---|---|---|
| 1 | 4.811 | VB | 0.1003 | 1.44253e4 | 2266.00562 | 100.0000 |
| Totals : | | | | 1.44253e4 | 2266.00562 | |

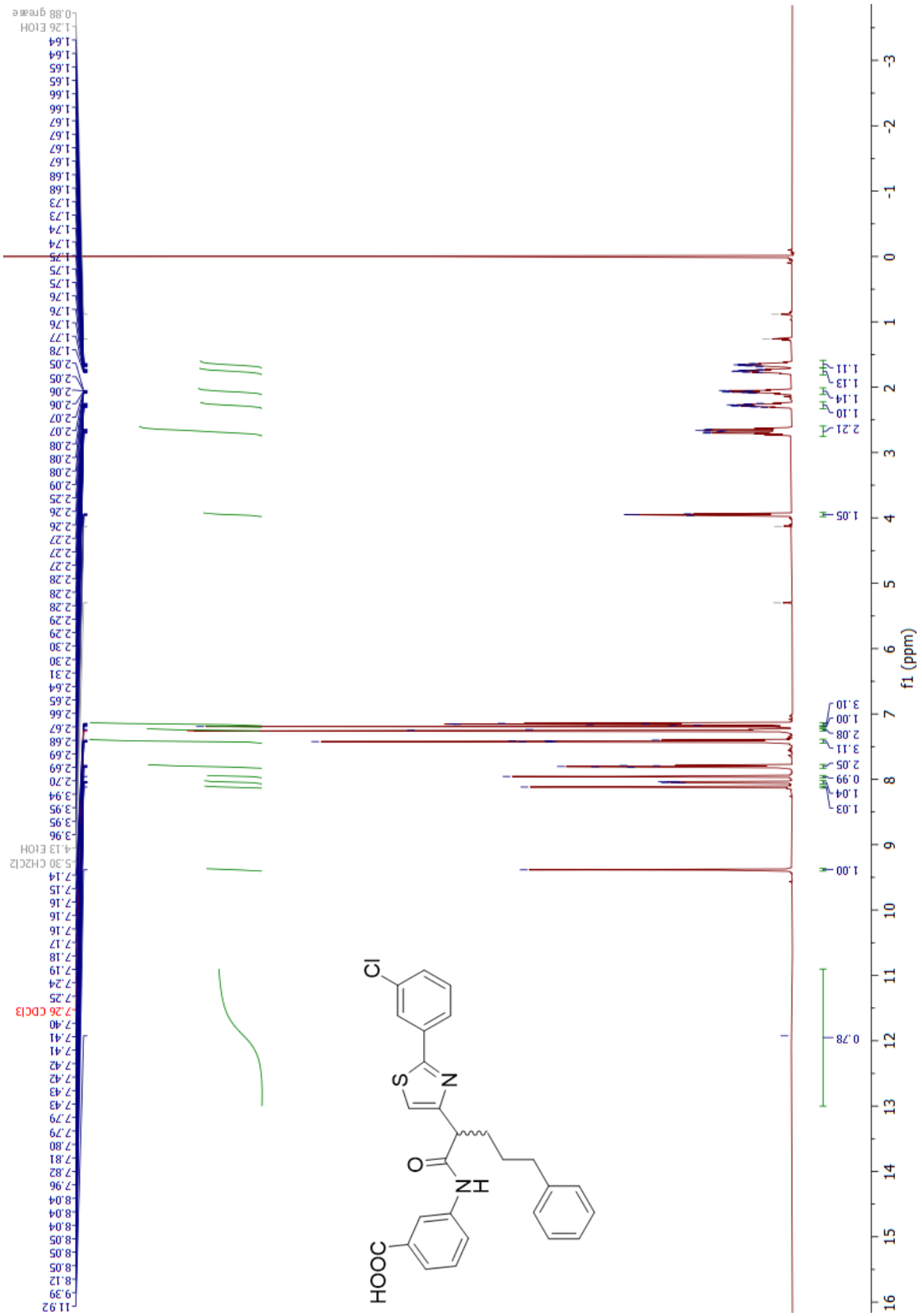
Cl
S
N
O
HN
HOOC
f1 (ppm)

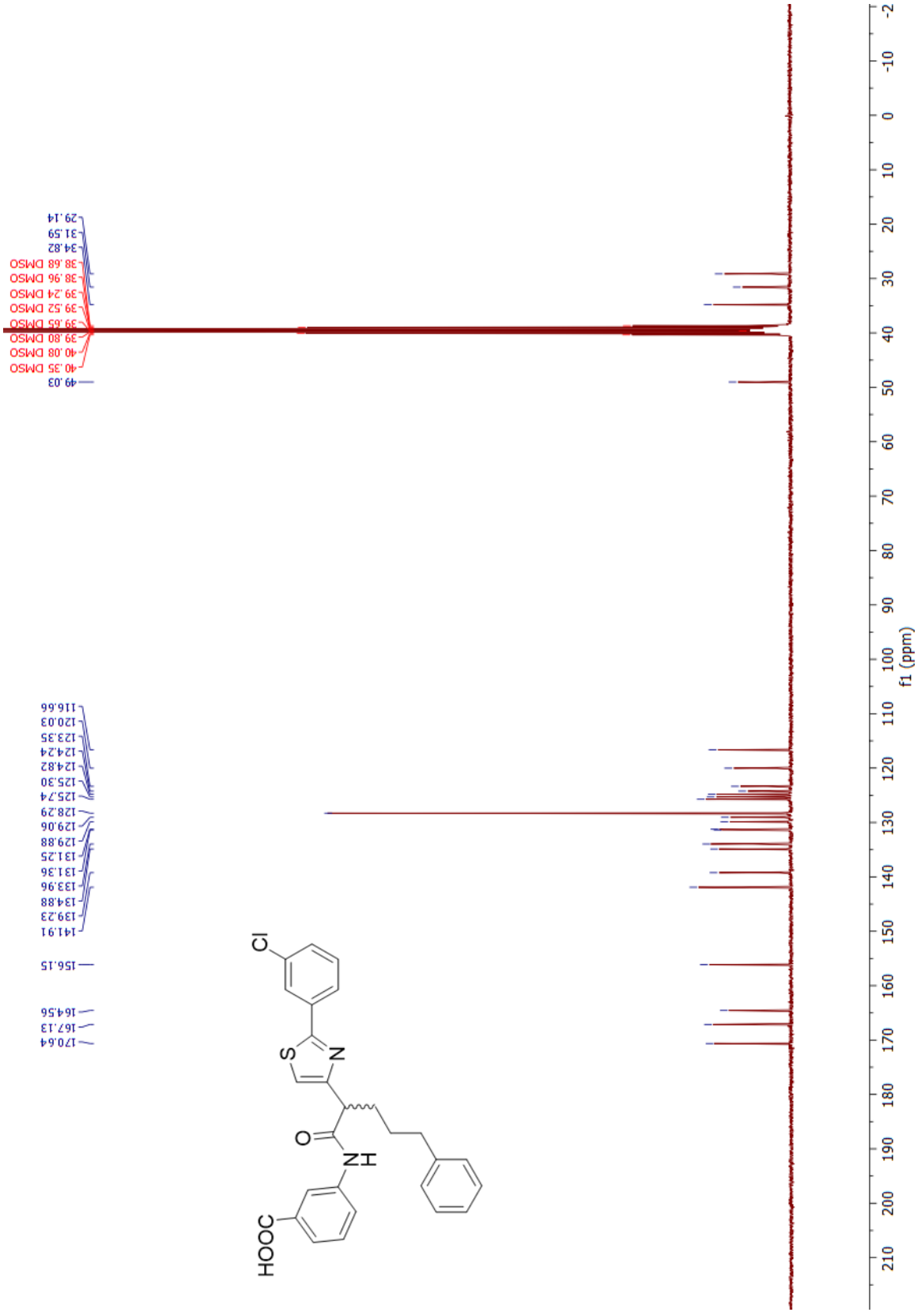
29.14
31.59
34.82
38.68 DMSO
38.96 DMSO
39.24 DMSO
39.52 DMSO
39.65 DMSO
39.80 DMSO
40.08 DMSO
40.35 DMSO
49.03
116.66
120.03
123.35
124.24
124.82
125.30
125.74
128.29
129.06
129.88
131.25
131.36
133.96
134.88
139.23
141.91
156.15
164.56
167.13
170.64
Cl
S
N
O
NH
HOOC
f1 (ppm)

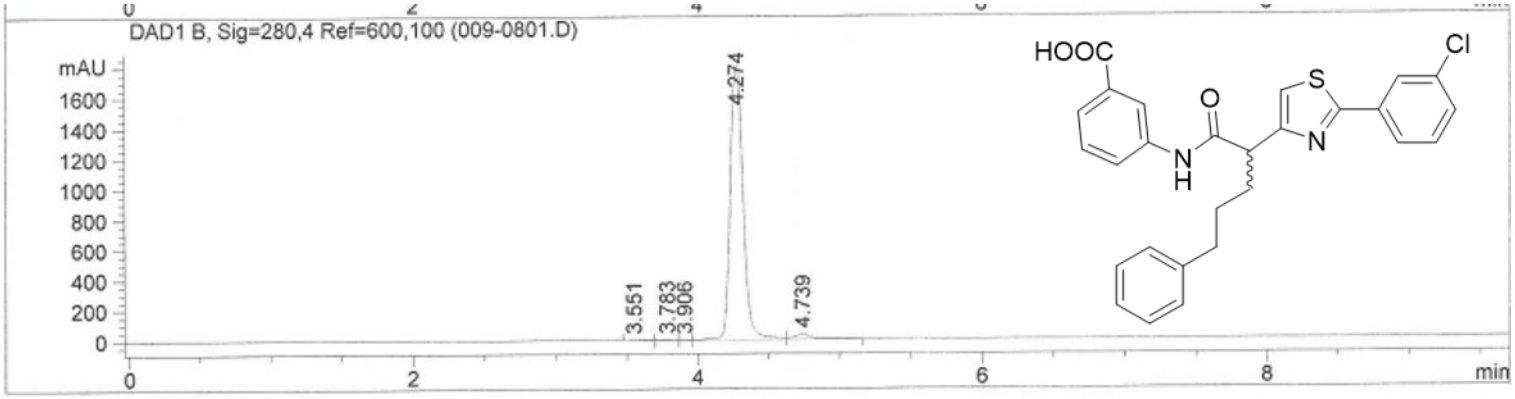


Signal 2: DAD1 B, Sig=280,4 Ref=600,100

| Peak # | RetTime [min] | Type | Width [min] | Area [mAU*s] | Height [mAU] | Area % |
|---|---|---|---|---|---|---|
| 1 | 3.551 | BV | 0.1408 | 19.35683 | 1.78031 | 0.1644 |
| 2 | 3.783 | VV | 0.1201 | 32.16793 | 4.35842 | 0.2732 |
| 3 | 3.906 | VV | 0.0756 | 13.52874 | 2.56384 | 0.1149 |
| 4 | 4.274 | VV | 0.0995 | 1.13845e4 | 1807.55298 | 96.7047 |
| 5 | 4.739 | VB | 0.1267 | 322.87875 | 36.69335 | 2.7427 |
| Totals : | | | | 1.17724e4 | 1852.94890 | |

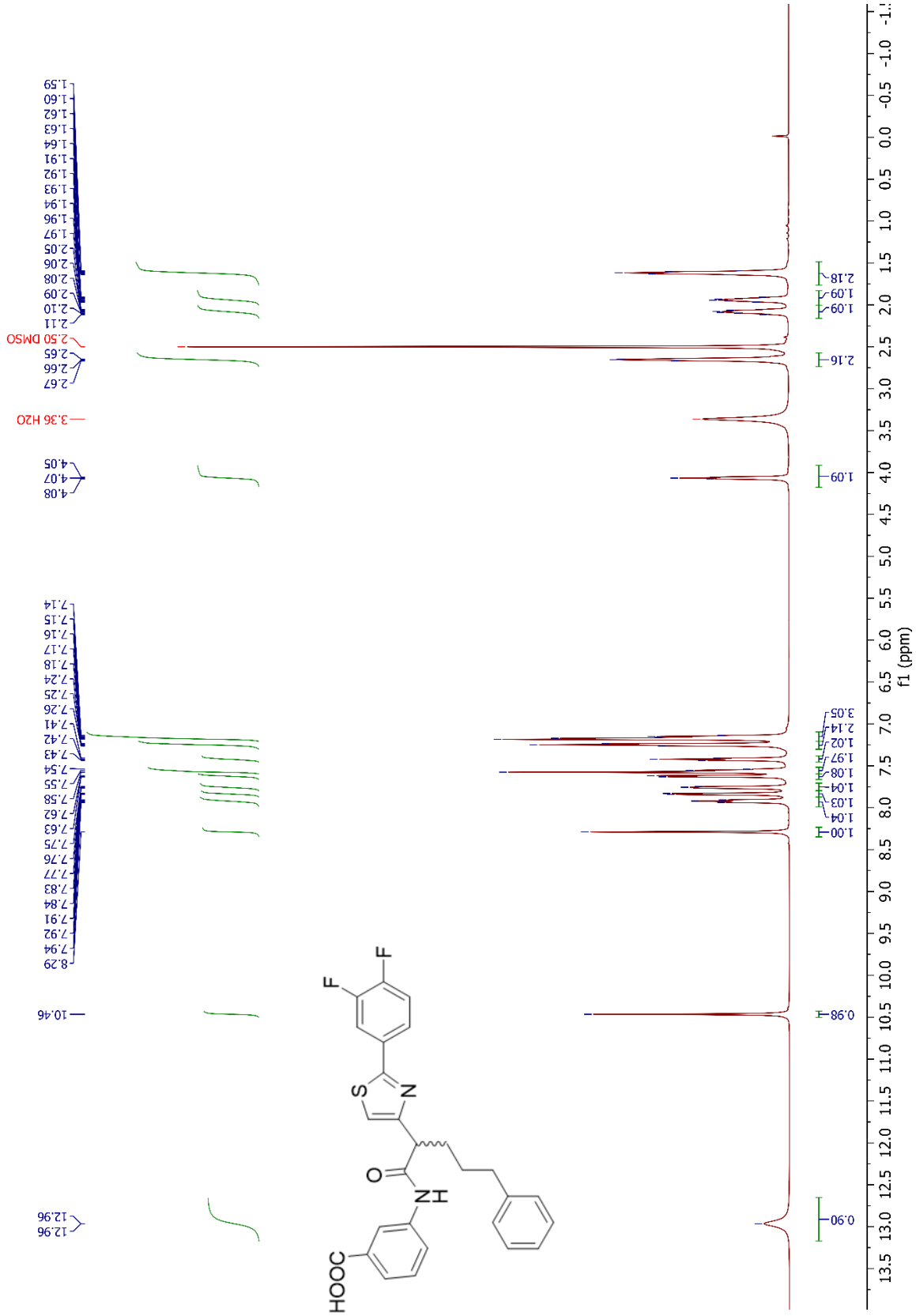
f1 (ppm)
HOOC
NH
O
N
S
F
F
12.96
10.46
8.29
7.94
7.92
7.91
7.84
7.83
7.77
7.76
7.75
7.63
7.62
7.58
7.55
7.54
7.43
7.42
7.41
7.26
7.25
7.24
7.18
7.17
7.16
7.15
7.14
4.08
4.07
4.05
3.36 H2O
2.67
2.66
2.65
2.50 DMSO
2.11
2.10
2.09
2.08
2.06
2.05
1.97
1.96
1.94
1.93
1.92
1.91
1.64
1.63
1.62
1.60
1.59
0.90
0.98
1.00
1.04
1.03
1.04
1.08
1.97
1.02
2.14
3.05
1.09
2.16
1.09
1.09
2.18

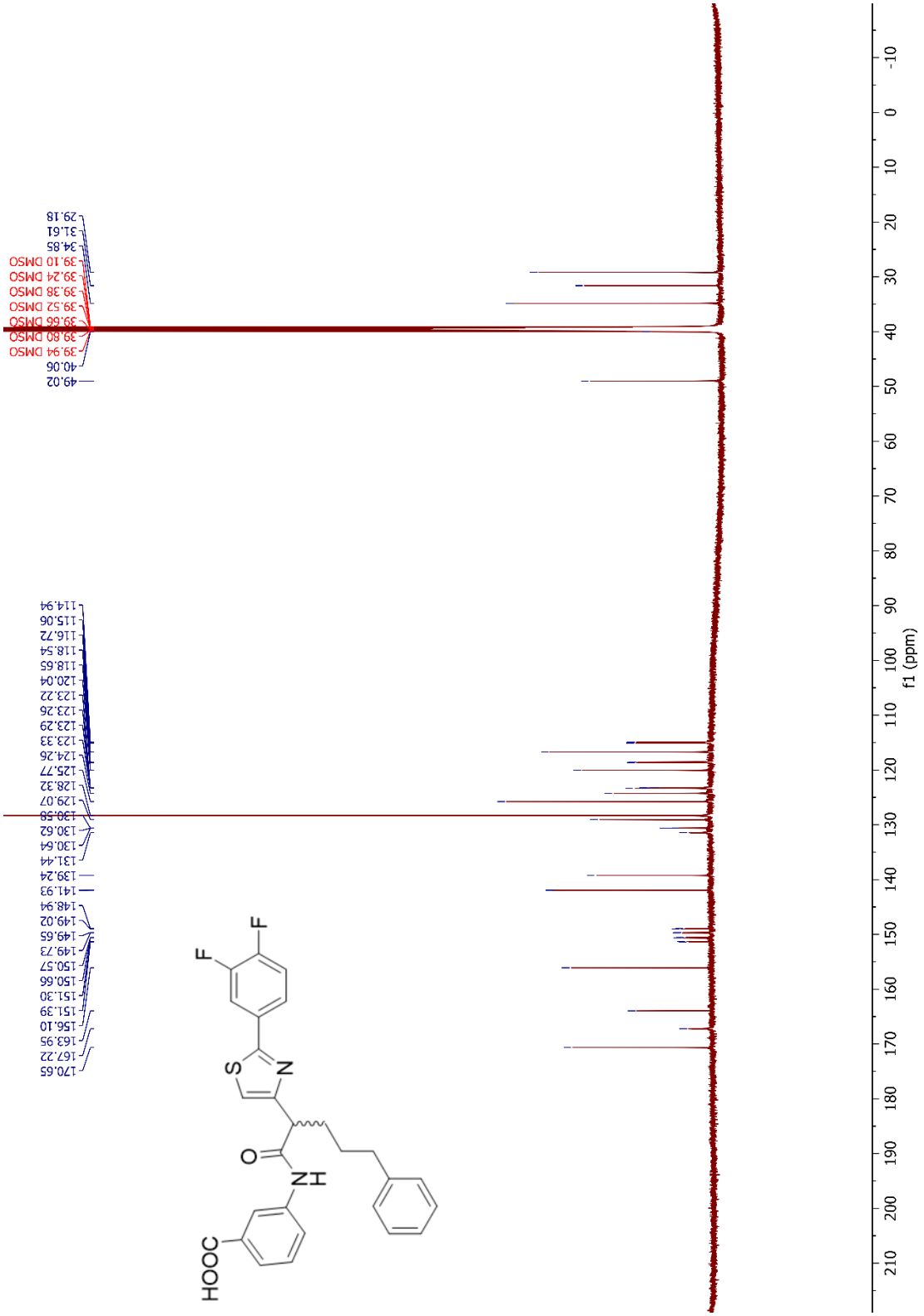
29.18
31.61
34.85
39.10 DMSO
39.24 DMSO
39.38 DMSO
39.52 DMSO
39.66 DMSO
39.80 DMSO
39.94 DMSO
40.06
49.02
114.94
115.06
116.72
118.54
118.65
120.04
123.22
123.26
123.29
123.33
124.26
125.77
128.32
129.07
130.58
130.62
130.64
131.44
139.24
141.93
148.94
149.02
149.65
149.73
150.57
150.66
151.30
151.39
156.10
163.95
167.22
170.65
F
F
S
N
O
NH
HOOC
-10
0
10
20
30
40
50
60
70
80
90
100
110
120
130
140
150
160
170
180
190
200
210
f1 (ppm)

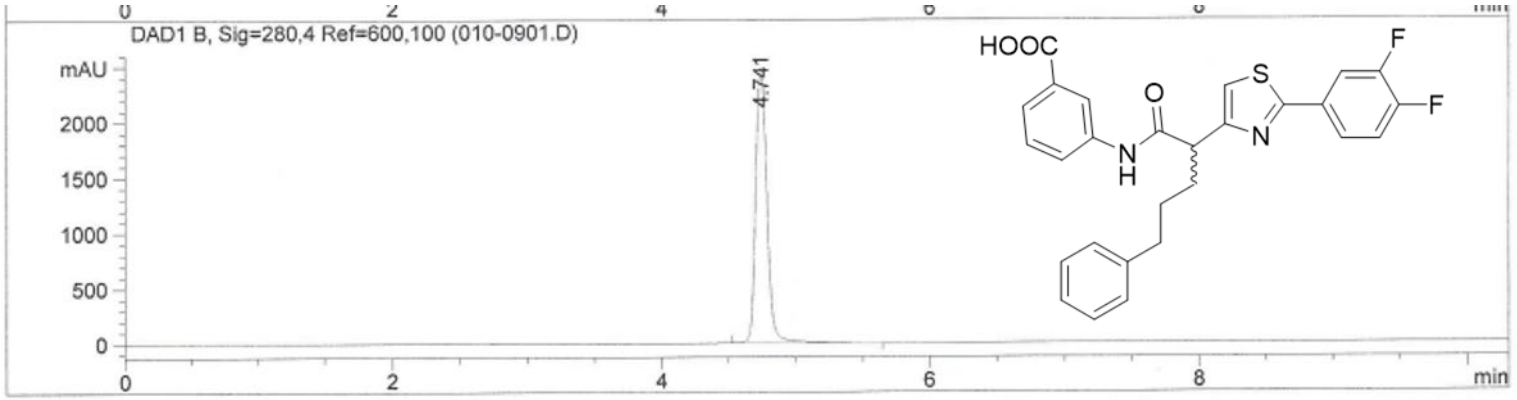


Signal 2: DAD1 B, Sig=280,4 Ref=600,100

| Peak # | RetTime [min] | Type | Width [min] | Area [mAU*s] | Height [mAU] | Area % |
|---|---|---|---|---|---|---|
| 1 | 4.741 | VB | 0.0924 | 1.45808e4 | 2485.30005 | 100.0000 |
| Totals : | | | | 1.45808e4 | 2485.30005 | |

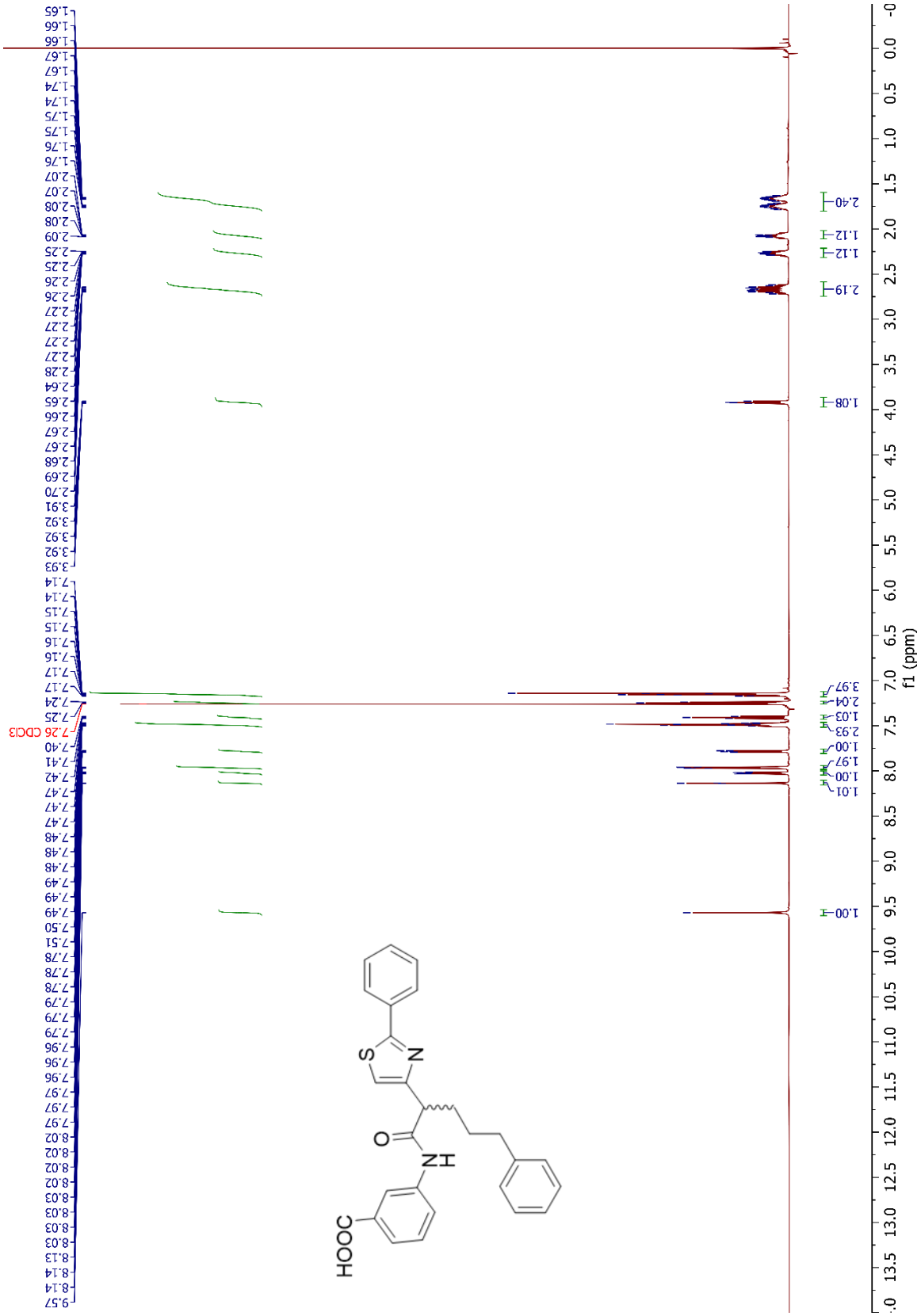
7.26 CDCl3
HOOC
HN
O
S
N
f1 (ppm)

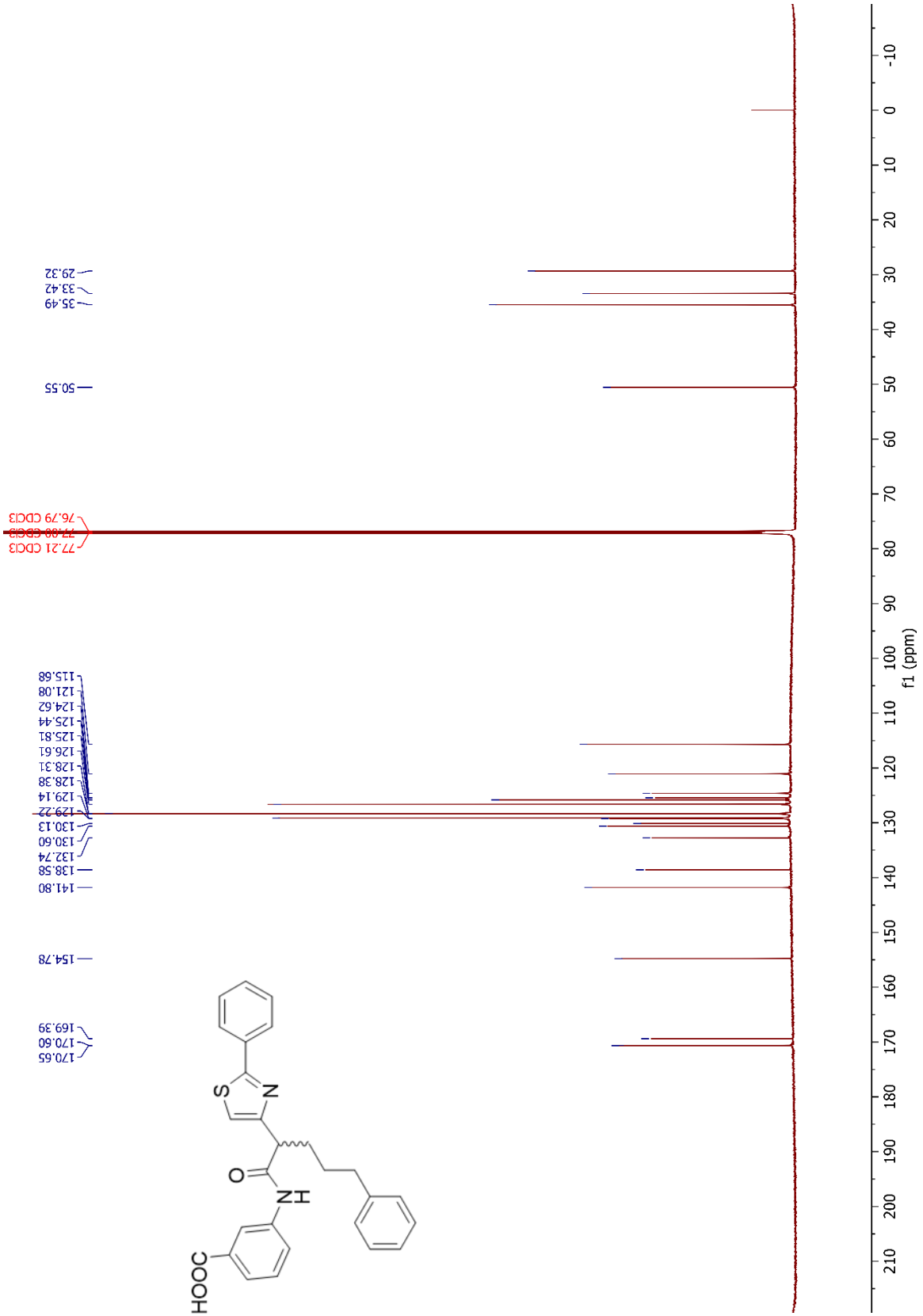
29.32
33.42
35.49
50.55
76.79 CDCl3
77.08 CDCl3
77.21 CDCl3
115.68
121.08
124.62
125.44
125.81
126.61
128.31
128.38
129.14
129.22
130.13
130.60
132.74
138.58
141.80
154.78
169.39
170.60
170.65
HOOC
NH
O
N
S
f1 (ppm)

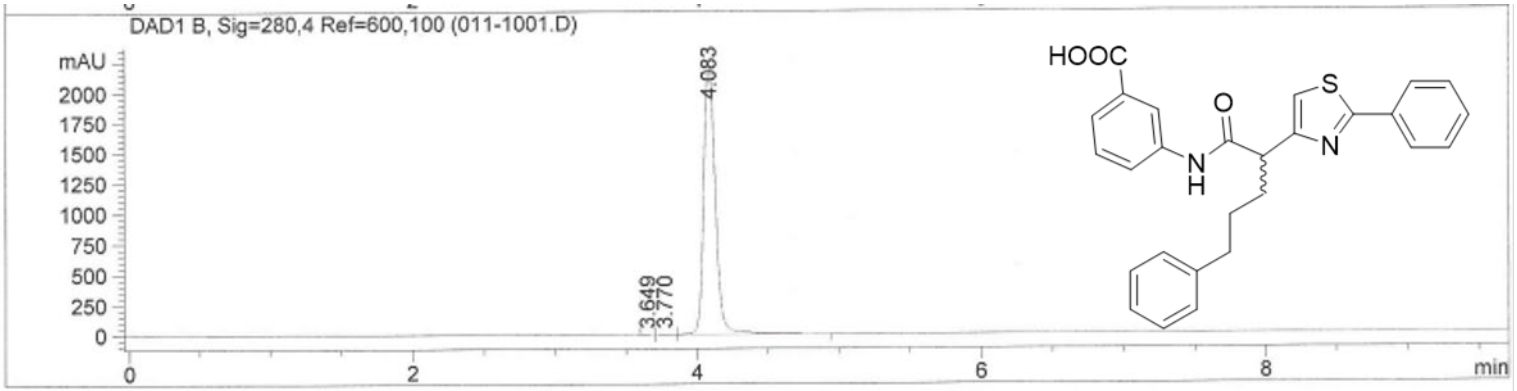


Signal 2: DAD1 B, Sig=280,4 Ref=600,100

| Peak # | RetTime [min] | Type | Width [min] | Area [mAU*s] | Height [mAU] | Area % |
|---|---|---|---|---|---|---|
| 1 | 3.649 | BV | 0.0642 | 7.82145 | 1.81893 | 0.0612 |
| 2 | 3.770 | VV | 0.1163 | 26.75304 | 3.79129 | 0.2092 |
| 3 | 4.083 | VB | 0.0877 | 1.27530e4 | 2265.58643 | 99.7296 |
| Totals : | | | | 1.27876e4 | 2271.19664 | |

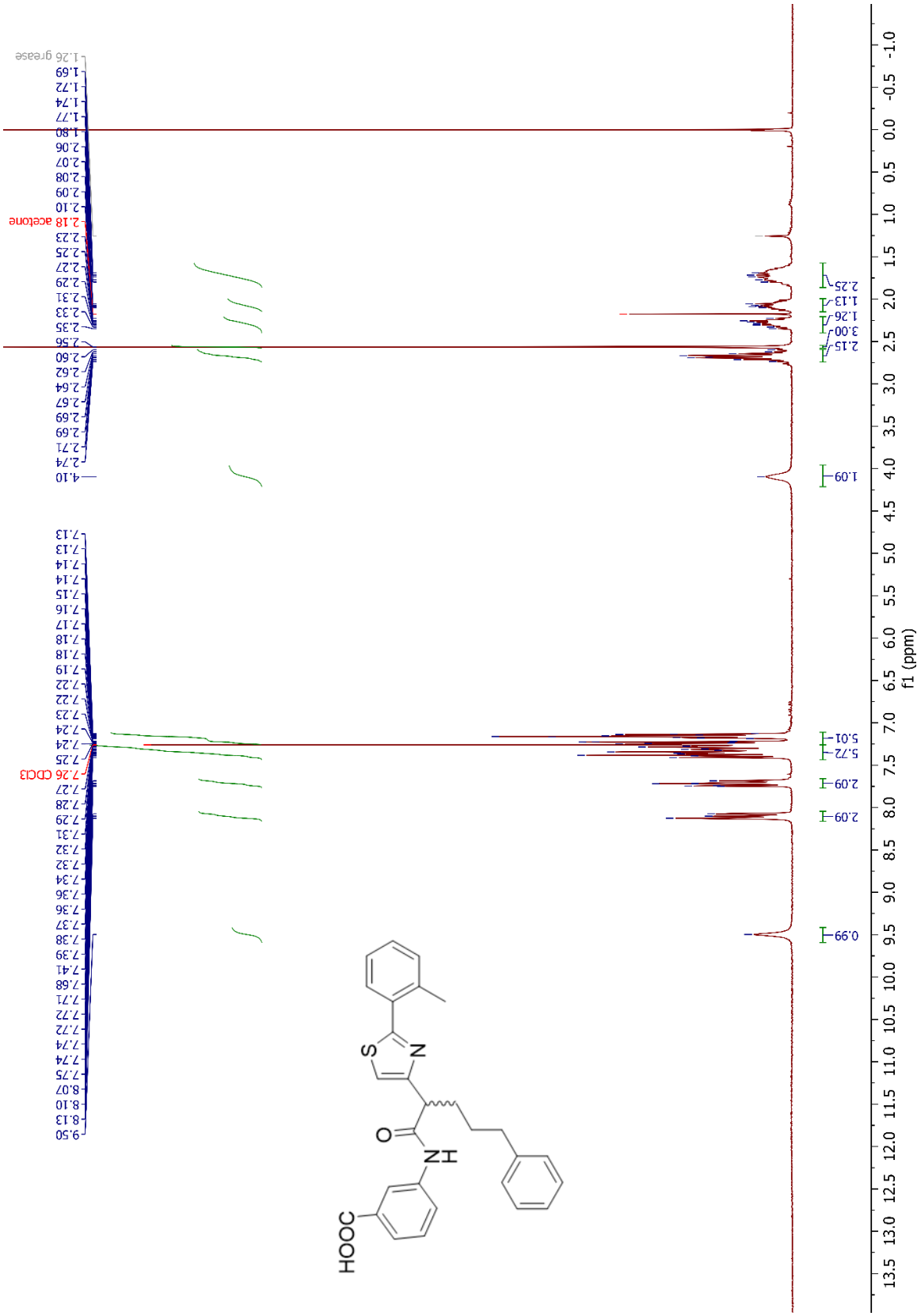
f1 (ppm)
HOOC
NH
O
S
N
acetone
CDCl3
grease

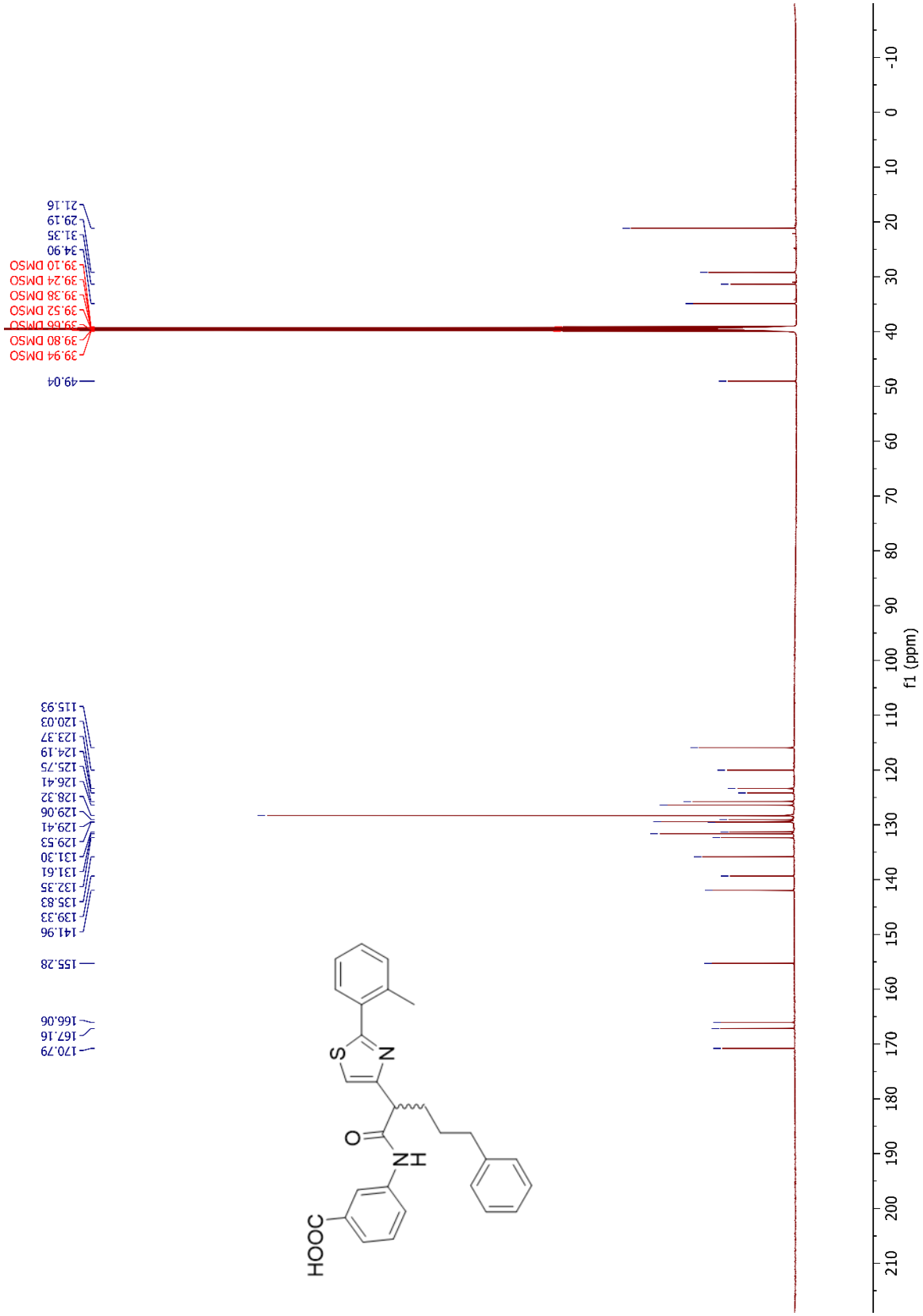
21.16
29.19
31.35
34.90
39.10 DMSO
39.24 DMSO
39.38 DMSO
39.52 DMSO
39.66 DMSO
39.80 DMSO
39.94 DMSO
49.04
115.93
120.03
123.37
124.19
125.75
126.41
128.32
129.06
129.41
129.53
131.30
131.61
132.35
135.83
139.33
141.96
155.28
166.06
167.16
170.79
HOOC
NH
O
N
S
f1 (ppm)

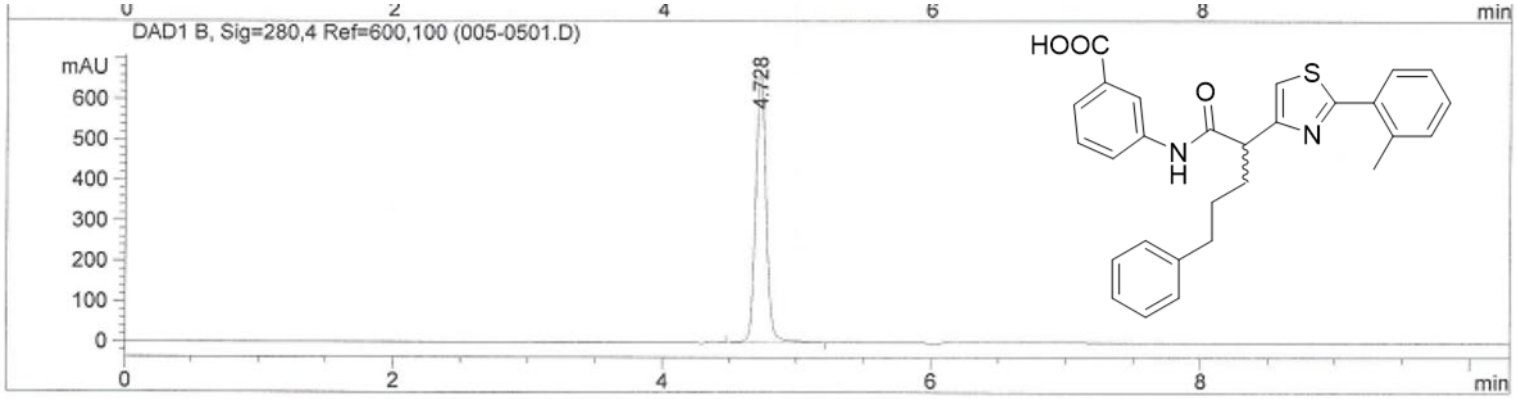


Signal 2: DAD1 B, Sig=280,4 Ref=600,100

| Peak # | RetTime [min] | Type | Width [min] | Area [mAU*s] | Height [mAU] | Area % |
|---|---|---|---|---|---|---|
| 1 | 4.728 | VB | 0.0824 | 3620.86328 | 676.69232 | 100.0000 |
| Totals : | | | | 3620.86328 | 676.69232 | |

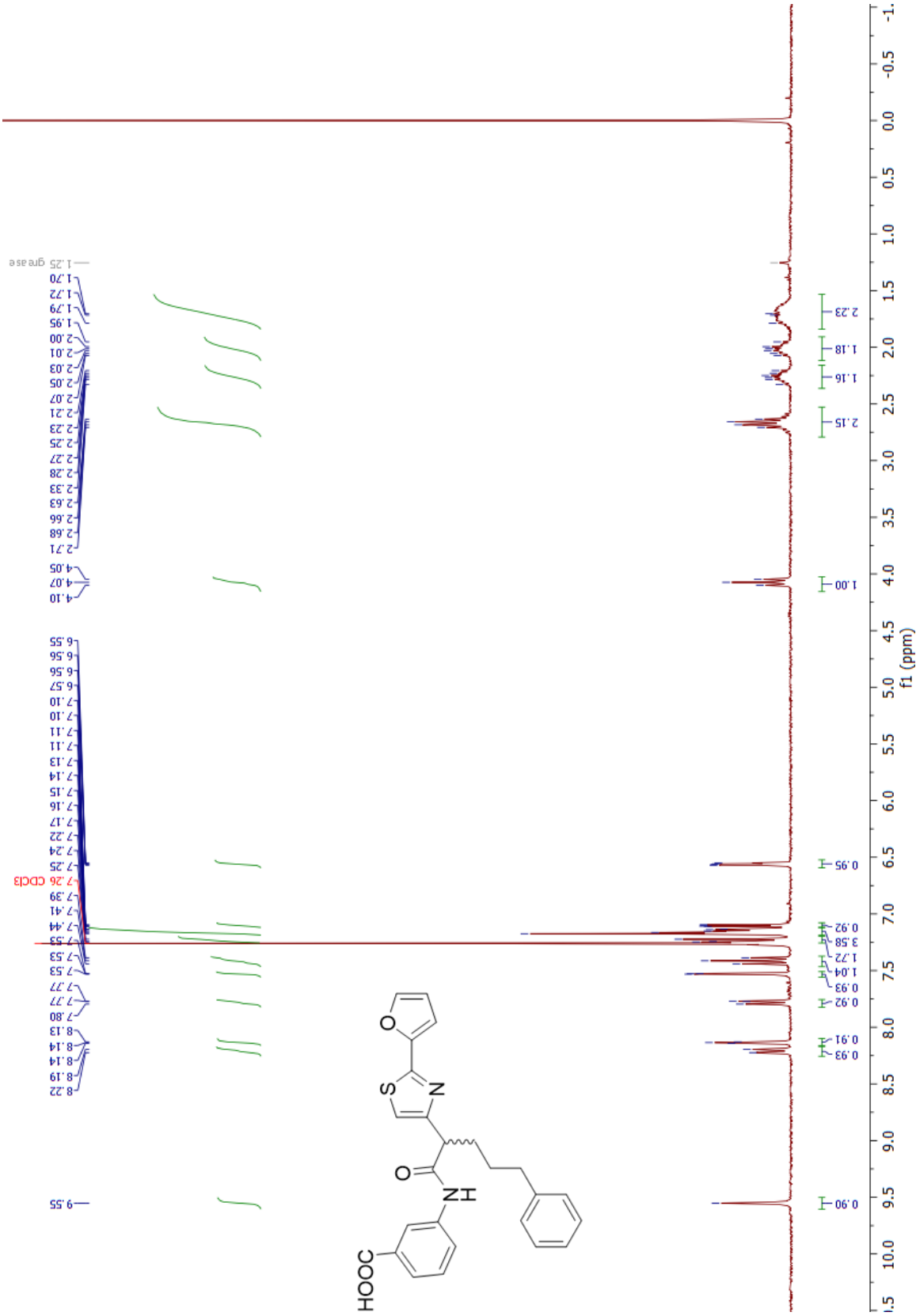
HOOC
O
S
N
O
NH
f1 (ppm)
CDCl3
grease

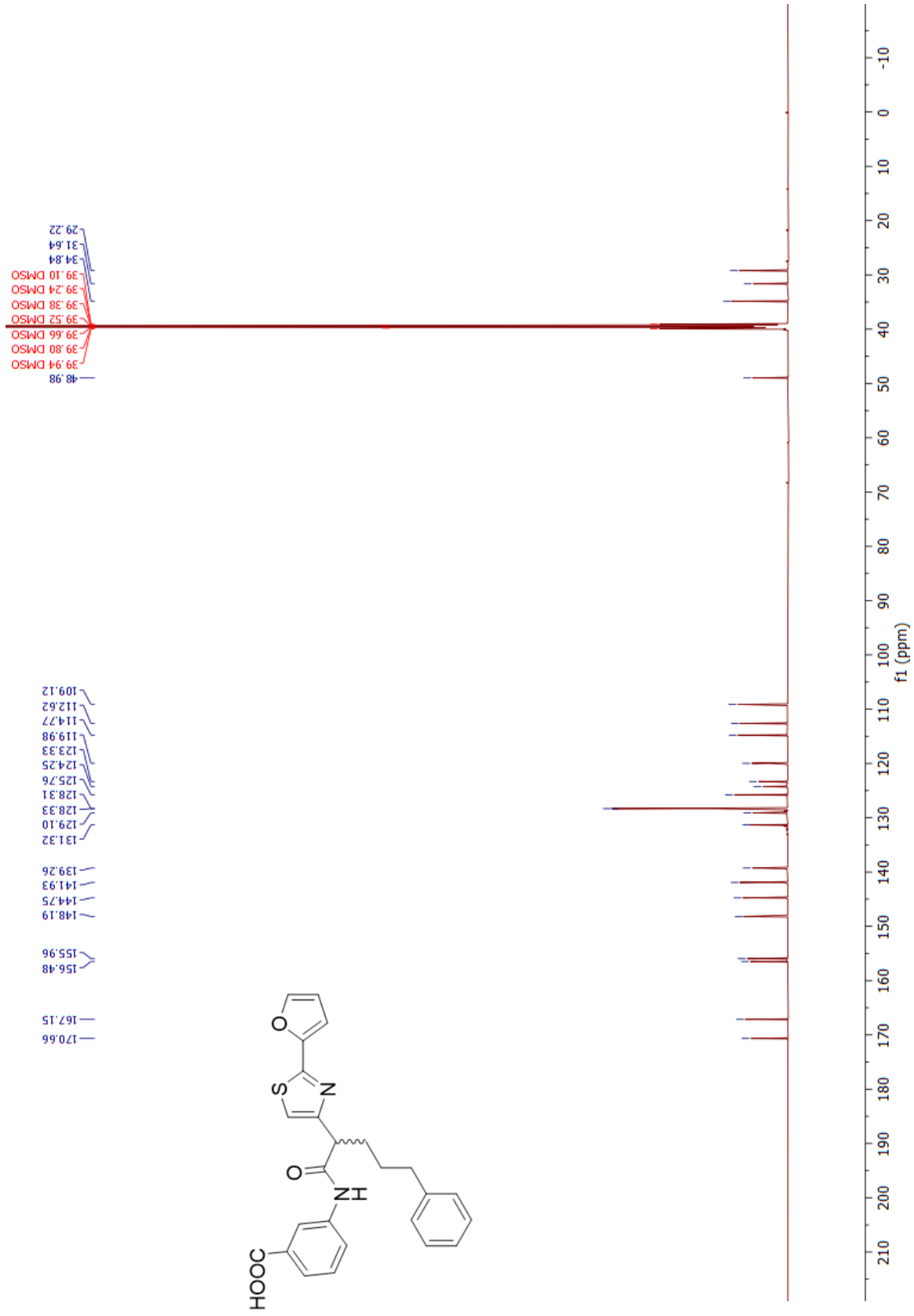
29.22
31.64
34.84
39.10 DMSO
39.24 DMSO
39.38 DMSO
39.52 DMSO
39.66 DMSO
39.80 DMSO
39.94 DMSO
48.98
109.12
112.62
114.77
119.98
123.33
124.25
125.76
128.31
128.33
129.10
131.32
139.26
141.93
144.75
148.19
155.96
156.48
167.15
170.66
f1 (ppm)
HOOC
O
S
N
O
NH

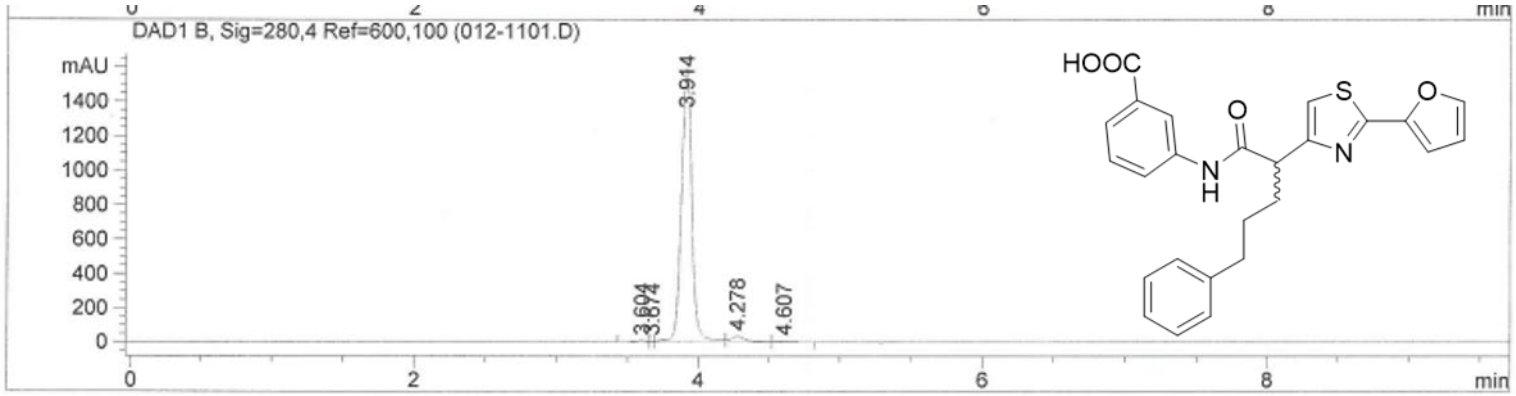


Signal 2: DAD1 B, Sig=280,4 Ref=600,100

| Peak # | RetTime [min] | Type | Width [min] | Area [mAU*s] | Height [mAU] | Area % |
|---|---|---|---|---|---|---|
| 1 | 3.604 | BV | 0.1062 | 51.29907 | 7.65563 | 0.6032 |
| 2 | 3.674 | VV | 0.0330 | 14.99305 | 6.48147 | 0.1763 |
| 3 | 3.914 | VV | 0.0777 | 8153.95508 | 1593.06323 | 95.8750 |
| 4 | 4.278 | VV | 0.1086 | 244.58636 | 32.94292 | 2.8759 |
| 5 | 4.607 | VB | 0.1097 | 39.94096 | 5.19355 | 0.4696 |
| Totals : | | | | 8504.77452 | 1645.33681 | |

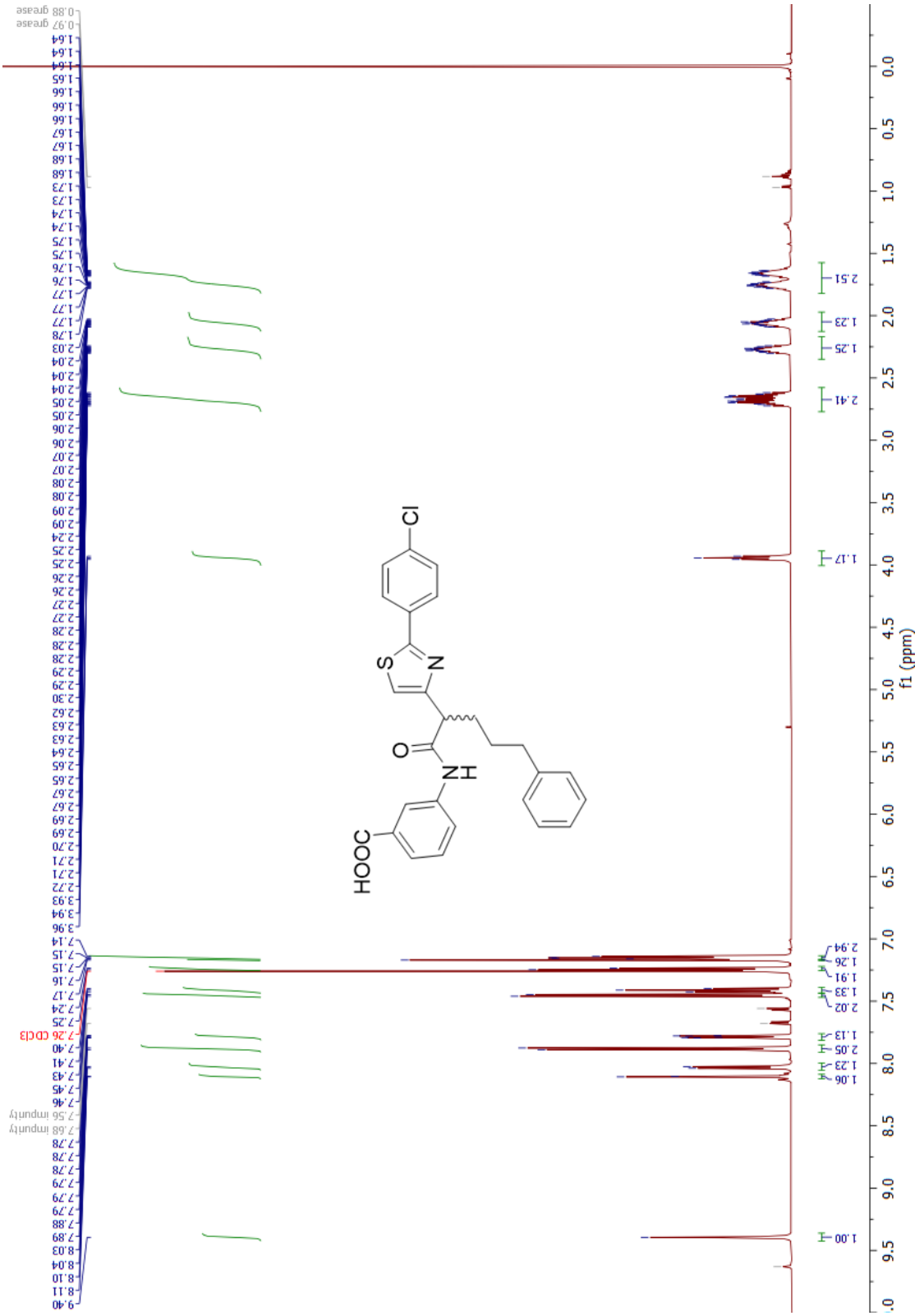
Cl
S
N
O
NH
HOOC
f1 (ppm)

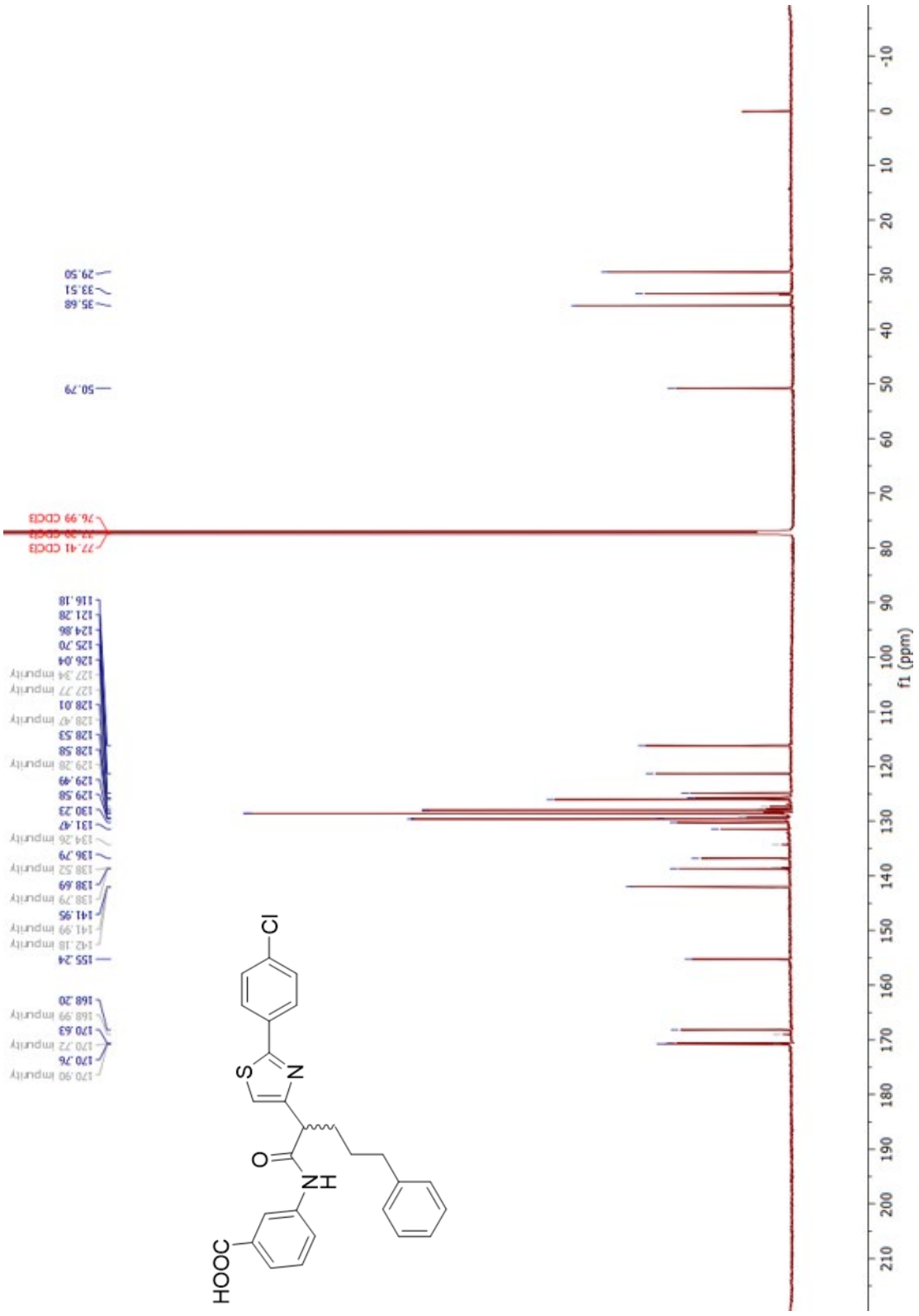
Cl
S
N
O
NH
HOOC
f1 (ppm)

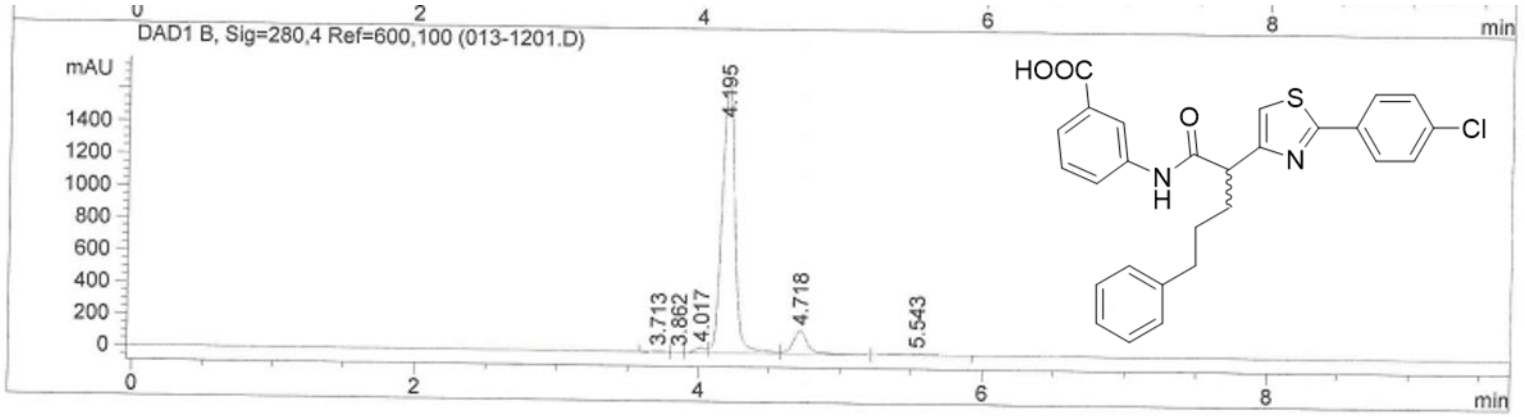


Signal 2: DAD1 B, Sig=280,4 Ref=600,100

| Peak # | RetTime [min] | Type | Width [min] | Area [mAU*s] | Height [mAU] | Area % |
|---|---|---|---|---|---|---|
| 1 | 3.713 | BV | 0.0822 | 10.48521 | 2.53640 | 0.0867 |
| 2 | 3.862 | VV | 0.0735 | 7.63196 | 1.54822 | 0.0631 |
| 3 | 4.017 | VV | 0.0748 | 146.23488 | 28.99506 | 1.2087 |
| 4 | 4.195 | VV | 0.0996 | 1.07883e4 | 1710.16174 | 89.1726 |
| 5 | 4.718 | VV | 0.1108 | 1052.22656 | 141.35396 | 8.6973 |
| 6 | 5.543 | VB | 0.2410 | 93.35408 | 5.11218 | 0.7716 |
| Totals : | | | | 1.20983e4 | 1889.70755 | |

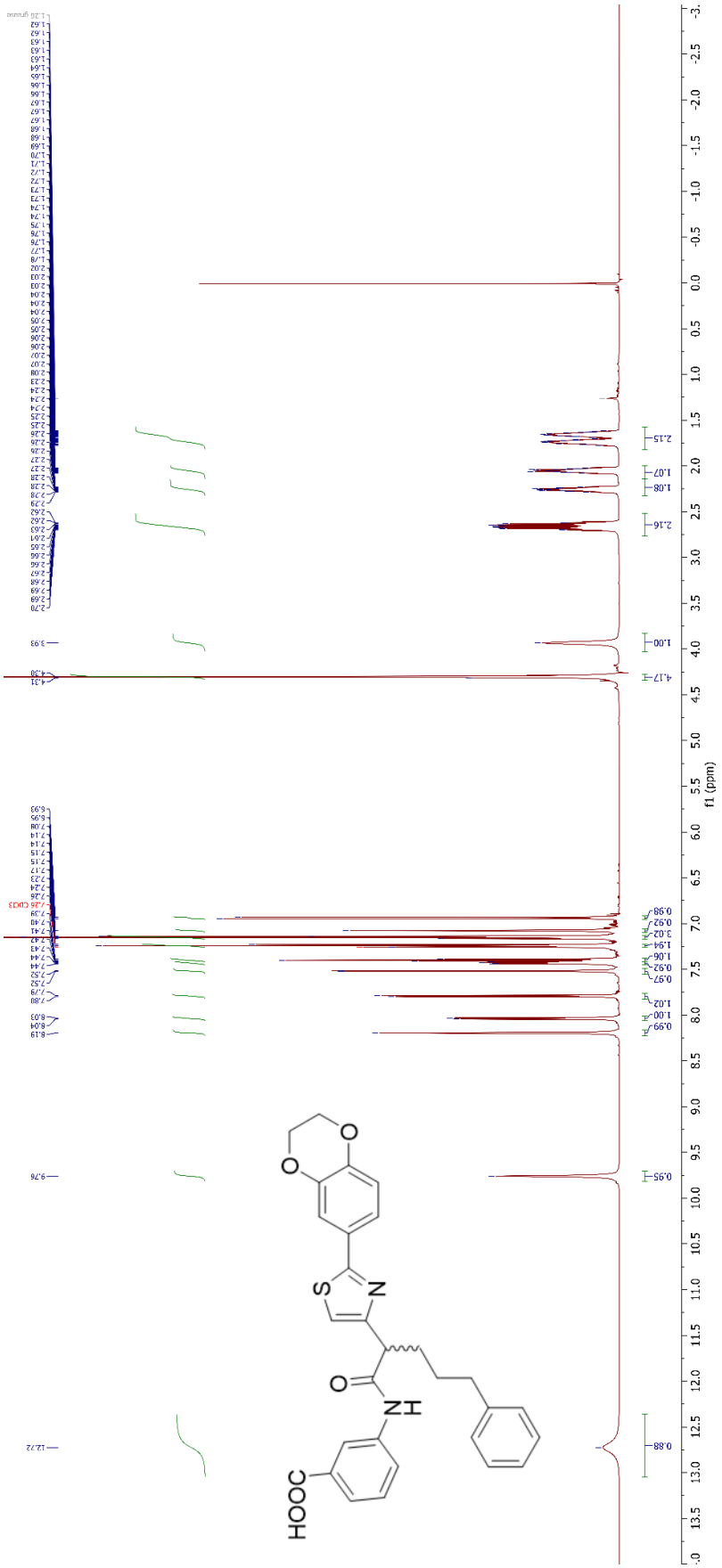
f1 (ppm)
HOOC
HN
O
N
S
O
O

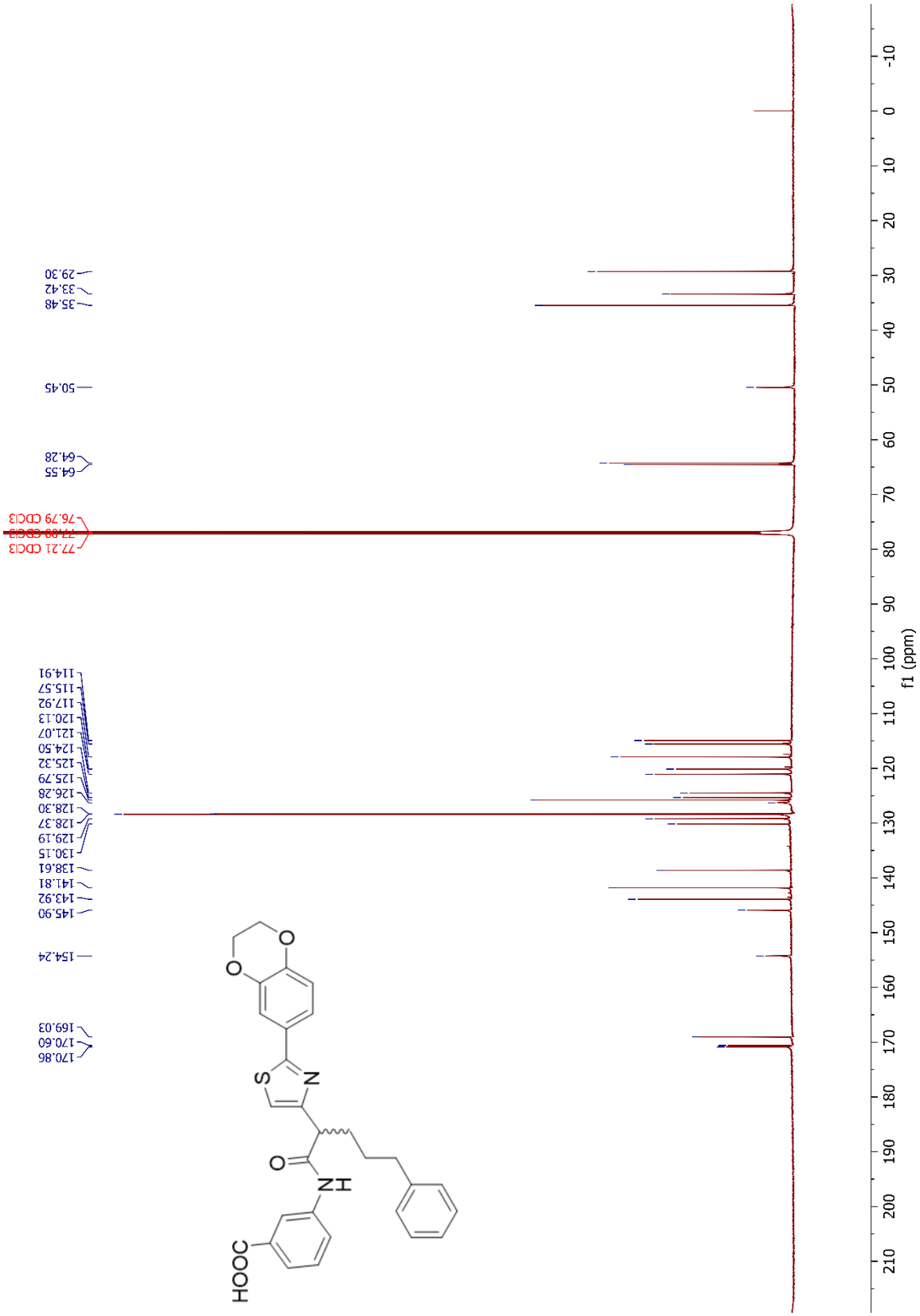
170.86
170.60
169.03
154.24
145.90
143.92
141.81
138.61
130.15
129.19
128.37
128.30
126.28
125.79
125.32
124.50
121.07
120.13
117.92
115.57
114.91
77.21 CDCl3
76.79 CDCl3
64.55
64.28
50.45
35.48
33.42
29.30
f1 (ppm)
HOOC
N
H
O
S
N
O
O

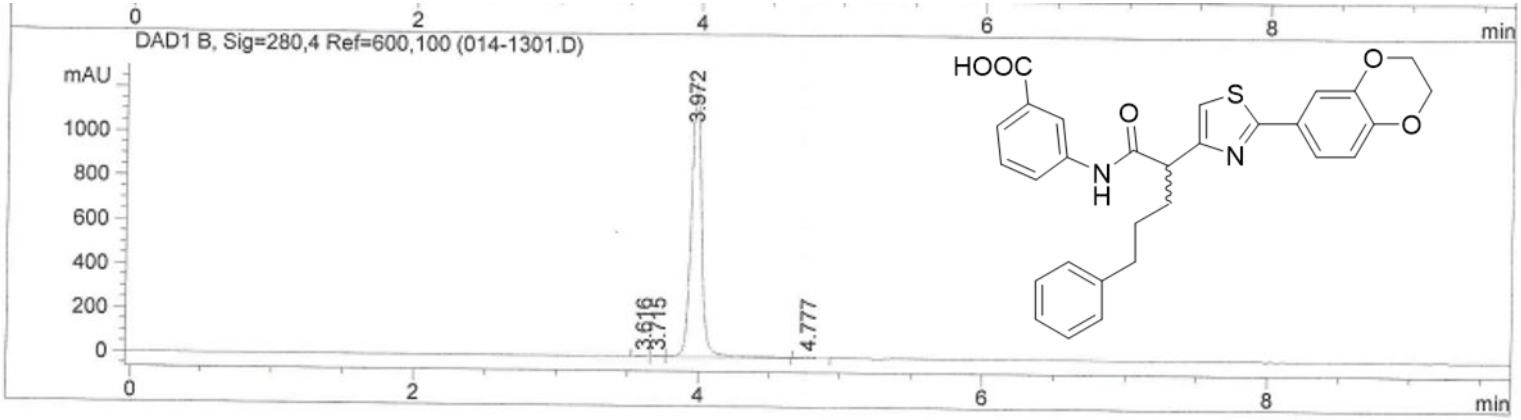


Signal 2: DAD1 B, Sig=280,4 Ref=600,100

| Peak # | RetTime [min] | Type | Width [min] | Area [mAU*s] | Height [mAU] | Area % |
|---|---|---|---|---|---|---|
| 1 | 3.616 | BV | 0.0625 | 7.53089 | 1.89139 | 0.1196 |
| 2 | 3.715 | VV | 0.0763 | 15.77417 | 3.05122 | 0.2506 |
| 3 | 3.972 | VB | 0.0768 | 6243.99072 | 1237.88525 | 99.2008 |
| 4 | 4.777 | BB | 0.0967 | 26.99952 | 4.10829 | 0.4290 |

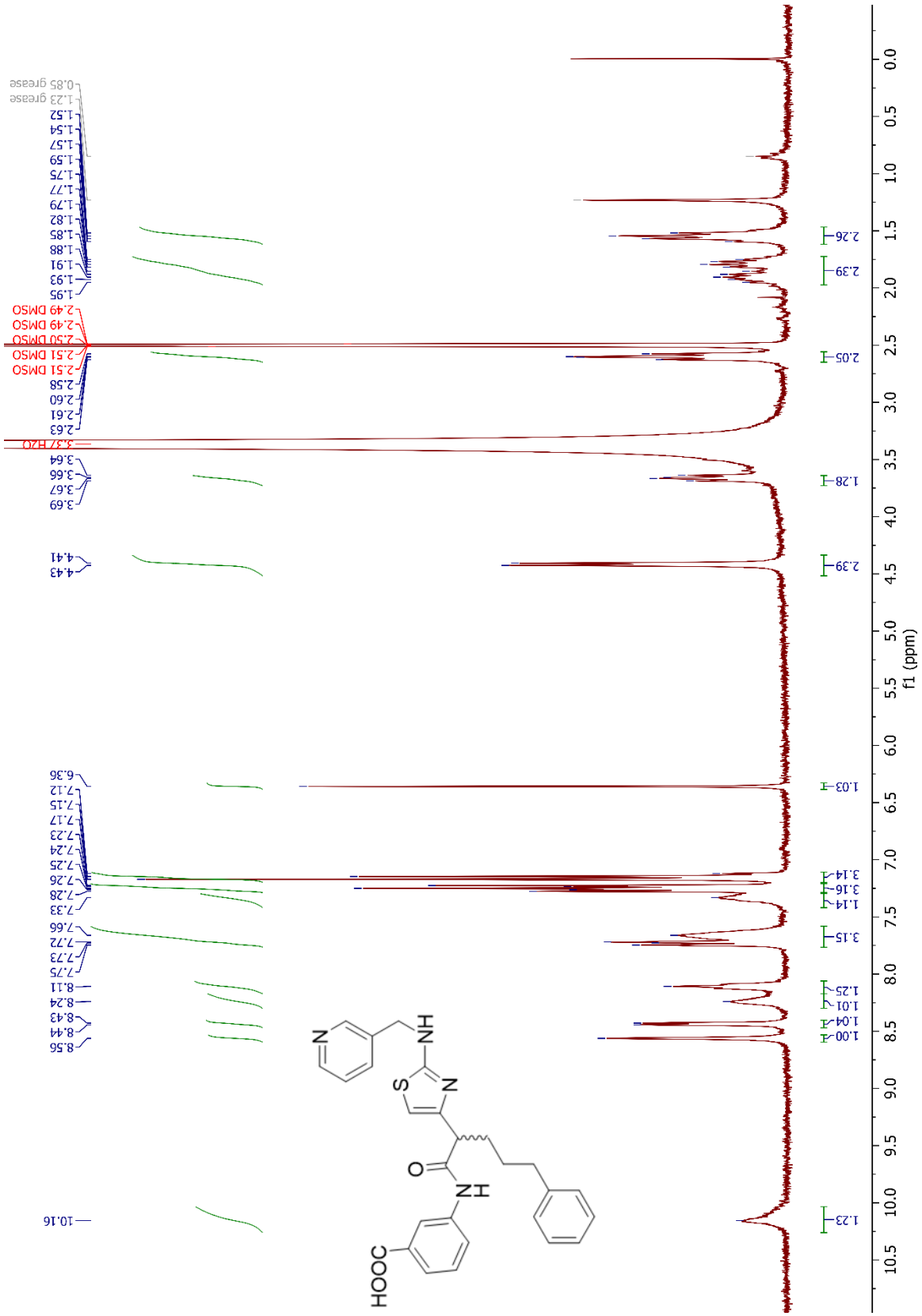
f1 (ppm)
HOOC
HN
O
N
S
N
HN
N

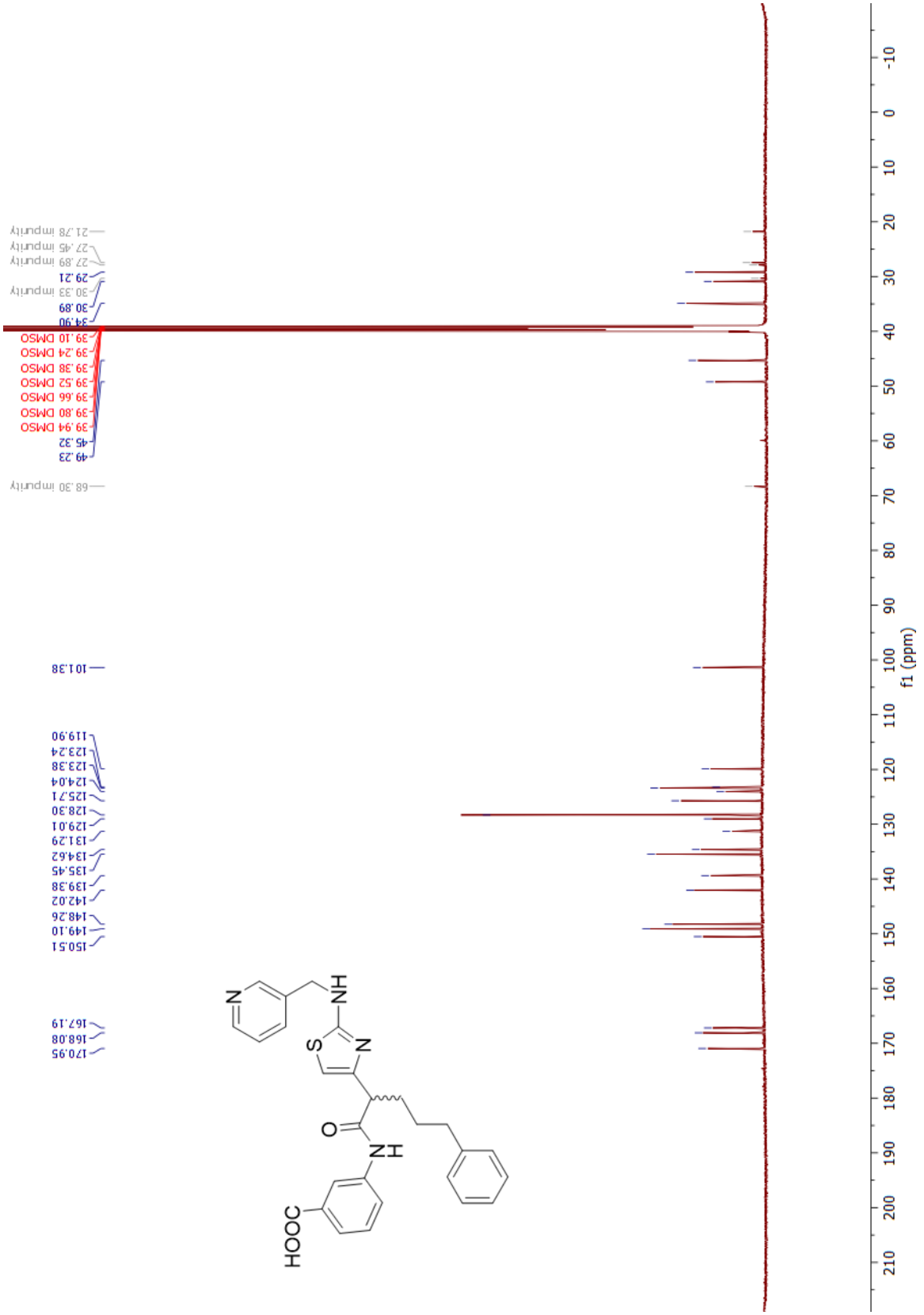
21.78 impurity
27.45 impurity
27.89 impurity
29.21
30.33 impurity
30.89
34.90
39.10 DMSO
39.24 DMSO
39.38 DMSO
39.52 DMSO
39.66 DMSO
39.80 DMSO
39.94 DMSO
45.32
49.23
68.30 impurity
101.38
119.90
123.24
123.38
124.04
125.71
128.30
129.01
131.29
134.62
135.45
139.38
142.02
148.26
149.10
150.51
167.19
168.08
170.95
HOOC
HN
O
HN
S
N
N
f1 (ppm)

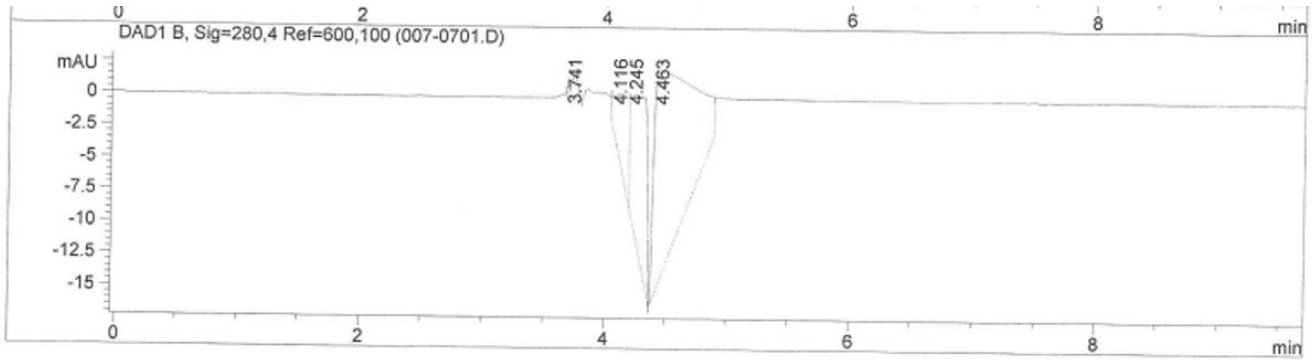


Signal 2: DAD1 B, Sig=280,4 Ref=600,100

| Peak # | RetTime [min] | Type | Width [min] | Area [mAU*s] | Height [mAU] | Area % |
|---|---|---|---|---|---|---|
| 1 | 3.741 | BV | 0.0608 | 7.62057 | 1.98474 | 1.5857 |
| 2 | 4.116 | BV | 0.1236 | 48.41344 | 5.15387 | 10.0739 |
| 3 | 4.245 | VV | 0.1300 | 108.30750 | 10.89029 | 22.5367 |
| 4 | 4.463 | VB | 0.2677 | 316.24048 | 16.06338 | 65.8036 |
| Totals : | | | | 480.58199 | 34.09228 | |

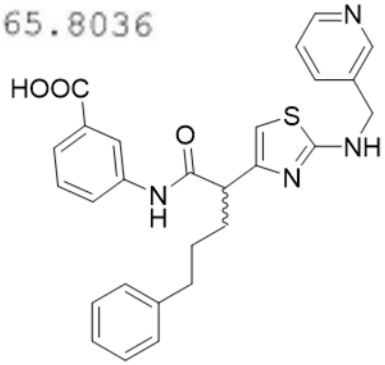

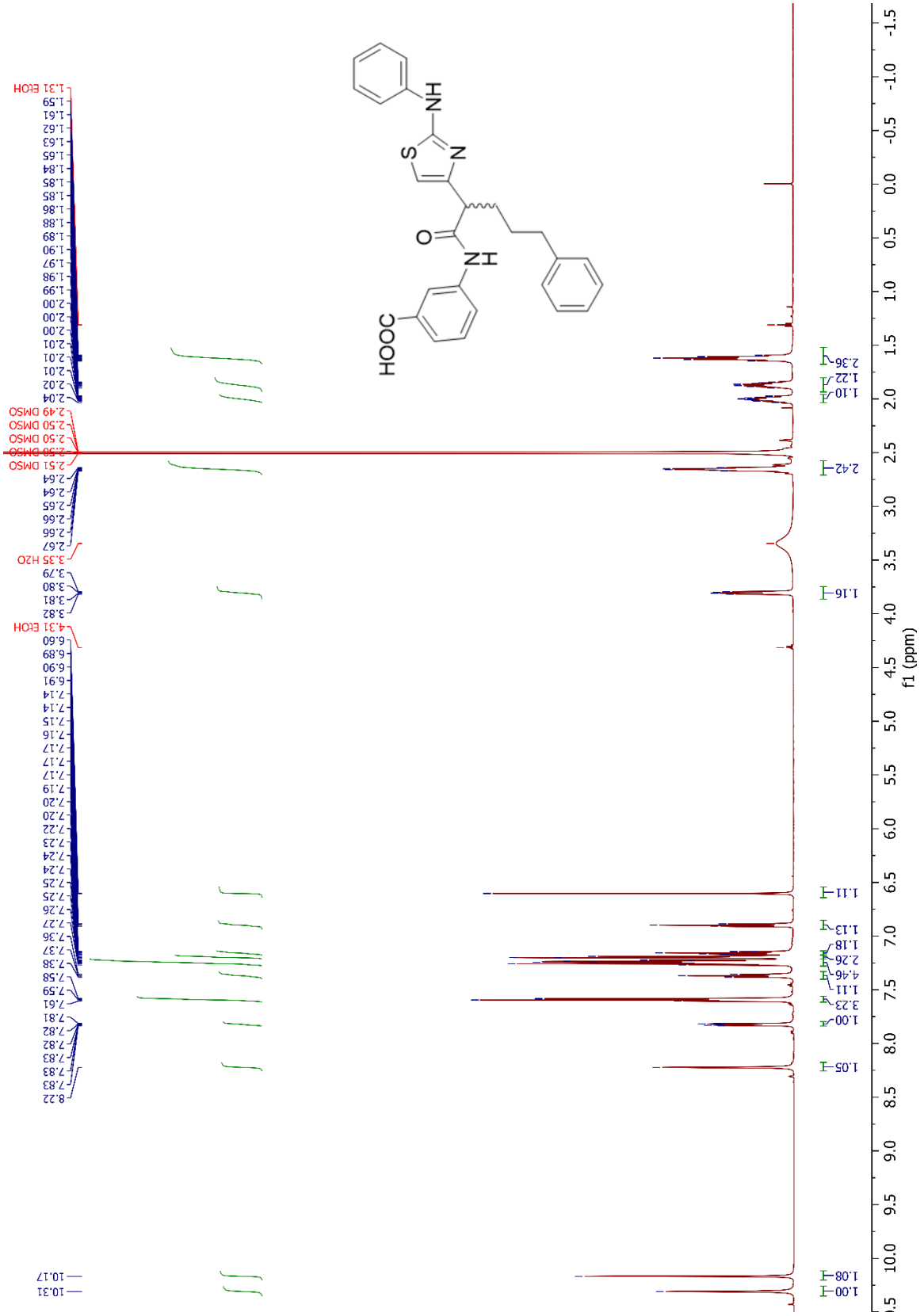
HOOC
HN
O
HN
S
N
f1 (ppm)

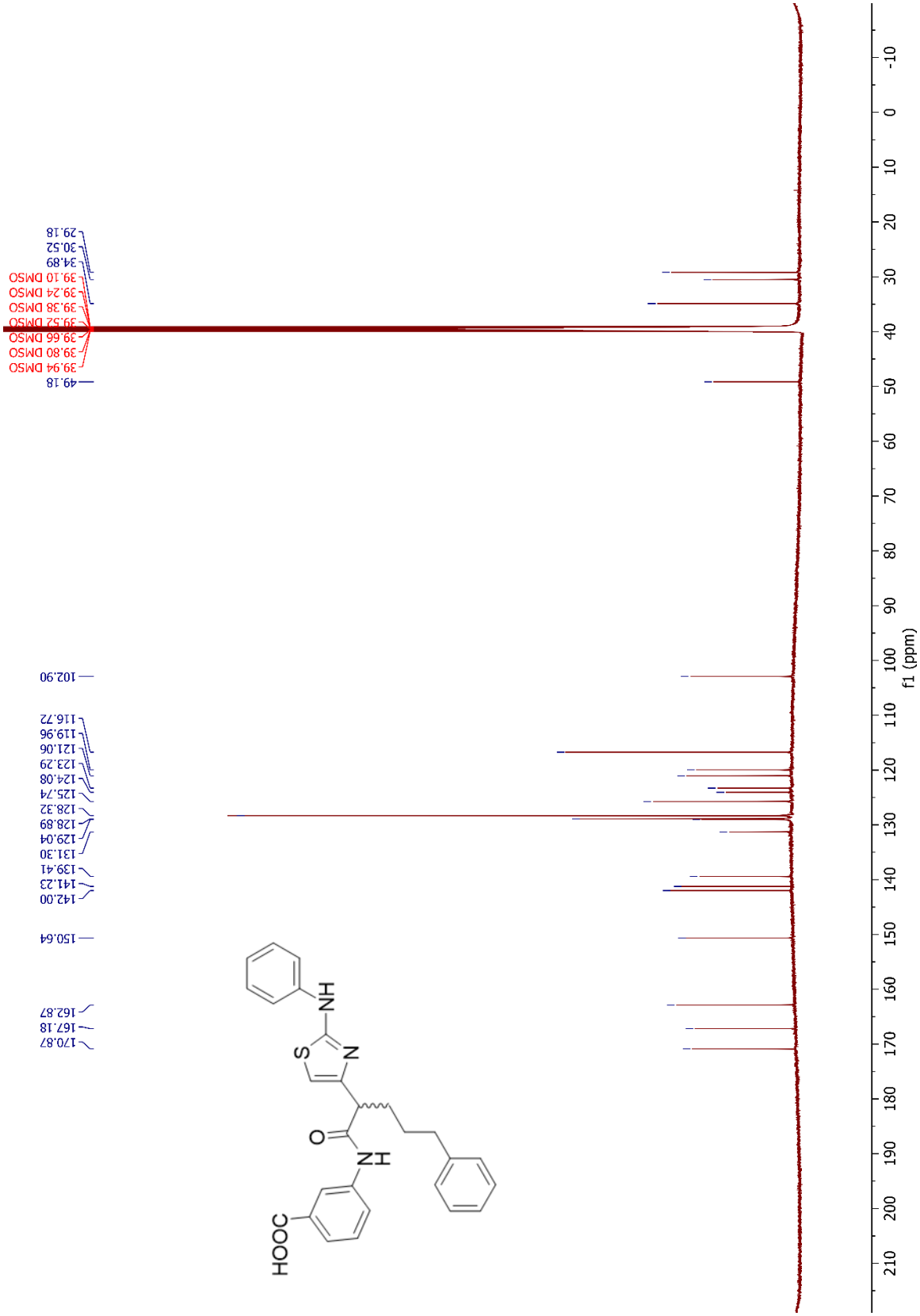
170.87
167.18
162.87
150.64
142.00
141.23
139.41
131.30
129.04
128.89
128.32
125.74
124.08
123.29
121.06
119.96
116.72
102.90
49.18
39.94 DMSO
39.80 DMSO
39.66 DMSO
39.52 DMSO
39.38 DMSO
39.24 DMSO
39.10 DMSO
34.89
30.52
29.18
HOOC
NH
O
NH
S
N
f1 (ppm)

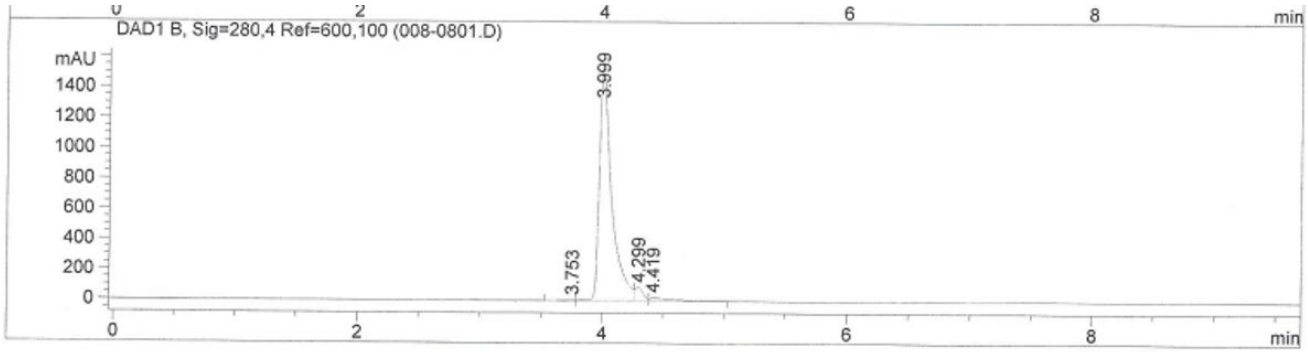


Signal 2: DAD1 B, Sig=280,4 Ref=600,100

| Peak # | RetTime [min] | Type | Width [min] | Area [mAU*s] | Height [mAU] | Area % |
|---|---|---|---|---|---|---|
| 1 | 3.753 | BV | 0.1005 | 38.14238 | 5.02827 | 0.3299 |
| 2 | 3.999 | VV | 0.0968 | 1.08255e4 | 1563.82190 | 93.6176 |
| 3 | 4.299 | VV | 0.0675 | 421.82318 | 88.69579 | 3.6479 |
| 4 | 4.419 | VB | 0.1654 | 278.05737 | 21.42048 | 2.4046 |
| Totals : | | | | 1.15635e4 | 1678.96644 | |

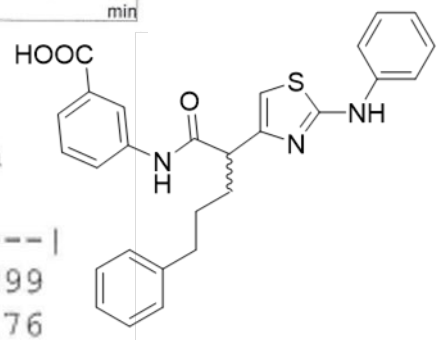

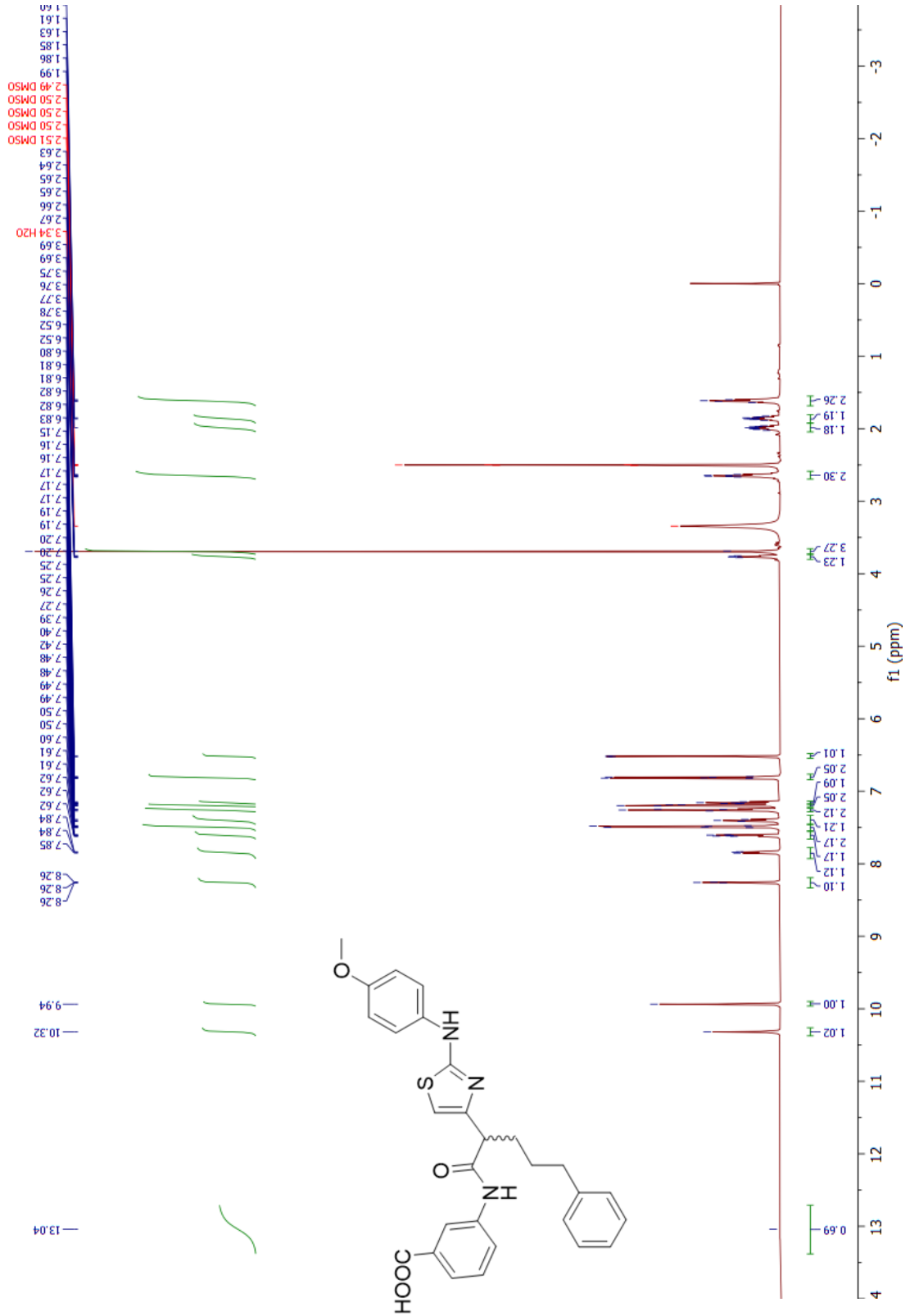
f1 (ppm)
HOOC
HN
N
S
O
O

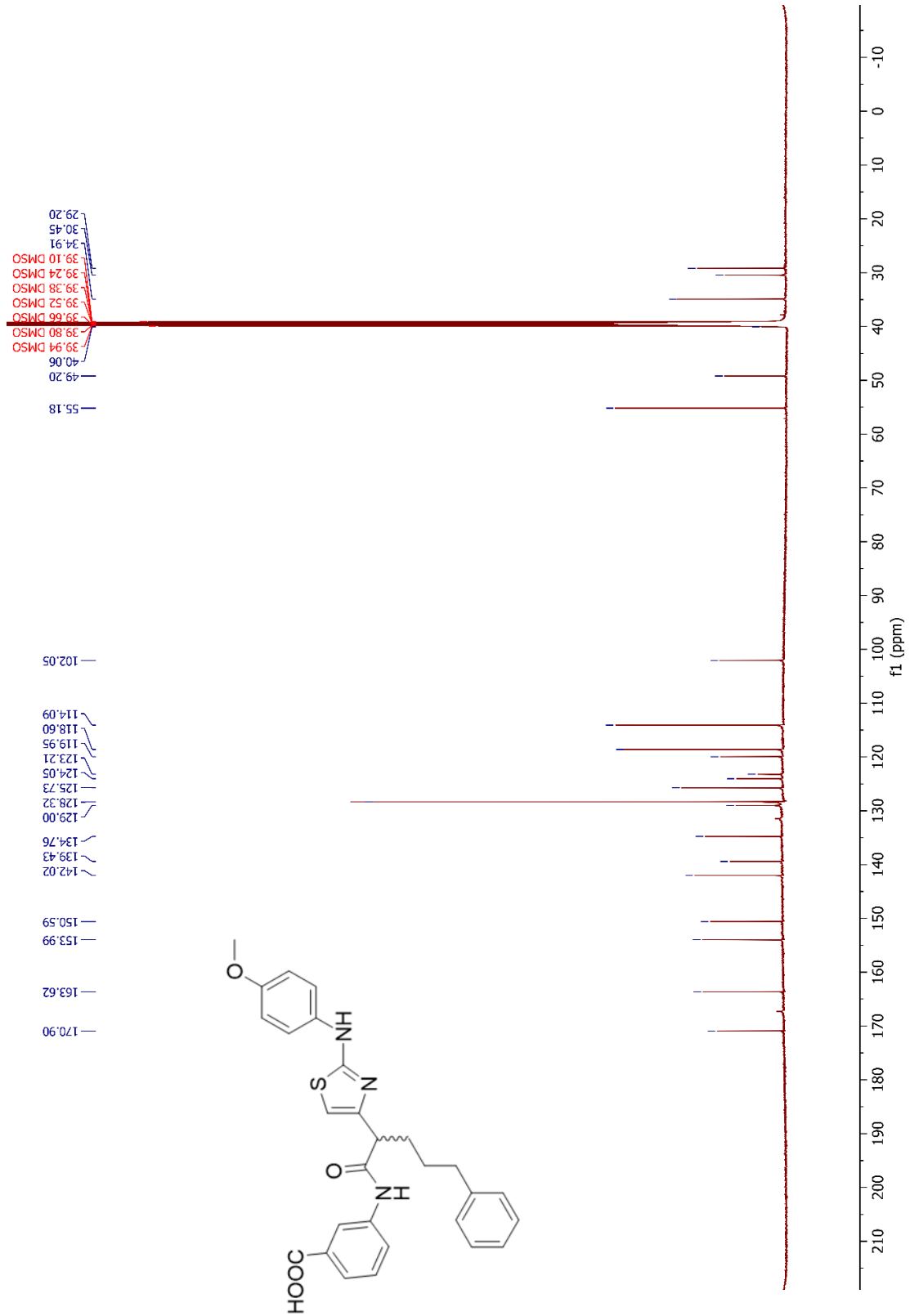
29.20
30.45
34.91
39.10 DMSO
39.24 DMSO
39.38 DMSO
39.52 DMSO
39.66 DMSO
39.80 DMSO
39.94 DMSO
40.06
49.20
55.18
102.05
114.09
118.60
119.95
123.21
124.05
125.73
128.32
129.00
134.76
139.43
142.02
150.59
153.99
163.62
170.90
HOOC
HN
O
N
S
HN
O
f1 (ppm)

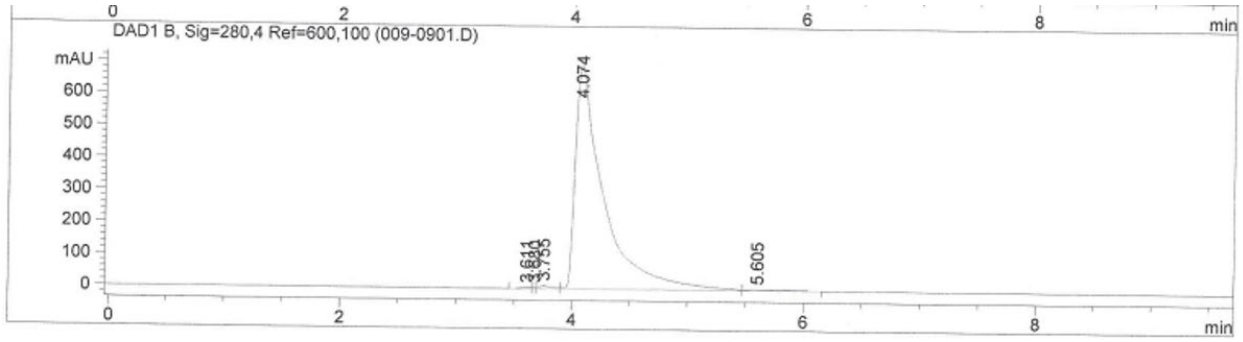


Signal 2: DAD1 B, Sig=280,4 Ref=600,100

| Peak # | RetTime [min] | Type | Width [min] | Area [mAU*s] | Height [mAU] | Area % |
|---|---|---|---|---|---|---|
| 1 | 3.611 | VV | 0.1034 | 22.91413 | 3.45604 | 0.1894 |
| 2 | 3.680 | VV | 0.0305 | 7.82486 | 3.44576 | 0.0647 |
| 3 | 3.755 | VV | 0.1072 | 65.74100 | 8.60269 | 0.5435 |
| 4 | 4.074 | VB | 0.2323 | 1.19246e4 | 694.70258 | 98.5819 |
| 5 | 5.605 | BB | 0.2859 | 75.05804 | 3.31882 | 0.6205 |
| Totals : | | | | 1.20962e4 | 713.52588 | |

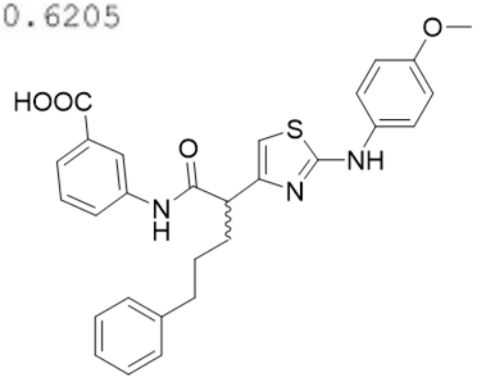

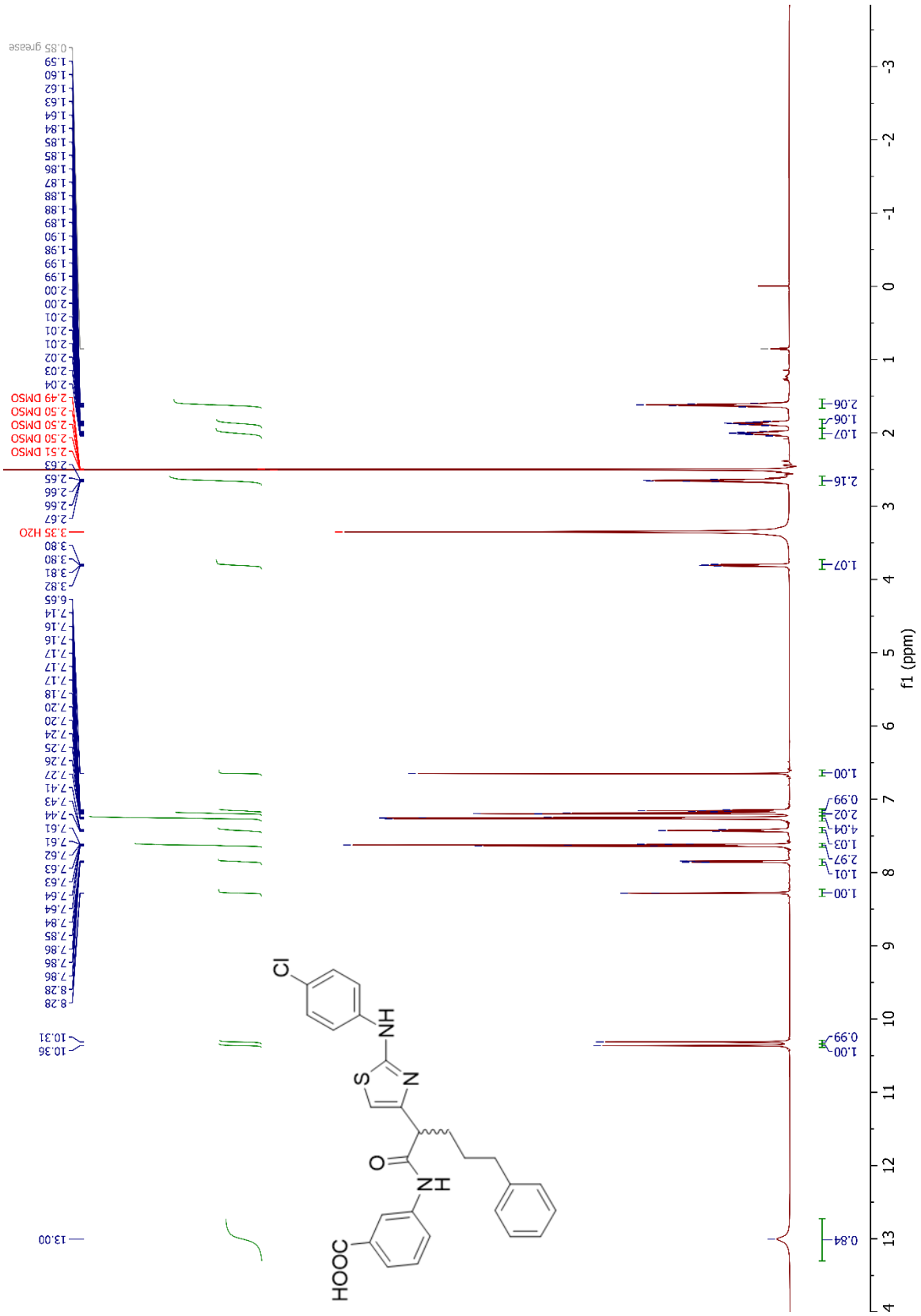
f1 (ppm)
HOOC
HN
O
N
S
HN
Cl
3.35 H2O
2.49 DMSO
2.50 DMSO
2.50 DMSO
2.50 DMSO
2.51 DMSO
0.85 grease

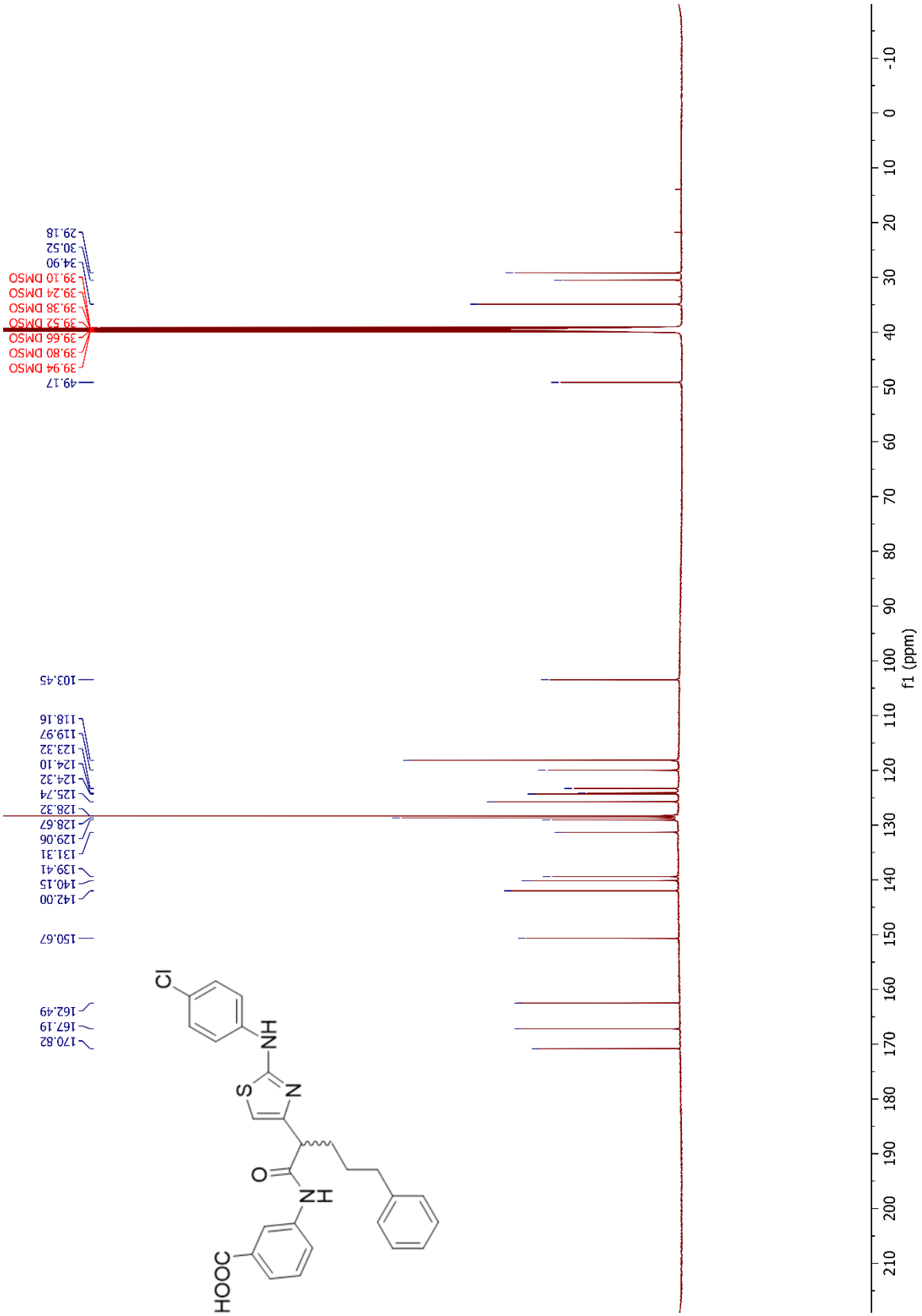
29.18
30.52
34.90
39.10 DMSO
39.24 DMSO
39.38 DMSO
39.52 DMSO
39.66 DMSO
39.80 DMSO
39.94 DMSO
49.17
103.45
118.16
119.97
123.32
124.10
124.32
125.74
128.32
128.67
129.06
131.31
139.41
140.15
142.00
150.67
162.49
167.19
170.82
Cl
NH
S
N
O
NH
HOOC
f1 (ppm)

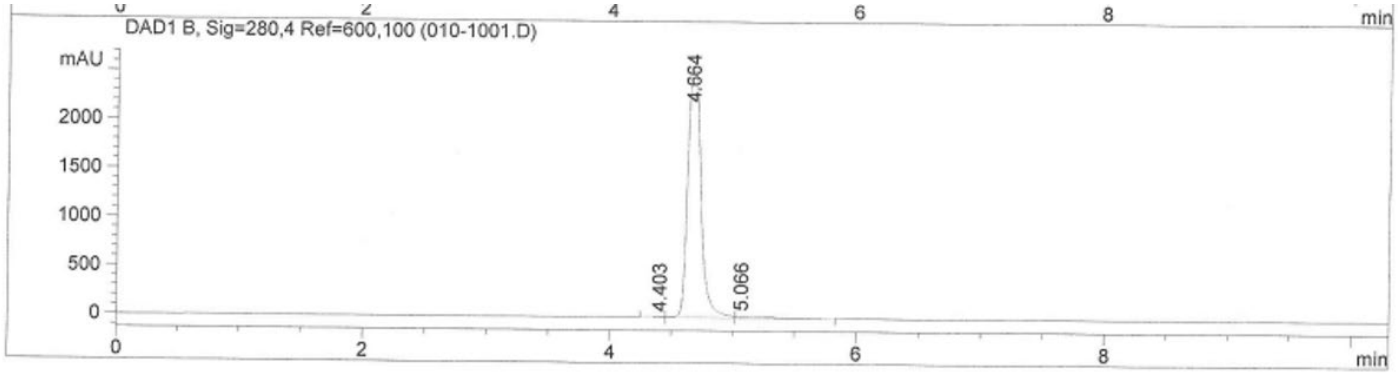


Signal 2: DAD1 B, Sig=280,4 Ref=600,100

| Peak # | RetTime [min] | Type | Width [min] | Area [mAU*s] | Height [mAU] | Area % |
|---|---|---|---|---|---|---|
| 1 | 4.403 | BV | 0.0934 | 27.18814 | 4.31860 | 0.1376 |
| 2 | 4.664 | VV | 0.1177 | 1.93895e4 | 2579.87842 | 98.1223 |
| 3 | 5.066 | VB | 0.2328 | 343.85059 | 19.21381 | 1.7401 |
| Totals : | | | | 1.97605e4 | 2603.41083 | |

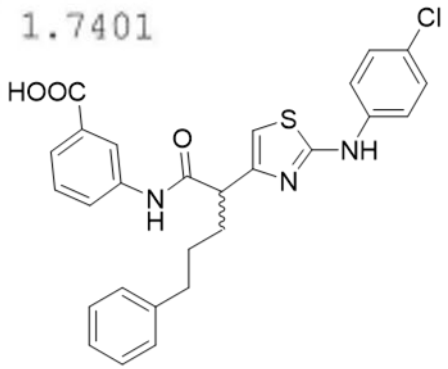

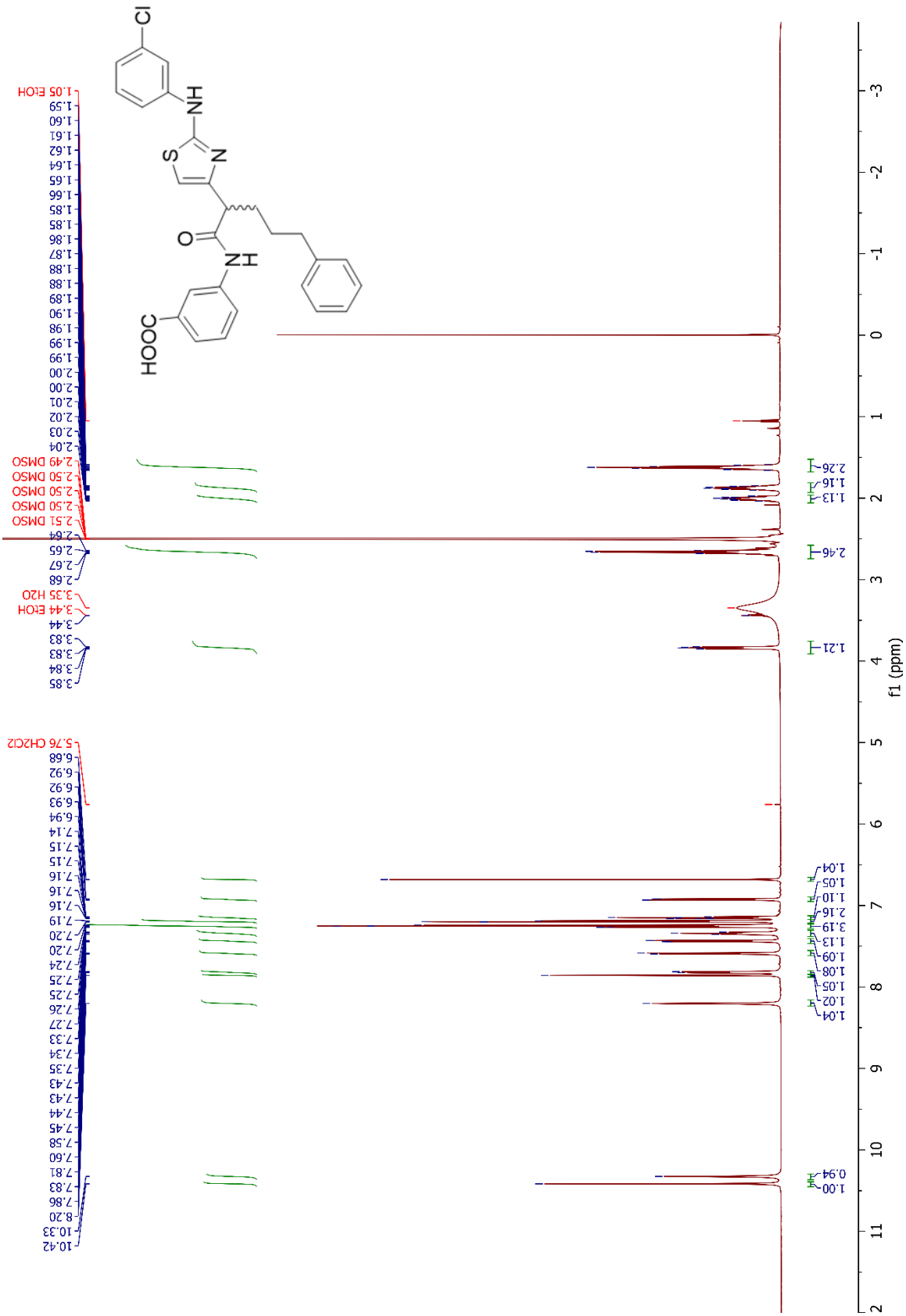
Cl
NH
S
N
O
NH
HOOC
f1 (ppm)

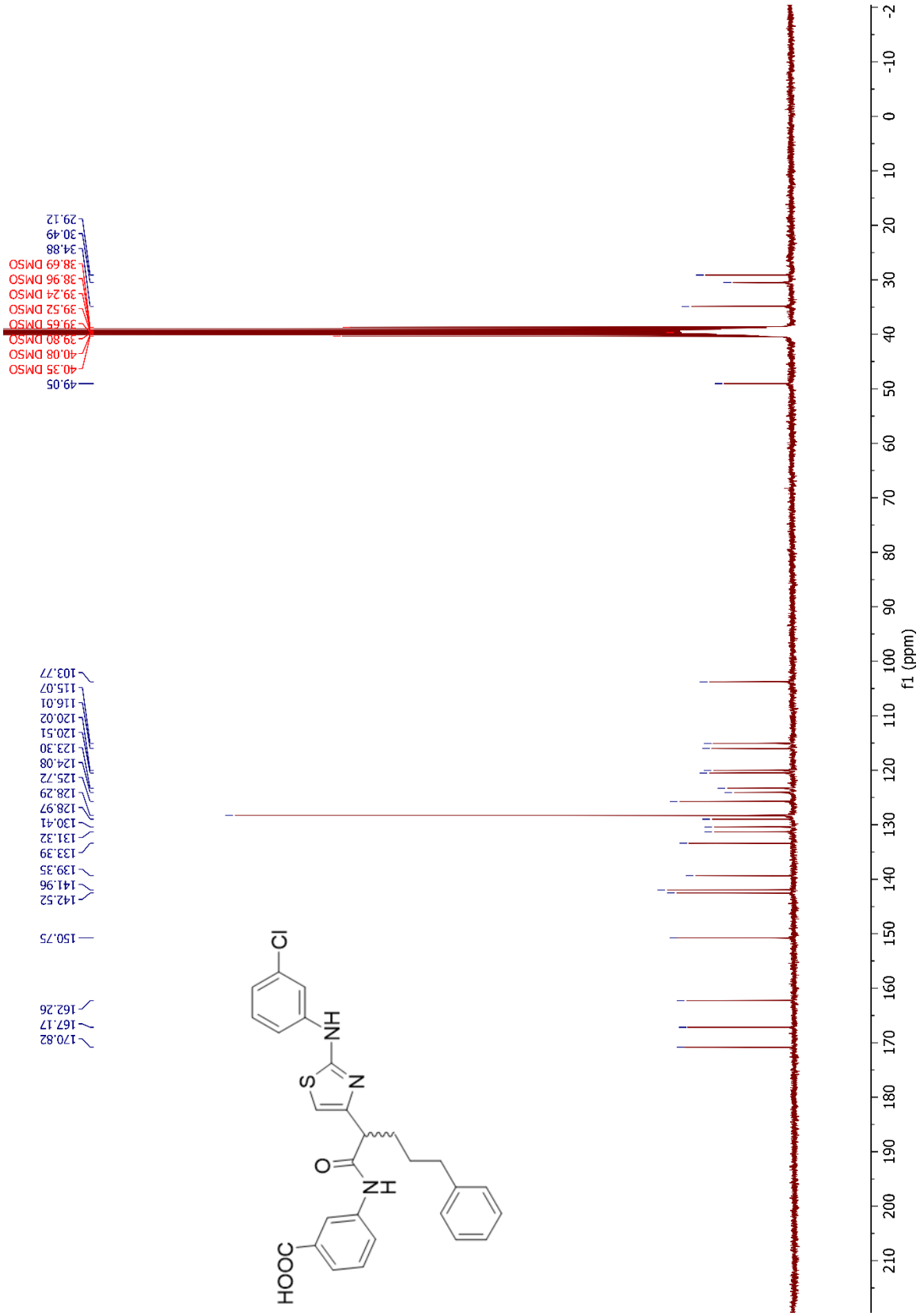
29.12
30.49
34.88
38.69 DMSO
38.96 DMSO
39.24 DMSO
39.52 DMSO
39.65 DMSO
39.80 DMSO
40.08 DMSO
40.35 DMSO
49.05
103.77
115.07
116.01
120.02
120.51
123.30
124.08
125.72
128.29
128.97
130.41
131.32
133.39
139.35
141.96
142.52
150.75
162.26
167.17
170.82
Cl
NH
S
N
O
HN
HOOC
f1 (ppm)

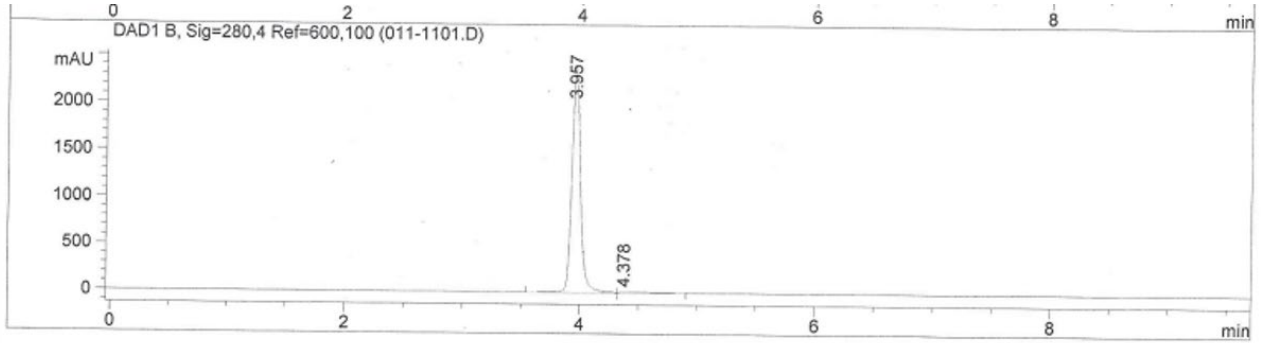


Signal 2: DAD1 B, Sig=280,4 Ref=600,100

| Peak # | RetTime [min] | Type | Width [min] | Area [mAU*s] | Height [mAU] | Area % |
|---|---|---|---|---|---|---|
| 1 | 3.957 | BV | 0.0806 | 1.25727e4 | 2421.06348 | 97.8505 |
| 2 | 4.378 | VB | 0.2363 | 276.18304 | 15.17578 | 2.1495 |
| Totals : | | | | 1.28489e4 | 2436.23925 | |

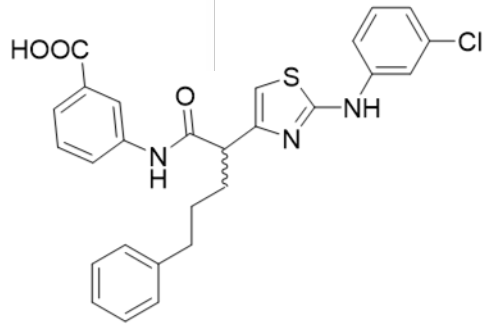

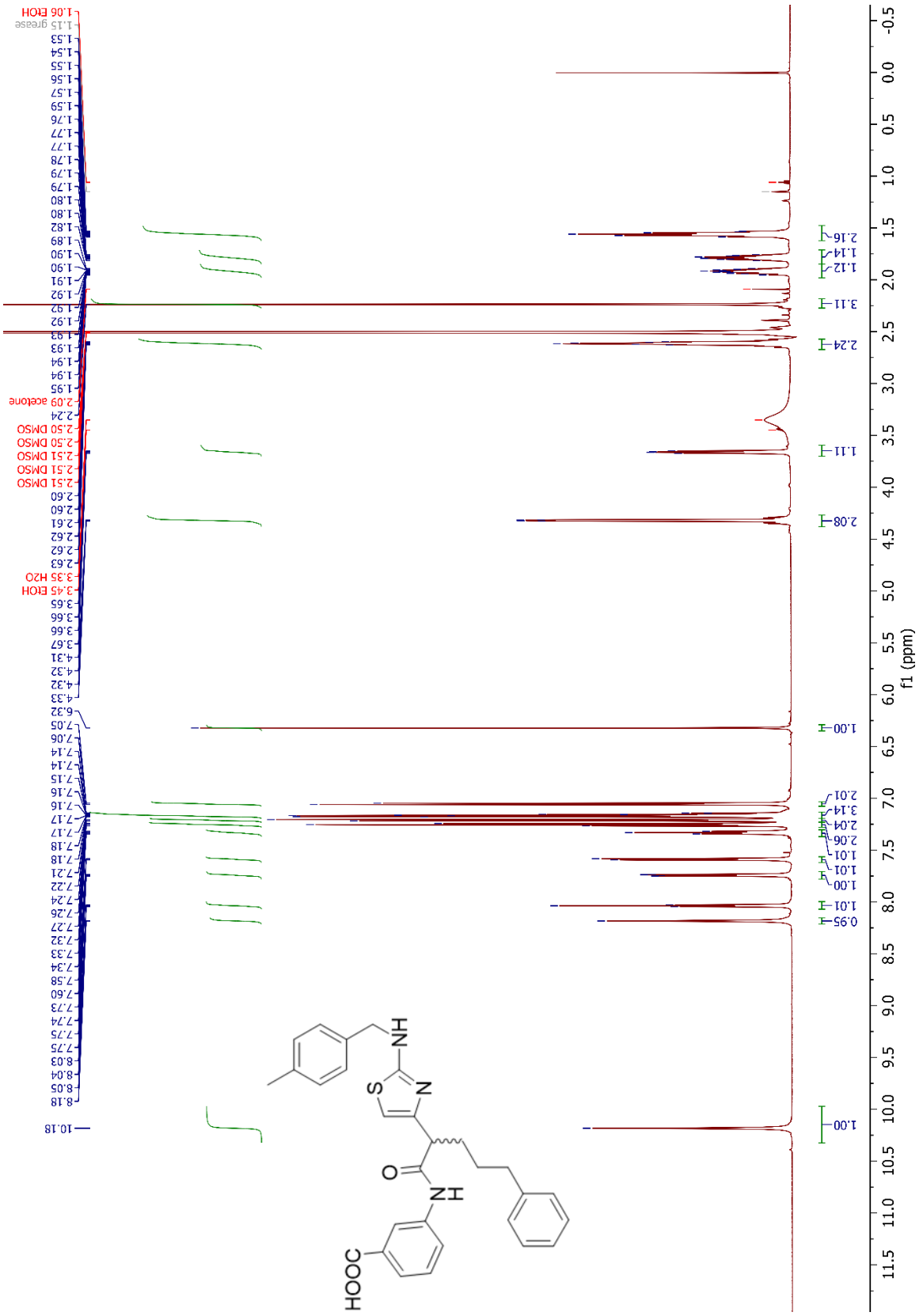
1.06 EtOH
1.15 grease
2.09 acetone
2.50 DMSO
2.51 DMSO
3.35 H2O
3.45 EtOH
10.18
HOOC
O
NH
S
N
NH
f1 (ppm)

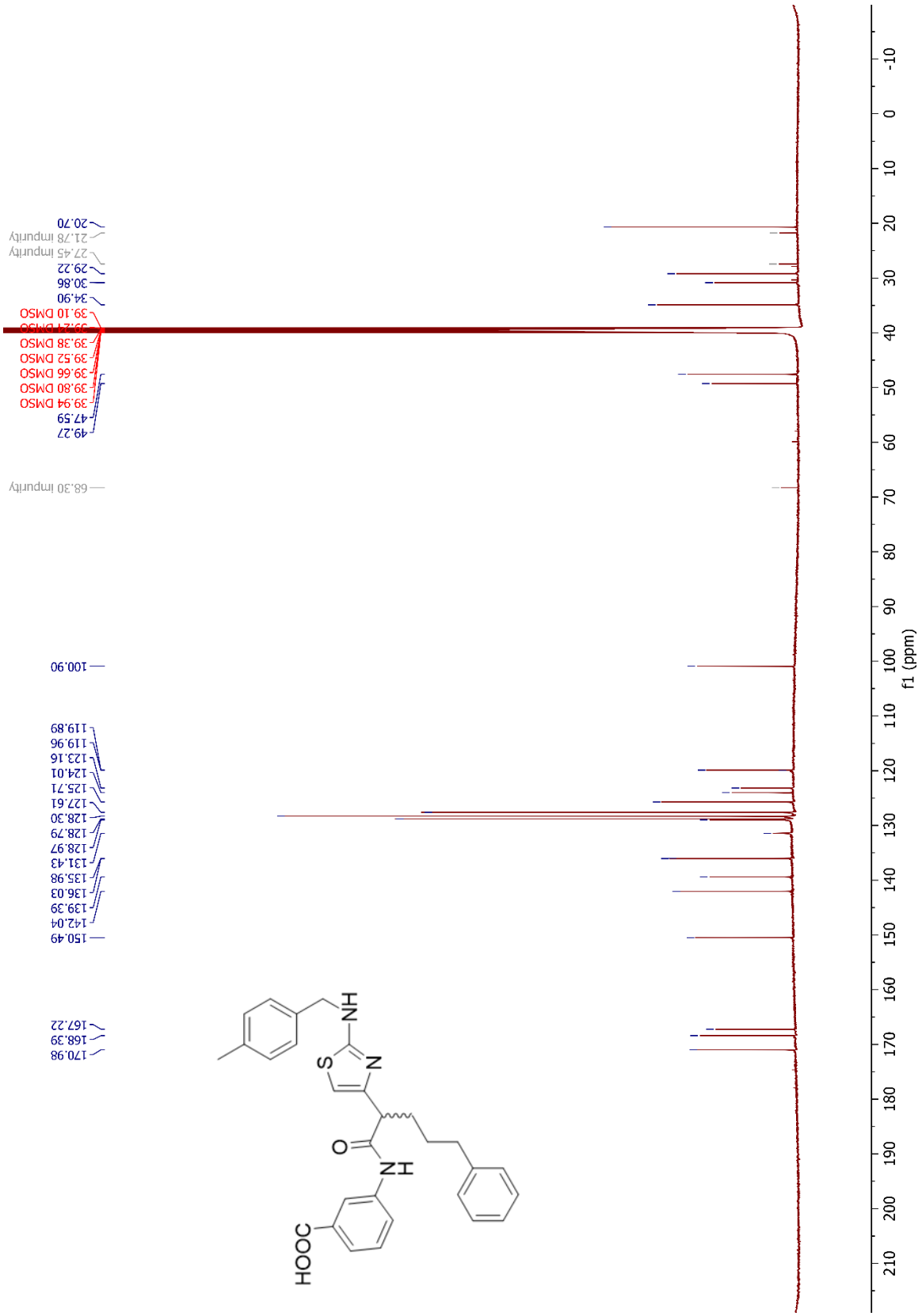
20.70
21.78 impurity
27.45 impurity
29.22
30.86
34.90
39.10 DMSO
39.38 DMSO
39.52 DMSO
39.66 DMSO
39.80 DMSO
39.94 DMSO
47.59
49.27
68.30 impurity
100.90
119.89
119.96
123.16
124.01
125.71
127.61
128.30
128.79
128.97
131.43
135.98
136.03
139.39
142.04
150.49
167.22
168.39
170.98
HN
S
N
O
HN
HOOC
f1 (ppm)

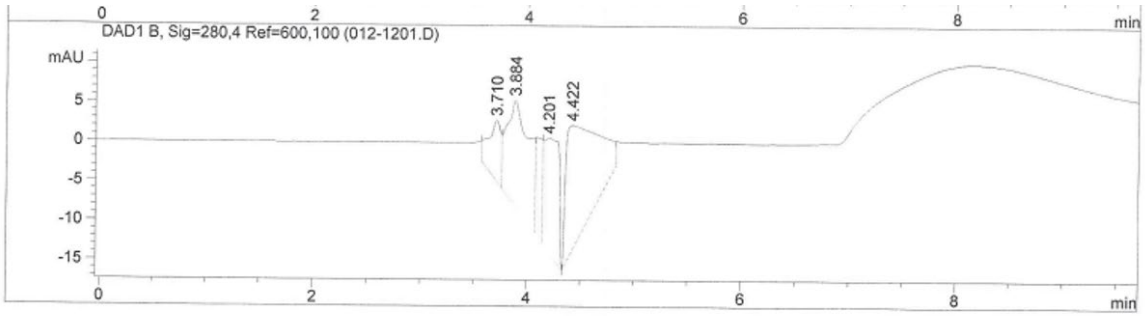


Signal 2: DAD1 B, Sig=280,4 Ref=600,100

| Peak # | RetTime [min] | Type | Width [min] | Area [mAU*s] | Height [mAU] | Area % |
|---|---|---|---|---|---|---|
| 1 | 3.710 | BV | 0.1083 | 61.00814 | 7.70938 | 8.5576 |
| 2 | 3.884 | VB | 0.1929 | 203.64543 | 13.42780 | 28.5652 |
| 3 | 4.201 | BV | 0.1340 | 147.67772 | 14.35649 | 20.7147 |
| 4 | 4.422 | VB | 0.2578 | 300.58215 | 15.95692 | 42.1625 |
| Totals : | | | | 712.91345 | 51.45058 | |

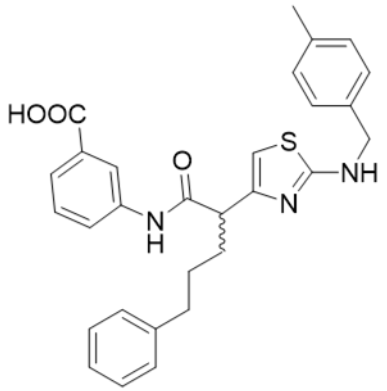

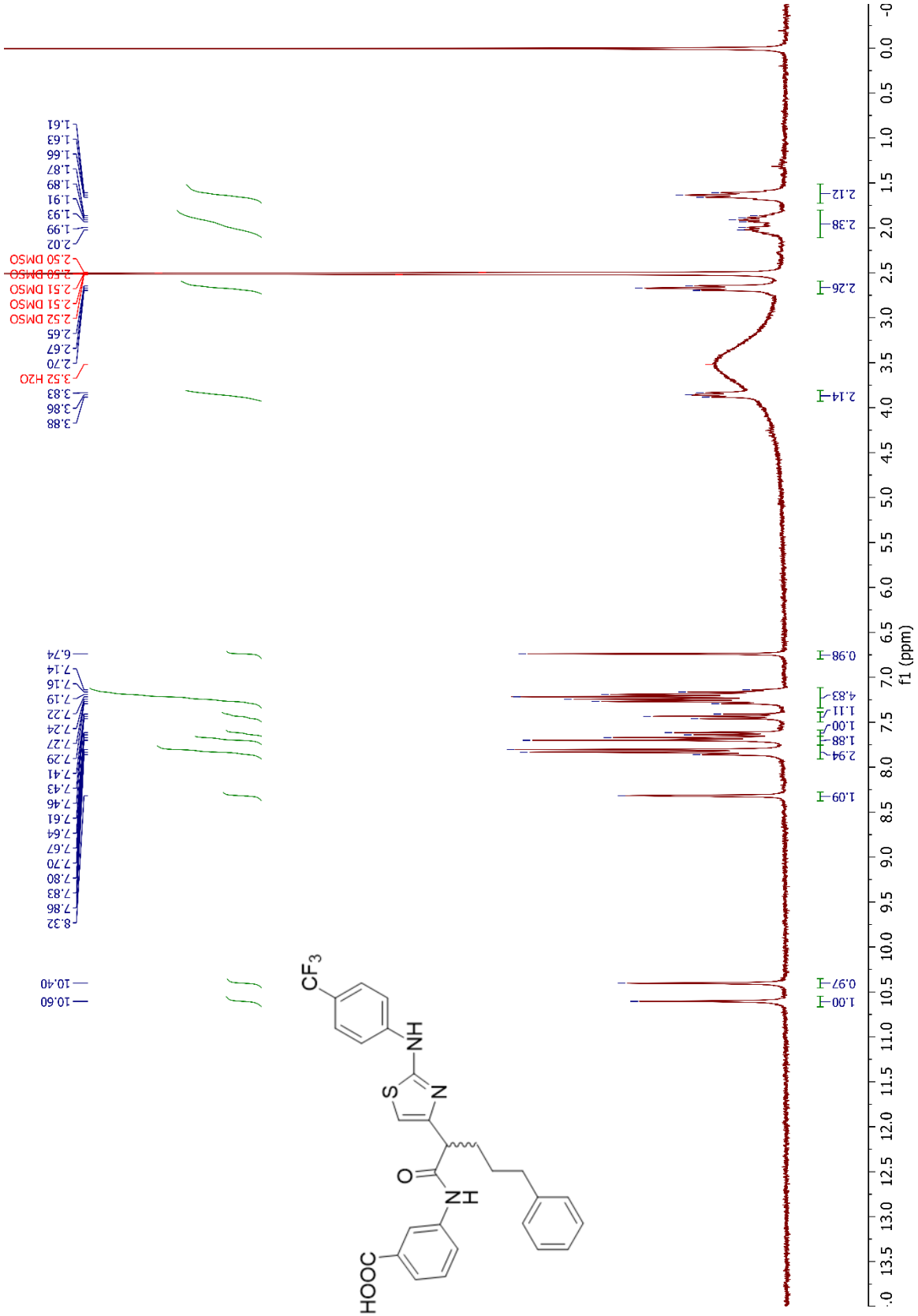
1.61
1.63
1.66
1.87
1.89
1.91
1.93
1.99
2.02
2.50 DMSO
2.50 DMSO
2.51 DMSO
2.51 DMSO
2.52 DMSO
2.65
2.67
2.70
3.52 H2O
3.83
3.86
3.88
6.74
7.14
7.16
7.19
7.22
7.24
7.27
7.29
7.41
7.43
7.46
7.61
7.64
7.67
7.70
7.80
7.83
7.86
8.32
10.40
10.60
2.12
2.38
2.26
2.14
0.98
4.83
1.11
1.00
1.88
2.94
1.09
0.97
1.00
CF3
NH
S
N
O
NH
HOOC
f1 (ppm)

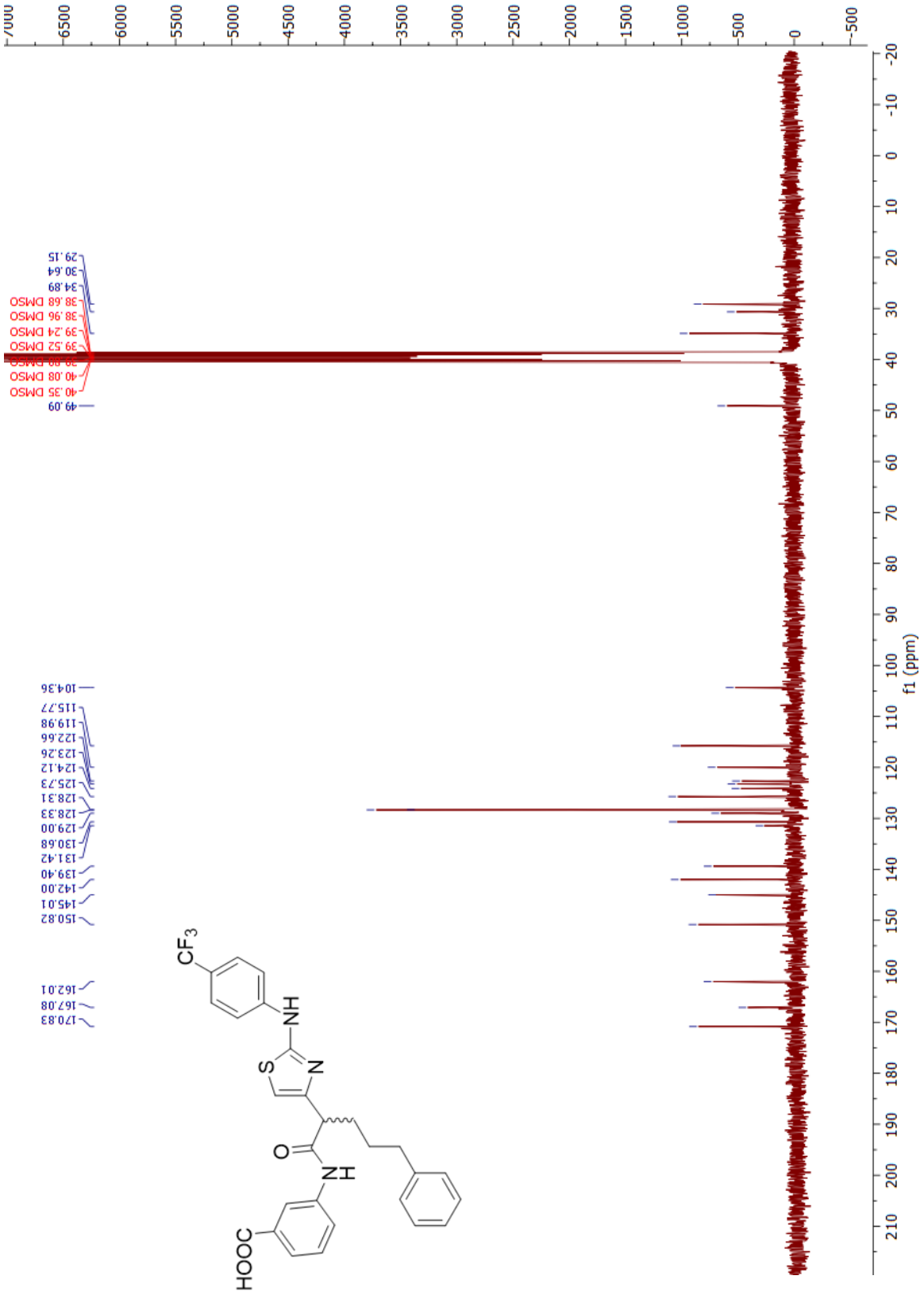
f1 (ppm)
29.15
30.64
34.89
38.68 DMSO
38.96 DMSO
39.24 DMSO
39.52 DMSO
40.08 DMSO
40.35 DMSO
49.09
104.36
115.77
119.98
122.66
123.26
124.12
125.73
128.31
128.33
129.00
130.68
131.42
139.40
142.00
145.01
150.82
162.01
167.08
170.83
CF3
NH
S
N
O
NH
HOOC

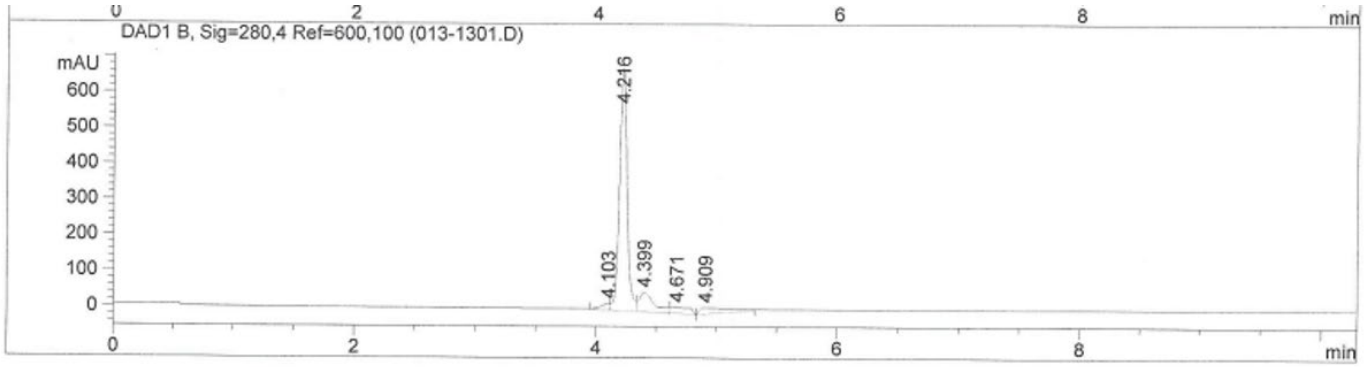


Signal 2: DAD1 B, Sig=280,4 Ref=600,100

| Peak # | RetTime [min] | Type | Width [min] | Area [mAU*s] | Height [mAU] | Area % |
|---|---|---|---|---|---|---|
| 1 | 4.103 | BV | 0.0733 | 99.00372 | 18.85451 | 2.4532 |
| 2 | 4.216 | VV | 0.0672 | 2990.34351 | 681.56464 | 74.0982 |
| 3 | 4.399 | VV | 0.1313 | 476.45511 | 53.79618 | 11.8062 |
| 4 | 4.671 | VV | 0.1514 | 190.42976 | 16.65012 | 4.7187 |
| 5 | 4.909 | VB | 0.2401 | 279.41898 | 15.81436 | 6.9238 |
| Totals : | | | | 4035.65107 | 786.67981 | |